Growth of Metal Organic Frameworks (MOFs) layers on functionalized surfaces

Hongye Yuan

▶ **To cite this version:**

Hongye Yuan. Growth of Metal Organic Frameworks (MOFs) layers on functionalized surfaces. Material chemistry. Université Paris Saclay (COmUE), 2017. English. NNT : 2017SACLX058 . tel-01680169

HAL Id: tel-01680169
https://pastel.hal.science/tel-01680169

Submitted on 10 Jan 2018

HAL is a multi-disciplinary open access archive for the deposit and dissemination of scientific research documents, whether they are published or not. The documents may come from teaching and research institutions in France or abroad, or from public or private research centers.

L'archive ouverte pluridisciplinaire **HAL**, est destinée au dépôt et à la diffusion de documents scientifiques de niveau recherche, publiés ou non, émanant des établissements d'enseignement et de recherche français ou étrangers, des laboratoires publics ou privés.

NNT : 2017SACLX058

Etude de la croissance de films MOF sur des surfaces fonctionnalisées de silicium

Thèse de doctorat de l'Université Paris-Saclay
préparée à l'Ecole Polytechnique

École doctorale n°573 **Interfaces : approches interdisciplinaires, fondements, applications et innovation**
Spécialité de doctorat: Les Matériaux innovants et leurs applications

Thèse présentée et soutenue à Polytechnique, le 20 sep, par

Hongye YUAN

Composition du Jury :

Nathalie STEUNOU	
Professeur, Université Versailles-St Quentin (ILV)	Présidente
Rob AMELOOT	
Professeur, Université de Louvain (CSCC)	Rapporteur
Aude DEMESSENCE	
Chargée de Recherche, Université LYON-I (IRCELYON)	Rapporteur
Christian SERRE	
Directeur de Recherche, ENS Paris (IMPP)	Examinateur
Philippe ALLONGUE	
Directeur de Recherche, Ecole Polytechnique (LPMC)	Directeur de thèse
Catherine HENRY de VILLENEUVE	
Chargée de Recherche, Ecole Polytechnique (LPMC)	Co-Directeur de thèse

Thèse de doctorat

Acknowledgements

This work was conducted in the Laboratory of Physics of Condensed Matters (PMC), thanks to the China Scholarship Council (CSC) fellowship.

I am deeply indebted to Prof. Aude Demessence and Prof. Rob Ameloot, who reviewed my manuscript and wrote the report. I am also thankful to Prof. Christian Serre and Prof. Nathalie Steunou, for carefully reading my work and their suggestions. It really meant a lot to me.

I would like to express my sincere gratitude to my supervisors-Philippe Allongue and Catherine Henry de Villeneuve who gave me this opportunity to work on such an extremely interesting topic-controlling the nucleation and growth of Metal-Organic Framework (MOF) films on functionalized Si surfaces. I am deeply indebted to them, for having guided me for experiments, data analysis, and report/presentation writing/organizing of the work.

I also would like to thank Fouad Maroun, for his enthusiasm and kindness to help me correct my first result chapter (Chapter 3), for his solid knowledge background and great ideas to polish this chapter. I am also indebted to him for the SEM training.

I need to thank Maria Castellano Sanz as well, who helped me a lot at the beginning of my PhD and her precious accompanying in this wonderful topic. There are also other people in and/or out of the lab who helped me, gave me suggestions and cheered me up, Sandrine Tusseau-Nenez, Isabelle Maurin and Robert Cortes for XRD characterizations, Melanie Poggi for the SEM training, Andre Wack for his ingenious

design for my set-up, Alain Louis-Joseph for the NMR measurements, Eric Larguet for the TEM characterization, the talented glass maker--Jean-Michel Wierniezky, Stefan Klaes, Anne Moraillon, and so many other people I need to thank them a lot, it's really a pleasure to have you here.

Last but not least, I want to thank Anne-Marie Dujardin, who is always of great patience and efficiency to help me deal with the administrative documents, which saved me a lot of time so that I could focus on research. I also need to thank Melanie Fourmon-my dearest officemate for her kindness and her help in managing the trivial things for conference. Yeah, there are still so many people but I not gonna list one by one, thanks all of you.

At last, I would like to thank the most important people to me-my family, for your always unconditional support and understanding, without you, the world is nothing to me. I also would like to thank my friends, thanks a lot for your listening, your sharing, and for the time we spent together, for playing basketball, for playing games and so many tiny things that I will never forget.

Thanks again for all of you!

One step is ended, another one is undergoing, life is continuing…

Table of contents

Abstract ..... **III**
Chapter 1: Introduction **1**
1.1 Context of MOFs 1
1.2 Synthesis and properties of MOFs 2
1.3 Fabrication and characterizations of MOF Films 6
1.3.1 Assembly of preformed micro/nano crystals onto surfaces 7
1.3.2 Seeded growth 8
1.3.3 Electrochemical deposition 8
1.3.4 Layer-by-layer and Langmuir-Blodgett layer-by-layer deposition (LB-LbL) 9
1.3.5 Evaporation-induced formation of MOFs films 12
1.3.6 Direct growth/deposition of MOFs from solutions 14
1.4 Description of Fe^{3+}/BDC and NDC MOFs 15
1.5 Objectives and outline of the manuscript 19
1.6 References 21
Chapter 2: Experimental details **29**
2.1 Substrate preparation 29
2.2 Characterizations of as prepared substrates 33
2.3 Growth of MOF films 34
2.3.1 Preparation of solutions for film growth 34
2.3.2 Film growth 35
2.4 Film characterizations 35
2.5 References 37
Chapter 3: Direct growth of Fe^{3+}/BDC MOFs onto functionalized Si surfaces: effect of surface chemistry **38**
3.1 Introduction 38
3.2 Results 39
3.2.1 Growth onto carboxylic acid terminated Si surfaces (Si-COOH) 39
3.2.2 Growth onto pyridine terminated Si surfaces (Si-Pyridine) 49
3.2.3 Growth onto oxidized Si surfaces 53
3.2.4 Growth onto methyl terminated Si surfaces (Si-CH_3) 57
3.3 Effect of post-treatment 59
3.3.1 Thermal annealing 59
3.3.2 Soxhlet rinsing 62
3.3.3 Adhesion tests 65
3.4 Discussion 66
3.4.1 Identification of structural phases 66
3.4.2 Crystallite growth mode 74
3.4.3 Influence of the substrate surface chemistry 76
3.5 Conclusion 81
3.6 References 82
Chapter 4: Direct growth of Fe^{3+}/BDC MOF onto carboxylic acid terminated Si

surfaces: influence of synthesis conditions 84
4.1 Introduction 84
4.2 Results 85
4.2.1 Growth at different temperature 85
4.2.2 Influence of solution composition (T = 90 °C) 91
4.2.2.1 Influence of ratio and precursor concentration 91
4.2.2.2 Influence of additives 96
4.2.3 Time evolution of the film morphology and structure 101
4.2.3.1 Growth in solution with metal excess (R = 0.5) 102
4.2.3.2 Growth in solution with ligand excess (R = 2) 104
4.3 Discussion 108
4.3.1 Structural identification 108
4.3.2 Effect of solution composition 112
4.3.3 Nucleation and growth 114
4.4 Conclusion 117
4.5 References 119
Supplementary information of Chapter 4 121
Chapter 5: Nucleation and growth of Fe^{3+}/NDC MOF films on carboxylic functionalized Si surfaces 126
5.1 Introduction 126
5.2 Results 127
5.2.1 Influence of temperature 127
5.2.2 Influence of solution composition 130
5.2.2.1 Influence of ratio of ligand to metal 130
5.2.2.2 Influence of [Fe^{3+}] concentration 133
5.2.3 Influence of immersion time 140
5.2.4 Effect of post-treatments 143
5.2.4.1 Thermal annealing 144
5.2.4.2 Soxhlet rinsing 146
5.2.4.3 Solvent capture and release 148
5.3 Discussion 150
5.4 Conclusion 153
5.5 References 154
Supplementary information of Chapter 5 155
General summary and conclusion 161

Abstract

This work investigates the direct growth of materials - metal-organic frameworks (MOFs) - onto functionalized Si(111) substrates with different surface chemistries. Fe-based MOFs layers are obtained by exposing the silicon substrate to a solution containing Fe^{3+} and BDC or NDC in variable amounts. The morphology and structure of MOFs films are investigated by SEM, AFM and XRD.

For Fe^{3+}/BDC system, which may exist as MIL-101 and MIL-88B phases in solution, films always consist of isolated octahedral MIL-101 crystallites with the [111] direction perpendicular to the plane of pyridyl and hydroxyl terminated surfaces. On acid terminated surfaces (COOH), similar layers are obtained (isolated MIL-101 crystallites) when metal cations are in excess in solution. Data analysis suggests that crystallites are first formed in solution and then adsorbed on the surface along with further growth. A strong linkage with the substrate is however observed.

The growth of MIL-88B crystals with (001) texture is only observed onto COOH-functionalized surfaces and greatly favored by an excess of ligand in solution. In such conditions, addition of small amount of HCl promotes the formation of polycrystalline and continuous MIL-101 layers. Addition of triethylamine favors the formation of MIL-88B crystals. Data analysis suggests that both the MIL-88B and MIL-101 (in the presence of HCl) crystallites follow a Volmer-Weber growth mode, during which isolated crystals formed and grow laterally and vertically on the surface. A weak adhesion of MIL-88B crystals with the substrate is nevertheless found.

Textured MIL-88C films are obtained on COOH-terminated surface in all conditions. Ex-situ and in-situ XRD measurements demonstrate clearly the flexibility and reversibility of MIL-88C framework during molecule adsorption and desorption.

Résumé

Ce travail porte sur l'étude de la croissance directe de couches de matériaux - métal-organiques frameworks (MOFs) - sur substrats de Si(111) fonctionnalisées avec différentes chimies de surface. Les couches de MOF à base de fer sont construites lors de la mise en contact du substrat de silicium avec une solution contenant des espèces Fe^{3+} et BDC ou NDC en proportions variables. La morphologie et la structure des couches sont étudiées par SEM, AFM et XRD.

Pour le système Fe^{3+}/BDC, qui existe sous la forme MIL-101 ou MIL-88B en solution, les films sont systématiquement composés de cristallites MIL-101 isolés de forme octaédrique avec leur direction [111] perpendiculaire au plan de la surface si celle-ci est terminée par des groupements pyridyles ou hydroxyles. Sur les surfaces avec une terminaison acide (COOH), l'excès de cations métalliques favorise la formation de couches similaires (cristallites MIL-101). L'analyse des données suggère que les cristallites sont d'abord formés en solution et qu'ils s'adsorbent progressivement sur la surface avec une croissance supplémentaire en formant néanmoins une liaison forte avec le substrat.

La croissance de cristaux MIL-88B avec une texture (001) est uniquement observée sur des surfaces fonctionnalisées COOH et fortement favorisée en présence d'un excès de ligands. L'introduction d'une faible quantité de HCl favorise cependant la

formation de couches polycristallines et continues de MIL-101. L'addition de triéthylamine favorise la formation de MIL-88B. L'analyse des données indique que la formation des couches MIL-88B et MIL-101 (en présence de HCl) suit une loi de croissance de Volmer-Weber sur les surfaces COOH, au cours duquel les cristaux isolés nucléent et se développent latéralement et verticalement sur la surface. L'ancrage des cristallites (MIL-88B) sur la surface est cependant faible.

Des films texturés MIL-88C ont également été obtenus sur des surfaces COOH. Les mesures expérimentales ex situ et in situ de XRD démontrent clairement la flexibilité et la réversibilité du cadre MIL-88C pendant l'adsorption et la désorption des molécules.

Chapter 1: Introduction

1.1 Context of MOFs

Metal-organic frameworks (MOFs) or porous coordination polymers (PCPs) are essentially crystalline inorganic-organic hybrid materials with coordinative bonding formed by association of metal centers or clusters (inorganic part) and organic linker(s) bearing functional groups. Since the foremost definition as metal-organic frameworks by Omar Yaghi in 1995 [1-3], MOFs have emerged as promising porous materials featuring versatile and adjustable porous topologies, resulting from the modular concept of combining metal centers and organic ligands for the construction of extended three-dimensional framework structures (**Figure 1.1**). A large variety of metal centers concerning di-, tri- (including rare earth) or tetravalent cations can participate in the building of MOFs architectures. The functional groups of organic linkers connected to the metal centers are most frequently carboxylates, phosphonates, sulfonates and nitrogen derivatives such as pyridines, cyanides and imidazoles [2-8]. Furthermore, the backbone network of the bridging molecules (rigid or flexible) can be functionalized, for instance, with halogeno, amino and sulfonic groups prior to and/or after MOF synthesis, resting with the desired applications. The above three factors contribute to the enormous variety of potential MOF structures with variable (average) pore size, porosity and surface area, triggering massive consistent efforts toward the exploration of synthesis of novel frameworks as nano/micro crystalline powder that possess new topologies and open structures with exceptionally large surface area [9-13].

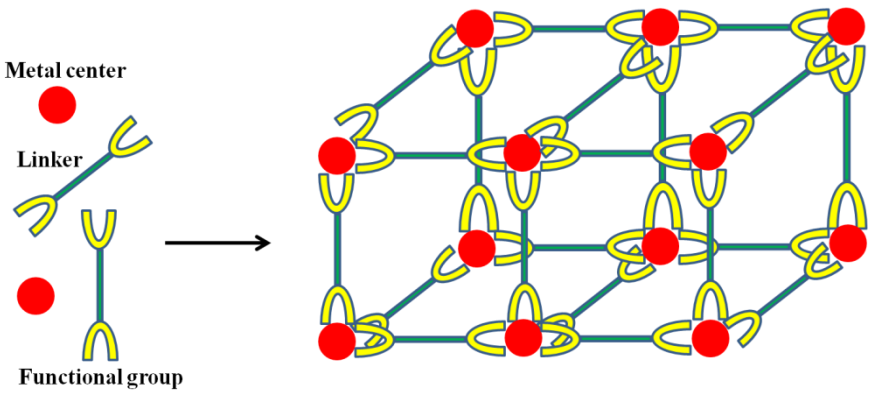

Figure 1.1 General scheme for construction of MOFs: organic linkers with at least two functional groups coordinate with metal ions or cluster centers leading to 3 dimensional framework structures.

1.2 Synthesis and properties of MOFs

Synthesis of MOFs requires conditions that lead to formation of well-defined inorganic building blocks (often termed as second building units (SBUs) firstly defined by Férey [14]) without decomposition of the organic linkers. Meanwhile, the thermodynamics and kinetics of crystallization must be satisfied to allow for the nucleation and growth of desired phases to take place. Experimentally, many parameters like compositional (molar ratios of ligand to metal, starting precursor concentration, starting metallic salt, pH value, solvent, etc.) and process parameters (temperature, pressure and even reaction time) are found vital to the formation of resulted framework structures [15-23]. Diverse synthesis methods such as conventional hydrothermal/solvothermal, micro-wave assisted, electrochemistry, mechanochemistry and ultrasonic ones as depicted in **Figure 1.2** are considered important as well to the crystal morphologies, size, yields of the MOFs product and thus their physical and chemical properties.

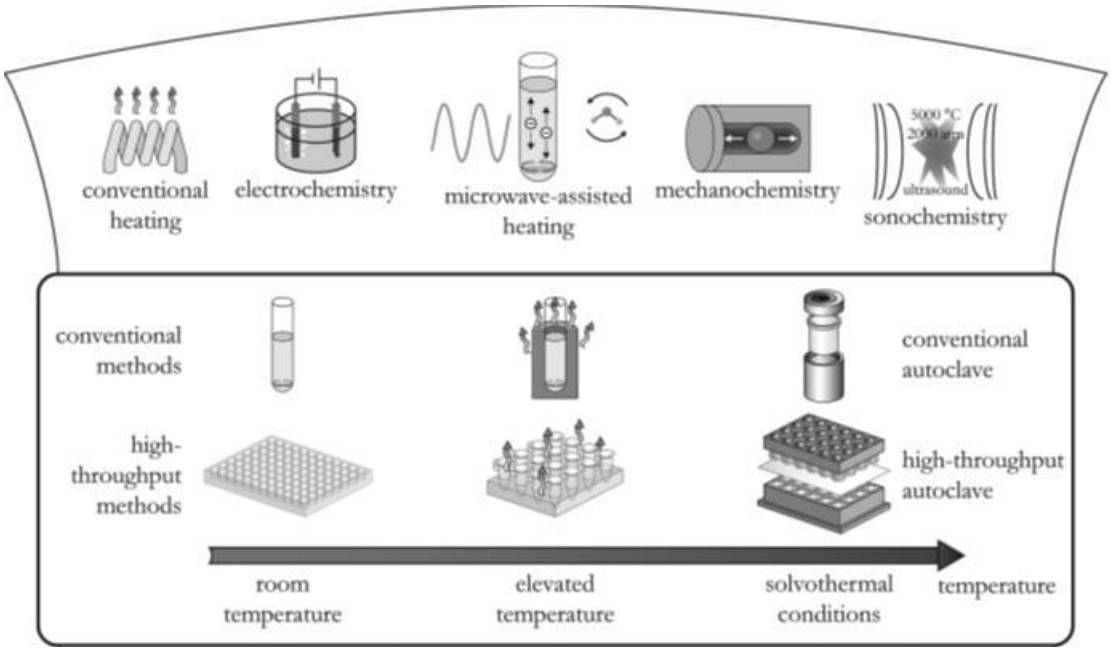

Figure 1.2 Overview of synthesis methods and possible reaction temperatures regarding the formation of MOFs. Figure reproduced from Ref [15].

For example, by variety to the conventional heating way like electric resistance heating, the introduction of micro-wave irradiation into the synthesis of MOFs provides an efficient methodology to synthesize them with short reaction time, narrow particle size distribution, facile morphology control, high crystallinity and relatively efficient determination of compositional and process parameters [24-27] etc., attributed to the rapid and uniform heating of the reaction solutions. As mentioned above, the richness of possibility of linkage between inorganic moieties and linkers renders the delicate estimation of synthesis parameters extremely time-consuming and unachievable. Since its popularity in the synthesis of zeolites and zeotypes inorganic compounds, the high-throughput method which enables the systematic investigation of synthesis parameters and faster and less expensive access to a large variety of synthesis information has been proven an ideal tool to better understand the role of parameters involving the formation of MOFs materials [19,28,29,30,31,32]. While, the application of high-throughput method does not enlighten one on the reaction mechanism or synthesis pathways for distinct phases (including intermediate phase) because of the fair complexity of metal ions-anions-solvent interactions and also the high number of competing events happening during MOF construction. Before the

mastery of a precise and thorough understanding toward the formation mechanisms, the phrase “design” of structures or “tailor-made” structure referring to the synthesis of MOFs is still debatable according to several reviews although the trial-and-error or automated approaches provide valuable empirical assembly rules of known and well-defined structures [33-36]. Currently, ex-situ or in-situ studies have been performed by means of specific equipments such as extended X-ray absorption fine structure spectroscopy (EXAFS), X-ray powder diffraction (XRPD), energy-dispersive X-ray diffraction (EDXRD), small/wide angle X-ray scattering (SAXS/WAXS), static light scattering (SLS), surface plasmon resonance (SPR) etc, to monitor the crystallization process [37-45]. Thanks to the above techniques, a broad range of information such as the formation and duration of inorganic bricks, the influence of metal ions, heating methods on crystallization kinetics and detection/isolation of intermediate phase involving the key points of MOFs formation mechanism can be obtained and/or evaluated.

Millange and his co-workers [43] presented the first report of time-resolved in situ EDXRD study on crystallization of various MOFs (HUKST-1 ($[Cu_3(BTC)_2]$, BTC=benzene-1,3,5-tricarboxylic acid), MIL-53 ($Fe(OH,F)\{O_2C\text{-}C_6H_4\text{-}CO_2\}\cdot mH_2O]$)) in solvothermal condition. Two distinguished crystallization scenarios were observed for the two transition-metal carboxylate MOFs. The crystallization kinetics of HUKST-1 was evaluated using the Avrami Erofeev model and a classical nucleation controlled reaction was observed, with nucleation happening over the time-scale. Whereas, the formation of MIL-53 occurred via the metastable phase-MOF-235 [46], in which trimers of FeO_6-octahedra are in linkage with terephthalate ligands, and the trapped species inside the porous three-dimensional network are not only DMF molecules but also $[FeCl_4]^-$ anions that balance the positive charge of the MIL-53 framework. The intermediate phase MOF-235 can also be isolated by quenching the reaction mixture at intermediate temperatures (between 100-125 ^oC). In situ SAXS/WAXS study on the crystallization process of NH_2-MIL-101(Al) and NH_2-MIL-53(Al) was reported afterwards by E.

Stavitski et al. [44]. Their findings also confirm the existence of the metastable phase MOF-235(Al)-NH_2 and as a kinetic phase it has inclination to transform first into MIL-101(Al)-NH_2 phase and then the resulted MIL-101(Al)-NH_2 phase can also further dissolve and transform into NH_2-MIL-53(Al) in DMF when the reaction temperature rises. The formed MOF-235(Al)-NH_2 in a mixture medium of H_2O and DMF could hydrolyze and then transfer into the thermodynamically stable phase NH_2-MIL-53(Al) under higher temperature. And yet, considerable efforts still need to be made to correlate the synthesis conditions with the formation of inorganic bricks and with desired framework topologies to eventually realize the fine-design of MOFs in synthesis and goal-seeking performances that will be presented next.

MOFs materials featuring large porosity, high specific surface area, well-defined pore shape and controllable size are regarded as good candidates for applications such as gas storage [47,48], drug delivery [49-51], molecular separation/purification [52,53], heterogeneous catalysis [54,55], chemical/biochemical sensors [56,57] etc. More interestingly, possibility of tailoring the pore size, accessibility and engineering crystal surfaces and internal interfaces, either by typically controlling the length of organic linkers or through pre- and/or post-synthesis functionalization of frameworks or just by intentionally creating defects within the frameworks has been attracting huge attention and efforts for their applications [5,15]. In addition, it is striking that some types of MOFs frameworks, pioneered by the groups of S. Kitagawa and G. Férey, exhibit so-called "breathing" phenomenon with response to external stimuli (temperature, mechanical force, light, electric or magnetic field, molecule guests…), which are very interesting for applications involving host-guest interactions such as gas separation, chemical sensors and biochemical purposes [20,58,59]. The networks of those materials usually transform between open pore and closed pore or narrow pore and large pore forms and therefore feature a drastic structural change in pore volume, not necessarily with phase transition. Literatures addressing the classification of different modes of framework flexibility based on various mechanisms, monitoring/characterization of transformation process and their applications are

currently abundant [60-63]. While, the two most prototypical examples that were most-extensively studied are the MIL-53(M) family ([M(bdc)(OH/F)]n with bdc = terephthalic acid, and M =Al [64], Fe [65], Cr [20,66], Sc [67], Ga [68], In [69]) and MIL-88(A-D) class ($M_3O(X)_3$ (M = Fe^{3+},Cr^{3+}; X= fumaric acid (MIL-88A), bdc (MIL-88B), 2,6-ndc (2,6-naphthalenedicarboxylic acid; MIL-88C) or bpdc (4,4'-biphenyldicarboxylic acid; MIL-88D) [20].

1.3 Fabrication and characterizations of MOF Films

More recently, the fabrication of MOF layers on solid supports has received increasing interests as it opens up perspectives for the development of MOFs-based devices, which can be applied to many applications like chemical sensors, membranes and catalysis. The basic idea for preparation of MOFs films contains first choosing one interested MOF (*e.g.*, by the porosity, pore size and properties) and then employing a suitable method to process it as a film on top of a substrate. Depending on the preparation approach, surface structure and composition of the given substrates and even synthesis conditions (specifically in the work we are about to present), MOFs films with and without preferential orientation can be obtained. Hereon, non-oriented films can be seen as an assembly of MOF crystals or particles with random orientation that are attached to a chosen substrate. The crystals can either be inter-grown to totally cover the surface or scattered in a non-continuous fashion. In the contrary, the binding/attachment of MOFs crystals to the substrate can be realized in a preferred direction, giving rise to textured MOF layers or isolated crystallites or islands with preferential orientation [70-72]. To date, different approaches have been developed for the formation of MOFs films: direct growth/deposition from solutions [73-75]; stepwise or layer-by-layer growth by immersing the substrate alternatively in solutions of the metal precursor and the organic ligand [76]; assembly of preformed micro/nano crystals onto surfaces [27,77,78]; electrochemical deposition [79-83] and evaporation-induced growth [84,85]. Meanwhile, the concept of using self-assembled

monolayers (SAMs) to direct the nucleation, growth and orientation of MOFs on solid supports has been initiated by Fischer et al. [73,76,86] and Bein et al [74,87,88]. **Figure 1.3** presents the scheme of MOF growth on SAM-functionalized surface where the head-end functional groups of the SAM could coordinate to the metal centers or SBUs from the solution to initial the nucleation. Crystal growth will be subsequently continued by the further linkage of organic ligands present in the solution, in such a way, leading to the growth of MOF crystals being directly bound to the substrate. In the following, an overview of different preparation ways of MOFs films and their characterizations based on the reported works are presented. Growth of oriented MOFs layers with well arrangement of channels of porous modules promising for nano-devices remains however a challenge for most of MOFs.

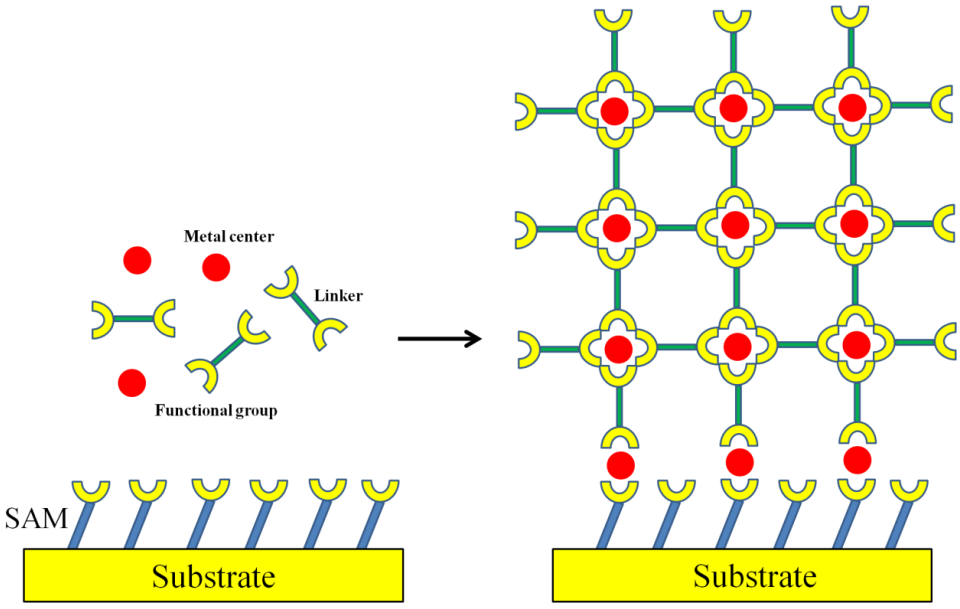

Figure 1.3 Scheme of MOFs growth on SAM-functionalized surface. Note that the functional groups of the SAMs are not necessarily the same to the terminated functional groups of organic linkers.

1.3.1 Assembly of preformed micro/nano crystals onto surfaces

Preparation of MOF films by assembly of preformed objects has been extensively investigated by A. Demessence, C. Serre, and their co-workers [27,89,90]. Their approach relies on the fabrication of well-defined MOF crystals first and afterwards transferring them onto the substrate just by dip-coating. The preparation of nanocrystals with

homogenous size was achieved under microwave irradiation for quite a short time (1 min). After harvesting and characterization, the obtained particles were re-dispersed in ethanol to form a stable colloidal suspension solution, into which bare silicon substrates were dip coated. Thickness of MOF layers is controllable by varying the particle concentration in ethanol and also the repetition times for coating. The successful fabrication of three different kinds of MOFs films-MIL-89(Fe) [89], MIL-101(Cr) [27], and ZIF-8 [90] strongly demonstrates the generality of this method. However, the adhesive properties of such films on substrate, especially for thicker ones, are expected to be problematic.

1.3.2 Seeded growth

Just as its name implies, this method involves the preparation of seeded layers or isolated particles/crystals onto the substrate prior to the further film growth. The pre-formed seeds are of various natures: MOF nanocrystals or thin layers [91-93], zinc oxide [94], zinc phosphate [95], coordination polymers [96] etc., which can be fabricated by several types of techniques such as wiping, dip coating, spin coating and in-situ crystallization [97]. And the procedure for seeding is of vital importance to the further MOF film growth. The sequent growth is usually done in solvothermol conditions and commonly dense and crystalline MOFs films without orientation can be obtained.

1.3.3 Electrochemical deposition

Based on the electrochemical synthesis of MOFs which has been introduced by researchers at BASF [98], R. Ameloot et al. [79] firstly demonstrated that it is feasible to coat the metal electrodes by a HKUST-1 MOF film through modifying the conditions and without stirring the solution during film preparation. When exposing to a biased voltage, the copper electrode immersed in a BTC solution starts to release the Cu^{2+} ions into the solution. MOF layer is formed once the Cu^{2+} ions encounter the BTC linkers adjacent to the anodic electrode surface. The formed layers comprised of highly intergrown and homogeneous crystallites and with variable thicknesses ranging

from 2 to 50 μm by variation of the water content of the solution as well as the parameters of the applied voltage were successfully got in 30 min or less. The drawbacks of this method are that the deposition will terminate at some point when the MOF film covers the whole anodic surface and only conductive substrates are amenable to this method. Two years later, M. Dincă et al. [81] presented the first example of fabrication of MOF-5 films ($Zn_4O(BDC)_3$) onto inert fluorine-doped tin oxide (FTO) working electrode by cathodic electro-deposition at room temperature. Different from the above example, a Pt auxiliary served as the anodic electrode. Rough films whose thickness varies from 20 to 40 μm were obtained after only 15 min, suggesting a fast and facile method of synthesizing MOF films. The proposed mechanism for the formation of MOF-5 films elucidates that the reduction of nitrate (NO_3^-) to NO_2^- occurred in the vicinity of cathode and thereby allows the accumulation of HO^- anions near the conductive surface, which in return contributes to the deprotonation of BDC and further confines the MOF-5 crystallization at cathodic electrode. A further study concerning the mechanism of MOF-5 formation under cathodic bias [82] from the same group evidenced that the nitrate anions play an essential role in the formation of the $Zn_4O(O_2C-)_6$ SBUs and thus determines the subsequent formation of MOF-5 on FTO substrate regardless of the hydration content.

1.3.4 Layer-by-layer and Langmuir-Blodgett layer-by-layer deposition (LB-LbL)

Originally designed for polyelectrolyte held together by electrostatic interactions [99], the layer-by-layer or step-by-step method was firstly introduced into the fabrication of MOFs films by R. A. Fischer, Ch. Wöll and their co-workers [76]. The reactants (metal source and ligand) for constructing MOF frameworks are separated during the layer-by-layer approach. The substrate functionalized by organic monolayers bearing suitable terminal functional groups is immersed alternatively into two solutions containing the two precursors at low temperature (between 25 and 40 ^oC). For each circle, rinsing step is carried out toward the sample to remove unreacted precursor from the surface (see **Figure 1.4**).

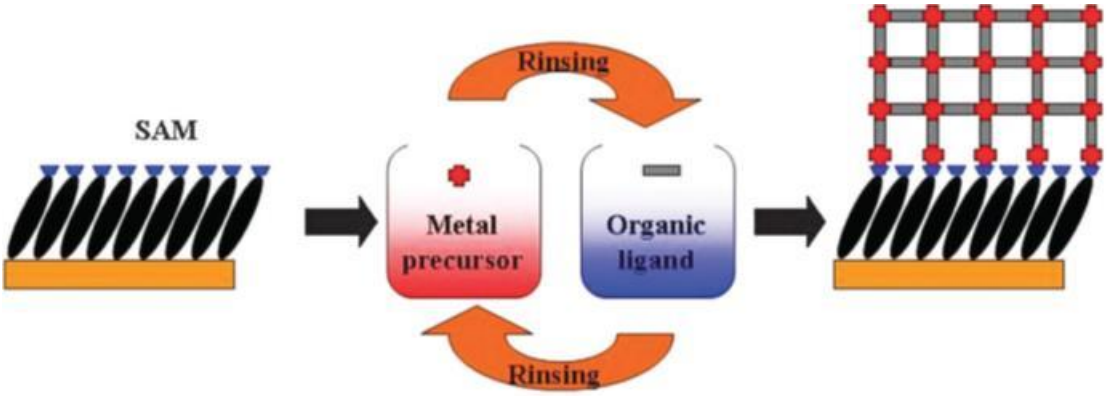

Figure 1.4 Schematic diagram for the layer-by-layer growth of MOFs on substrates functionalized with SAMs. The approach is done by repeated immersion cycles first in solution containing metal precursor and subsequently in the solution of organic ligand. Rinsing procedure is needed in between. Figure reproduced from Ref [100].

Homogeneous, crystalline and various types of MOFs films, for instance, two components-HKUST-1 ($Cu_3(btc)_2$) [76,100], three components with the formula [M_2L_2P], where M=Cu^{2+} or Zn^{2+}, L=a rigid, linear dicarboxylate linker, and P=an optional diamine pillar [101-103], with controllable thickness and texture have been successfully obtained using the stepwise growth fashion. More interesting, the layer-by-layer method provides the possibility of monitoring each deposition of inorganic parts and the ligands by AFM, SPR spectroscopy or a quartz crystal microbalance (QCM) etc. Bear in mind that this method is only applicable to MOFs that can be constructed at lower temperatures and also has high requirement for the quality of SAMs on substrates, which plays a crucial role in the quality of deposited MOFs.

In 2010, H. Katagawa and his co-workers [104] reported the first example of fabrication of ultrathin and oriented MOF nanofilms (NAFS-1 and NAFS-2) on solid surfaces at room temperature, combing the layer-by-layer method with the Langmuir Blodgett technique. **Figure 1.5** presents the schematic illustration of fabrication approach of NAFS-1 using this approach.

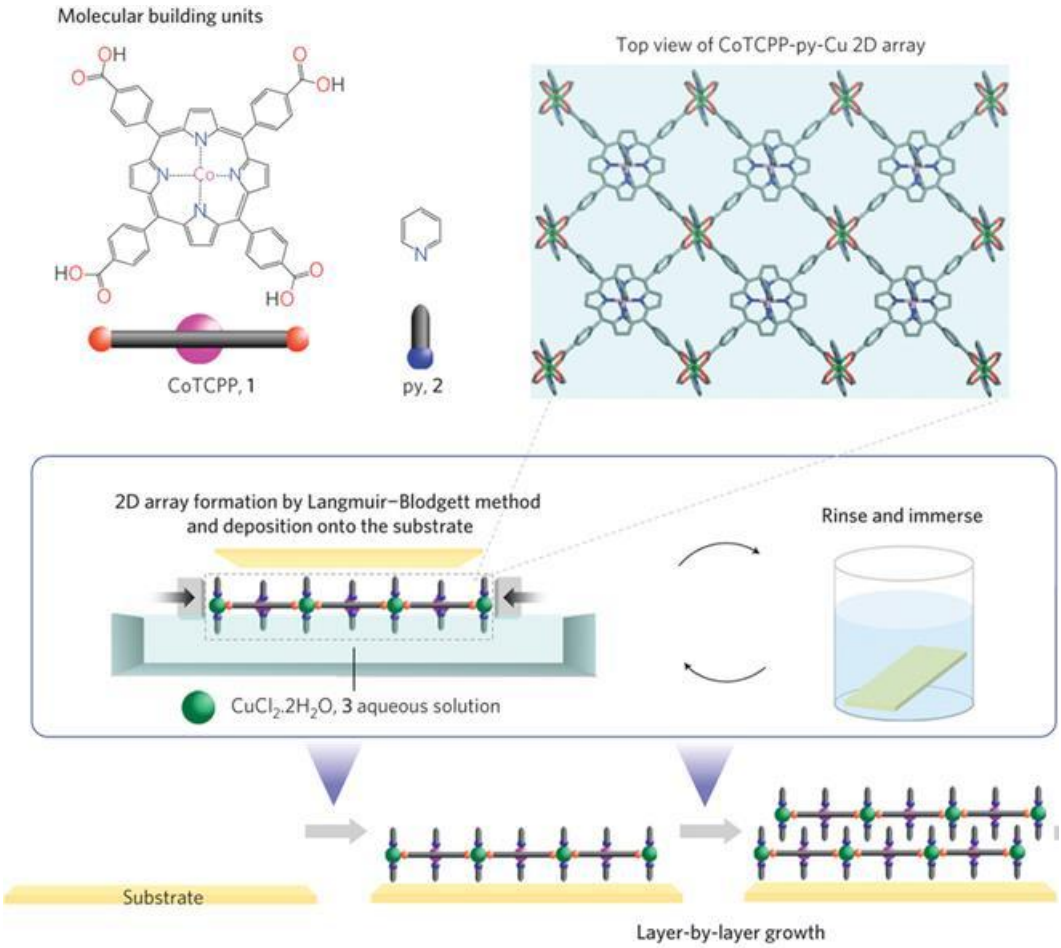

Figure 1.5 Schematic illustration of the fabrication method of NAFS-1. The solution mixture of CoTCPP (1) and pyridine (2) molecular building units is spread onto an aqueous solution of $CuCl_2$ $2H_2O$ (3) in a Langmuir trough. Pressing the surface with barrier walls leads to the formation of a copper-mediated CoTCPP 2D array (CoTCPP-Py-Cu) (Langmuir–Blodgett method). The 2D arrays are deposited onto the substrate by the horizontal dipping method at room temperature. Figure reproduced from Ref [104].

Cobalt-porphyrine units (CoTCCP) are assembled together by binuclear copper paddle-wheel units in terms of coordination bonds to form two-dimensional arrays due to the increasing the precursor concentration and surface pressure when the trough is compressed. Meanwhile, the vertical positions of the copper ions are connected by the pyridine molecules and proper π-stacking (norml to the 2D arrays) between different layers can thus be established so as that the prefect preferentially oriented NAFS-1 thin films are achieved layer-by-layer. In plane and out of plane XRD measurements clearly show that the NAFS-1 films are highly crystalline and well-oriented.

1.3.5 Evaporation-induced formation of MOFs films

R. Ameloot et al. [105] proposed a particularly facile way for making patterned MOFs layers on a variety of substrates with different terminations (silanol, vinyl or carboxylic acid). This method is based on the first preparation of precursor solution containing the two constituents but without any MOF nuclei (confirmed by dynamic light scattering (DLS)). The solution was afterwards transferred to substrates by a polydimethylsiloxane (PDMS) stamps possessing differently sized and spaced square protrusions. The solution was only confined under these protrusions due to the capillary forces. In situ crystallization occurred at solvent evaporation. Monodispersed HKUST-1 crystals in various motifs were obtained at last as a consequence of physical boundaries present during MOF construction. Later, an alternative way to realize the localized transformation of metal oxides to crystalline and compact MOF films under solvent and/or solvent-free synthesis conditions was reported by several groups (R. Ameloot, S. Kitagawa and R. A. Fischer) [106-108].

R. Ameloot and his co-workers [84] reported quite recently a novel strategy for fabricating MOF films in a conformal way using a chemical vapour deposition (MOF-CVD) approach. The 'MOF-CVD' method entails two steps: a uniform thin metal oxide layer with controllable thickness (serve as the metal source for constructing the desired MOF) is fabricated by atomic layer deposition (ALD) first and then a vapour-solid reaction is implemented from outside to internal of the deposited layer (see **Figure 1.6**). The organic linkers are supplied as a vapour instead of in solution, which allows the localized transformation of ultrathin zinc oxide precursor into MOF layers. A series of ultrathin, conformal and homogeneous MOF films like ZIF-8, ZIF-61, ZIN-67 and ZIF-72 (ZIFs stands for zeolitic imidazolate frameworks) were successfully prepared using this method. The authors also studied the oxide-to-MOF conversion efficiency of ZIF-8 (with the 2-methylimidazole (HmI) as the ligand) films on zinc oxide precursor layers of various thickness via multiple techniques such as transmission electron microscopy (TEM), high-angle annular

dark-field (HAADF), energy dispersive X-ray spectroscopy (EDS) mapping and profiling, time-of-flight secondary ion mass spectroscopy (TOF-SIMS) and X-ray diffraction. Results clearly show that a complete transformation of precursor films of less than 10 nm thickness can be easily achieved, accompanied by the interference change (colour from dark to mirror-finish) and film thickness expansion (around 17-fold). Combing with the soft lithography or lift-off patterning, the solvent-free MOF-CVD method where corrosion, chemical contamination and processability and cost concerns can be avoided is greatly promising for the integration of MOF materials in microelectronic devices both in research and production facilities.

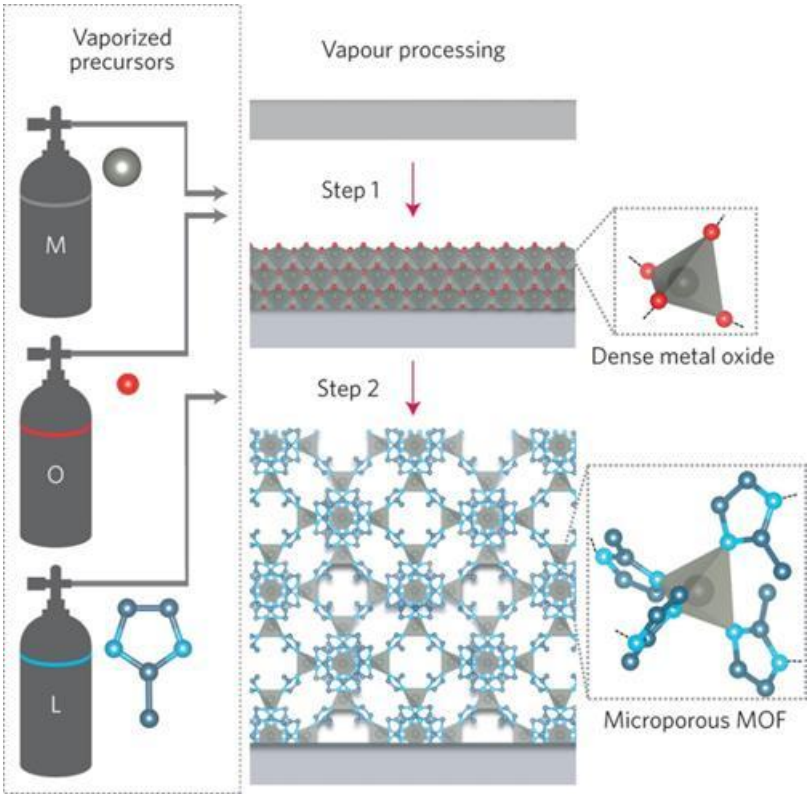

Figure 1.6 Chemical vapour deposition of ZIF-8 thin films. The procedure consists of a metal oxide vapour deposition (Step 1) and a consecutive vapour–solid reaction (Step 2). Metal, oxygen and ligand sources are labelled as M, O and L, respectively. Metal oxide deposition can be achieved by atomic layer deposition (M, diethylzinc; O, oxygen/water) or by reactive sputtering (M, zinc; O, oxygen plasma). Atom colours: zinc (grey) oxygen (red), nitrogen (light blue) and carbon (dark blue); hydrogen atoms are omitted for clarity. Illustration reproduced from Ref [84].

1.3.6 Direct growth/deposition of MOFs from solutions

A much more straightforward way to make MOF films is just immersing the substrate (bare or modified) in solution containing the necessary organic and inorganic bricks and let the crystallization (heterogeneous nucleation and growth) upon surface proceed under an appropriate condition for a certain time. Given the homogeneous nucleation and growth taking place simultaneously in solution, the active surface of substrate is supposed to being placed vertically or being kept face-down to avoid the precipitation from solution. Generally, heating (conventional or unconventional) is mandatory for most of the MOFs (above 100 ^{o}C). While, for the most common used thiol-based SAMs on gold in order to direct/initial the heterogeneous nucleation and subsequent growth the thermal stability is hugely problematic to work at such condition. To tackle this issue, R. A. Fischer and his co-workers [73] firstly tried to pre-heat the precursor solution for building MOF-5 at 75 ^{o}C for 3 d and then at 105 ^{o}C. After, the solution was cooled down to 25 ^{o}C and kept at this temperature for 24 h. The thiol-modified gold substrates were immersed into the solution after filtering the sediments. Film composed of MOF-5 crystallites with a thickness of 5 μm was found only on COOH-terminated SAM after 24 h crystallization at room temperature whereas no film growth happened onto CF_3-terminated stripes. Zn complexes (SBUs) and/or MOF-5 nuclei were considered to be selectively coordinated to COOH groups at the surface and the further construction of MOF-5 was subsequently continued. T. Bein et al. applied this approach to several other MOF structures: HKUST-1 [74], Fe-MIL-88B [87], and CAU-1($[Al_4(OH)_2(OCH_3)_4(H_2N\text{-}bdc)_3]\cdot xH_2O$, CAU=Christian-Albrechts-University) [109]. The starting solution composition and the pre-treating program are thought as key parameters, which probably determine the formation of SBUs and/or the size and concentration of nuclei. They also demonstrated for the first time the attached crystal orientation can be tailored by varying the terminal functionalities of SAMs. One interesting aspect regarding the formation of hexagonal MIL-88B film is that the bulk phase is MIL-53, formed in the pre-treating procedure. The selective nucleation and growth of MIL-88B onto

COOH-ended SAM gold surface is assigned to the match between the 6-fold axis of the MIL-88B crystals and the hexagonal symmetry of the thiolate SAM. Nevertheless, as stated by R. A. Fischer [71], the main drawbacks of this method are in the lengthy and sometimes complicated preparation procedure (typically a couple of days with several heating steps) and the poor morphology of the obtained layers. In addition, the films obtained are often noncontinuous, in which the crystals are not really intergrown. Compromise can be made by using silane-based SAMs (usually on oxides) with a higher thermal stability above 120 ^{o}C but possessing inferior homogeneity that will worsen the quality of MOF films, comparing with that of alkanethiols SAMs[86,110]. Direct growth of other MOFs on substrates without SAMs and improvements towards this method for the growth of MOFs on surfaces with SAMs are now available in some review articles [70,71].

1.4 Description of Fe^{3+}/BDC and NDC MOFs

G. Férey, C. Serre and their co-workers developed a series of MOF materials named MILs materials (MIL stands for Matériaux de l'Institut Lavoisier), constructed by trivalent metal cations such as Al^{3+}, Cr^{3+} and Fe^{3+} in coordination with terephthalic acid (or benzene-1,4-dicarboxylic acid (BDC)) and other ligands under solvothermal synthesis in the past decade. Considering the non-toxicity and easy-accessibility of Fe source, the well-known system Fe^{3+}/BDC is of special interest, where three different phases MIL-101, MIL-88B, and MIL-53 are reported depending on synthesis conditions (solution composition, temperature, pressure) [111]. The three structures differ in the connectivity of the inorganic nodes with the organic linkers, leading to different porous structures: MIL-53 and MIL-88B exhibit framework flexibility and MIL-101 possesses an unusually large pore volume and specific surface area [112,59,113].

MIL-101: The first synthesis of MIL-101 was implemented with Chromium (III) (Cr^{3+}) at 220 ^{o}C after 8 h solvothermal reaction by G. Férey, C. Serre and their co-workers in 2005. The resulted crystalline solid (MIL-101) with formula

($Cr_3F(H_2O)_2O[(O_2C)-C_6H_4-(CO_2)]_3 \cdot nH_2O$, n ≈ 25) crystallizes in a cubic space group Fd-3m (89Å) with surface area (5900 m^2/g) and pore sizes (29 Å and 34 Å). Single crystal is difficult to be obtained for MIL-101 with such a huge unit cell. Computational simulation (typically automated assembly of secondary building units (AASUB)) was employed to predict the potential 3D frameworks built by the same inorganic cluster and the linker. Comparison of the obtained calculated XRD patterns with the targeted experimental structure was made to give access to the structural information. The eventual crystal structure was achieved through fitting the experimental results with the theoretical data at the help of Rietveld method (as shown in **Figure 1.7**).

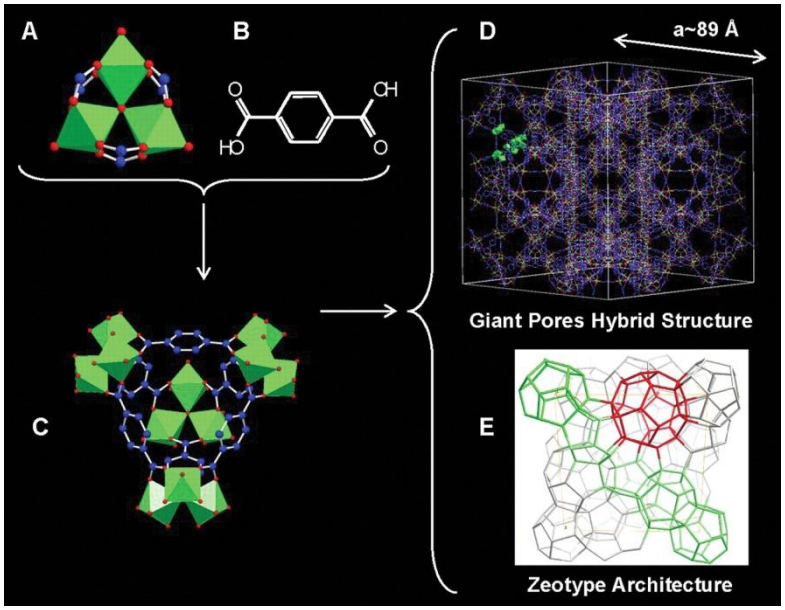

Figure 1.7 (A) the computationally designed trimeric building block chelated by three carboxylic groups. The supertetrahedra hereafter named ST (C) was built by terephthalic acid (B) and the trimers, which lies on the edges of the ST. (D) Ball-and-stick representation of one unit cell. (E) Schematic 3D representation of the Mobil Thirty-Nine (MTN) zeotype architecture (the vertices represent the centers of each ST) with the medium (in green, with 20 tetrahedra) and large (in red with 28 tetrahedra) cages delimited by the vertex sharing of the ST. Chromium octahedron, oxygen, fluorine and carbon atoms are in green, red and blue, respectively. The Cr atoms localize at the centers of the octahedral. Figure reproduced from Ref [112].

MIL-88B: The MIL-88B presents a hexagonal structure (space group P-62c or P63/mmc) with formula of $Fe_3O(BDC)_3 \cdot xsolv$ (solvent molecule). It is built up from the linkage of trimers of iron(III) or chromium(III) octahedra that share a μ_3O oxygen

with dicarboxylates in such a way that two types of cavities exist: tunnels along [001] and bipyramidal cages with trimers at the vertices. The height of the bipyramid corresponds to the c cell parameter (**Figure 1.8**), whereas the distance between two adjacent trimers in the equatorial plane represents a cell parameter (**Figure 1.9**) [59].

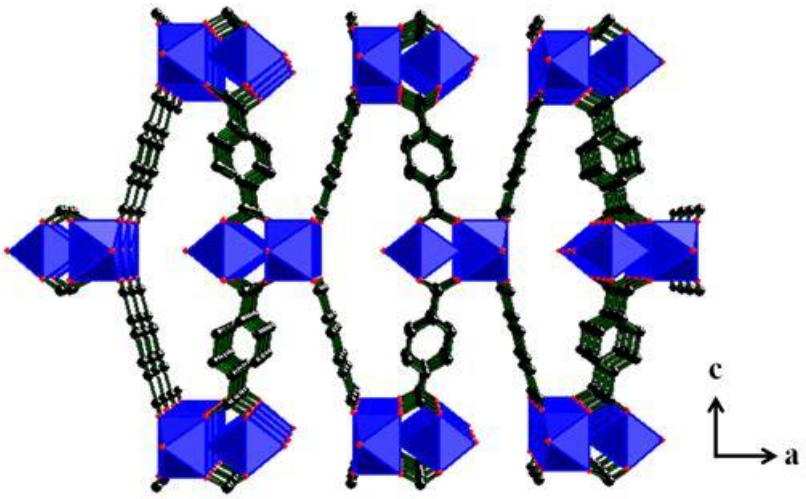

Figure 1.8 View of crystal structure of MIL-88B along b axis. Octahedron, oxygen and carbon atoms are in blue, red and black, respectively. The metal atoms localize at the center of the octahedra.

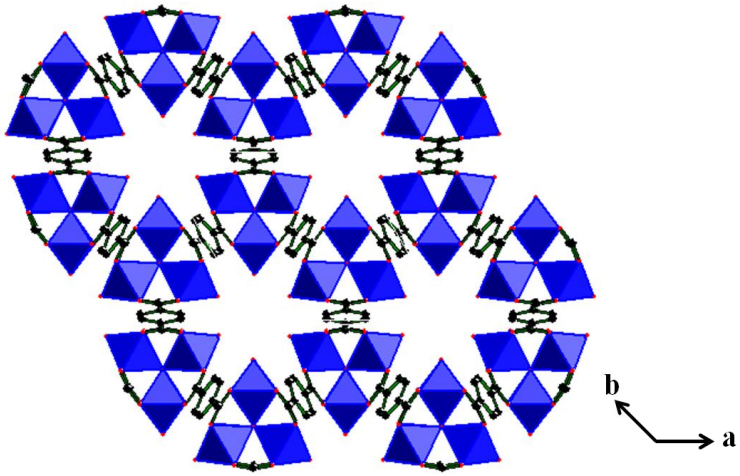

Figure 1.9 View of crystal structure of MIL-88B along c axis. Octahedron, oxygen and carbon atoms are in blue, red and black, respectively. The metal atoms localize at the center of the octahedra.

Other numbers of isoreticular MIL-88B family exhibit the similar framework structures but constructed with other organic ligands like fumaric acid (MIL-88A), 2,6-naphthalenedicarboxylic acid (MIL-88C) and 4,4'-biphenyldicarboxylate acid

(MIL-88D).

MIL-53: The MIL-53 (formula: M(OH/F)(BDC) solv) presents a monoclinic structure (space group-I2/a). It was also first synthesized by Férey'group with the metal ions of chromium [66] and aluminum [114]. The iron analogue was synthesized later by Whitfield et al., [115] which is constructed by chains of trans-corner-shared metal centered octahedra, where the bridging atom is either the oxygen of hydroxide ion or a halogen ion (F^-). The inorganic chains are cross-linked by carboxylates to present rhomb-shaped channels running parallel to the a axis of the structure (**Figure 1.10**).

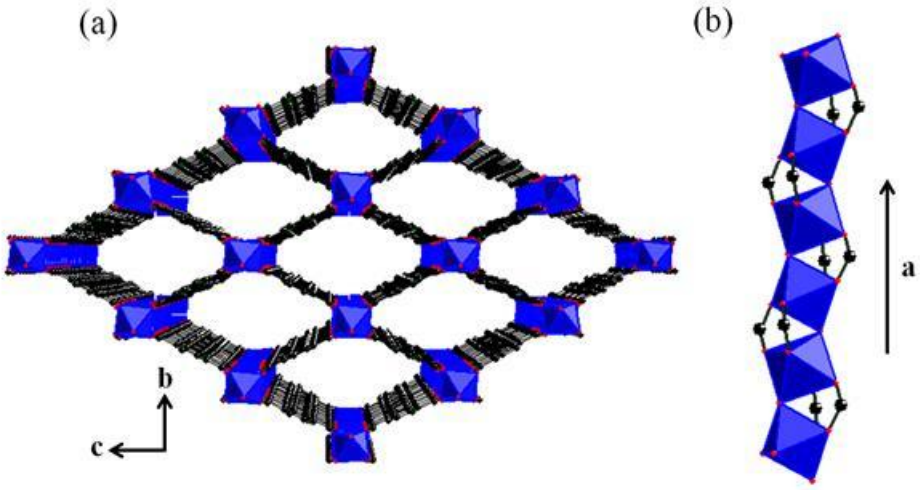

Figure 1.10 Crystal structure of MIL-53 with view along the a axis (a) and the inorganic chains of FeO_6 octahedra along the channels (b).

Note that as we mentioned in **Section 1.2**, a transient intermediate phase proposed first by O. M. Yaghi named after MOF-235 ($[Fe_3O(BDC)_3(DMF)_3]^+$ $[FeCl_4]^-$ x(DMF)) with a space group P-62c can also be isolated by using $FeCl_3$ as the metal precursor, in which trimers of iron(III) oxy-octahedra are linked by terephthalate linkers, and trapped molecules within the porous three-dimensional network are not only DMF molecules but also $[FeCl_4]^-$ anions that balance the positive charge of the MOF framework (**Figure 1.11**).

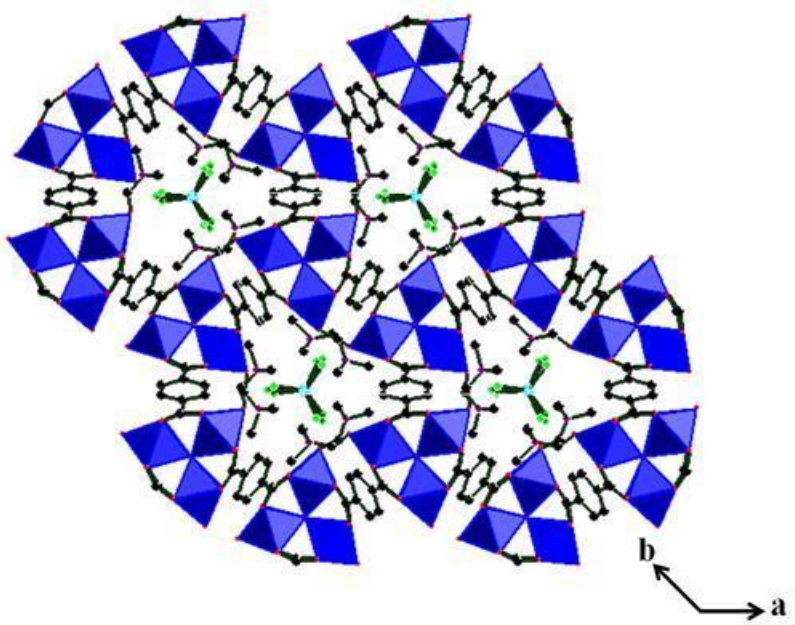

Figure 1.11 View of crystal structure of MOF-235 along c axis. Octahedron, oxygen, carbon, iron, nitrogen and chlorine atoms are in blue, red, black, wathet blue, purple and green, respectively. Axial coordinating ligands and hydrogen atoms have been omitted for clarity.

Properties of the above interesting framework structures make them interesting for various applications ranging from gas sorption/storage, to heterocatalyst, chemical sensors and drug delivery up to now [5,20,21,27,49,50,59,89,90]. Shaping them on solid supports might expand their applications.

1.5 Objectives and outline of the manuscript

The objective of this PhD project is to investigate mainly synthesis conditions for the direct growth of Fe^{3+}/BDC and Fe^{3+}/NDC MOFs onto functionalized silicon (111) surfaces exhibiting well-defined structure and whose surface chemistry can be tailored in order to favor/direct the heterogeneous nucleation and growth of the MOFs. By varying the compositional and process parameters of synthesis conditions and/or surface chemistry of grafted monolayers on substrates, the following work is expected to contribute to a better understanding of phase selection (if possible) and growth mechanism of the targeted MOFs, which are crucial for achieving tailored properties via tuning the film morphologies and structures. The structure of this dissertation is as

below: After a chapter devoted to experimental details (Chapter 2), three chapters deal with MOF film formation.

- Chapter 3 deals with the influence of surface chemistry on the formation of Fe^{3+}/BDC MOFs films. The structure of crystallite is identified from correlation between SEM and XRD results and the interaction of crystallite with surface is also discussed.
- Chapter 4 presents a detailed study of Fe^{3+}/BDC MOFs films on acid-terminated surfaces. The influence of synthesis conditions (temperature, ratio of ligand to metal precursors, starting precursor concentration, additives and growth time) is investigated to discuss the nucleation and growth of films.
- Chapter 5 presents the film growth of Fe^{3+}/NDC MOF on carboxylic acid terminated Si surfaces. The flexible property of Fe^{3+}/NDC MOF involving molecular trapping and release is preliminarily studied by ex/in situ XRD diffractometer.

The manuscript ends with a general conclusion and gives some perspectives to the present work.

1.6 References

[1] E. A. Tomic, Thermal stability of coordination polymers, J. Appl. Polym. Sci., 9 (1965) 3745-3752.

[2] O. M. Yaghi, G. Li, H. Li, Selective binding and removal of guests in a microporous metal-organic framework, Nature, 378 (1995) 703-706.

[3] H. Li, M. Eddaoudi, M. O'Keeffe, O. M. Yaghi, Design and synthesis of an exceptionally stable and highly porous metal-organic framework, Nature, 402 (1999) 276-279.

[4] M. Cavellec, D. Riou, J.-M. Grenèche, G. Férey, Hydrothermal Synthesis, Structure, and Magnetic Properties of a Novel Monodimensional Iron Phosphate: $[FeF(HPO_4)_2,N_2C_3H_{12},(H_2O)_x]$ ($x \approx 0.20$) (ULM-14), Inorg. Chem., 36 (1997) 2187-2190.

[5] G. Férey, Hybrid porous solids: past, present, future, Chem. Soc. Rev., 37 (2008) 191-214.

[6] C. Serre, F. Taulelle, G. Férey, Rational design of porous titanophosphates, Chem. Commun., (2003) 2755-2765.

[7] M. I. Khan, L. M. Meyer, R. C. Haushalter, A. L. Schweitzer, J. Zubieta, J. L. Dye, Giant Voids in the Hydrothermally Synthesized Microporous Square Pyramidal−Tetrahedral Framework Vanadium Phosphates $[HN(CH_2CH_2)_3NH]K_{1.35}[V_5O_9(PO_4)_2]\cdot xH_2O$ and $Cs_3[V_5O_9(PO_4)_2]\cdot xH_2O$, Chem. Mater., 8 (1996) 43-53.

[8] J. Chen, S. Natarajan, J.M. Thomas, R.H. Jones, M.B. Hursthouse, A Novel Open-Framework Cobalt Phosphate Containing a Tetrahedrally Coordinated Cobalt(II) Center: $CoPO_4$ 0.5 $C_2H_{10}N_2$, Angew. Chem. Int. Ed. Engl., 33 (1994) 639-640.

[9] S. Kitagawa, R. Kitaura, S.-i. Noro, Functional Porous Coordination Polymers, Angew. Chem. Int. Ed., 43 (2004) 2334-2375.

[10] G. Férey, Microporous Solids: From Organically Templated Inorganic Skeletons to Hybrid Frameworks...Ecumenism in Chemistry, Chem. Mater., 13 (2001) 3084-3098.

[11] A. R. Millward, O. M. Yaghi, Metal−Organic Frameworks with Exceptionally High Capacity for Storage of Carbon Dioxide at Room Temperature, J. Am. Chem. Soc., 127 (2005) 17998-17999.

[12] N. W. Ockwig, O. Delgado-Friedrichs, M. O'Keeffe, O. M. Yaghi, Reticular Chemistry: Occurrence and Taxonomy of Nets and Grammar for the Design of Frameworks, Acc. Chem. Res., 38 (2005) 176-182.

[13] C. N. R. Rao, S. Natarajan, R. Vaidhyanathan, Metal Carboxylates with Open Architectures, Angew. Chem. Int. Ed., 43 (2004) 1466-1496.

[14] G. Férey, Building Units Design and Scale Chemistry, J. Solid State Chem., 152 (2000) 37-48.

[15] N. Stock, S. Biswas, Synthesis of Metal-Organic Frameworks (MOFs): Routes to Various MOF Topologies, Morphologies, and Composites, Chem. Rev., 112 (2012) 933-969.

[16] C. Gerardin, M. In, L. Allouche, M. Haouas, F. Taulelle, In Situ pH Probing of Hydrothermal

Solutions by NMR, Chem. Mater., 11 (1999) 1285-1292.

[17] D. Riou, G. Férey, Hybrid open frameworks (MIL-n). Part 3 Crystal structures of the HT and LT forms of MIL-7: a new vanadium propylenediphosphonate with an open-framework. Influence of the synthesis temperature on the oxidation state of vanadium within the same structural type, J. Mater. Chem., 8 (1998) 2733-2735.

[18] C. Livage, C. Egger, M. Nogues, G. Férey, Hybrid open frameworks (MIL-n). Part 5 Synthesis and crystal structure of MIL-9: a new three-dimensional ferrimagnetic cobalt(II) carboxylate with a two-dimensional array of edge-sharing Co octahedra with 12-membered rings, J. Mater. Chem., 8 (1998) 2743-2747.

[19] S. Bauer, T. Bein, N. Stock, High-Throughput Investigation and Characterization of Cobalt Carboxy Phosphonates, Inorg. Chem., 44 (2005) 5882-5889.

[20] S. Surblé, C. Serre, C. Mellot-Draznieks, F. Millange, G. Férey, A new isoreticular class of metal-organic-frameworks with the MIL-88 topology, Chem. Commun., (2006) 284-286.

[21] C. Serre, F. Millange, S. Surblé, G. Férey, A Route to the Synthesis of Trivalent Transition-Metal Porous Carboxylates with Trimeric Secondary Building Units, Angew. Chem. Int. Ed., 43 (2004) 6285-6289.

[22] E. Biemmi, T. Bein, N. Stock, Synthesis and characterization of a new metal organic framework structure with a 2D porous system: $(H_2NEt_2)_2[Zn_3(BDC)_4]\cdot 3DEF$, Solid. State. Sci., 8 (2006) 363-370.

[23] U. Mueller, M. Schubert, F. Teich, H. Puetter, K. Schierle-Arndt, J. Pastre, Metal-organic frameworks-prospective industrial applications, J. Mater. Chem., 16 (2006) 626-636.

[24] Y. K. Hwang, J.-S. Chang, S.-E. Park, D. S. Kim, Y.-U. Kwon, S. H. Jhung, J.-S. Hwang, M. S. Park, Microwave Fabrication of MFI Zeolite Crystals with a Fibrous Morphology and Their Applications, Angew. Chem. Int. Ed., 44 (2005) 556-560.

[25] S. H. Jhung, T. Jin, Y. K. Hwang, J.-S. Chang, Microwave Effect in the Fast Synthesis of Microporous Materials: Which Stage Between Nucleation and Crystal Growth is Accelerated by Microwave Irradiation, Chem. Eur. J., 13 (2007) 4410-4417.

[26] Y.-K. Seo, G. Hundal, I. T. Jang, Y. K. Hwang, C.-H. Jun, J. -S. Chang, Microwave synthesis of hybrid inorganic–organic materials including porous $Cu_3(BTC)_2$ from Cu(II)-trimesate mixture, Micropor. Mesopor. Mat., 119 (2009) 331-337.

[27] A. Demessence, P. Horcajada, C. Serre, C. Boissière, D. Grosso, C. Sanchez, G. Férey, Elaboration and properties of hierarchically structured optical thin films of MIL-101(Cr), Chem. Commun., (2009) 7149-7151.

[28] P. M. Forster, N. Stock, A. K. Cheetham, A High-Throughput Investigation of the Role of pH, Temperature, Concentration, and Time on the Synthesis of Hybrid Inorganic–Organic Materials, Angew. Chem. Int. Ed., 44 (2005) 7608-7611.

[29] S. Bauer, N. Stock, Implementation of a Temperature-Gradient Reactor System for High-Throughput Investigation of Phosphonate-Based Inorganic–Organic Hybrid Compounds, Angew. Chem. Int. Ed., 46 (2007) 6857-6860.

[30] R. Banerjee, A. Phan, B. Wang, C. Knobler, H. Furukawa, M. Keeffe, O. M. Yaghi, High-Throughput Synthesis of Zeolitic Imidazolate Frameworks and Application to CO_2 Capture, Science, 319 (2008) 939.

[31] T. Ahnfeldt, N. Guillou, D. Gunzelmann, I. Margiolaki, T. Loiseau, G. Férey, J. Senker, N. Stock, $[Al_4(OH)_2(OCH_3)_4(H_2N\text{-}bdc)_3]\cdot x\,H_2O$:A12-Connected Porous Metal–Organic Framework with an Unprecedented Aluminum-Containing Brick, Angew. Chem. Int. Ed., 48 (2009) 5163-5166.

[32] S. Han, Y. Huang, T. Watanabe, Y. Dai, K. S. Walton, S. Nair, D. S. Sholl, J. C. Meredith, High-Throughput Screening of Metal–Organic Frameworks for CO_2 Separation, ACS. Comb. Sci., 14 (2012) 263-267.

[33] K. Sumida, S. Horike, S. S. Kaye, Z. R. Herm, W. L. Queen, C. M. Brown, F. Grandjean, G. J. Long, A. Dailly, J. R. Long, Hydrogen storage and carbon dioxide capture in an iron-based sodalite-type metal-organic framework (Fe-BTT) discovered via high-throughput methods, Chem. Sci., 1 (2010) 184-191.

[34] H. Reinsch, N. Stock, High-throughput studies of highly porous Al-based MOFs, Micropor. Mesopor. Mat., 171 (2013) 156-165.

[35] O. K. Farha, A. Özgür Yazaydın, I. Eryazici, C. D. Malliakas, B. G. Hauser, M. G. Kanatzidis, S. T. Nguyen, R. Q. Snurr, J. T. Hupp, De novo synthesis of a metal–organic framework material featuring ultrahigh surface area and gas storage capacities, Nat Chem., 2 (2010) 944-948.

[36] D. C. Cantu, B. P. McGrail, V.-A. Glezakou, Formation Mechanism of the Secondary Building Unit in a Chromium Terephthalate Metal–Organic Framework, Chem. Mater., 26 (2014) 6401-6409.

[37] S. Surblé, F. Millange, Serre, C. Serre, G. Férey, R. I. Walton, An EXAFS study of the formation of a nanoporous metal-organic framework: evidence for the retention of secondary building units during synthesis, Chem. Commun., 14(2006), 1518-1520.

[38] J. A. Rood, W. C. Boggess, B. C. Noll, K. W. Henderson, Assembly of a Homochiral, Body-Centered Cubic Network Composed of Vertex-Shared Mg12 Cages: Use of Electrospray Ionization Mass Spectrometry to Monitor Metal Carboxylate Nucleation, J. Am. Chem. Soc., 129 (2007) 13675-13682.

[39] E. Haque, J. H. Jeong, S. H. Jhung, Synthesis of isostructural porous metal-benzenedicarboxylates: Effect of metal ions on the kinetics of synthesis, CrystEngComm., 12 (2010) 2749-2754.

[40] N. A. Khan, M. M. Haque, S. H. Jhung, Accelerated Syntheses of Porous Isostructural Lanthanide–Benzenetricarboxylates (Ln–BTC) Under Ultrasound at Room Temperature, Eur. J. Inorg. Chem., 2010 (2010) 4975-4981.

[41] S. R. Venna, J. B. Jasinski, M. A. Carreon, Structural Evolution of Zeolitic Imidazolate Framework-8, J. Am. Chem. Soc., 132 (2010) 18030-18033.

[42] T. Ahnfeldt, J. Moellmer, V. Guillerm, R. Staudt, C. Serre, N. Stock, High-Throughput and Time-Resolved Energy-Dispersive X-Ray Diffraction (EDXRD) Study of the Formation of

CAU-1-$(OH)_2$: Microwave and Conventional Heating, Chem. Eur. J., 17 (2011) 6462-6468.

[43] F. Millange, M. I. Medina, N. Guillou, G. Férey, K. M. Golden, R. I. Walton, Time-Resolved In Situ Diffraction Study of the Solvothermal Crystallization of Some Prototypical Metal–Organic Frameworks, Angew. Chem. Int. Ed., 49 (2010) 763-766.

[44] E. Stavitski, M. Goesten, J. Juan-Alcañiz, A. Martinez-Joaristi, P. Serra-Crespo, A. V. Petukhov, J. Gascon, F. Kapteijn, Kinetic Control of Metal–Organic Framework Crystallization Investigated by Time-Resolved In Situ X-Ray Scattering, Angew. Chem. Int. Ed., 50 (2011) 9624-9628.

[45] Juan-Alcaniz, M. Goesten, A. Martinez-Joaristi, E. Stavitski, A. V. Petukhov, J. Gascon, F. Kapteijn, Live encapsulation of a Keggin polyanion in NH_2-MIL-101 (Al) observed by in situ time resolved X-ray scattering, Chem. Commun., 47 (2011) 8578-8580.

[46] A. C. Sudik, A. P. Côté, O. M. Yaghi, Metal-Organic Frameworks Based on Trigonal Prismatic Building Blocks and the New "acs" Topology, Inorg. Chem., 44 (2005) 2998-3000.

[47] B. Li, H.-M. Wen, W. Zhou, B. Chen, Porous Metal–Organic Frameworks for Gas Storage and Separation: What, How, and Why?, J. Phys. Chem. Lett., 5 (2014) 3468-3479.

[48] D. Alezi, Y. Belmabkhout, M. Suyetin, P. M. Bhatt, Ł. J. Weseliński, V. Solovyeva, K. Adil, I. Spanopoulos, P. N. Trikalitis, A.-H. Emwas, M. Eddaoudi, MOF Crystal Chemistry Paving the Way to Gas Storage Needs: Aluminum-Based soc-MOF for CH_4, O_2, and CO_2 Storage, J. Am. Chem. Soc., 137 (2015) 13308-13318.

[49] P. Horcajada, T. Chalati, C. Serre, B. Gillet, C. Sebrie, T. Baati, J. F. Eubank, D. Heurtaux, P. Clayette, C. Kreuz, J.-S. Chang, Y. K. Hwang, V. Marsaud, P.-N. Bories, L. Cynober, S. Gil, G. Férey, P. Couvreur, R. Gref, Porous metal-organic-framework nanoscale carriers as a potential platform for drug delivery and imaging, Nat Mater., 9 (2010) 172-178.

[50] S. Keskin, S. Kızılel, Biomedical Applications of Metal Organic Frameworks, Ind. Eng. Chem. Res., 50 (2011) 1799-1812.

[51] M.-X. Wu, Y.-W. Yang, Metal–Organic Framework (MOF)-Based Drug/Cargo Delivery and Cancer Therapy, Adv. Mater., 29 (2017) 1606134-n/a.

[52] J.-R. Li, R. J. Kuppler, H.-C. Zhou, Selective gas adsorption and separation in metal-organic frameworks, Chem. Soc. Rev., 38 (2009) 1477-1504.

[53] Z. Wang, A. Knebel, S. Grosjean, D. Wagner, S. Bräse, C. Wöll, J. Caro, L. Heinke, Tunable molecular separation by nanoporous membranes, Nat. Commun., 7 (2016) 13872.

[54] A. Dhakshinamoorthy, H. Garcia, Metal-organic frameworks as solid catalysts for the synthesis of nitrogen-containing heterocycles, Chem. Soc. Rev., 43 (2014) 5750-5765.

[55] J. Liu, L. Chen, H. Cui, J. Zhang, L. Zhang, C.-Y. Su, Applications of metal-organic frameworks in heterogeneous supramolecular catalysis, Chem. Soc. Rev., 43 (2014) 6011-6061.

[56] F.-Y. Yi, D. Chen, M.-K. Wu, L. Han, H.-L. Jiang, Chemical Sensors Based on Metal–Organic Frameworks, ChemPlusChem., 81 (2016) 675-690.

[57] L. E. Kreno, K. Leong, O. K. Farha, M. Allendorf, R. P. Van Duyne, J. T. Hupp, Metal–Organic Framework Materials as Chemical Sensors, Chem. Rev., 112 (2012) 1105-1125.

[58] D. Tanaka, A. Henke, K. Albrecht, M. Moeller, K. Nakagawa, S. Kitagawa, J. Groll, Rapid preparation of flexible porous coordination polymer nanocrystals with accelerated guest adsorption kinetics, Nat Chem., 2 (2010) 410-416.

[59] C. Serre, C. Mellot-Draznieks, Surblé, S., N. Audebrand, Y. Filinchuk, G. Férey, Role of Solvent-Host Interactions That Lead to Very Large Swelling of Hybrid Frameworks, Science, 315 (2007) 1828-1831.

[60] T. K. Trung, P. Trens, N. Tanchoux, S. Bourrelly, P. L. Llewellyn, S. Loera-Serna, C. Serre, T. Loiseau, F. Fajula, G. Férey, Hydrocarbon Adsorption in the Flexible Metal Organic Frameworks MIL-53(Al, Cr), J. Am. Chem. Soc., 130 (2008) 16926-16932.

[61] A. Schneemann, V. Bon, I. Schwedler, I. Senkovska, S. Kaskel, R. A. Fischer, Flexible metal-organic frameworks, Chem. Soc. Rev., 43 (2014) 6062-6096.

[62] S. S. Nagarkar, A. V. Desai, S. K. Ghosh, Stimulus-Responsive Metal–Organic Frameworks, Chem. Asian J., 9 (2014) 2358-2376.

[63] L. Sarkisov, R. L. Martin, M. Haranczyk, B. Smit, On the Flexibility of Metal–Organic Frameworks, J. Am. Chem. Soc., 136 (2014) 2228-2231.

[64] T. Loiseau, C. Serre, C. Huguenard, G. Fink, F. Taulelle, M. Henry, T. Bataille, G. Férey, A Rationale for the Large Breathing of the Porous Aluminum Terephthalate (MIL-53) Upon Hydration, Chem. Eur. J., 10 (2004) 1373-1382.

[65] F. Millange, N. Guillou, R. I. Walton, J.-M. Greneche, I. Margiolaki, G. Férey, Effect of the nature of the metal on the breathing steps in MOFs with dynamic frameworks, Chem. Commun., (2008) 4732-4734.

[66] F. Millange, C. Serre, G. Férey, Synthesis, structure determination and properties of MIL-53as and MIL-53ht: the first Cr^{3+} hybrid inorganic-organic microporous solids: CrIII(OH) {O_2C-C_6H_4-CO_2} {HO_2C-C_6H_4-CO_2H}x, Chem. Commun., (2002) 822-823.

[67] J. P. S. Mowat, V. R. Seymour, J. M. Griffin, S. P. Thompson, A. M. Z. Slawin, D. Fairen-Jimenez, T. Duren, S. E. Ashbrook, P. A. Wright, A novel structural form of MIL-53 observed for the scandium analogue and its response to temperature variation and CO_2 adsorption, Dalton Trans., 41 (2012) 3937-3941.

[68] C. Volkringer, T. Loiseau, N. Guillou, G. Férey, E. Elkaïm, A. Vimont, XRD and IR structural investigations of a particular breathing effect in the MOF-type gallium terephthalate MIL-53 (Ga), Dalton Trans., (2009) 2241-2249.

[69] E. V. Anokhina, M. Vougo-Zanda, X. Wang, A. J. Jacobson, In(OH)BDC 0.75$BDCH_2$ (BDC = Benzenedicarboxylate), a Hybrid Inorganic−Organic Vernier Structure, J. Am. Chem. Soc., 127 (2005) 15000-15001.

[70] O. Shekhah, J. Liu, R. A. Fischer, C. Woll, MOF thin films: existing and future applications, Chem. Soc. Rev., 40 (2011) 1081-1106.

[71] A. Bétard, R. A. Fischer, Metal–Organic Framework Thin Films: From Fundamentals to Applications, Chem. Rev., 112 (2012) 1055-1083.

[72] J.-L. Zhuang, A. Terfort, C. Wöll, Formation of oriented and patterned films of metal–organic

frameworks by liquid phase epitaxy: A review, Coord. Chem. Rev., 307 (2016) 391-424.

[73] S. Hermes, F. Schröder, R. Chelmowski, C. Wöll, R. A. Fischer, Selective Nucleation and Growth of Metal−Organic Open Framework Thin Films on Patterned COOH/CF3-Terminated Self-Assembled Monolayers on Au(111), J. Am. Chem. Soc., 127 (2005) 13744-13745.

[74] E. Biemmi, C. Scherb, T. Bein, Oriented Growth of the Metal Organic Framework Cu3(BTC)2(H2O)3·xH2O Tunable with Functionalized Self-Assembled Monolayers, J. Am. Chem. Soc., 129 (2007) 8054-8055.

[75] C. Carbonell, I. Imaz, D. Maspoch, Single-Crystal Metal−Organic Framework Arrays, J. Am. Chem. Soc., 133 (2011) 2144-2147.

[76] O. Shekhah, H. Wang, S. Kowarik, F. Schreiber, M. Paulus, M. Tolan, C. Sternemann, F. Evers, D. Zacher, R. A. Fischer, C. Wöll, Step-by-Step Route for the Synthesis of Metal−Organic Frameworks, J. Am. Chem. Soc., 129 (2007) 15118-15119.

[77] M. Kubo, W. Chaikittisilp, T. Okubo, Oriented Films of Porous Coordination Polymer Prepared by Repeated in Situ Crystallization, Chem. Mater., 20 (2008) 2887-2889.

[78] H. Guo, Y. Zhu, S. Qiu, J. A. Lercher, H. Zhang, Coordination Modulation Induced Synthesis of Nanoscale $Eu_{1-x}Tb_x$ Metal-Organic Frameworks for Luminescent Thin Films, Adv. Mater., 22 (2010) 4190-4192.

[79] R. Ameloot, L. Stappers, J. Fransaer, L. Alaerts, B. F. Sels, D. E. De Vos, Patterned Growth of Metal-Organic Framework Coatings by Electrochemical Synthesis, Chem. Mater., 21 (2009) 2580-2582.

[80] R. Ameloot, L. Pandey, M. V. d. Auweraer, L. Alaerts, B. F. Sels, D. E. De Vos, Patterned film growth of metal-organic frameworks based on galvanic displacement, Chem. Commun., 46 (2010) 3735-3737.

[81] M. Li, M. Dincă, Reductive Electrosynthesis of Crystalline Metal–Organic Frameworks, J. Am. Chem. Soc., 133 (2011) 12926-12929.

[82] M. Li, M. Dincă, On the Mechanism of MOF-5 Formation under Cathodic Bias, Chem. Mater., 27 (2015) 3203-3206.

[83] I. Stassen, M. Styles, T. Van Assche, N. Campagnol, J. Fransaer, J. Denayer, J.-C. Tan, P. Falcaro, D. De Vos, R. Ameloot, Electrochemical Film Deposition of the Zirconium Metal–Organic Framework UiO-66 and Application in a Miniaturized Sorbent Trap, Chem. Mater., 27 (2015) 1801-1807.

[84] I. Stassen, M. Styles, G. Grenci, H. V. Gorp, W. Vanderlinden, S. D. Feyter, P. Falcaro, D. D. Vos, P. Vereecken, R. Ameloot, Chemical vapour deposition of zeolitic imidazolate framework thin films, Nat Mater., 15 (2016) 304-310.

[85] M. D. Allendorf, V. Stavila, Nanoporous films: From conventional to conformal, Nat Mater., 15 (2016) 255-257.

[86] D. Zacher, A. Baunemann, S. Hermes, R. A. Fischer, Deposition of microcrystalline $[Cu_3(btc)_2]$ and $[Zn_2(bdc)_2(dabco)]$ at alumina and silica surfaces modified with patterned self assembled organic monolayers: evidence of surface selective and oriented growth, J. Mater. Chem.,

17 (2007) 2785-2792.

[87] C. Scherb, A. Schödel, T. Bein, Directing the Structure of Metal–Organic Frameworks by Oriented Surface Growth on an Organic Monolayer, Angew. Chem. Int. Ed., 47 (2008) 5777-5779.

[88] A. Schoedel, C. Scherb, T. Bein, Oriented Nanoscale Films of Metal–Organic Frameworks By Room-Temperature Gel-Layer Synthesis, Angew. Chem. Int. Ed., 49 (2010) 7225-7228.

[89] P. Horcajada, C. Serre, D. Grosso, C. Boissière, S. Perruchas, C. Sanchez, G. Férey, Colloidal Route for Preparing Optical Thin Films of Nanoporous Metal–Organic Frameworks, Adv. Mater., 21 (2009) 1931-1935.

[90] A. Demessence, C. Boissière, D. Grosso, P. Horcajada, C. Serre, G. Férey, G. J. A. A. Soler-Illia, C. Sanchez, Adsorption properties in high optical quality nanoZIF-8 thin films with tunable thickness, J. Mater. Chem., 20 (2010) 7676-7681.

[91] Y. Yoo, H.-K. Jeong, Heteroepitaxial Growth of Isoreticular Metal−Organic Frameworks and Their Hybrid Films, Cryst. Growth Des., 10 (2010) 1283-1288.

[92] X. Zou, G. Zhu, F. Zhang, M. Guo, S. Qiu, Facile fabrication of metal-organic framework films promoted by colloidal seeds on various substrates, CrystEngComm., 12 (2010) 352-354.

[93] Y. Hu, X. Dong, J. Nan, W. Jin, X. Ren, N. Xu, Y. M. Lee, Metal-organic framework membranes fabricated via reactive seeding, Chem. Commun., 47 (2011) 737-739.

[94] E. Zanchetta, L. Malfatti, R. Ricco, M. J. Styles, F. Lisi, C. J. Coghlan, C. J. Doonan, A. J. Hill, G. Brusatin, P. Falcaro, ZnO as an Efficient Nucleating Agent for Rapid, Room Temperature Synthesis and Patterning of Zn-Based Metal–Organic Frameworks, Chem. Mater., 27 (2015) 690-699.

[95] P. Falcaro, A. J. Hill, K. M. Nairn, J. Jasieniak, J. I. Mardel, T. J. Bastow, S. C. Mayo, M. Gimona, D. Gomez, H. J. Whitfield, R. Riccò, A. Patelli, B. Marmiroli, H. Amenitsch, T. Colson, L. Villanova, D. Buso, A new method to position and functionalize metal-organic framework crystals, Nat. Commun., 2 (2011) 237.

[96] J. Gascon, S. Aguado, F. Kapteijn, Manufacture of dense coatings of $Cu_3(BTC)_2$ (HKUST-1) on α-alumina, Micropor. Mesopor. Mat., 113 (2008) 132-138.

[97] P. Falcaro, R. Ricco, C. M. Doherty, K. Liang, A. J. Hill, M. J. Styles, MOF positioning technology and device fabrication, Chem. Soc. Rev., 43 (2014) 5513-5560.

[98] U. Mueller, M. Schubert, F. Teich, H. Puetter, K. Schierle-Arndt, J. Pastre, Metal-organic frameworks-prospective industrial applications, J. Mater. Chem., 16 (2006) 626-636.

[99] G. Decher, Fuzzy Nanoassemblies: Toward Layered Polymeric Multicomposites, Science, 277 (1997) 1232-1237.

[100] O. Shekhah, Layer-by-layer method for the synthesis and growth of surface mounted metal-organic frameworks (SURMOFs), Materials, 3 (2010) 1302-1315.

[101] K. Yusenko, M. Meilikhov, D. Zacher, F. Wieland, C. Sternemann, X. Stammer, T. Ladnorg, C. Wöll, R. A. Fischer, Step-by-step growth of highly oriented and continuous seeding layers of $[Cu_2(ndc)_2(dabco)]$ on bare oxide and nitride substrates, CrystEngComm., 12 (2010) 2086-2090.

[102] J. Zhuang, J. Friedel, A. Terfort, The oriented and patterned growth of fluorescent

metal–organic frameworks onto functionalized surfaces, Beilstein J. Nanotechnol., 3 (2012) 570.

[103] X.-J. Yu, J.-L. Zhuang, J. Scherr, T. Abu-Husein, A. Terfort, Minimization of Surface Energies and Ripening Outcompete Template Effects in the Surface Growth of Metal–Organic Frameworks, Angew. Chem. Int. Ed., 55 (2016) 8348-8352.

[104] R. Makiura, S. Motoyama, Y. Umemura, H. Yamanaka, O. Sakata, H. Kitagawa, Surface nano-architecture of a metal–organic framework, Nat Mater., 9 (2010) 565-571.

[105] R. Ameloot, E. Gobechiya, H. Uji-i, J. A. Martens, J. Hofkens, L. Alaerts, B. F. Sels, D. E. De Vos, Direct Patterning of Oriented Metal–Organic Framework Crystals via Control over Crystallization Kinetics in Clear Precursor Solutions, Adv. Mater., 22 (2010) 2685-2688.

[106] I. Stassen, N. Campagnol, J. Fransaer, P. Vereecken, D. De Vos, R. Ameloot, Solvent-free synthesis of supported ZIF-8 films and patterns through transformation of deposited zinc oxide precursors, CrystEngComm., 15 (2013) 9308-9311.

[107] J. Reboul, S. Furukawa, N. Horike, M. Tsotsalas, K. Hirai, H. Uehara, M. Kondo, N. Louvain, O. Sakata, S. Kitagawa, Mesoscopic architectures of porous coordination polymers fabricated by pseudomorphic replication, Nat Mater., 11 (2012) 717-723.

[108] K. Khaletskaya, S. Turner, M. Tu, S. Wannapaiboon, A. Schneemann, R. Meyer, A. Ludwig, G. Van Tendeloo, R. A. Fischer, Self-Directed Localization of ZIF-8 Thin Film Formation by Conversion of ZnO Nanolayers, Adv. Funct. Mater., 24 (2014) 4804-4811.

[109] F. Hinterholzinger, C. Scherb, T. Ahnfeldt, N. Stock, T. Bein, Oriented growth of the functionalized metal-organic framework CAU-1 on -OH- and -COOH-terminated self-assembled monolayers, Phys. Chem. Chem. Phys., 12 (2010) 4515-4520.

[110] F. Schreiber, Structure and growth of self-assembling monolayers, Prog. Surf. Sci., 65 (2000) 151-257.

[111] S. Bauer, C. Serre, T. Devic, P. Horcajada, J. Marrot, G. Férey, N. Stock, High-Throughput Assisted Rationalization of the Formation of Metal Organic Frameworks in the Iron(III) Aminoterephthalate Solvothermal System, Inorg. Chem., 47 (2008) 7568-7576.

[112] O. I. Lebedev, F. Millange, C. Serre, G. Van Tendeloo, G. Férey, First Direct Imaging of Giant Pores of the Metal−Organic Framework MIL-101, Chem. Mater., 17 (2005) 6525-6527.

[113] F. Millange, C. Serre, N. Guillou, G. Férey, R. I. Walton, Structural Effects of Solvents on the Breathing of Metal–Organic Frameworks: An In Situ Diffraction Study, Angew. Chem. Int. Ed., 47 (2008) 4100-4105.

[114] G. Férey, M. Latroche, C. Serre, F. Millange, T. Loiseau, A. Percheron-Guegan, Hydrogen adsorption in the nanoporous metal-benzenedicarboxylate $M(OH)(O_2C\text{-}C_6H_4\text{-}CO_2)$ ($M = Al^{3+}$, Cr^{3+}), MIL-53, Chem. Commun., (2003) 2976-2977.

[115] T. R. Whitfield, X. Wang, L. Liu, A. J. Jacobson, Metal-organic frameworks based on iron oxide octahedral chains connected by benzenedicarboxylate dianions, Solid. State. Sci., 7 (2005) 1096-1103.

Chapter 2: Experimental details

2.1 Substrate preparation

In this work, oxide free silicon (111) surfaces are grafted with organic chains bearing different chemical functions (-COOH, -CH_3 and -Pyridine) using protocols established in the electrochemistry group at PMC [1-4]. The routes for achieving grafting organic monolayers are schematically presented in **Figure 2.1**. The key point is the formation of strong covalent Si-C bonds (~ 4.5 eV) [5-9] which provides higher chemical and thermal stability compared to the thiol-based self assembled monolayers (SAMs) on gold with Au-S bond energy ~ 2.6 eV. For silane SAMs on alumina and/or silica surfaces the thermal stability is not problematic (the average bond energy for covalent bond Al-O ~ 5.2 eV, for Si-O ~ 6.5 eV), while, they do not exhibit the same level of homogeneity as alkanethiols on gold [10-12]. Oxidized Si (111) surface will be also used.

Si(111) slides in size of around 60×10 mm were cut from one side-polished N-type wafer (500-550 μm thick) with a miscut angle of 0.2 ^{o} along $[11\bar{2}]$ direction (Siltronix, France).

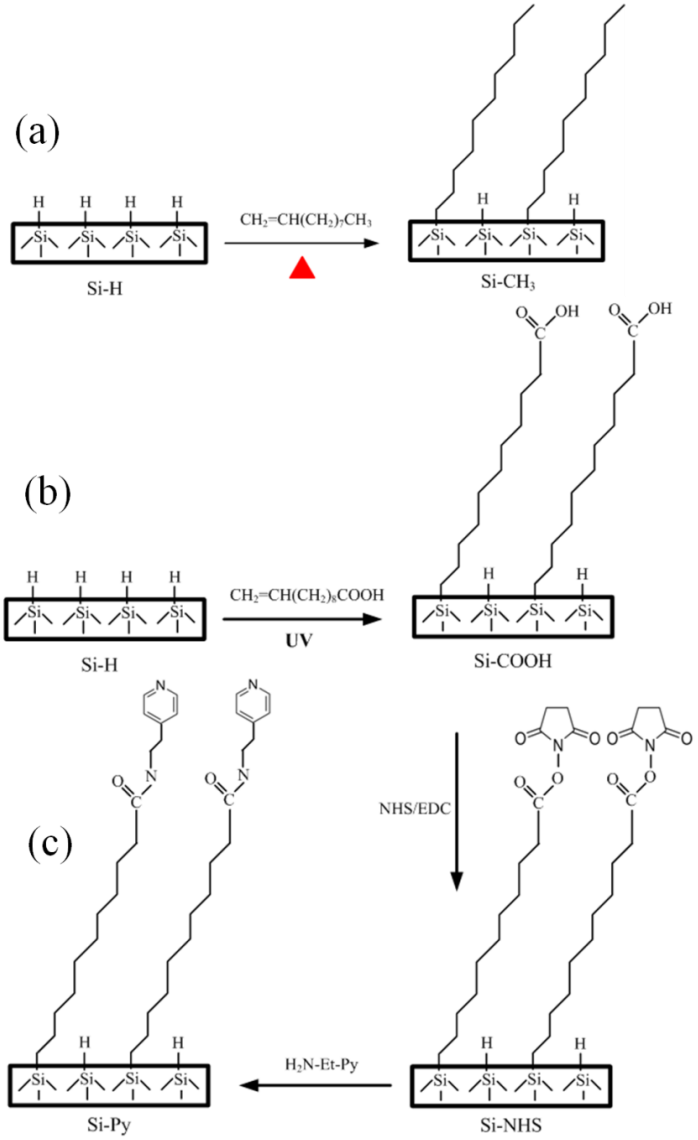

Figure 2.1 Reaction scheme of the protocol used for the functionalization of Si (111) surfaces bearing with tailorable terminated groups: (a) thermal grafting of 1-decene onto hydrogenated Si surface; (b) UV-induced grafting of undecylenic acid onto hydrogenated Si surface and (c) UV-induced grafting of aminethyl pyridine onto hydrogenated Si surface. Note that the reason we use the thermal grafting of 1-decene on oxide-free Si is that this method experimentally gives more compact monolayers on surfaces.

Etching procedure: Si pieces was etched in oxygen free 40 % NH_4F solution to obtain surfaces with staircase structure as reported previously [13,14]. These surfaces are terminated by Si-H bonds and are relatively inert in air. Prior to etching, the samples were cleaned twice in piranha solution (a mixture of 30 % H_2O_2 and 96 % H_2SO_4 at the volume ratio of 1:2) for 10 min to remove organic contaminants. After

thorough rinsing with ultra-pure water (UPW, 18 MΩ·cm), Si substrates were afterwards immersed in the etching solution for 15 min in which the ammonium sulfite ($(NH_4)_2SO_3 \cdot H_2O$) was added to remove the trace of dissolved oxygen. After being taken out of the etching solution the sample was rinsed under flowing UPW and then blown dried under argon flow. For the preparation of oxidized Si surfaces, once the H-terminated Si(111) surface is obtained, it is kept in piranha solution (a mixture of 30 % H_2O_2 and 96 % H_2SO_4 at the volume ratio of 1:2) for 10 min for further oxidization.

Organic monolayer formation

The experimental procedures used here have been previously established in the electrochemistry group at PMC [1-4].

a) Methyl terminated surfaces

1-Decene (CH_2=CH-$(CH_2)_7$)-CH_3, 97 % Sigma-Aldrich) after purification by passing slowly through a column containing fluorisil absorbent was collected in a schlenk reactor, which is always flushed with Ar flow. Afterwards, schlenk reactor containing the neat reagent was heated at 100 ^oC under Ar flowing for 30 min to eliminate oxygen and water traces. The freshly prepared H-terminated surface was introduced into the reactor after cooling it down to room temperature under continuous Ar flow. The grafting reaction was performed at 180 ^oC for 20 h with the schlenk tube hermetically sealed to avoid contamination with oxygen and water traces [1]. Finally, the surface with alkyl monolayer was successively rinsed in tetrahydrofuran (THF) and dichloromethane (DCM) at room temperature for twice and blown dried under Ar flow.

b) Carboxylic acid terminated Si (111) surfaces

The grafted monolayer with carboxylic acid terminated functional groups was achieved by immersing the freshly prepared Si-H surfaces in undecylenic acid solution under UV irradiation. Before grafting, a schlenk tube containing undecylenic acid solution was previously heated at 85 ℃ and outgassed under Argon flowing for 30 min to get rid of traces of water and oxygen. Before the introduction of Si-H

sample the schlenk was cooled down to 40 ℃. Once the immersion of sample is done, the solution was further flushed with Ar at 40 ℃ for another 20 min. Then, the schlenk tube was tightly sealed and transferred into a home-made rayonnet reactor equipped with UV lamps (6 mW/cm^2, 312 nm) for 3 h irradiation. Copious rinsing in hot acetic acid (70 ^{o}C) was done twice afterwards under Ar flowing to the sample to remove the physisorbed acid chains that tend to strongly interact with the monolayer via hydrogen bonding [8]. Finally the acid surface was rinsed by UPW, dried by Ar and stored in plastic tube under protection of N_2 for further functionalization and/or film preparation.

c) Pyridine terminated Si (111) surfaces

Once the grafting of undecylenic acid onto the H-terminated Si(111) surface through robust covalent Si-C linkage is done, the Si-COOH surfaces is immersed into a freshly prepared solution containing 0.1 M N-hydrosuccinimide (NHS) and 0.1 M N-ethyl-N'-(3-(dimethylamino) propyl) carbodiimide (EDC) in 0.1M buffer solution at pH 5. The reaction of transformation of carboxylic acids into succinimidyl ester was let to proceed at 15 ^{o}C for 1 h. The resulting surfaces with –COOSuc termination were then cleansed successively in **1)** warm NaH_2PO_4 (0.1 M, pH = 5, 50 ^{o}C) solution for 10 min, **2)** diluted NaH_2PO_4 solution (NaH_2PO_4, 0.1 M/H_2O, v:v = 1:1, 50 ^{o}C) and last **3)** in UPW for another 10min. The –COOSuc surfaces were kept in acetonitrile solution after careful drying under Ar flow. The final step concerns the coupling of pyridyl groups onto the targeted surface through reacting –COOSuc surfaces with aminethyl pyridine. The reaction was done by immersion of the –COOSuc surfaces in 5 mM aminethyl pyridine for 1 h at 25 ^{o}C in a closed schlenk. Before the introduction of the surfaces, the solution was flushed with Ar for 5 min to remove O_2. The surfaces functionalized with pyridyl groups were rinsed sequentially by acetonitrile and water and finally dried under nitrogen flow [3,4].

2.2 Characterizations of as prepared substrates

Substrates were characterized by AFM. No IR spectroscopy was performed, since the organic grafting protocols have been extensively studied in the group and the protocols prove to be highly reproducible.

Representative AFM (in non-contact mode) images of functionalized Si surfaces with various surface chemistries are presented in **Figure 2.2**. The Si-H surface exhibits a staircase structure with atomically-flat terraces. The height of steps is around 4 Å, close to calibrated monatomic distance (3.14 Å). After functionalization, the surfaces, including the oxidized one, keep the same topography.

It is important to notice that there are no significant contaminants or residues on these surfaces suggesting that homogeneous and thin dense monolayers were formed on these surfaces. This clearly indicates that the above preparation procedures render the substrate with high quality (atomically cleanness and flatness) without any obvious defect. Moreover, the staircase structure can serve as the benchmark to verify whether there is film growth.

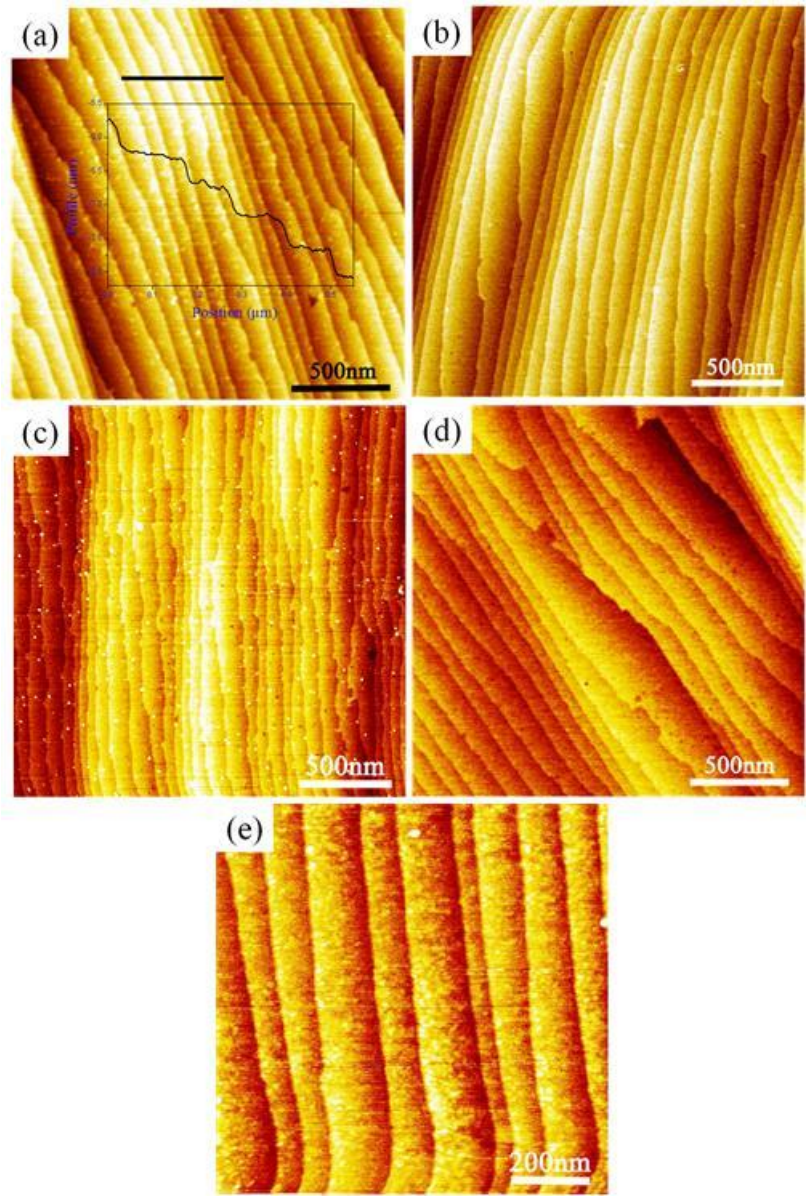

Figure 2.2 Atomic force microscopy (AFM) images of functionalized Si (111) surfaces with various terminated groups: (a) hydrogenated Si surface (Si-H); (b) oxidized Si surface (Si-OH); (c) carboxylic acid ended Si surface (Si-COOH); (d) pyridine-terminated Si surface (Si-Pyridine) and (e) methyl terminated Si surface (Si-CH_3). The inset profile in (a) corresponds to the black mark in the image.

2.3 Growth of MOF films

2.3.1 Preparation of solutions for film growth

The precursor solutions were prepared by dissolving $FeCl_3$ $6H_2O$ (ACS reagent, 97 %,

Sigma-Aldrich) in 7 ml dimethylformamide (DMF) (for molecular biology, ≥ 99 %, Sigma-Aldrich). The ligands H_2BDC (benzene-1,4-dicarboxylic acid or terephthalic acid) (98 %, Sigma-Aldrich) and/or H_2NDC (2,6-naphthalenedicarboxylic acid) (99 %, Sigma-Aldrich) was then after added and the solution was heated at around 60 ℃ for 10 min under stirring in order to obtain a homogeneous solution. For samples prepared from solutions containing additives, certain amounts of additives were added just after the obtaining homogeneous solutions. Then continuous stirring for another 10 min was done to the whole solution.

2.3.2 Film growth

The functionalized Si surfaces were rinsed with DMF prior to their immersion into the reactor containing the precursor solution. The polished face of the Si samples (active surface) was placed either face-down or in up-right position in the reactor to avoid precipitation of material from solution. The reactor was then transferred to an oil bath heated at a given temperature and the growth was let to proceed for a given time. At the end of reaction, the solution was extracted from the reactor prior to withdrawing the sample. The samples were rinsed successively in DMF, ethanol and finally dried under nitrogen flow. The materials formed in solution was collected by centrifugation at a speed of 14000 rpm for 5 min and then redispersed and centrifuged in DMF and ethanol twice. Finally, the powder was dried in an oven at 150 ^{o}C overnight.

2.4 Film characterizations

Atomic force microscopy (AFM)

The surface morphologies of the films were investigated using a Pico SPM microscope (Molecular Imaging, Phoenix, AZ) equipped with silicon nitride cantilevers (Nanoprobe, spring constant of 0.2 N·m^{-1}). Images were recorded in non-contact mode under a protected N_2 atmosphere.

Scanning electron microscopy (SEM)

Micro-structural characterizations were also carried out by scanning electron microscopy (SEM) using a Hitachi S4800 microscope equipped with a field emission gun. Plane view and cross section images were recorded using secondary electrons.

X-ray diffraction (XRD)

X-ray diffraction (XRD) patterns were recorded in Bragg-Brentano geometry using a PANalytical X'Pert diffractometer equipped with Cu Kα radiation (λ = 0.15406 nm) and a rear-side (0002) graphite monochromator.

For the in-situ and ex-situ measurements regarding the molecule uptake and release shown in **Chapter 5**, a Bruker machine equipped with a Göbel mirror optic to produce a parallel incidence beam (λ = 0.15406 nm) and with a position sensitive detector (PSD) located behind a set of long Soller slits/parallel foils was used. The sample remains flat throughout the measurement but can be rotated to allow for better sampling.

2.5 References

[1] X. Wallart, C. Henry de Villeneuve, P. Allongue, Truly Quantitative XPS Characterization of Organic Monolayers on Silicon: Study of Alkyl and Alkoxy Monolayers on H−Si(111), J. Am. Chem. Soc., 127 (2005) 7871-7878.

[2] P. Gorostiza, C. Henry de Villeneuve, Q. Y. Sun, F. Sanz, X. Wallart, R. Boukherroub, P. Allongue, Water Exclusion at the Nanometer Scale Provides Long-Term Passivation of Silicon (111) Grafted with Alkyl Monolayers, J. Phys. Chem. B., 110 (2006) 5576-5585.

[3] A. Moraillon, A. C. Gouget-Laemmel, F. Ozanam, J. N. Chazalviel, Amidation of Monolayers on Silicon in Physiological Buffers: A Quantitative IR Study, J. Phys. Chem. C., 112 (2008) 7158-7167.

[4] S. Sam, L. Touahir, J. Salvador Andresa, P. Allongue, J. N. Chazalviel, A. C. Gouget-Laemmel, C. Henry de Villeneuve, A. Moraillon, F. Ozanam, N. Gabouze, S. Djebbar, Semiquantitative Study of the EDC/NHS Activation of Acid Terminal Groups at Modified Porous Silicon Surfaces, Langmuir, 26 (2010) 809-814.

[5] S. Ciampi, J. B. Harper, J. J. Gooding, Wet chemical routes to the assembly of organic monolayers on silicon surfaces via the formation of Si-C bonds: surface preparation, passivation and functionalization, Chem. Soc. Rev., 39 (2010) 2158-2183.

[6] J. M. Buriak, Organometallic Chemistry on Silicon and Germanium Surfaces, Chem. Rev., 102 (2002) 1271-1308.

[7] P. Thissen, O. Seitz, Y. J. Chabal, Wet chemical surface functionalization of oxide-free silicon, Prog. Surf. Sci., 87 (2012) 272-290.

[8] A. Faucheux, A. C. Gouget-Laemmel, C. Henry de Villeneuve, R. Boukherroub, F. Ozanam, P. Allongue, J. -N. Chazalviel, Well-Defined Carboxyl-Terminated Alkyl Monolayers Grafted onto H−Si(111): Packing Density from a Combined AFM and Quantitative IR Study, Langmuir, 22 (2006) 153-162.

[9] A. Faucheux, F. Yang, P. Allongue, C. Henry de Villeneuve, F. Ozanam, J. N. Chazalviel, Thermal decomposition of alkyl monolayers covalently grafted on (111) silicon, Appl. Phys. Lett., 88 (2006) 193123.

[10] H. Häkkinen, The gold-sulfur interface at the nanoscale, Nat. Chem., 4 (2012) 443-455.

[11] S. H. Chen, C. W. Frank, Infrared and fluorescence spectroscopic studies of self-assembled n-alkanoic acid monolayers, Langmuir, 5 (1989) 978-987.

[12] Y. R. Luo, Comprehensive Handbook of Chemical Bond Energies, CRC Press, Boca Raton, FL, 2007.

[13] M. L. Munford, R. Cortès; P. Allongue, The preparation of ideally ordered flat HSi(111) surface. Sensors and Materials, 13 (2001), 259-269.

[14] P. Allongue, V. Kieling, H. Gerischer, Etching mechanism and atomic structure of H-Si(111) surfaces prepared in NH_4F, Electrochim. Acta., 40 (1995) 1353-1360.

Chapter 3: Direct growth of Fe^{3+}/BDC MOFs onto functionalized Si surfaces: effect of surface chemistry

3.1 Introduction

The structure and physico-chemical properties of solid surfaces are anticipated to play a crucial role in the heterogeneous nucleation and growth of MOF films on solid supports. Indeed, the surface roughness, surface free energy, acid/base property, hydrophobicity or hydrophilicity character, and the presence of potential coordinating sites, are factors that may strongly influence the thermodynamics and the kinetics of the nucleation and the growth processes [1-6]. This has been notably verified by the well-studied system of Cu^{3+}/BTC (HKUST-1 phase with a formula of $Cu_3(BTC)_2(H_2O)_3 \cdot xH_2O$, BTC stands for 1,3,5-benzenetricarboxylic acid). The growth of HKUST-1 was investigated on different surfaces (Au, Al_2O_3, SiO_2) functionalized or not with self-assembled monolayers (SAMs) [7-9]. No film growth was observed on the bare surfaces except onto alumina, on which the formation of polycrystalline HKUST-1 films was evidenced. Conversely, the growth of films exhibiting preferential orientations are found onto surfaces functionalized with variable terminated functional groups: [111] direction on -OH terminated SAM, [100] direction on -COOH ended SAM, homogeneous and less oriented thin film on methyl-based SAM. The different behavior observed on the two oxide surfaces (SiO_2 and Al_2O_3) as well as the different crystalline textures observed on surfaces functionalized with different types of functional terminations well illustrate how the physico-chemical properties of surfaces affect the nucleation and growth processes in such a drastic way and how much the mastering of the surface chemistry play a vital role in the nucleation and growth of supported MOFs. To date, few works report the fabrication of oriented Fe^{3+}/BDC MOF films. Bein's group [10,11] have investigated the growth of Fe/BDC and Fe/NH_2-BDC onto thiol-functionalized Au (111) surfaces at room temperature and showed the selective growth of oriented

MIL-88B/MIL-88B-NH_2 crystallites from pre-treated solutions for long time exposure. In their synthesis procedure, the solution was obtained by filtrating the homogenous phase MIL-53 that solvothermally formed at 150 ℃. The modified gold surfaces were afterwards immersed in the supernatant solution for varied time, ranging from 16 h to 9 days. Remarkably, despite the possible/expected existence of MIL-53 nuclei in the filtered solution, they only evidenced the growth of oriented MIL-88B or MIL-88B-NH_2 phase with (001) texture on the surface. While, to the best of our knowledge, the issue of the heterogeneous nucleation and growth mechanisms of Fe/BDC MOFs was rarely addressed.

In this chapter we investigate the direct growth of Fe^{3+}/BDC MOF on Si surfaces with different surface chemistries (see chapter 2). The film preparation was carried out on surfaces terminated with different chemical groups, i.e. carboxylic acid (-COOH), pyridyl (-C_5H_4N), hydroxyl (–OH) groups that are able to coordinate to Fe ions or clusters or nuclei. Methyl (-CH_3) terminated monolayers are also considered for comparison because no specific interaction is expected with either the metal ions or the ligand. For each kind of surface, all the samples were prepared at 90 ^oC in DMF solution containing the same Fe^{3+} concentration (25 mM) and variable ligand to metal ratios R = [L] / [Fe^{3+}] (L = Ligand). The structure and the morphology of the as-grown MOFs were characterized by X-Ray Diffraction (XRD), Scanning Electron Microscopy (SEM) and Atomic Force Microscopy (AFM).

3.2 Results

3.2.1 Growth onto carboxylic acid terminated Si surfaces (Si-COOH)

Figure 3.1 shows SEM images of films grown on Si-COOH surfaces for R = [L] / [Fe^{3+}] = 0.5. The images reveal a homogeneous coverage of the surface and the formation of a non-continuous layer made of isolated crystallites. Most of the crystallites present a triangular facet (**Figure 3.1(a)**) and will be hereafter named

crystallite A. Each A crystallite is composed of two pyramids with a common square base and opposite summits, i.e., has an octahedral shape. If one of their facets is parallel to the substrate surface, the opposite parallel facet is the triangle we observe in the images. The inset of **Figure 3.1(a)** shows a side view drawing of the octahedral crystallite sitting flat on one of its facets. Most of the octahedral crystallites exhibit triangular facets with equal side length indicating that they are parallel to the substrate surface (**Figure 3.1(a)**, crystallite A1) whereas others are tilted (**Figure 3.1(a)**, crystallite A2). The in-plane orientation of the triangles differs significantly from random orientation. Indeed, in **Figure 3.1(a,b)**, one may easily find groups of connected crystallites whose top facets are oriented almost in the same direction (some of them are indicated by yellow circles in **Figure 3.1(b)**).

Other crystallites are also observed in much lower density that exhibit hexagonal symmetry: flat hexagonal crystallites (**Figure 3.1(b)**, crystallite B) and hexagonal pyramids (**Figure 3.1(b)**, crystallite C). Rod-like crystallites (**Figure 3.1(d)**, crystallite D) are rarely observed as well. The cross-section images (**Figure 3.1(e-f)**) show that the hexagonal crystallites (B, C) have their hexagonal planes of symmetry (top and bottom facets) parallel to the sample substrate surface. In the case of a hexagonal lattice, this suggests that they are oriented with c-axis perpendicular to the surface. On the other hand, the top surface of crystallites B present lines with 3 fold symmetry recalling very much the triangular facets of A type crystallites. The inset of **Figure 3.1(b)** shows a crystallite with an intermediate shape between A type and B type. We indeed observe triangular facets as well as some characteristics of flat hexagonal crystallites. The cross-section images (**Figure 3.1(e,f)**) allow to determine the height of the different crystallites and their 3D form (angles of the facets of hexagonal crystallites, shape of the octahedral crystallites). In addition, these images show that the crystallites are in direct contact with the substrate surface and, within the image resolution, no intermediate layer forms between the crystallites and the surface (**Figure 3.1(e,f)**). **Figure 3.1(g)** corresponds to crystallites formed in solution in the same conditions. These particles are collected at the end of the growth procedure and deposited on a Si surface for SEM observation. The majority of these

crystallites have an octahedral shape (A). Occasionally some B and C crystallites are observed.

The density and the size of different crystallite types (A, B, C, D) determined from SEM images processing are plotted in **Figure 3.2**. These statistics are obtained from the analysis of at more than 100 crystallites and different images. The density of octahedral crystallites (A) is by far the largest compared to that of hexagonally shaped ($B = 8 \cdot 10^4 / cm^2$) and rod-like crystallites ($D \sim 10^4 / cm^2$). The octahedral crystalline (A) size is of ~ 915 ± 120 nm (the size was chosen as the triangle edge length) and their average height is ~ 750 nm. If crystallites A have their facets parallel to the substrate surface, the ratio between their height and their size should be $\sin(54.7^{o}) = 0.82$, which is in agreement with the average ratio we measure 750/915 = 0.82. This indicates that a large proportion of crystallites A have their facets parallel to the substrate surface. The size and size dispersion of crystallites A in solution (powder) is very close to that found on Si-COOH substrates. The flat hexagonal crystallites (B) exhibit a height of ~ 300 nm and in-plane dimension ~ 1.1 μm. The size in this case is defined as the average length of hexagon side. Among all crystallites, the hexagonal pyramids have the largest height (~ 2 μm) and size (~ 2.25 μm). Here again, the size is defined as the average length of hexagon side.

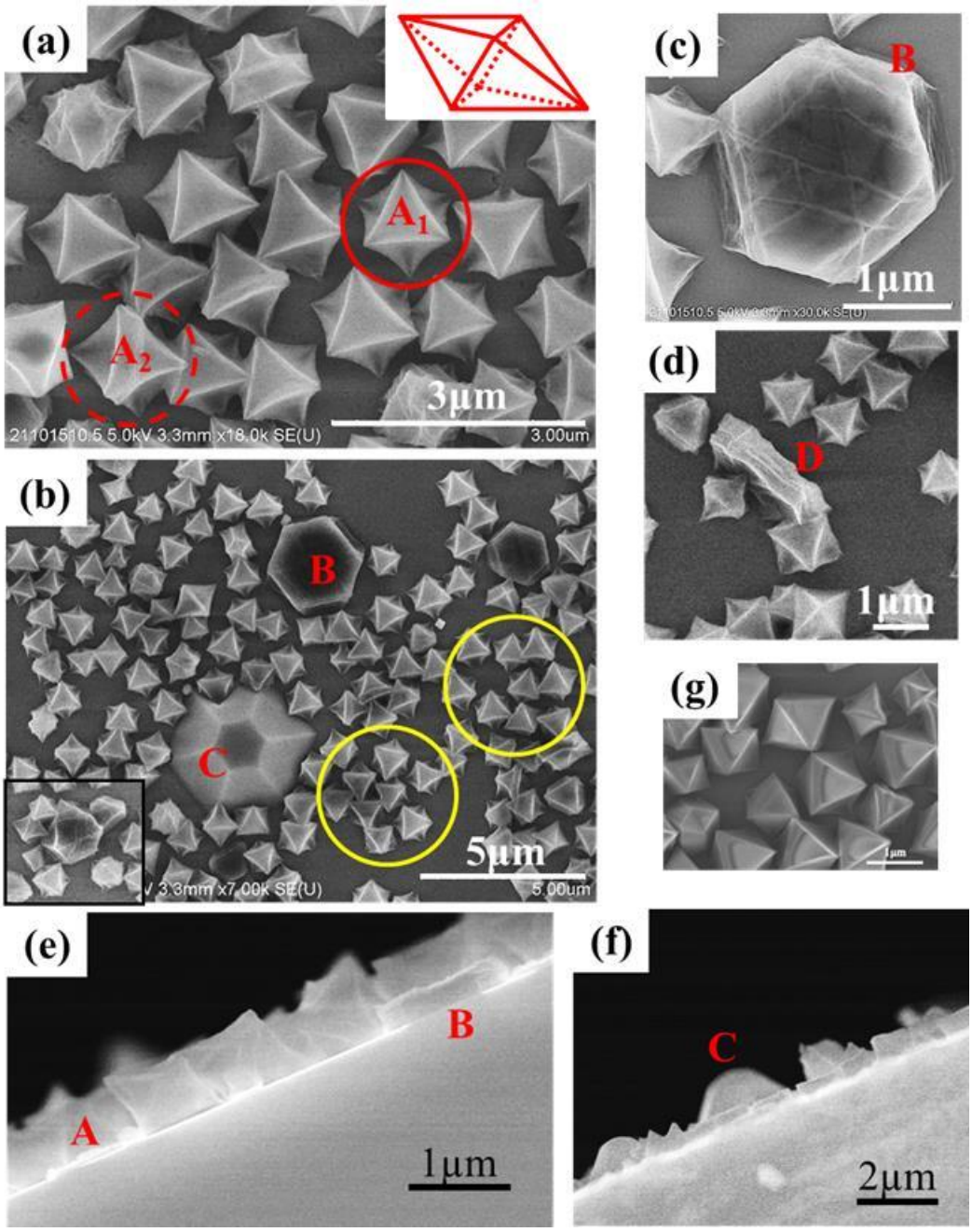

Figure 3.1 High magnification SEM images (a-d) showing the different crystalline shapes observed on the sample prepared in solution with metal excess (R = 0.5): octahedral crystallites (A), flat hexagons (B), hexagonal pyramids (C) and rod-like crystallites (D). Cross-section images (e, f) of crystallites (A-C). (g) Crystallites formed in solution in the same conditions. The inset in (a) shows a drawing of the side view of an octahedral crystallite laying flat on one facet and presenting an upper triangular facet parallel to the substrate surface. The inset in (b) shows a zoom on a particle with intermediate shape between A and B.

In **Figure 3.2(d)**, we plot the equivalent thickness which was estimated by computing the total volume of the crystallites (using the density, height and lateral size) normalized by the surface area. It corresponds to the deposit thickness if its

morphology is 2D. The equivalent thickness is dominated by the crystallites A. The contribution of crystallites B and C is nevertheless not negligible in spite of their low density because their sizes are relatively large.

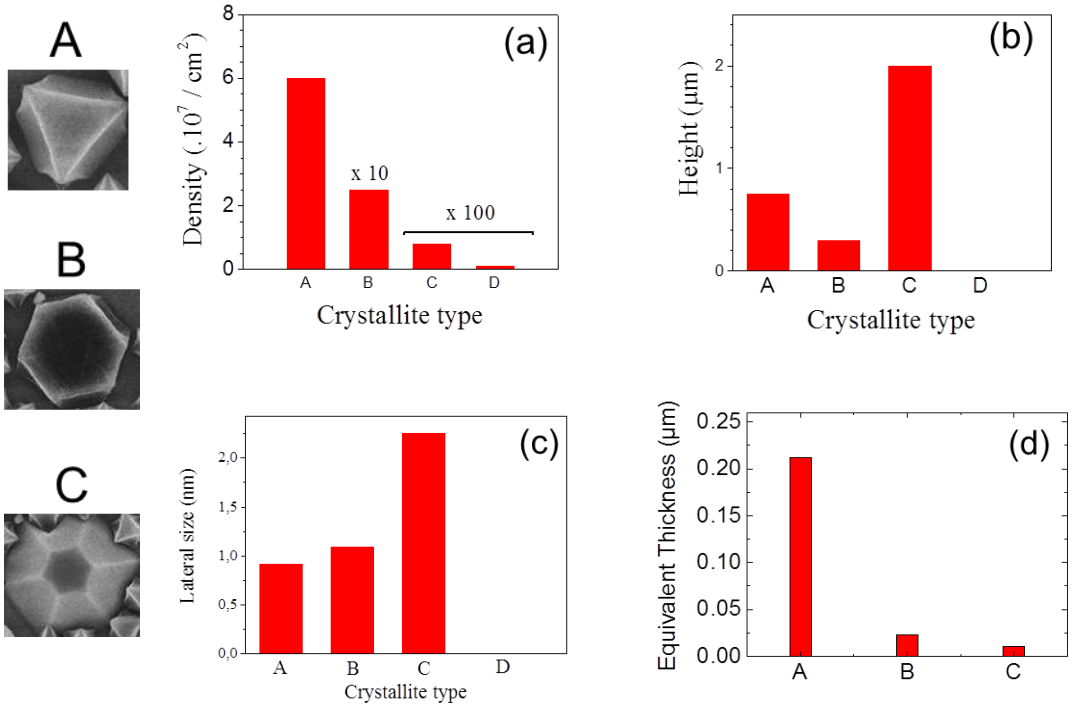

Figure 3.2 Density, height, size and equivalent thickness of the different crystallites (A, B, C, D) grown in solution with metal excess (R = 0.5). The crystallite nomenclature is shown on the left for the three main forms.

Influence of R on the MOF growth on Si-COOH surfaces

Figure 3.3 shows large field SEM images of films grown on Si-COOH surfaces for different R values. In all cases, the images reveal a homogeneous coverage of the surface but different morphologies. In contrast with the case of R = 0.5 where the layer is made of isolated crystallites mainly A type, when the relative fraction of ligand in solution increases (R ≥ 1), denser films exclusively made of close-packed crystallites of type C are observed (**Figure 3.3(b,c)**). This is also in striking contrast with the crystals which grow in solution which are mainly of A type (**Figure 3.3(d,e)**). High magnification images reveal that the C-type crystallites (hexagonal pyramids) are oriented with their c-axis perpendicular to the surface (**Figure 3.4(d)**). Between the crystallites, we observe a dense and compact layer composed of quasi-octahedral and/or octahedral crystals (**Figure 3.4(b**), red circle).

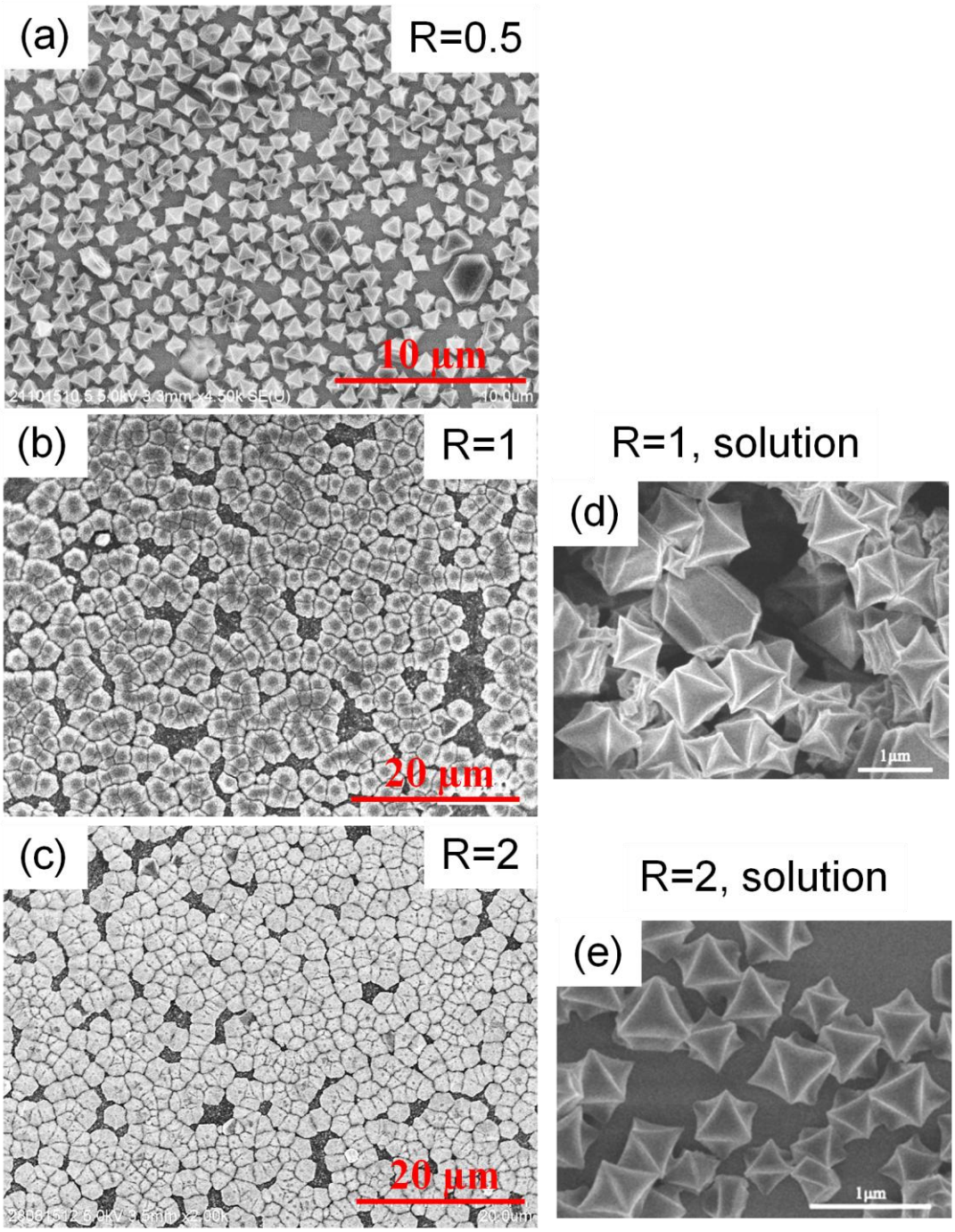

Figure 3.3 Large field SEM images showing the morphology of films grown onto Si-COOH surfaces in solutions containing various ligand to metal ratios R: (a) R = 0.5, (b) R = 1 and (c) R = 2. For all samples C_{Fe} = 25 mM, T = 90 ^{o}C and the growth time is 24 h. (d) And (e) crystals grown in solution in the same conditions with R = 1 and R = 2.

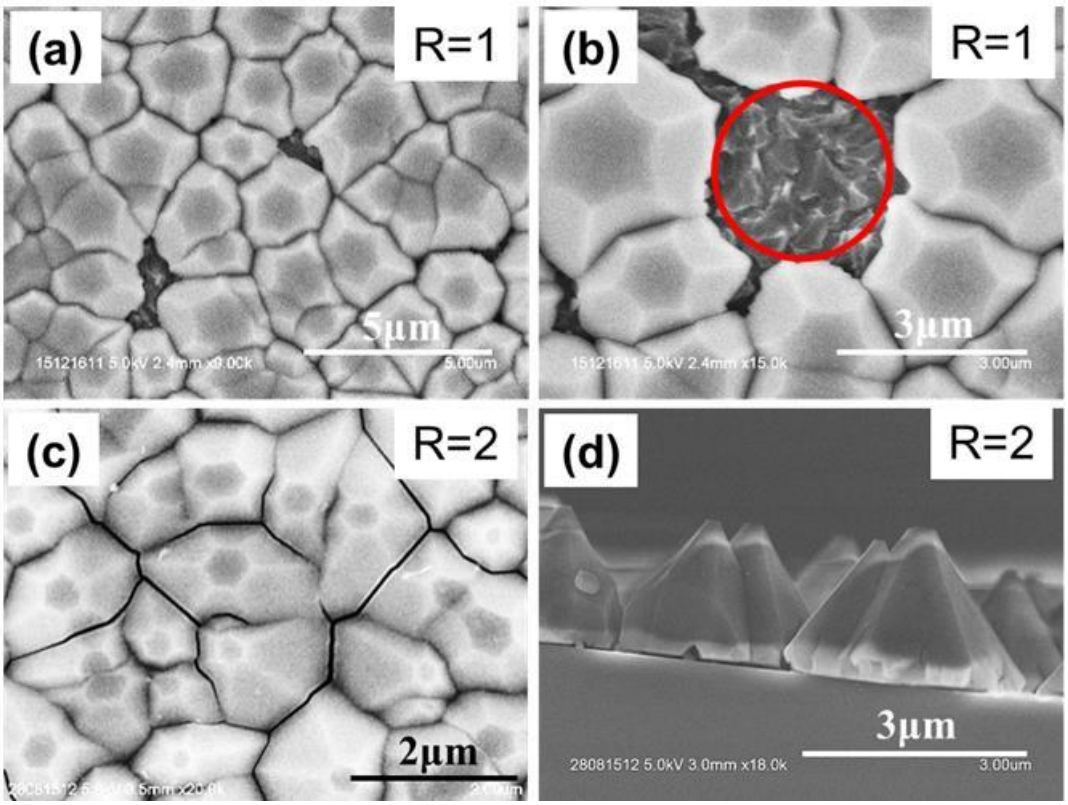

Figure 3.4 Higher magnification SEM images of films obtained in solution with R = 1 (a,b) and R = 2 (c,d).

The density and size of the hexagonal crystallites (C type) as a function of the three different ligand to metal ratios R are displayed in the **Figure 3.5**.

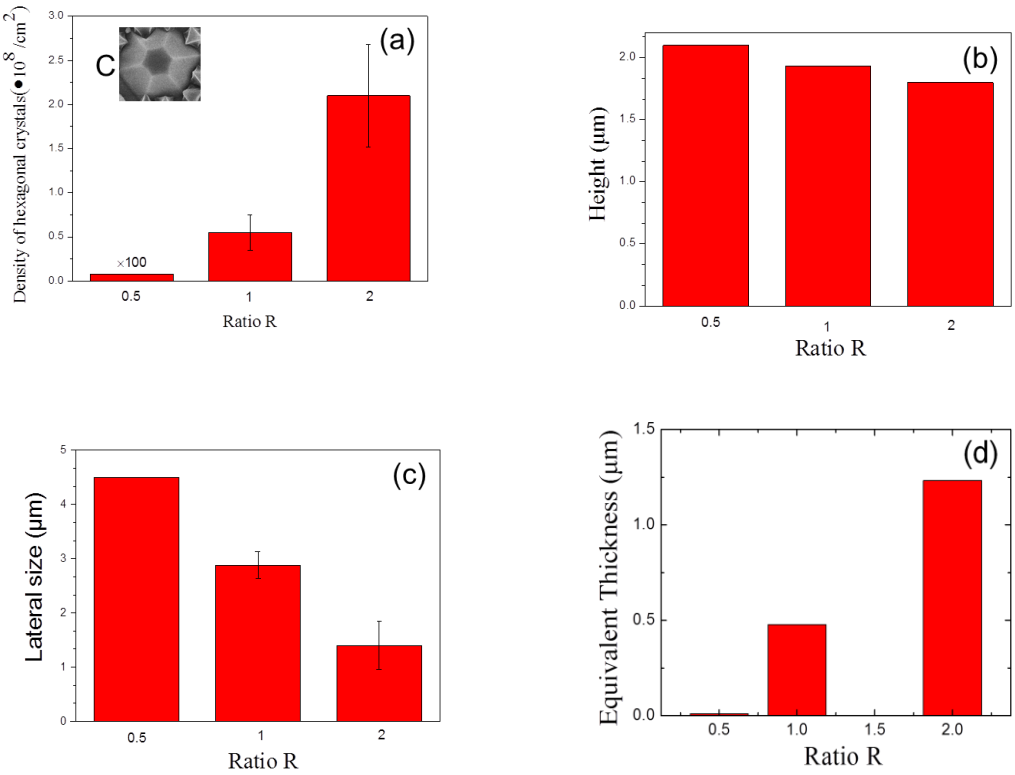

Figure 3.5 Density, dimensions and equivalent thickness of the hexagonal pyramids (C) of samples prepared under different ligand to metal ratios R. Note that the lateral size might have errors depending on the compactness of the film.

As shown in **Figure 3.5** the density of type C crystals increases dramatically as the ratio R increases, indicating a higher nucleation rate as the proportion of ligand increases. The height slightly decreases, whereas the lateral size (defined here as the hexagon diagonal) evidences an obvious decline as R increases most probably related with the increase of the island density. The size dispersion is 2.6 µm ± 0.5 for R = 1 and 1.4 µm ± 0.44 for R = 2. This dispersion of ± 20-30 % is significantly larger than that observed for crystallites A (± 13 %) in the case of R = 0.5.

The XRD patterns in Bragg Brentano configuration of the samples discussed above are presented in **Figure 3.6**. In **Figure 3.6(a)**, the pattern of the film grown at R = 2 is shown (Note that the y-axis is the log of intensity). **Figure 3.6(c)** presents the patterns for different R values in the angular range were peaks are observed. The pattern **in Figure 3.6(b)** corresponds to crystallites formed in solution.

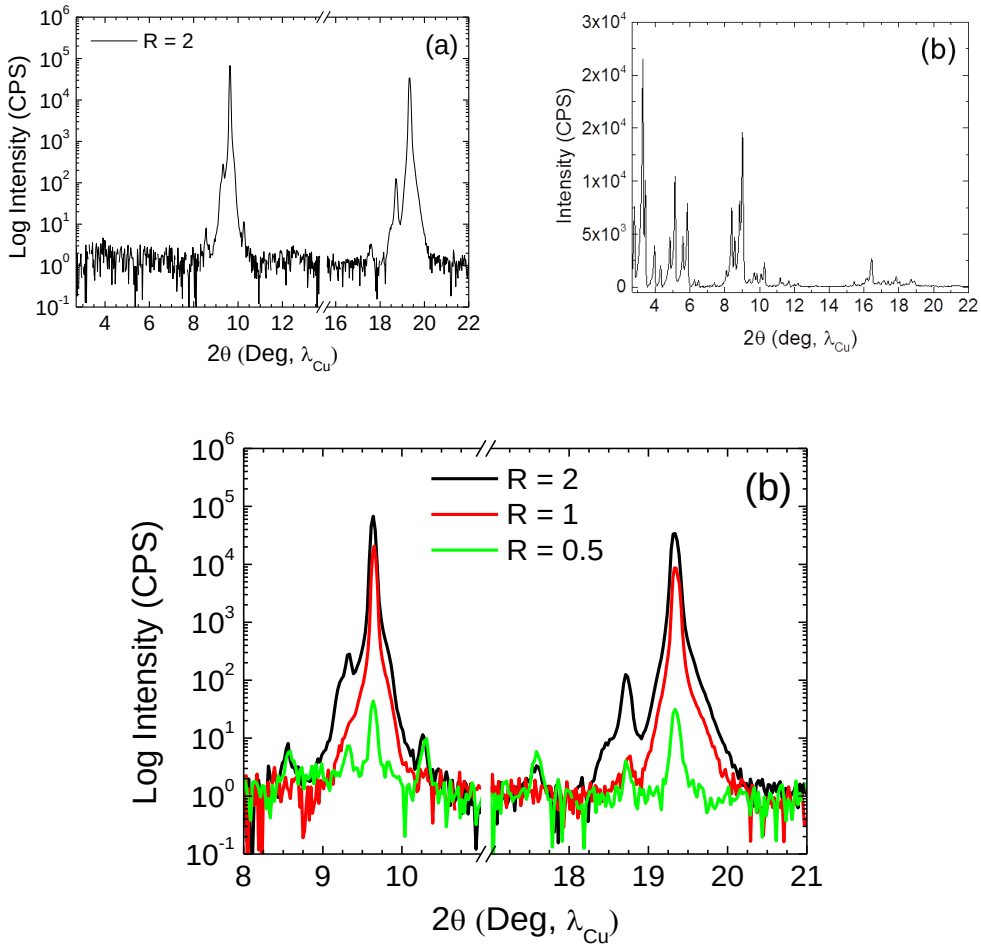

Figure 3.6 XRD patterns (a) in the case of R = 2 (full range) and (c) zoomed range of samples prepared in solutions with R = 0.5, R = 1, and R = 2. (b) XRD pattern of the crystallites grown in solution for R = 1. In (c), the arrows indicate diffraction peaks. Arrows of the same color correspond to coupled diffraction peaks. The SEM images of the samples are shown in **Figure 3.3**. For all samples C_{Fe} = 25 mM, T = 90 ^{o}C and the growth time is 24 h.

The peak positions obtained from the XRD patterns displayed in **Figure 3.6** are summarized in **Table 3.1**.

Table 3.1 Summary of the peak positions observed on the XRD patterns displayed in **Figure 3.6**.

	Peak position (2θ, deg, λ_{Cu})						
R = 0.5	8.55	9.33	9.64	10.29	17.6	18.72	19.34
R = 1		9.33	9.64			18.72	19.34
R = 2	8.55	9.33	9.64	10.29	17.6	18.72	19.34

Figure 3.6(c) shows that two main intense and coupled (the same crystallographic plane) reflections at 2θ = 9.64 ^{o} and 19.34 ^{o} are observed for all the three samples. They indicate that the particles are well crystallized. The peak width is 0.06 ° which corresponds to the instrument resolution, thus no indication may be obtained on the particle size from this information. The intensities of these two peaks are much larger in the case of R ≥ 1. No other peaks of similar intensities were found. In powder XRD diagrams of such compounds, we observe several intense peaks corresponding to different crystallographic planes. The fact that only two coupled peaks are observed indicates a growth with a preferential orientation of the corresponding hkl family of planes parallel to the substrate surface. Another two coupled and less intense peaks localized at 2θ = 9.33 ^{o} and 18.72 ^{o} are also observed. Three additional weak peaks at 2θ = 8.55 ^{o}, 10.29 ^{o} and 17.6 ^{o} are also found for the samples prepared at R = 0.5 and 2. The pattern of the crystallites formed in solution is very close to that expected for the MIL-101 phase. On the other hand, the XRD patterns in **Figure 3.6(c)** are not matching any of the powder XRD (PXRD) patterns reported for the three different structural phases known for this system: MIL-101[12], MIL-88B [13] and MIL-53 [14]. It is interesting to note that the 9.64 ° peak intensity decreases by a factor of 3.4 when R goes from 2 to 1 and by a factor of 1600 when R goes from 2 to 0.5. A similar trend is observed with the equivalent thickness of deposited C type material: it decreases by a factor of 2.5 when R goes from 2 to 1 and by a factor of 1500 when R goes from 2 to

0.5. This suggests that the peak at 9.64 °is correlated with the C crystallites.

3.2.2 Growth onto pyridine terminated Si surfaces (Si-Pyridine)

The morphology of MOFs grown onto **Si-Pyridine** surfaces at 90 ^{o}C are displayed in **Figure 3.7**.

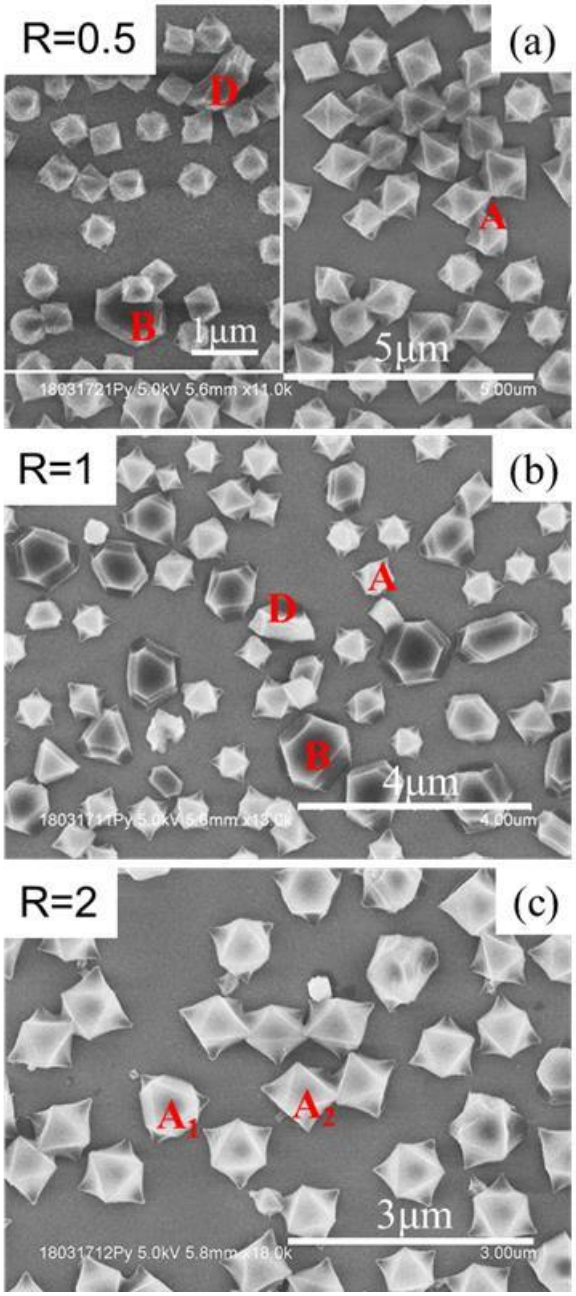

Figure 3.7 SEM images of Fe/BDC MOF grown onto pyridine terminated surfaces at 90 ^{o}C: (a) R = 0.5, (b) R = 1 and (c) R = 2, For all samples C_{Fe} = 25 mM and the growth time is 24 h.

Octahedral crystals (type A) and/or flat hexagons (B) with various density and size are found in SEM images. Unlike the films grown on carboxylic acid terminated surfaces, onto Si surfaces bearing pyridine groups, hexagonal pyramids (Type C) were not observed for all R values. The variation of density and mean crystal size of crystals A and B is displayed in **Figure 3.8**.

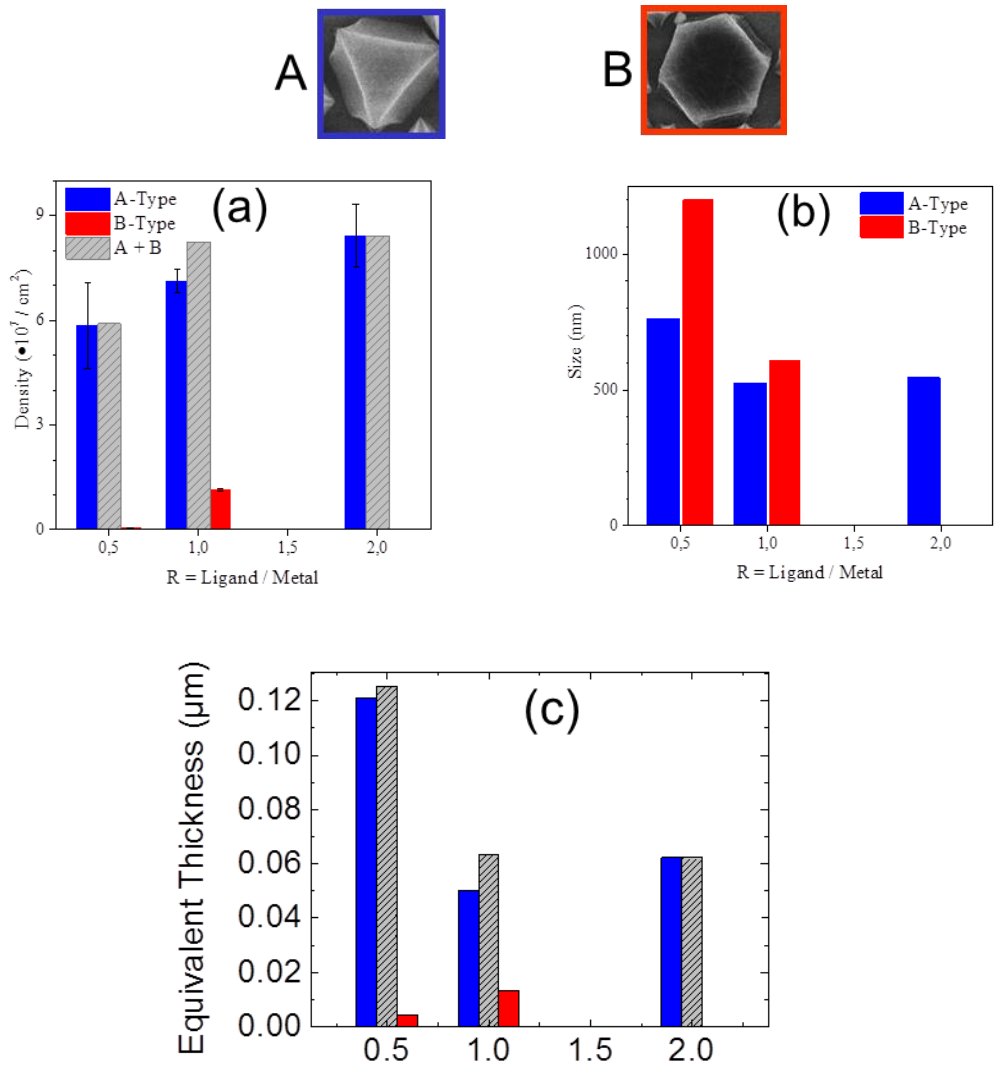

Figure 3.8 Density (a), lateral size (b) and equivalent thickness (c) of A-type crystals (blue) and B-type crystals (red) on pyridine terminated Si surfaces as a function of ligand to metal ratio R value in solutions. Grey bars correspond to the sum of A and B density (a) of equivalent thickness (c).

Majority of A-type crystallites is found on the Si-Pyridine surfaces for all R values. A slight increase of the density of A-type crystallites with R is observed. For B-type,

their density increases when R is raised from 0.5 to 1 but decreases when the ligand concentration is further increased. For R = 2, the SEM images show the quasi selective growth of A-type crystallites. An increase of the crystallite density (**Figure 3.8(a)**) is observed considering all the crystallites without shape discrimination (grey plot), indicating that the nucleation yield is slightly affected by the ligand concentration. The equivalent thickness of deposited material for each crystallite type is plotted as an equivalent thickness in **Figure 3.8(c)**.

XRD patterns of layers grown onto Si surfaces with pyridine-ended groups as a function of ratio R are presented in **Figure 3.9**. The calculated PXRD pattern of the well-known MIL-101 phase [12] for this system is also given in **Figure 3.9** (top black curves): the blue curve corresponds to the calculated diagram with additional broadening of the peaks (~ 1 °). The dark yellow curve is obtained using the same broadening procedure of the (111) diffraction peaks. In the experimental diagrams, a broad peak is found in the range $3° \leq 2\theta \leq 6°$ in addition to smaller coupled peaks at 9.33 ° and 18.72 ° (indicated by black triangles). The position of this broad peak is close to that of MIL-101 phase with restriction to the (111) peaks and with additional peak broadening.

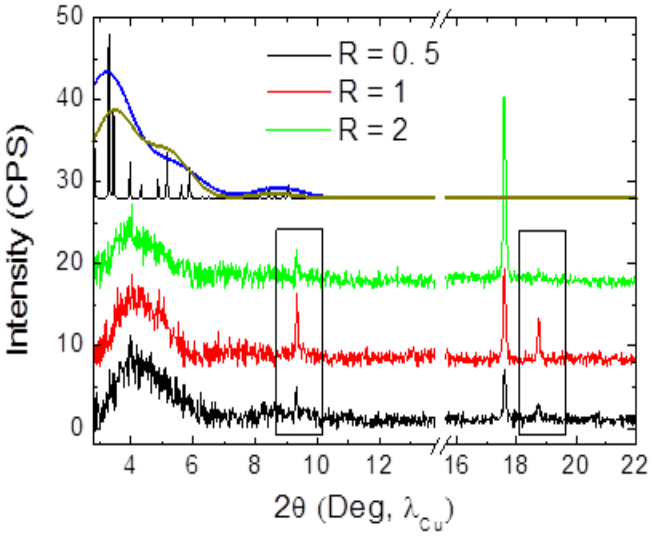

Figure 3.9 XRD experimental patterns (black, red and green curves) of Fe/BDC MOF films grown onto pyridine terminated Si surfaces under various ligand to metal ratios R in solution. Top curves are calculated PXRD pattern of MIL-101 phase. The two overlaid curves with broad peaks correspond to the same calculated pattern with additional broadening, in which the peak shape is considered to exhibit a Gaussian function. A new function of the peak shape could be obtained by substituting the already known peak positions and intensity of the simulated peaks of MIL-101 into the Gaussian function and afterwards making a superposition of all of them. Calculated curves with different extent of broadening can thus be plotted according to the new resulted function. For the blue curve, all diffraction peaks were considered; for the dark yellow curve, only the (111) family was considered. For all samples C_{Fe} = 25 mM, T = 90 ^{o}C and the growth time is 24 h. The experimental peak positions are summarized in **Table 3.2**.

No peaks related to the MIL-88B and MIL-53 phases are expected within the (3 - 6 °) range. This experimentally observed broad peak could probably be assigned to MIL-101 phase of poor crystallinity and/or of too small thickness, both leading to peak broadening effects. The peak at 17.6 ^{o} was always observed on samples without any correlation with the MOF growth. It might indicate the presence of residual crystallized H_2BDC ligands or the formation of FeO(OH) in some synthesis conditions.

Table 3.2 Summary of the peak positions observed on the XRD patterns of samples fabricated on pyridine terminated surfaces as a function of ratio R.

	Peak position (2θ, deg, λ_{Cu})			
R = 0.5, 1, 2	3-6	9.33	17.6	18.72

3.2.3 Growth onto oxidized Si surfaces

The morphologies of Fe/BDC MOFs grown onto Si oxidized surfaces are displayed in the SEM images in **Figure 3.10**. Similar to Si-Pyridine surfaces, a distribution of isolated A-type and B-type crystallites and rare D-type is observed on oxidized Si surfaces disregarding the relative ligand concentration in solution. We also occasionally found very large hexagonal bipyramids lying on one of their facets (**Figure 3.10(d)**). These crystallites most probably formed in solution. Their density is very low and it is hard to quantify with small uncertainty. However, it does show a clear dependence on R.

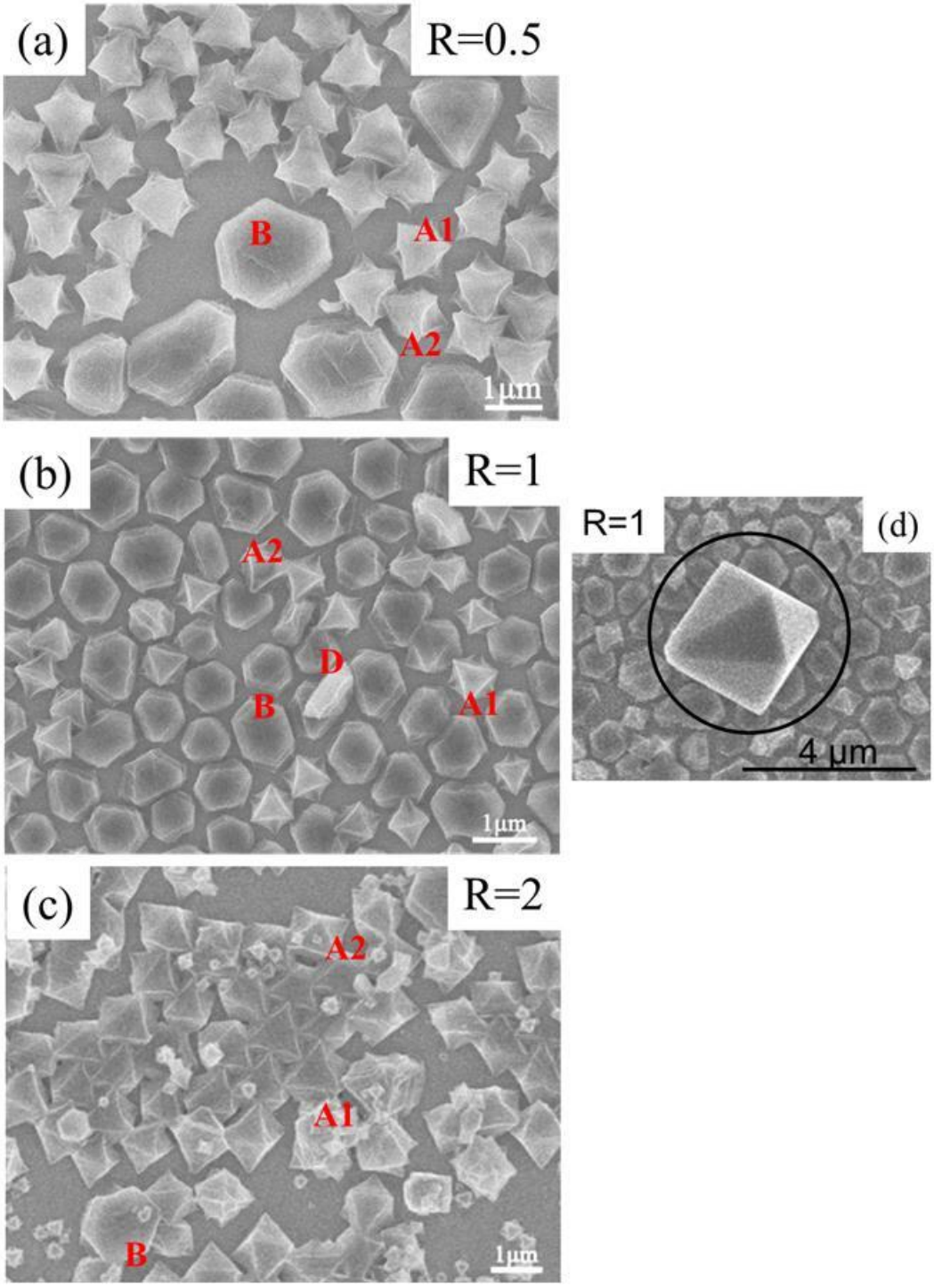

Figure 3.10 (a-c) Morphology of Fe/BDC MOFs as grown onto Si oxidized surfaces as a function of the ligand to metal ratio R in solutions. (d) R = 1 with some specific crystallites with a much lower density but with a much larger size. For all samples C_{Fe} = 25 mM and the growth time is 24 h.

The density and mean lateral size of A-type and B-type crystallites are plotted in **Figure 3.11**.

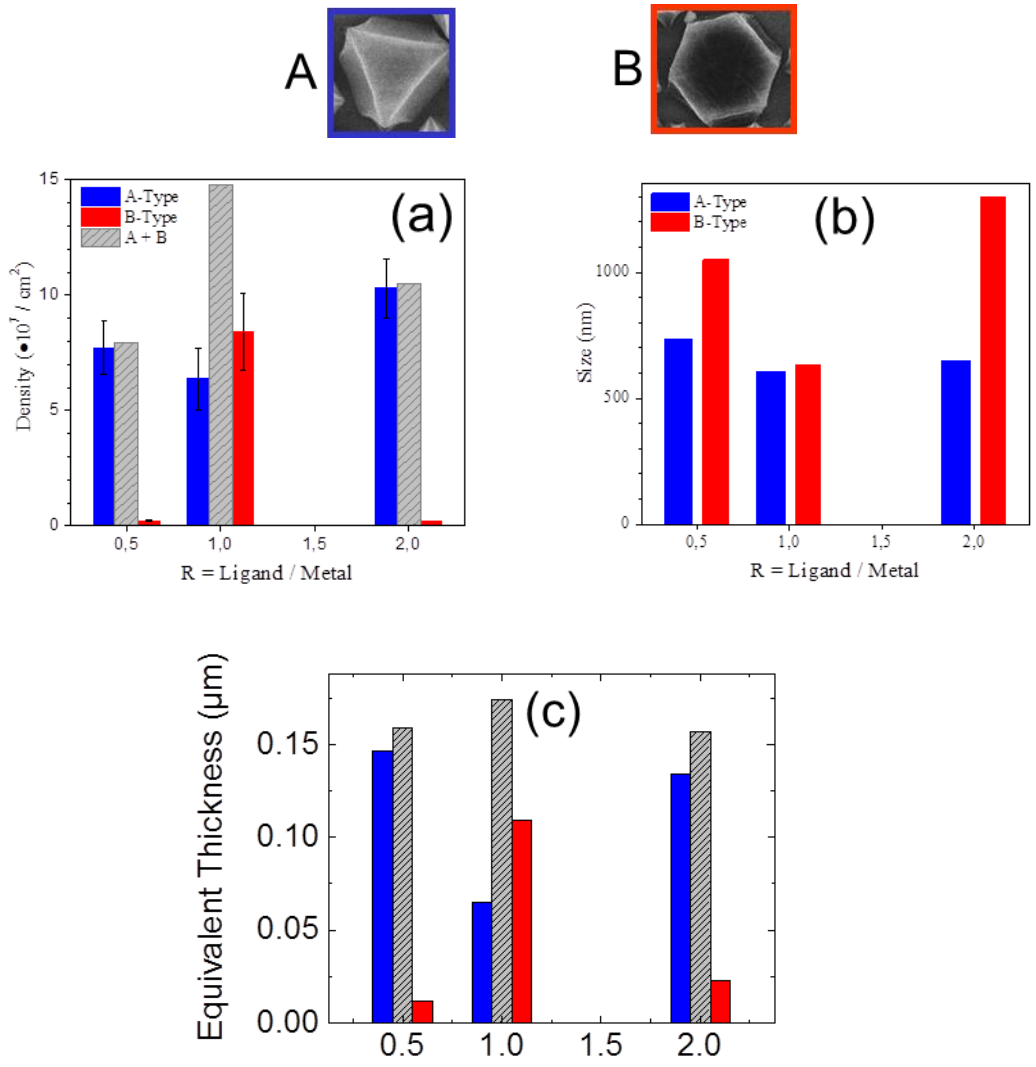

Figure 3.11: Density (a), lateral size (b) and equivalent thickness (c) of A-Type (blue) and B-Type (red) crystallites as grown on Si oxidized surfaces as a function of the ligand to metal ratio R. Grey bars correspond to the sum of A and B density (a) of equivalent thickness (c).

As in the case of Si-Pyridine surfaces, on the oxidized Si surfaces the crystallite total density is found to slightly increase when the solution is richer in ligand. The fraction of B-type crystallites has a maximum at R = 1. For R = 2, the images show the formation of large agglomerates consisting of several individual crystallites.

The XRD patterns of the MOFs grown on oxidized Si surfaces are displayed in **Figure 3.12**. The pattern of the MOF film prepared in solution with metal excess R = 0.5 (**Figure 3.12(a)** black curve) shows several sharp peaks: two coupled peaks at 9.33 ° and 18.72 ° (indicated by black rectangles), two sharp peaks below 2θ = 6 °, and two other peaks at 8.55 ° and 10.3 °. For R = 1 (**Figure 3.12(a)** red curve), we

find the two coupled peaks at 9.33 °and 18.72 °of almost equal intensities as for R = 0.5, and one peak below 6 °. In **Figure 3.12(b)** we focus on the low 2θ range. The MIL-101 phase PXRD is also shown (green and red vertical bars). The two peaks at 2θ = 3.43 °and 5.15 °fit well with the position of (222) and (333) Bragg peaks (red bars in **Figure 3.12(b)**) reported in the literature for of the MIL-101. The fact that mainly (111) peaks are observed indicates an oriented growth of MIL-101 phase with (111) texture. In addition, other peaks not fitting the MIL-101 phase are also observed at larger angles (9.33 °and 18.72 °) suggesting the growth of at least two different structural phases.

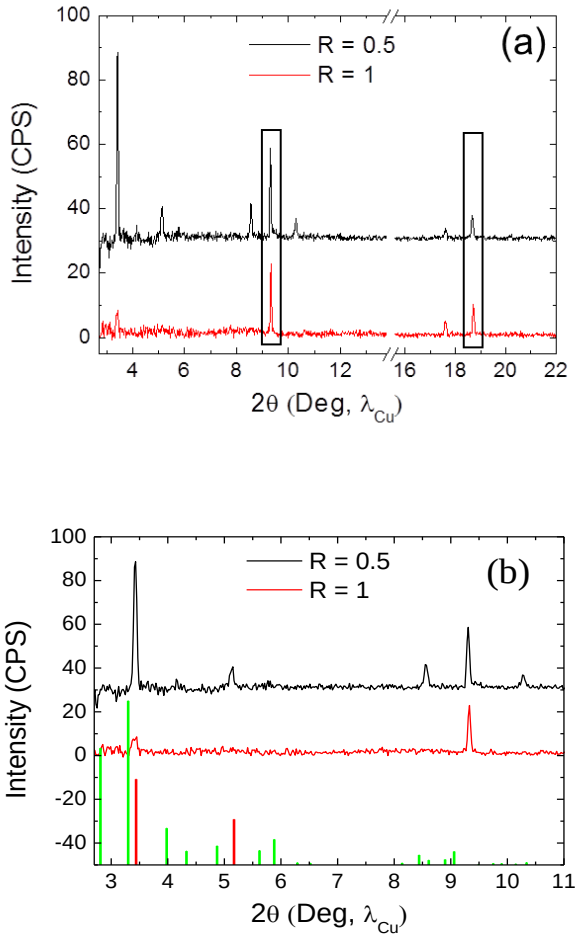

Figure 3.12 (a) XRD patterns of Fe/BDC MOFs grown onto oxidized Si surfaces for ligand to metal ratio R at 0.5 (black curve) and 1 (red curve). The rectangles indicate coupled peaks. (b) Zoom on the low angular range. The green and red bars correspond to the calculated XRD pattern of MIL-101. For all samples C_{Fe} = 25 mM and the growth time is 24 h. The peak positions are listed in **Table 3.3**.

Table 3.3 Summary of the peak positions observed on the XRD patterns of samples fabricated on oxidized terminated surfaces at R = 0.5 and 1.

	Peak position (2θ, deg)						
R = 0.5	3.43	5.15	8.55	9.33	10.29	17.6	18.72
R = 1	3.43 (weak)			9.33		17.6	18.72

3.2.4 Growth onto methyl terminated Si surfaces (Si-CH_3)

Morphologies of methyl terminated Si surfaces after 24 h immersion in solutions containing various amount of ligand at 90 ^{o}C are presented in **Figure 3.13**. As revealed by SEM images, no crystallites indicating MOF growth on Si surfaces with -CH_3 termination have been found for all R values. The occasional sub-100 nm islands may be some surface impurities. Representative AFM image of the sample prepared at R = 2 exhibits the typical and atomically flat structure with terraces of the Si(111) surface, ruling out the formation of any MOF layer on this kind of substrate. The absence of any diffraction peaks in the XRD patterns is in agreement also with the absence of MOF growth on this surface (See **Figure 3.14**).

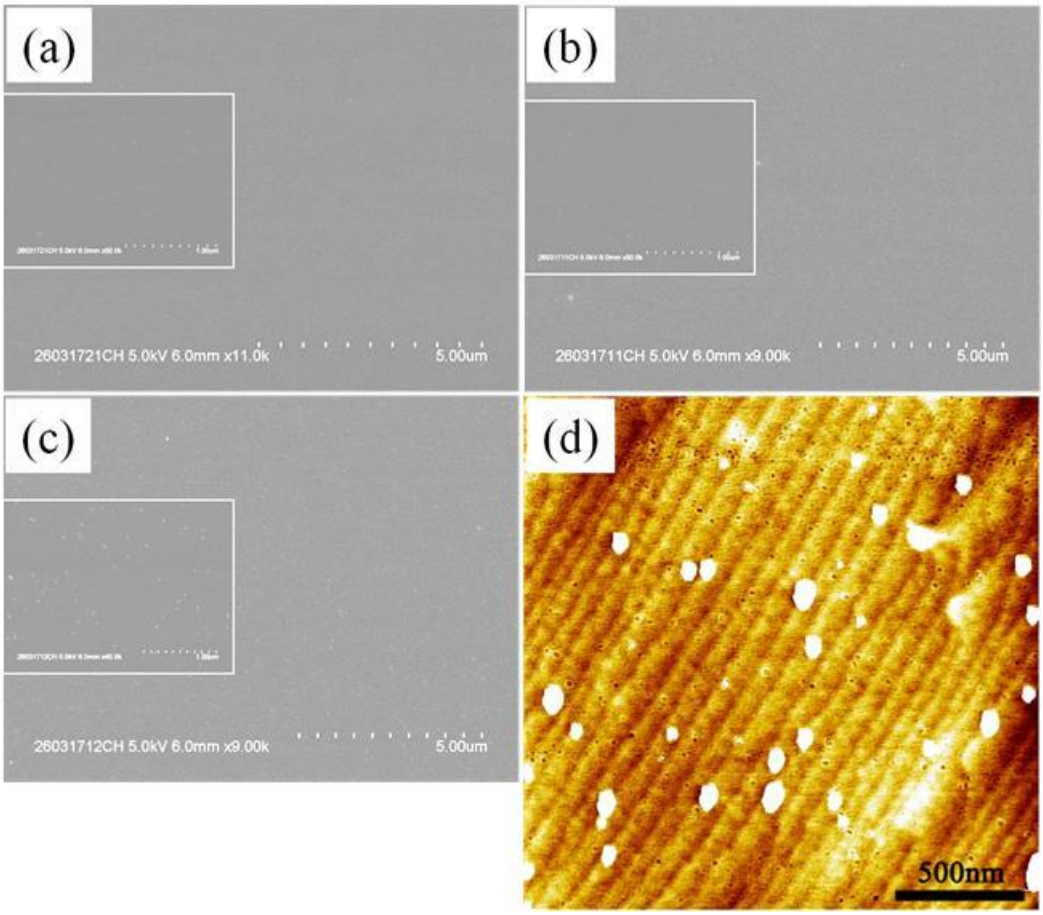

Figure 3.13 SEM images of methyl terminated Si surfaces after immersion in solutions containing variable R values at 90 ^{o}C: (a) R = 0.5, (b) R = 1 and (c) R = 2. (d) AFM image of sample as shown in (c). For all samples C_{Fe} = 25 mM and the growth time is 24 h.

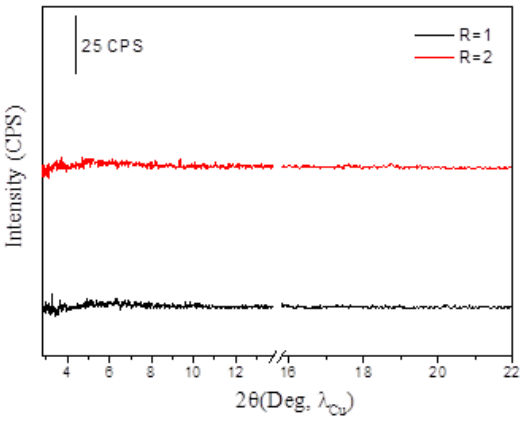

Figure 3.14 XRD patterns (background corrected) of methyl terminated Si surfaces after 24 h immersion in solutions containing equal amount of ligand to metal and excess of ligand. For all samples [Fe^{3+}] concentration is 25 mM and the growth time is 24 h.

3.3 Effect of post-treatment

Post synthesis treatments are very often used to remove residual solvent molecules/unreacted precursors trapped inside the MOFs and/or to improve their crystallinity [15]. Within this section we investigated the effect of thermal annealing and soxhlet rinsing on the as-prepared surface-mounted Fe/BDC MOFs. In the last part, we investigate the adhesion properties of the MOF layers.

3.3.1 Thermal annealing

Thermal annealing of as-prepared MOF layers exhibiting different composition in term of type of the crystalline structures/habits observed on the SEM images and/or morphologies was performed in an oven at ambient pressure. The sample was put into a pre-heated oven at 150 ^{o}C for various durations. XRD and SEM characterizations were carried out to monitor the morphology and structural changes.

Figure 3.15 shows the evolution of XRD patterns during annealing sequences of a sample exhibiting two types of crystallites grown on Si-COOH at 70 ℃: isolated octahedral (A-type) and hexagonal pyramid-like (C-type). Two coupled peaks at 2θ = 9.64 ^{o} and 19.34 ^{o} are observed in the XRD pattern. In **Figure 3.15** only the 9.64 ° peak is shown. During annealing the main feature observed on the XRD patterns is a fast and quasi total disappearance of the peak standing initially at 2θ = 9.64 °and the appearance of a new peak at lower angle 2θ ~ 9.5 °after 2 h annealing.

As with subsequent annealing the peak is shifting progressively to an even lower angle, down to 2θ = 9.24 °after 86 h total annealing time. Together with the peak shift a broadening and a loss of its intensity is observed. The peak intensity and position as a function of annealing time are shown in **Figure 3.16(a)**. The SEM images prior to and after 22 h thermal annealing are displayed **Figure 3.16(b2)** and **(c2)** respectively. They show that the C type crystallites present a very irregular shape upon annealing.

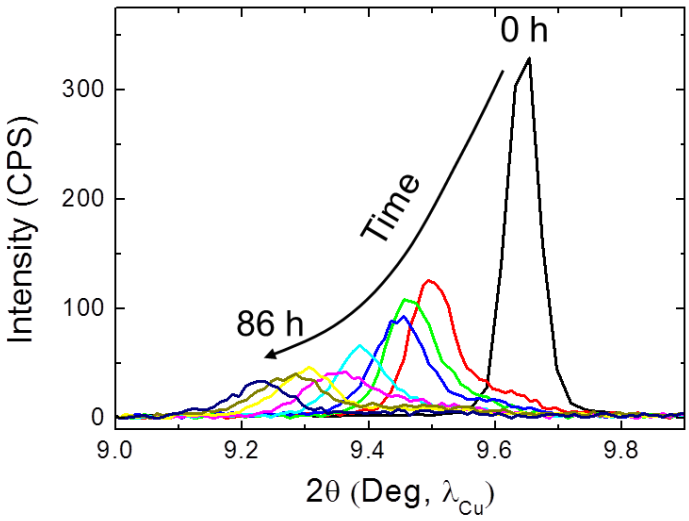

Figure 3.15 Evolution of the peak at 2θ = 9.64 ° of the film deposited on Si-COOH with R = 2, 70 °C and [Fe^{3+}] = 25 mM (for 1day growth) along with the post-treating time in an oven under 150 °C over 86 h.

It is noteworthy that the peak evolution takes place in two steps: a fast left-shift of around 0.15 °in position and a loss of ~30 % in intensity after the first annealing 2 h and then a slower and monotonous shift accompanied by additional loss in intensity. Around 70-75 % of intensity is lost after 22 h annealing. After then the intensity evolves slightly whereas the peak position is still shifting continuously towards lower angle. The significant decrease of the peak intensity is correlated with the observation of breakdown of most hexagonal pyramid-like crystallites. No other sizeable morphology change was found on the SEM images after the thermal treatment.

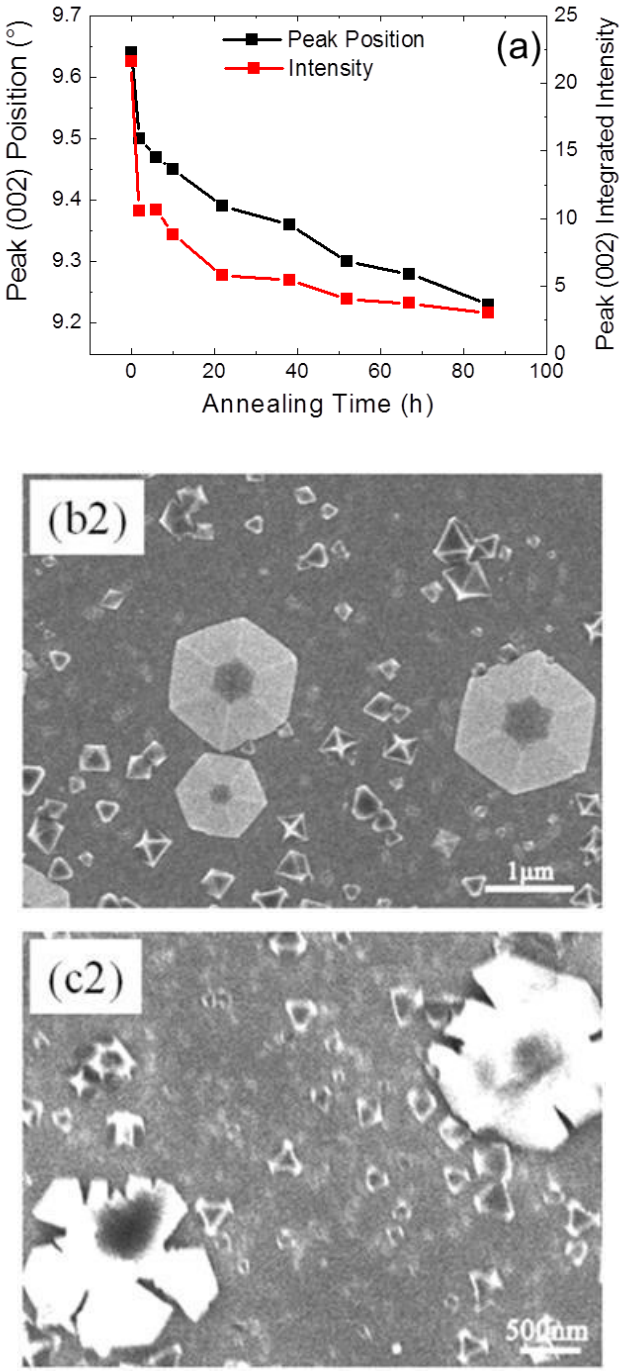

Figure 3.16 (a) Time dependence of peak position (black) and integrated area (red) of the (002) peak as a function of annealing time in the oven at 150 °C. SEM images prior to (b2) and after (c2) annealing for 22 h.

It must be noted that for the films composed of compact assembly of hexagonal crystals the results after thermal annealing show a shifting of the XRD peaks towards lower angle but with a slower rate. Meanwhile, the intensity of the relevant peaks also evidence a drastic decrease related to the collapse of the hexagonal pyramids.

3.3.2 Soxhlet rinsing

The SEM images and XRD patterns of Fe/BDC MOF grown onto Si-COOH surface prior to and after long term soxhlet rinsing in EtOH are displayed on **Figure 3.17(a-d)** and **Figure 3.17(e)**, respectively. In the case of layers mainly composed of close packed hexagonal pyramid (C) crystallites obtained with $R \geq 1$, the SEM images evidenced the disappearance of most of the crystallites after the rinsing. This may be due to a weak anchoring force of this phase with the Si-COOH surface or that this phase dissolves in this rinsing condition. Conversely, the thinner layer observed in between the hexagonal phase remains present, surrounded by the 'foot-print' of the removed crystallites. The removal of C-type crystallites is correlated with the disappearance of the two intense coupled peaks at $2\theta = 9.64\ ^\circ$ and $19.34\ ^\circ$ on the XRD patterns and the appearance a coupled sharp and much weaker peaks at $2\theta = 9.07\ ^\circ$ and $18.19\ ^\circ$. A similar treatment done to layers grown on Si-COOH surface mainly composed of A and B-type crystallites and a few hexagonal crystallites (C) demonstrates that after 16 h in soxhlet the A and B-type crystals are intact whereas the hexagonal crystals (C) are removed.

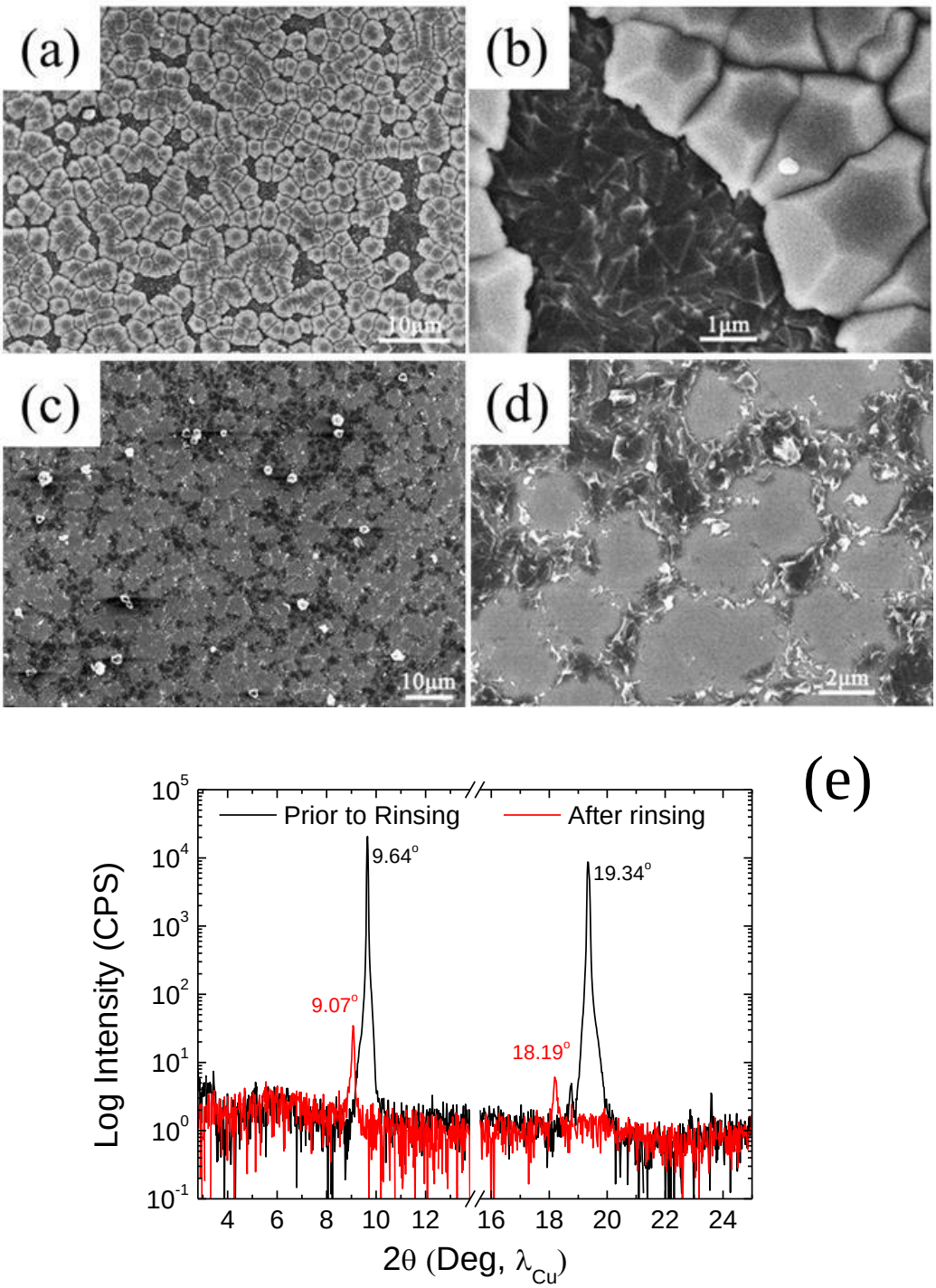

Figure 3.17 SEM images of sample prepared at 90 °C on Si-COOH surface under R = 1 prior to (a,b) and after (c,d) rinsing in soxhlet with ethanol for 16 h. (e) XRD patterns before (black curve) and after (red curve) the rinsing procedure. The peak position is indicated nearby each peak. [Fe^{3+}] concentration is 25 mM and the growth time is 24 h.

We performed similar experiments on films prepared onto pyridine-terminated Si surfaces where only types A and B crystals were observed. **Figure 3.18** shows the result of rinsing such samples in soxhlet with ethanol. SEM images prior to and after

rinsing do not show any significant difference confirming the strong adhesion of octahedral and flat hexagonal crystals on this surface. On the other hand, the few features present in the XRD diagrams (broad peak below 6 °and two coupled peaks at 9.33 °and 18.72 °) disappear upon rinsing (**Figure 3.18(c)**).

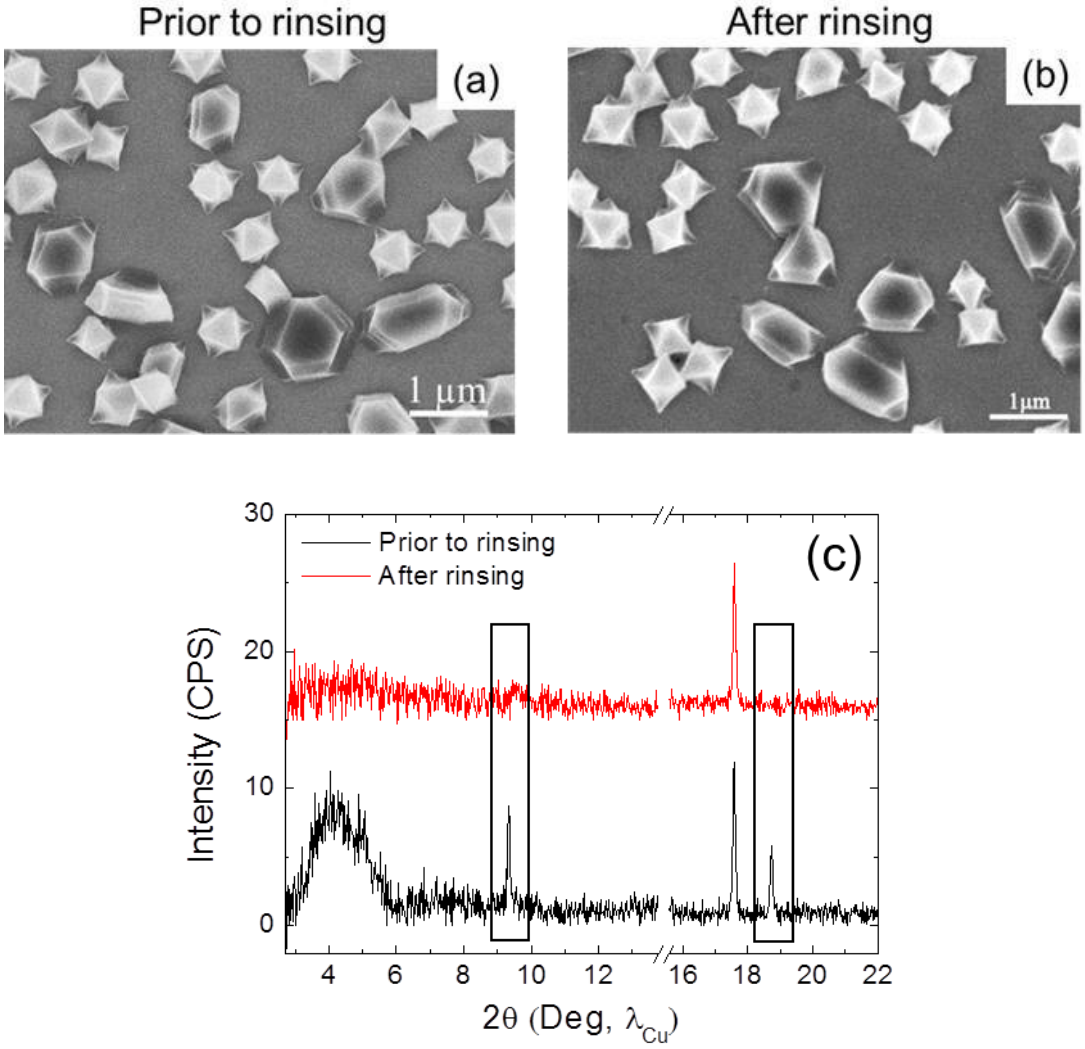

Figure 3.18 (a) and (b) SEM images of sample prepared on Si-Pyridine surface at R = 1 prior to and after rinsing in soxhlet with ethanol for 2 h. XRD patterns (c) prior to (black) and after (red) the rinsing procedure.

3.3.3 Adhesion tests

The adhesion of the supported MOFs on the different types of surfaces has been investigated using scotch tape peeling method. The SEM images **(Figure 3.19(a-f))** reveal the removal of most of the crystallites for the different kinds of MOF films. However different behaviors have been observed depending on the crystallite type. Indeed, the SEM images show the removal of entire hexagonal pyramids (C) **(Figure 3.19(a-b))** indicating weak anchoring of these crystallites on the Si-COOH surfaces. In the case of crystallites B, the SEM **(Figure 3.19(c,e))** images show that they are still present on the surface after the scotch peeling experiment. In the case of crystallites A, the SEM **(Figure 3.19(c-f))** and AFM **(Figure 3.19(g))** images indicate that only upper part of the octahedral crystallites was removed. For A and B-type crystallites similar behavior was observed on surfaces with other chemical termination.

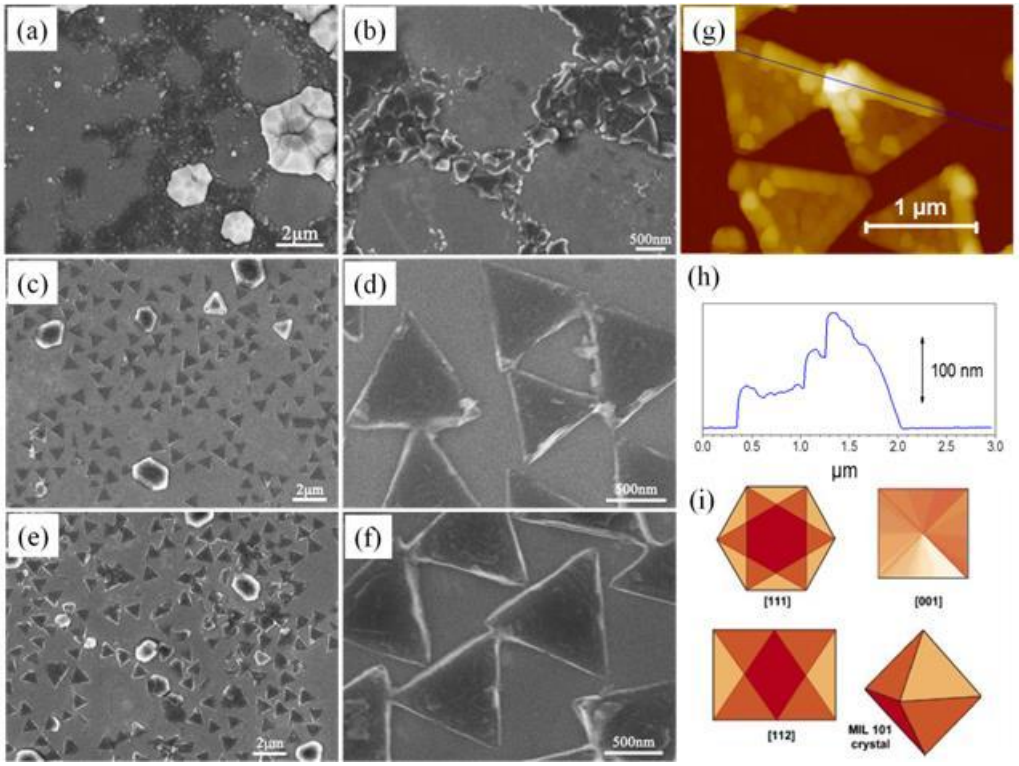

Figure 3.19 SEM images of samples exhibiting different types of crystallites after scotching test: (a,b) composed of assembly of hexagonal crystals and compact layer in between; (c,d) Sample prepared on Si-COOH surface mainly comprised of octahedral and flat hexagonal crystals; (e,f) Sample prepared on Si-Oxidized surface also made of octahedral and flat hexagonal crystallites. AFM image (g) and cross section (h) showing the 3D morphology and height of the triangular residues remaining on the surface after the removal of octahedral crystallites as shown in (c,d). (i) Schematic crystal orientation of MIL-101[12]. Synthesis conditions for all samples: C_{Fe}^{3+} = 25 mM, T = 90 °C. Growth time and ratio of ligand to metal are all 24 h and R = 0.5 for (c-f), respectively. While, for (a,b) the R equals 2 and the growth time is 10 h.

3.4 Discussion

3.4.1 Identification of structural phases

The SEM characterizations of Fe/BDC supported MOFs prepared on surfaces with different chemistry revealed the growth of crystalline materials. Different types of crystallites exhibiting different shapes were identified, suggesting the presence of different crystalline phases on the surface and/or with different orientations.

The observation of crystallites exhibiting well defined octahedral shape (A-type)

is consistent with that of the rigid MIL-101 fcc phase. Indeed, the crystallites formed in solution are mainly of A type and their XRD pattern is similar to that expected for the MIL-101 phase. In addition, we found in the case of films prepared on oxidized Si surfaces the signature of the MIL-101 phase in the XRD patterns. The exclusive observation of the (111) family planes in this case indicate an oriented growth with (111) texture. A drawing of a fcc lattice is shown in **Figure 3.20(a)**, where an octahedron with isosceles triangular facets is highlighted. It is clear from this drawing that the facets are along the 111 direction. The (111) oriented growth is also consistent with the observation of A-type crystallites exhibiting flat triangular facets parallel to the surface as confirmed by the SEM images.

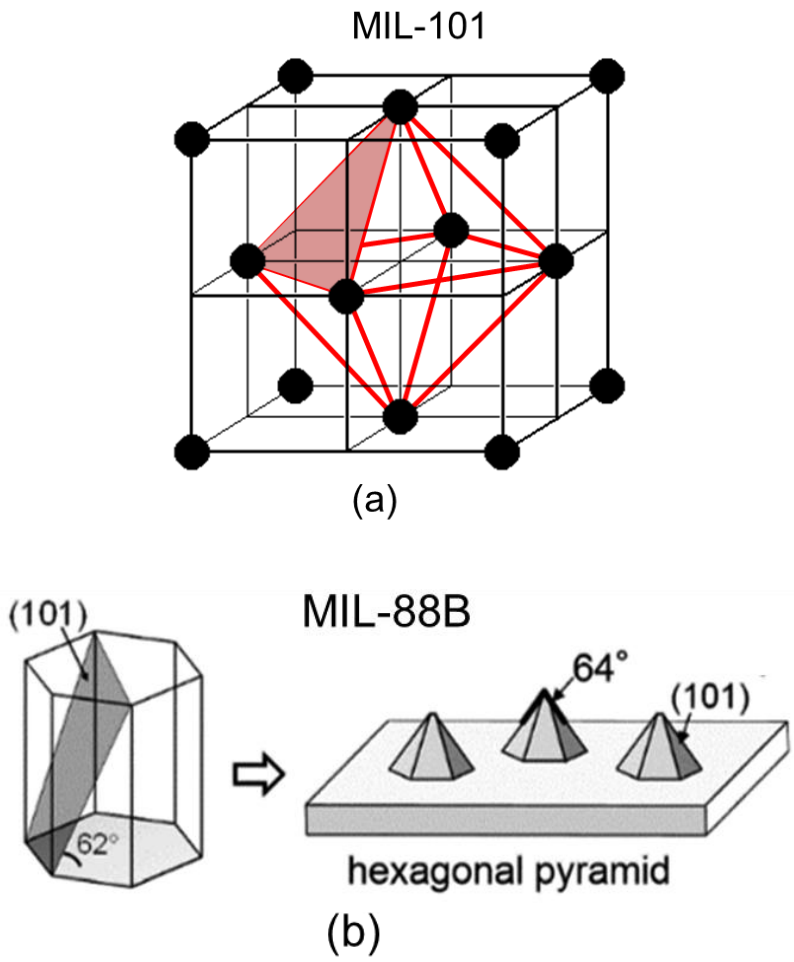

Figure 3.20 Drawings showing the crystalline structure of the MIL-101 (a) and the MIL-88B (b). In (a), the red octahedra is a representation of the symmetry of the A crystallites. The colored area highlights one of the 8 facets which are oriented along the 111 direction. In (b), the grey plane on the left highlights the facets of the C crystallites. These facets are oriented along the 101 direction.

We did not observe a clear signature for the presence of MIL-101 in the XRD data in the case of Si-COOH with R = 0.5 or on Si-Pyridine despite the crystallites exhibit a well-defined octahedral geometry in the SEM images. This behavior may have different origins.

- A first explanation is a slight mis-orientation of crystallographic axis [111] with respect to the surface normal. That would make difficult observing the corresponding Bragg reflections in the Bragg Brentano geometry used for the XRD measurements. Indeed, SEM images show that some A-type crystallites look like quasi perfectly oriented with triangular (111) facets parallel to the surface, whereas others look like tilted. Since the divergence of the X-ray beam is in the range 0.5-1 °, if the crystallite

tilt is larger than 1 °, their diffraction intensity is going to be weak.

- A second possible explanation is the small scattering intensity of the MIL-101 phase because of its high degree of porosity and the small amount of diffracting material on the Si surface.

- A third possibility is that the as-prepared MIL-101phase filled with solvent molecules and/or unreacted precursors inducing poor crystallinity. However no significant improvement of the crystallinity was observed on the XRD pattern after soxhlet rinsing. On the contrary, the disappearance of the diffraction upon rinsing while the crystallite form, size and density remaining the same may suggest that the diffraction peaks originate from other crystallites having a very low surface density making difficult their observation and quantification. These crystallites may come from the solution and attach to the surface during the MOF film formation.

Apart from the octahedral crystallites (A-type) that may be identified as MIL-101 phase, the SEM images reveal the growth of crystallites exhibiting hexagonal symmetry. Two types are distinguished: hexagonal pyramids (C-type crystallites) and hexagonal crystallites with flat top (B-type crystallites).

The C-type crystallites with the coupled peaks at 9.64 ° and 19.34 ° may be identified as MIL-88B phase because of their characteristic hexagonal shape similar to that of the reported MIL-88B crystallites as-obtained from synthesis in homogeneous phase. A drawing of a hexagonal crystallite is shown in **Figure 3.20(b)**, where the 101 plane is highlighted. As shown in the figure, the MIL-88B pyramids have six facets which are oriented along the 101 direction. This is consistent with our SEM observations of C crystallites. The XRD peak attribution is however delicate because the MIL-88B phase has a flexible structure and is well known to undergo drastic structural changes upon solvent uptake or release [13]. As a result, very different XRD patterns are reported depending on the filling degree of the porous matrix by solvent molecules and/or the nature of the solvents (size, polarity). Examples of experimental PXRD patterns of dry MIL-88B and solvated MIL-88B with various solvents are shown in **Figure 3.21**.

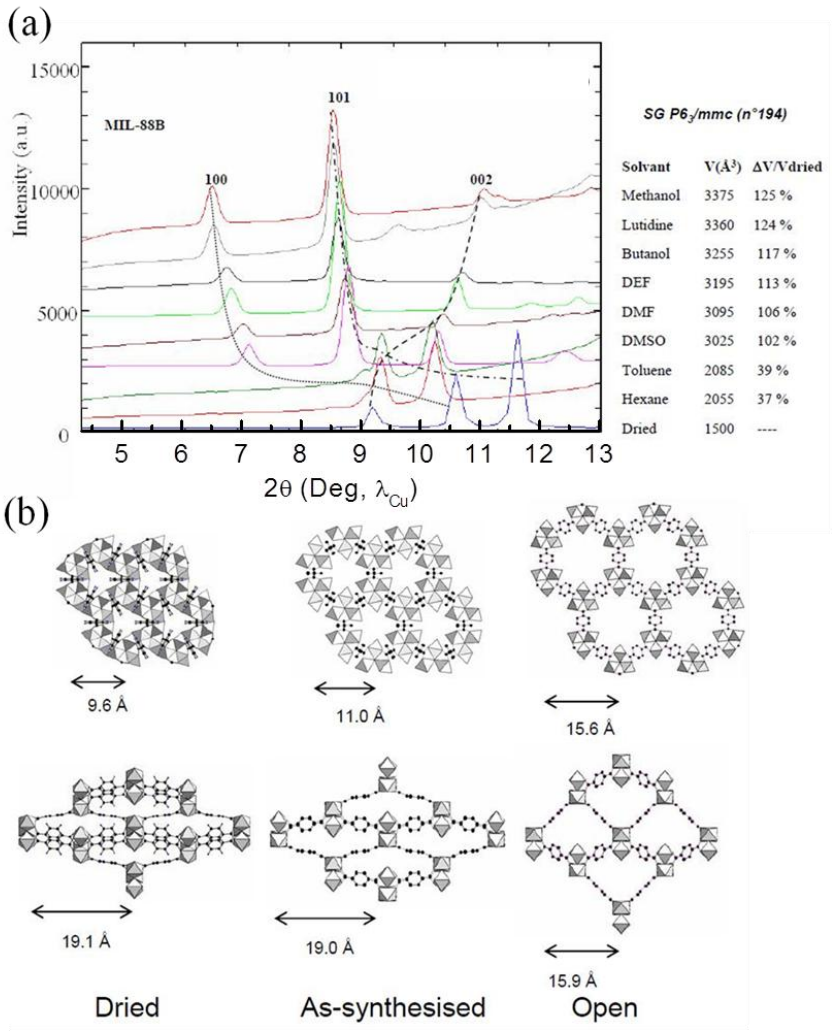

Figure 3.21 (a) Experimental PXRD patterns of dry MIL-88B (blue plot) and solvated MIL-88B with different solvents as inferred from in-situ XRD measurements. (b) Scheme of the network swelling upon solvent uptake. Figure reproduced from Ref [13].

The variable amplitude of the shift of the three main Bragg peaks (100, 002, and 101 planes) suggests variable degree of network swelling, with a larger pore opening observed in MeOH. In **Figure 3.21(a)**, the 9.64 °peak is at a position larger than that of the 002 peak of the dry phase. A larger peak position indicates that the C crystallites are partly solvated. The assignment of the peak at 2θ ~ 9.64 °to 002 Bragg reflection of partially *solvated* MIL-88B phase is further sustained by the observation of the shift of the peak towards lower angles after post-synthesis annealing at 150 ℃ (**Figure 3.15**)

The XRD patterns of Fe/BDC MOF layers grown onto the three different

functionalized surfaces show another set of two sharp coupled peaks at 2θ ~ 9.33 ° and 2θ ~ 18.72 °. These two peaks are present in the case of Si-pyridine and oxidized Si surfaces where no C type crystallite have been identified by SEM. In addition, these peaks disappear after a soxhlet rinsing with ethanol, indicating that they are not correlated with A or B type crystallites. On the other hand, we found sometimes on the substrate surface large hexagonal double sided pyramids (**Figure 3.10(d)**). These crystallites resembles C type ones. They disappear from the SEM images upon soxhlet rinsing together with the disappearance of the coupled peaks at 9.33 ° and 18.72 °. This correlation suggests that the diffracted intensity in these peaks may originate from these crystallites and particularly, from the atomic planes parallel to the facets. As for the C crystallites the c-axis is perpendicular to the pyramid basis, the facets are oriented 101. The expected (101) peak for MIL-88B phase depends on the solvation and may be found close to 9.33 ° in the case of Toluene (**Figure 3.21(a)**). This yields a rather consistent picture.

The crystalline structure of B-type crystallites that also exhibit hexagonal geometry is much more difficult to determine. The larger crystallites exhibit hexagonal shapes with non vertical facets at edges and irregular sides whereas other smaller ones look like truncated octahedrons. All these different crystal habits are known to possibly exist for cubic crystallographic phases which would suggest that these crystallites (B-type) may also be MIL-101 phase. However, we couldn't find evidence for the XRD signature of these crystallites.

The crystalline structure of the compact layer observed in between the dense assembly of C-type crystallites on Si-COOH surfaces when R = 2 and 1 (**Figure 3.4(b)**) remains unresolved. The observation of triangular and/or octahedral like geometry within this layer suggests it might be MIL-101 phase. No clear organization is observed which might indicate a non oriented growth. Unfortunately no clear-cut Bragg peaks corresponding to this phase are observed on the XRD patterns (**Figure 3.6**). In addition, since it is much thinner than the C type crystallites, its diffracted intensity is expected to be low. Interestingly, the **Figure 3.17** shows that after long term soxhlet rinsing in EtOH, the remaining film on the surface is composed of this

layer and a few C type crystallites which have undergone a serious deformation. This is correlated with the appearance of two coupled sharp peaks at 2θ = 9.07 ° and 18.19 °. Their intensities are ~ 500 times weaker and their positions are significantly lower than the 002 (9.24 °) and 004 (18.54 °) Bragg reflections reported for the *dry* MIL-88B phase, allowing for discarding the assignment of these peaks to the (001) reflections of solvent free MIL-88B residual C-type crystallites. But as we observed in **Figure 3.21(a)**, they might correspond to the (100) and/or (101) reflections of solvated MIL-88B originating from the residual C crystallite. However, their strong deformation should yield a XRD pattern close to powder XRD with broad peaks, which is clearly not the case.

Another possibility is that the soxhlet rinsing induces a phase transition of the dense layer to more crystallized phase. **Figure 3.22** shows that the peak at 2θ = 9.07 ° stands within the range where Bragg peaks of MIL-88B (100 and 101) and MIL-53 (002 and 110) are reported, depending on their solvation degree [13,14,16,17]. Therefore a transformation of the as-grown layer into MIL-88B phase with a different texture *or* into MIL-53 phase can't be totally disregarded. Phase transitions from the MIL-101 kinetic phase to more stable MIL-88B or MIL-53 thermodynamic phases upon aging or post-treatment have already been reported in the literature [18,19]. We will see additional experimental data in Chapter 4 which suggest that this dense layer structure is that of MIL-101.

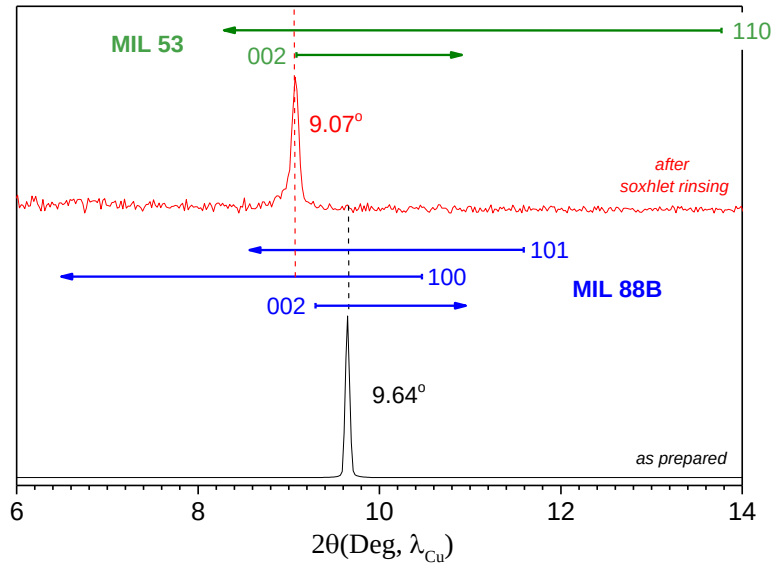

Figure 3.22 XRD pattern prior to (black plot) and after (red plot) long term soxhlet rinsing in EtOH of supported MOFs exhibiting two structural phases: dense assembly of hexagonal pyramids and isolated compact layer (the same sample as in **Figure 3.17**). The peak positions are compared to the angular range where Bragg peaks of MIL-88B (002, 100, 101) and MIL-53 (002, 110) phases are reported. Note that both phases exhibit a flexible structure and therefore variable XRD patterns depending on their solvation degree. The arrows represent the amplitude of peak shift, starting from the position reported for the *dry* phases.

Table 3.4 summaries the crystallite shapes, structure and XRD peaks positions of crystallites A, B, C, dense layer and bipyramids formed in solution.

Table 3.4 Summary of the crystallite shape, structure and XRD peak positions. The text in italics indicates that the attribution is not founded on direct experimental observations but on a deduction based on several data.

Crystallite shape	Crystallite structure	Texture	XRD peak 2θ positions (λ_{Cu})
A 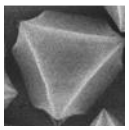	*MIL-101*	*(111)*	3.43 °; 5.15 °
B 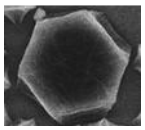	*MIL-101*	*(111)*	3.43 °; 5.15 °
C 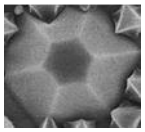	MIL-88B	(001)	9.64 °; 19.34 °
Dense layer 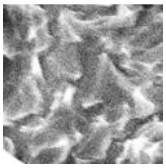	*MIL-101*	polycrystalline	
Bi-pyramid 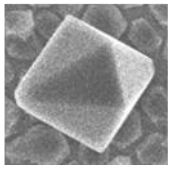	MIL-88B	101	9.33 °; 18.72 °

3.4.2 Crystallite growth mode

The fact that the top surface of B crystallites presents shapes recalling A type crystallites strongly suggests that the formation of A and B crystallites are related. We

will first start by discussing the formation of A crystallite. Three different nucleation/growth mechanisms may be considered:

i) A direct nucleation and growth on the surface (heterogeneous nucleation) leading to the formation of the A-type crystallites.

ii) The anchoring of MIL-101 octahedral nuclei/seeds that pre-formed in solution and their subsequent growth on the surface leading to the formation of the 3D octahedrons.

iii) The nucleation and growth of the A crystallite in solution and attachment to the surface.

The last scenario is rather improbable because we clearly observe the formation of C crystallite on top of some A crystallites. The first scenario is plausible but some facts remain inconsistent: (i) the crystallite size at the surface is very close to that of the crystallite formed in solution; (ii) the size distribution is rather narrow and even closely packed crystallites have a similar size as independent crystallites; (iii) the alignment of A crystallites which are closely packed and oriented is counter intuitive for a nucleation and growth mechanism entirely taking place on the substrate surface. The second scenario seems the most plausible. It allows explaining the alignment of close packed crystallite. Indeed, a crystallite arriving to the surface with enough mobility will attach with one of its facets and if it arrives close to another crystallite already attached, it will attach by two adjacent facets and align with the second crystallite. It also allows explaining the similar crystallite size as that formed in solution and the narrow size distribution. It finally give a hint about the absence of diffracted intensity of the A crystallites since the orientation on the surface of these crystallites coming from the solution may not be parallel to the surface within 1 °, in contrast with C crystallites.

The same scenarios may be proposed for the formation of B type crystallites. However, since they seem to present characteristics which strongly recall A type crystallites, a similar scenario as that of A crystallite formation is most probable. The formation of B crystallites proceeds then by the agglomeration of two or more A type crystallites which nucleated and grew in solution and attached close to each other onto

the surface. Further growth and reorganization is necessary to transform the A crystallite agglomerates into B type crystallites. An example of B type crystallite during its formation is shown in the inset of **Figure 3.1(b)**. It is not clear from this scenario whether the merging of A type crystallites to form B type crystallites is accompanied by a structural transition.

These conclusions clearly suggest that massive mass transport and reorganization on the surface is possible during the formation of the crystallites on the surface. Such surface specific transformations may be induced by (i) the contact between the crystallite and the surface which modifies the crystallite surface energetics and (ii) the close packing of the crystallites on the surface which is less probable in the solution.

3.4.3 Influence of the substrate surface chemistry

The relative coverage - in term of crystallite type and/or structural phase - obtained on different types of surfaces as a function of the relative ratio of precursors in solution is summarized in **Figure 3.23**. Remarkably, the growth of MIL-88B hexagonal pyramids (C-type) is observed merely onto Si-COOH and is strongly promoted by ligand excess in solution. Further investigations of Fe/BDC growth on these surfaces will be presented in the next chapter.

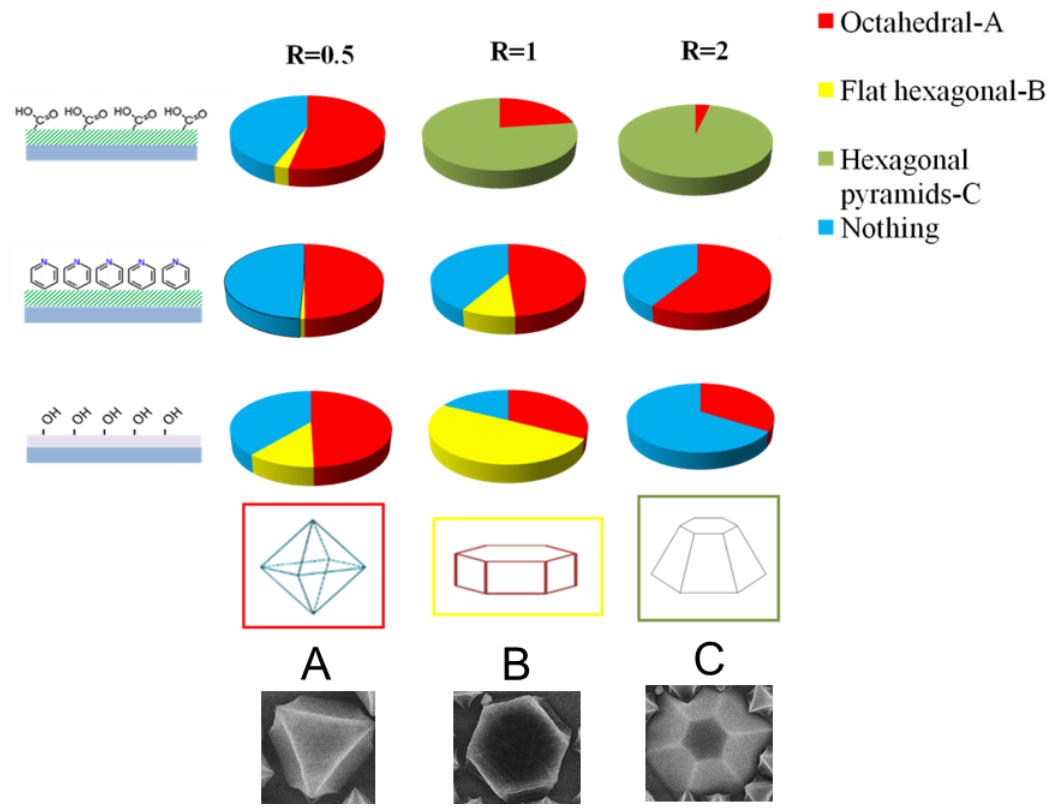

Figure 3.23 Relative surface coverage of different types of crystallites formed on functionalized Si surfaces as a function of ligand to metal ratio R and Si surface chemistry. From left to right the three columns correspond to R = 0.5, R = 1 and R = 2. The different rows correspond to different surface terminations: carboxylic acid, pyridine and hydroxyl, respectively from top to bottom.

Variable relative fractions of A-type (octahedrons) and B-type (flat hexagons) crystallites were observed depending on the surface chemistry and/or the relative ratio R of precursors in solutions. The presence of A crystallites on the surfaces whatever the chemical termination is consistent with their formation in solution and indicates weak attachment selectivity of these crystallites with respect to the surface chemistry. The variation of their coverage for different Si surface chemistry is probably due to the fluctuation of the attachment process and to the availability of free surface sites. The presence of clear triangular ‘foot-prints’ after adhesive tape test demonstrates a strong connection between the crystals and the substrate.

The growth of B-type crystallites looks much more selective, an oxidized Si surface and R = 1 being the optimal conditions for the highest B crystallite coverage. In these conditions, the total crystallite surface density is the largest among those observed for oxidized Si and Si-Pyridine for all R values. Following the growth model

presented above for B crystallite, a larger B crystallite coverage may be associated with a larger A crystallite density attaching to the surface. If the A crystallite density increases, the probability of crystallite merging to form B crystallites is larger. This may explain the larger B crystallite density. It is still unclear why in these conditions; more A crystallites attach on top the Si surface. The case of C type crystallites is probably the most interesting. The associated large XRD diffraction intensities and the orientation of the crystallite on the substrate surface are clear indications that their nucleation and their growth are taking place exclusively on carboxylic acid terminated surfaces. These crystallites substantially form on Si-COOH for $R \geq 1$. The dense layer (**Figure 3.4(b, circle)**) is also only observed in the later conditions. One may conclude that the COOH termination has a determining influence on the growth of the dense layer and the C crystallites. For the bidentate carboxylic terminated functional groups on Si substrate, carboxylates of 3 acid chains serve as the anchors to bind with 3 Fe^{3+} to form the FeO_6 trimer and then initial the sequent construction of MIL-88B framework. In such a way, all terephthalic acid molecules are configured along [001] direction, matching well with the orientation of terephthalic acid molecules within the bulk MIL-88B structures (See **Figure 3.24)**. This building scheme allows elaborating correctly the specific growth of the C crystallite on Si-COOH surface.

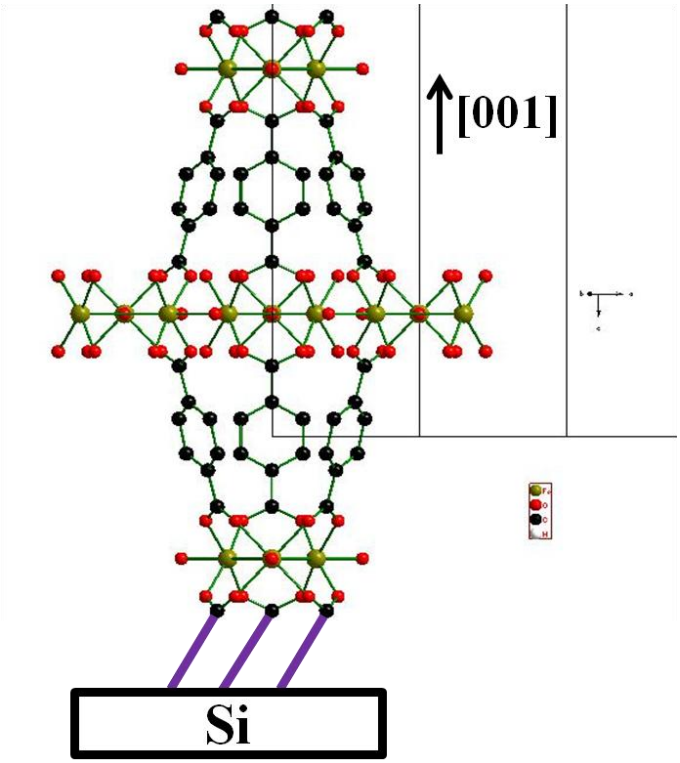

Figure 3.24 Schematic growth of MIL-88B crystals along [001] direction. The monolayer grafted on Si is simplified as purple stick. Oxygen, carbon and iron atoms are in red, black, and light green, respectively. Hydrogen atoms have been omitted for clarity.

For MIL-101 phase, it crystallizes in the cubic space group with a huge unit cell parameter of a = 89 angstrom. To interpret the orientation and/or alignment of MIL-101 along [111] direction, the second building unit-supertetrahedra constructed by four trimers of metal-oxygen octahedral and 6 deprotonated H_2BDC linkers [12] is brought in to simplify the interface between the MIL-101 crystal and substrate. For the textured MIL-101 along [111] direction observed on carboxylic terminated Si surfaces, it is expected that the substitution of terminal groups of grafted monolayer instead of linkers launches the coordination with the ferric ions as depicted in **Figure 3.25(b)** (the position 1, 2 and 3). Although the coordinating sites of Fe^{3+} are not arranged in the same horizontal plane, the flexibility of grafted molecule chains makes it achieve. Oriented MIL-101 crystallites are obtained once the further construction of the frameworks is maintained along [111] direction. Unlike the mere alignment of linkers along [001] direction of oriented MIL-88B crystals, linkers within MIL-101 frameworks configures in a much more complicated way, which can

probably be disturbed in terms of interactions by other molecules in the medium and/or steric hindrance. This might explain why in the case of R ≧1 randomly oriented MIL-101 islands were found on acid terminated Si surfaces. While, the observed preferred orientation of MIL-101 crystals on monodentate pyridine and hydroxyl ended Si surfaces can nicely be understood in the following way. As shown in **Figure 3.25(a)**, two different types of atoms and/or molecules coordinating the three ferric ions of one trimeric Fe^{3+} octahedral cluster is anticipated. Weakly bound water molecules and/or solvent (DMF in our case) connected to two of the three coordinating positions of one trimeric Fe^{3+} octahedral cluster are easy to be removed to make them become potential or active coordinating sites like the one bound by –OH and/or Cl^- [20-22]. Coincidently, the position marked with 4* (oxygen atom at present) is slantly pointing down. As such, this Fe^{3+} site of the trimer can of course be coordinated by N and O atoms of pyridyl and hydroxyl functional groups of the respective monolayer and oxidized Si. Thereafter, it enables the orientation of MIL-101 crystals along [111] direction for the functionalized Si surfaces bearing with pyridine and hydroxyl functional groups.

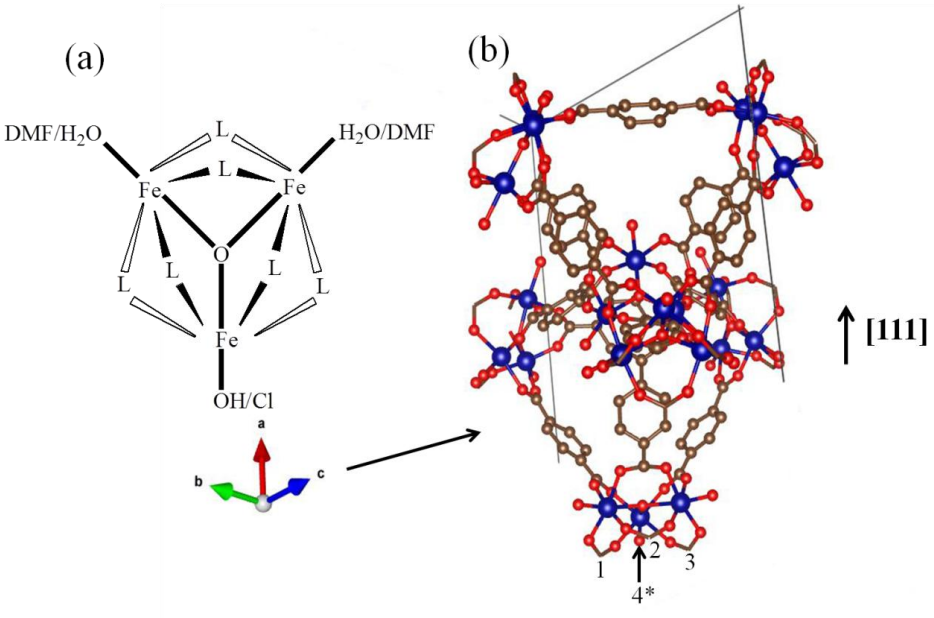

Figure 3.25: (a) Trimer of metal-oxygen octahedra with extended species; (b) Schematic representation of two supertetrahedras along with [111] direction. Note that in (b) 1, 2 and 3 positions are only for the linkers and positon 4* can be connected by the species shown in (a) for the metal ions.

3.5 Conclusion

Within this chapter we have investigated the growth of Fe/BDC MOFs onto Silicon surfaces with different surface chemistries. Our results show the existence of at least two different structural phases: MIL-88B and MIL-101, identified based on crystalline habits observed on the SEM images and/or structural characterization by XRD. Selective formation and orientation of MOFs were evidenced on various surface chemistries: the growth of MIL-88B phase with (001) texture was observed only onto surfaces functionalized with carboxylic acid monolayer (Si-COOH) whereas the formation of MIL-101 phase was observed disregarding the surface chemistry. Apart from this two identified phases, the growth of crystallites exhibiting flat hexagonal shape as well as the formation of the isolated compact layers/islands were also observed, whose crystalline structures are mostly likely MIL-101 phase as well. To the contrary, no film growth happened on methyl terminated Si surfaces. The availability of bidentate coordinating sites and arrangement of linkers inside the framework probably explain the observed selective nucleation and preferential growth of MIL-88B crystals on carboxylic acid terminated Si surfaces. The identical orientation phenomenon (along [111] direction) of MIL-101 crystals on varied termini of substrates (-COOH, pyridine and -OH) can be interpreted in terms of different coordinating sites of the trimeric Fe^{3+} octahedral cluster that all could bind the MIL-101 frameworks. Post-treatment results show that the anchoring of MIL-88B crystallites onto the Si-COOH surfaces is not as strong as that of other types of crystallites observed on substrates irrespective of surface chemistry.

3.6 References

[1] F. Schreiber, Structure and growth of self-assembling monolayers, Prog. Surf. Sci., 65 (2000) 151-257.

[2] R. Maoz, J. Sagiv, On the formation and structure of self-assembling monolayers. I. A comparative atr-wettability study of Langmuir-Blodgett and adsorbed films on flat substrates and glass microbeads, J. Colloid Interface Sci., 100 (1984) 465-496.

[3] J. C. Love, L. A. Estroff, J. K. Kriebel, R. G. Nuzzo, G. M. Whitesides, Self-Assembled Monolayers of Thiolates on Metals as a Form of Nanotechnology, Chem. Rev., 105 (2005) 1103-1170.

[4] C. -H. Lai, C. -Y. Chiang, P. -C. Lin, K. -Y. Yang, C. C. Hua, T. -C. Lee, Surface-Engineered Growth of $AgIn_5S_8$ Crystals, ACS Appl. Mater. Interfaces., 5 (2013) 3530-3540.

[5] J. W. P. Hsu, W. M. Clift, L. N. Brewer, Zinc Oxide Growth Morphology on Self-Assembled Monolayer Modified Silver Surfaces, Langmuir, 24 (2008) 5375-5381.

[6] D. Wang, J. Liu, Q. Huo, Z. Nie, W. Lu, R. E. Williford, Y. -B. Jiang, Surface-Mediated Growth of Transparent, Oriented, and Well-Defined Nanocrystalline Anatase Titania Films, J. Am. Chem. Soc., 128 (2006) 13670-13671.

[7] E. Biemmi, C. Scherb, T. Bein, Oriented Growth of the Metal Organic Framework $Cu_3(BTC)_2(H_2O)_3 \cdot xH_2O$ Tunable with Functionalized Self-Assembled Monolayers, J. Am. Chem. Soc., 129 (2007) 8054-8055.

[8] O. Shekhah, Layer-by-Layer Method for the Synthesis and Growth of Surface Mounted Metal-Organic Frameworks (SURMOFs), Materials, 3 (2010) 1302-1315.

[9] D. Zacher, A. Baunemann, S. Hermes, R. A. Fischer, Deposition of microcrystalline $[Cu_3(btc)_2]$ and $[Zn_2(bdc)_2(dabco)]$ at alumina and silica surfaces modified with patterned self assembled organic monolayers: evidence of surface selective and oriented growth, J. Mater. Chem., 17 (2007) 2785-2792.

[10] C. Scherb, A. Schödel, T. Bein, Directing the Structure of Metal–Organic Frameworks by Oriented Surface Growth on an Organic Monolayer, Angew. Chem. Int. Ed., 47 (2008) 5777-5779.

[11] A. Schoedel, C. Scherb, T. Bein, Oriented Nanoscale Films of Metal–Organic Frameworks By Room-Temperature Gel-Layer Synthesis, Angew. Chem. Int. Ed., 49 (2010) 7225-7228.

[12] O. I. Lebedev, F. Millange, C. Serre, G. Van Tendeloo, G. Férey, First Direct Imaging of Giant Pores of the Metal−Organic Framework MIL-101, Chem. Mater., 17 (2005) 6525-6527.

[13] C. Serre, C. Mellot-Draznieks, Surblé, S., N. Audebrand, Y. Filinchuk, G. Férey, Role of Solvent-Host Interactions That Lead to Very Large Swelling of Hybrid Frameworks, Science, 315 (2007) 1828-1831.

[14] T. R. Whitfield, X. Wang, L. Liu, A. J. Jacobson, Metal-organic frameworks based on iron oxide octahedral chains connected by benzenedicarboxylate dianions, Solid. State. Sci., 7 (2005) 1096-1103.

[15] P. Zhao, N. Cao, J. Su, W. Luo, G. Cheng, NiIr Nanoparticles Immobilized on the Pores of MIL-101 as Highly Efficient Catalyst toward Hydrogen Generation from Hydrous Hydrazine, ACS. Sustain. Chem. Eng., 3 (2015) 1086-1093.

[16] S. Surblé, C. Serre, C. Mellot-Draznieks, F. Millange, G. Férey, A new isoreticular class of metal-organic-frameworks with the MIL-88 topology, Chem. Commun., (2006) 284-286.

[17] F. Millange, C. Serre, G. Férey, Synthesis, structure determination and properties of MIL-53as and MIL-53ht: the first Cr^{3+} hybrid inorganic-organic microporous solids: CrIII(OH)·{O_2C-C_6H_4-CO_2}·{HO_2C-C_6H_4-CO_2H}$_x$, Chem. Commun., (2002) 822-823.

[18] F. Millange, C. Serre, N. Guillou, G. Férey, R. I. Walton, Structural Effects of Solvents on the Breathing of Metal–Organic Frameworks: An In Situ Diffraction Study, Angew. Chem. Int. Ed., 47 (2008) 4100-4105.

[19] E. Stavitski, M. Goesten, J. Juan-Alcañiz, A. Martinez-Joaristi, P. Serra-Crespo, A.V. Petukhov, J. Gascon, F. Kapteijn, Kinetic Control of Metal–Organic Framework Crystallization Investigated by Time-Resolved In Situ X-Ray Scattering, Angew. Chem. Int. Ed., 50 (2011) 9624-9628.

[20] G. Férey, C. Mellot-Draznieks, C. Serre, F. Millange, J. Dutour, S. Surblé, I. Margiolaki, A Chromium Terephthalate-Based Solid with Unusually Large Pore Volumes and Surface Area, Science, 309 (2005) 2040.

[21] L. Qin, Z. Li, Z. Xu, X. Guo, G. Zhang, Organic-acid-directed assembly of iron–carbon oxides nanoparticles on coordinatively unsaturated metal sites of MIL-101 for green photochemical oxidation, Appl. Catal., B., 179 (2015) 500-508.

[22] Y. Zhang, J. Wan, Y. Wang, Y. Ma, Synthesis of phosphotungstic acid-supported versatile metal-organic framework PTA@MIL-101(Fe)-NH_2-Cl, RSC Adv., 5 (2015) 97589-97597.

Chapter 4: Direct growth of Fe^{3+}/BDC MOF onto carboxylic acid terminated Si surfaces: influence of synthesis conditions

4.1 Introduction

Synthesis of metal-organic frameworks (MOFs) has attracted intense attention in the past two decades because of the large synthetic flexibility to obtain a huge variety of interesting porous structures with tailored physico-chemical properties (electrical, optical, magnetic or mechanical…) through combination of large variety of metals and ligands. Results have already demonstrated that many parameters, such as the solution composition (medium, precursors concentration and/or relative ratio, additives (pH modulator, structure-directing agents, mineralizers) and even the counter anion of the metallic salt) and process parameters (temperature, crystallization time and pressure) have profound influences on the crystallinity, morphology, crystal size, and even phase composition and thereby their physical and chemical properties of desired MOFs [1-9]. Regarding the solvothermal formation of Fe^{3+}/BDC and/or their analogues like Fe^{3+}/NH_2-BDC MOFs, S. Bauer and his co-workers investigated systemically the parameter space towards the formation of those MOFs thanks to the use of high-throughput method [6]. Their studies show that the nature of reaction medium exhibits the most profound impact on phase formation. The overall concentration of the reaction mixture, temperature and acidity/alkalinity are also found decisive factors for resulted product. For instance, both for amino-terephthalic and terephthalic acid, more basic reaction conditions lead to only the synthesis of MIL-88B phase in DMF at low temperature. Whereas, the addition of HF results in exclusively the formation of MIL-53 phase and incorporation of HCl in the solution enhances the synthesis of a mixture of MIL-53 and MIL-88B phases. In view of above-mentioned factors, they are likely to be vital as well involving the fabrication of MOF films on solid supports.

In the previous chapter, it has been shown that specific behavior was observed on

carboxylic acid terminated surfaces (Si-COOH). High coverage of the hexagonal MIL-88B phase was observed solely on these surfaces and the nucleation and growth of this phase were found to be strongly dependent on the ligand to metal ratio R in solution. In order to better understand the factors governing the nucleation and growth of the Fe^{3+}/BDC phases on these surfaces, we have undertaken additional studies. We varied the synthesis conditions, exploring in particular the influence of parameters that are known to play a role with respect to the nucleation/growth rate, the selectivity of synthesized phases, the size and/or the shape of the obtained crystallites, in the case of the growth of Fe^{3+}/BDC-based MOF compounds in homogeneous phase. The synthesis parameters we have investigated are: the growth temperature and time, the solution composition (precursor concentration, ligand to metal ratio and additives). The last part of this chapter will be devoted to the discussion of influence of solution composition on the formation of MOFs and also the growth mechanism of the obtained surface-grown MOFs.

4.2 Results

4.2.1 Growth at different temperature

The influence of temperature on the nucleation and growth of Fe/BDC MOF has been investigated for different Fe^{3+} concentrations and different ligand to metal ratios (R) in solutions. No sizeable growth has been observed at room temperature (RT) over time scale from one to few days. Examples of the morphology of the films obtained after 24 h growth at three different temperatures (70 ℃, 90 ℃ and 110 ℃), are shown in the **Figure 4.1**. All the samples were prepared with the same Fe^{3+} concentration in solution (C_{Fe} = 25 mM).

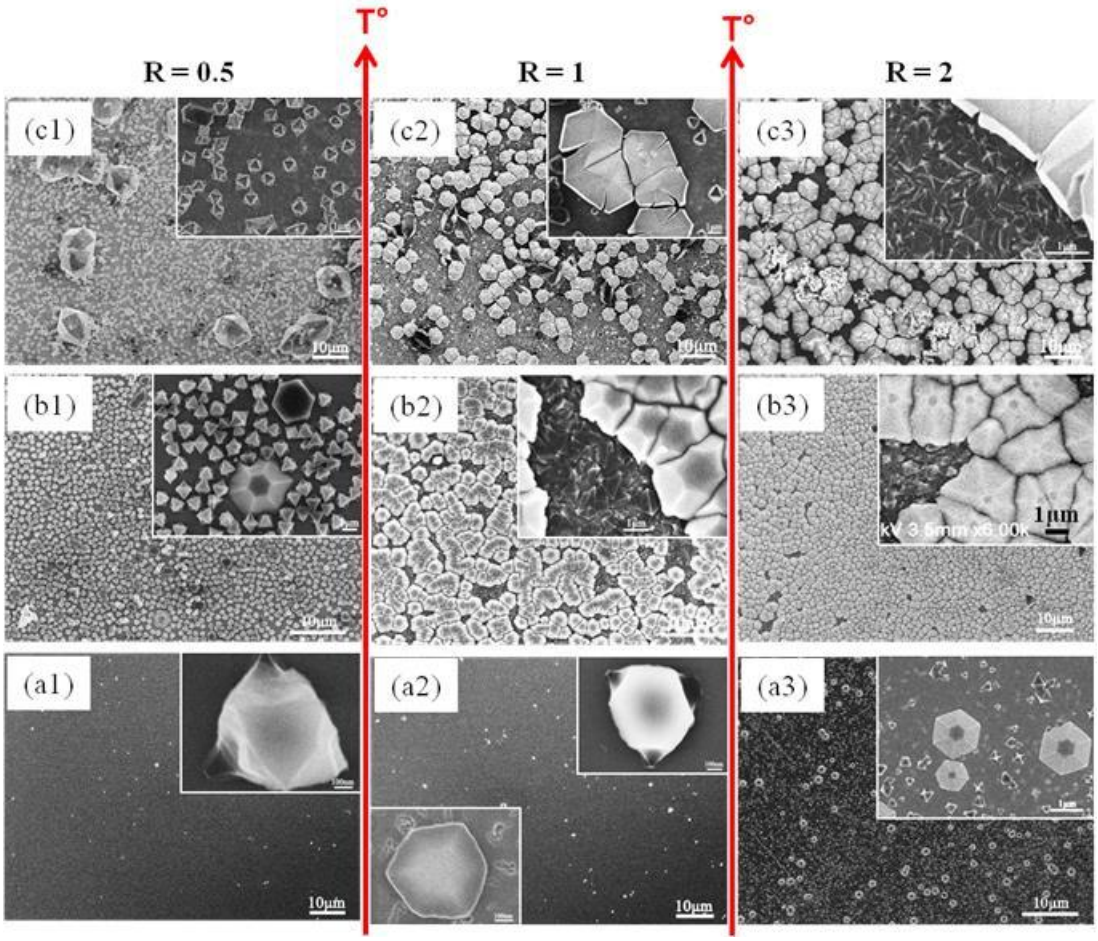

Figure 4.1 Film morphology (SEM images) as a function of the growth temperature (bottom to top) and the relative concentration of precursors (R) in solutions (left to right). From bottom to top: (a) T = 70 °C, (b) T = 90 °C and (c) T = 110 °C. From left to right R = 0.5, R = 1 and R = 2. For all samples, C_{Fe} = 25 mM and the growth time is 24 h.

Figure 4.1 reveals the existence of a temperature threshold T* for the onset of nucleation and growth of Fe^{3+}/BDC MOFs and T* depends on R: a certain density of crystallites are already observed at 70 °C in presence of ligand excess in solution (R = 2) whereas for lower ligand concentration (R ≤ 1) the onset of significant nucleation and growth is observed at higher temperature ~ 80 °C. Other results (not shown) indicate that T* also depends on the Fe^{3+} concentration. Indeed for a same growth temperature, higher coverage has been observed for higher concentrations, thus indicating a lowering of the threshold temperature T*.

As already detailed in the previous chapter, variable relative coverage of the different crystalline phases is observed depending on the relative concentration of ligand in solution. The presence of a majority of octahedral MIL-101 crystallites (A-type) are

observed in case of Fe^{3+} excess in solution (R = 0.5) whereas the MIL-88B hexagonal crystallites become the dominant phase when the ligand concentration is raised. This trend is observed whatever the temperature.

The density and sizes of the different crystallites observed in the different synthesis conditions are given in **Figure 4.2**. As quantitatively suggested by the SEM images, the crystallite density (octahedral MIL-101 and hexagonal MIL-88B) increases with the temperature with a maximum for T= 90 °C. For T > 90 °C, the density is found to decrease. This might be related to simultaneous high nucleation and growth rate in solution that consume the precursors and slow down the heterogeneous nucleation and growth on the surface.

Characterizations of the powders formed simultaneously in the homogeneous phase, during the growth of the supported MOF, indicate a dominant nucleation and grown of octahedral MIL-101 nano-crystallites (size) in any R conditions and to much less extent the nucleation and growth of bipyramidal hexagonal MIL-88B crystallites of much larger size (several µm).

XRD characterizations of the samples displayed in **Figure 4.1** have been done. Diffraction patterns with characteristic Bragg peaks were only obtained for samples showing the growth of oriented hexagonal MIL-88B crystallites. As presented in the previous chapter, despite the observation of – in some cases – large density of octahedral MIL-101 crystallites (A-type), no clear XRD signature that might be assigned to this phase was evidenced. This is the case for all samples prepared in solution with metal excess and at low T °C in the case R = 1 for which the images show only very rare crystallites. In others conditions, very similar XRD patterns were obtained showing essentially couples of peaks in the 9 – 10 ° and 18 – 20 ° (2θ) angular ranges, similarly to what was presented in **Chapter 3**.

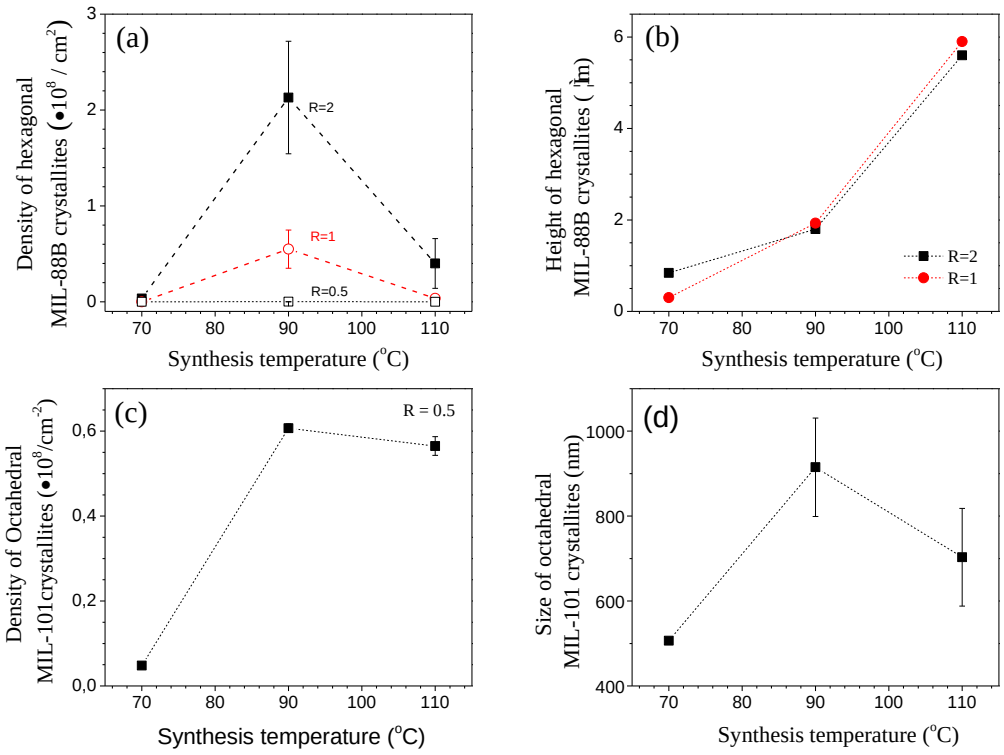

Figure 4.2 Evolution of the density (a,c) and height (b) of hexagonal MIL-88B and lateral size (d) of octahedral MIL-101 crystallites as a function of the synthesis temperature.

The evolution of the XRD patterns as a function of the synthesis temperature is shown in **Figure 4.3**, for the samples prepared in solution conditions (R = 2) in which the growth of oriented MIL-88B hexagonal crystallites (C-type) is dominating. Only two narrow angular ranges where peaks are found are displayed for better clarity. The intensity is plotted in log scale to better show the details of the peaks. On the side of the patterns, high magnification SEM images recall the morphology/structure of the as-grown MOF. Globally, an evolution is observed from a simple pattern exhibiting only a couple of peaks at low T° towards much more complex patterns showing in both angular ranges the existence of several peaks overlapping. Remarkably, all the peaks turn out coupled with interplanar spacing scaling by a factor 2. This strongly suggests that they correspond to diffractions on same hkl family of crystallographic planes, thus indicating a preferential orientation growth. This feature has been already highlighted in the previous chapter.

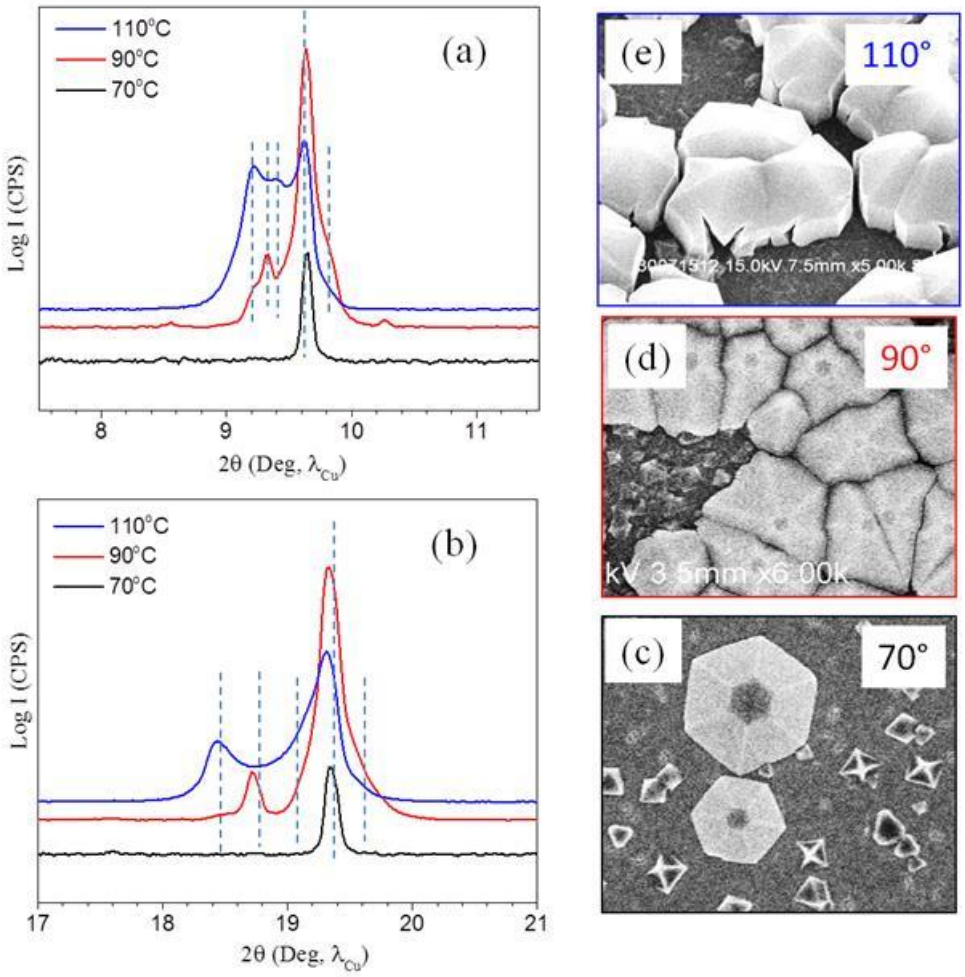

Figure 4.3 Narrow range XRD patterns (a-b) and SEM images (c-e) of Fe^{3+}/BDC MOFs grown onto carboxylic acid terminated Si surfaces at various temperatures. For all samples, C_{Fe} = 25 mM , C_{BDC} = 50 mM (R = 2) and the growth time is 24 h.

At low temperature (70 ℃), only two coupled peaks at 2θ = 9.64 °and 2θ = 19.34 °are observed. These peaks are assigned to (002) and (004) Bragg reflections of the MIL-88B hexagonal crystallites observed on the SEM images and the shift of their positions with respect to that expected for dry MIL-88B phase indicate partial solvation (as already discussed in **Chapter 3**). When the synthesis temperature is raised, the appearance of new couples of peaks is observed. Two additional peaks at 2θ = 9.2 °and 2θ = 18.46 °are observed overlapping with broader ones (shoulders). These two peaks are rather sharp indicating a high degree of crystallinity. Noticeably, the appearance of additional peaks on the XRD patterns is correlated to the observation of the formation of a compact layer in between the hexagonal MIL-88B

crystals, whose structural properties are difficult to identify only looking at its morphology. At this stage, it is not straightforward to clear-cut the assignment of the peaks appearing at high T °because of the structural flexibility of the MIL-88B phase. The appearance of new peaks might have several origins. They might indicate the growth of another structural phase, the growth of MIL-88B with different texture or variations of the solvation degree of MIL-88B crystallites with 001 texture (MIL-88B with less solvent content). The peak positions at the different temperatures are summarized in **Table 4.1**.

Table 4.1 Summary of the peak positions observed on the XRD patterns displayed in **Figure 4.3**.

	Peak position (2θ, deg)								
70 °C				9.64					19.34
90 °C	8.55	9.2	9.33	9.64	10.29	18.46	18.72	19.1	19.34
110 °C		9.2	9.4	9.64		18.46	18.72	19.1	19.34

The sample preparation turned out less reproducible at T °above 100 °C. At high T °, a large amount of material was found to form simultaneously in homogeneous phase, thus making less reliable the conditions for heterogeneous nucleation and growth on the surface (fast consumption of the precursors, deposit/insertion of crystallites formed in solution). An example of deposit of bipyramidal MIL-88B crystallites grown in solution can be seen on **Figure 4.1(c1)**. These crystallites are clearly identified as coming from the solution because of their random orientation and their bi-pyramidal shape and their size similar to those obtained from the solution.

In the following, all the samples were prepared at 90 ℃, at which significant nucleation and growth were observed and for which the synthesis conditions turned out much more reliable.

4.2.2 Influence of solution composition (T = 90 ℃)

Within this section, surface-grown MOFs were prepared in solutions with various compositions in term of precursor concentration and relative ratios in order to investigate the influence of these parameters on the nucleation and the growth of the Fe^{3+}/BDC phases. The effect of additives, i.e. HCl, triethylamine (TEA) and H_2O into the solution was also investigated. All the samples were prepared at 90 ℃ for 24 h.

4.2.2.1 Influence of ratio and precursor concentration

Influence of ligand to metal ratio

In the previous chapter we already showed that the relative concentration of H_2BDC ligand plays an important role with respect to the nucleation and growth of MIL-88B phase. **Figure 4.4** recalls the different structural phase and/or morphologies of the Fe/BDC MOF grown on the Si-COOH surfaces for different ligand to metal ratio R in solution. The structural phases formed on the surfaces are compared with those obtained simultaneously in homogeneous phase. Surprisingly, the nucleation and growth of MIL-88B phase is observed above a certain ligand concentration ($R \geqslant 1$) on the surfaces whereas MIL-101 phase is the dominant phase formed in solution disregarding the relative concentration of ligand. The evolution of the density and height of supported MIL-88B crystallites as a function of the relative concentration of ligand R are displayed on **Figure 4.5**. Whereas a quasi-full coverage is observed when $R \geqslant 1$ (~ 80%), the density of crystallites increases with R indicating enhancement of the nucleation rate when the ligand concentration increases. In parallel, the mean size of the crystallites decreases due to a faster coalescence. Conspicuously, the thickness of the MIL-88B layer decreases, indicating a diminution of the growth rate with increasing ligand concentration. Similar trend is observed in solution where the major structural phase is the MIL-101 phase. The mean size of the octahedral MIL-101 crystallites formed in homogeneous phase also decrease when the ligand concentration increases, indicating also a decrease of the growth rate.

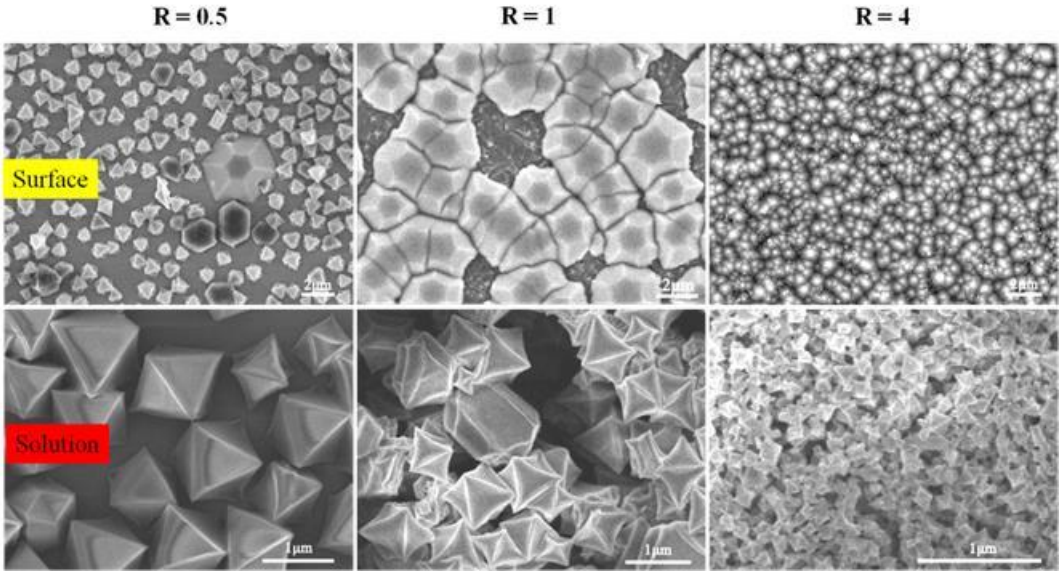

Figure 4.4 Morphology of Fe/BDC MOFs grown on Si-COOH surfaces and of powder formed simultaneously in solution for various ligand to metal ratio in solution R. Synthesis conditions: C_{Fe} = 25 mM, T = 90 ℃ and 24 h growth.

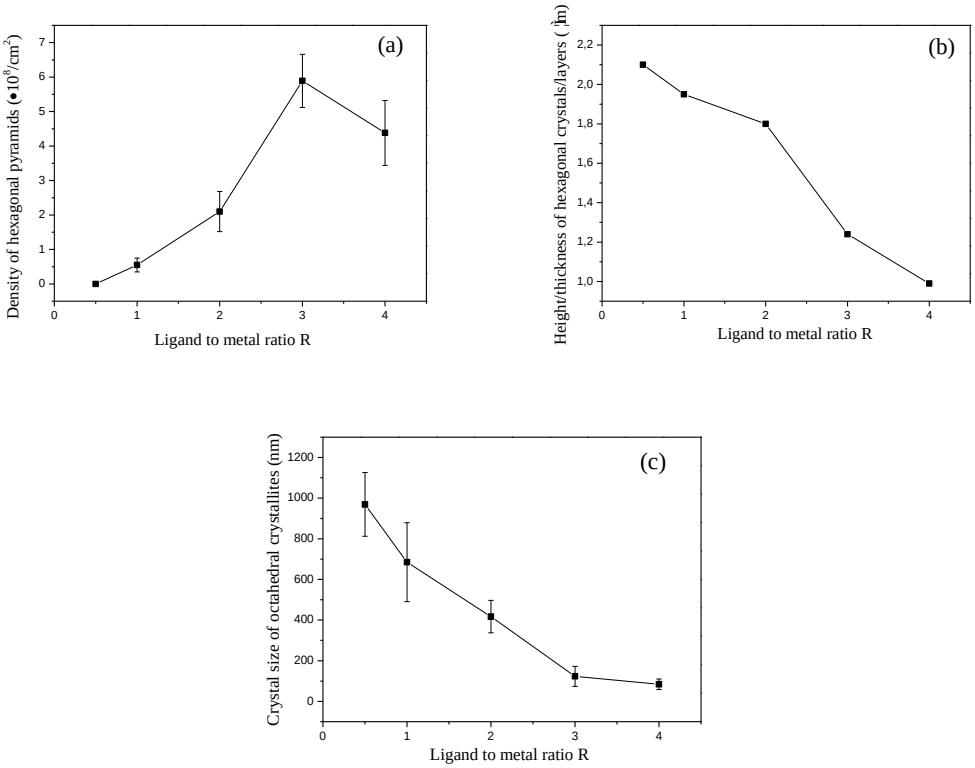

Figure 4.5 Evolution of the density (a) and height (b) of hexagonal MIL-88B crystallites as a function of the relative ligand concentration in solution. (c) Evolution of the mean size of MIL-101 crystallites formed simultaneously in solution. Synthesis conditions: C_{Fe} = 25 mM, T = 90 ℃ and 24 h growth.

Influence of precursor concentration

The evolution of the relative fraction of the different crystallites/structural phases – octahedral MIL-101 (A-type), flat hexagonal (B-type) and hexagonal MIL-88B crystallites - as a function the solution composition (C_{Fe} and R = [L] / [Fe^{3+}]) - as inferred from SEM image analysis - are displayed on **Figure 4.6**. The SEM images are provided in Supplementary Information **Figure S4.1**.

There is a concentration threshold to promote the formation of the two phases: high density of isolated octahedral MIL-101 crystallites is observed above C_{Fe} ~ 20 mM (R = 0.5) whereas already a large density of MIL-88B crystallites is observed for lower Fe concentration (C_{Fe} ~ 10 mM, R = 2). The density of MIL-101 crystallites increases with the concentration. Conversely, a maximum density of MIL-88B crystallites is observed for C_{Fe} = 25 mM, the density falling down for higher Fe concentration.

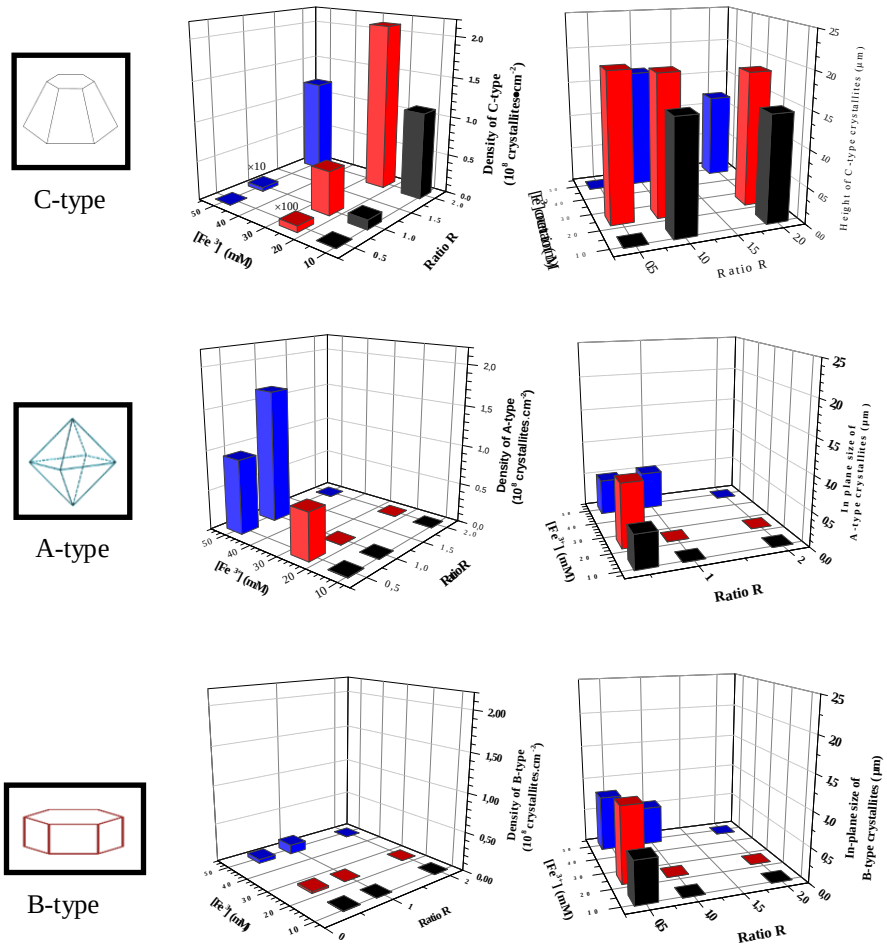

Figure 4.6 Density and size of the A, B and C-type crystallites as a function of the solution composition (C_{Fe} and R). Note that the same Y-axis scale is set for all density or size plots.

We tentatively estimated the mass of MIL-88B phase grown on the surface. The volume of matter was calculated by considering the coverage and the height of MIL-88B crystallites as inferred from SEM image analysis, and the volumic density of MIL-88B phase (1.5 g/cm^3) [7]. The result is plotted in **Figure 4.7**.

XRD patterns of samples prepared in solution with various (C_{Fe} and R) are displayed in **Figure 4.8**. Overall they mainly show the presence of two characteristic coupled peaks at 2θ = 9.64 ^{o} and 19.34 ^{o} that can be assigned to MIL-88B phase with (001) texture and only in very few cases XRD signatures indicating the growth of MIL-101 (C_{Fe} = 50 mM, R = 0.5, and R = 1) with preferential orientation along [111] direction.

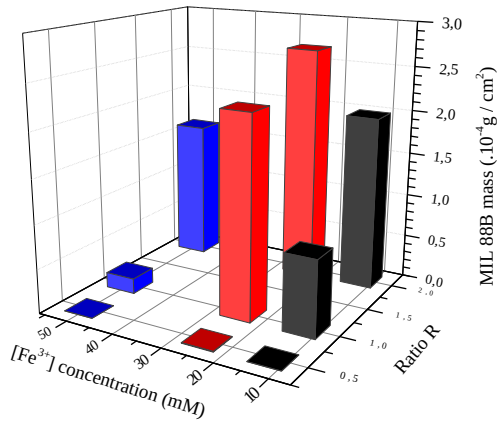

Figure 4.7 Mass of MIL-88B phase obtained after 24 h growth at 90 °C as a function of the solution composition ([Fe^{3+}] concentration and ratio R). The mass was calculated from the coverage and thickness of the MIL-88B crystallites as inferred from SEM images and a volumic density of 1.5 g/cm^3 for MIL-88B phase.

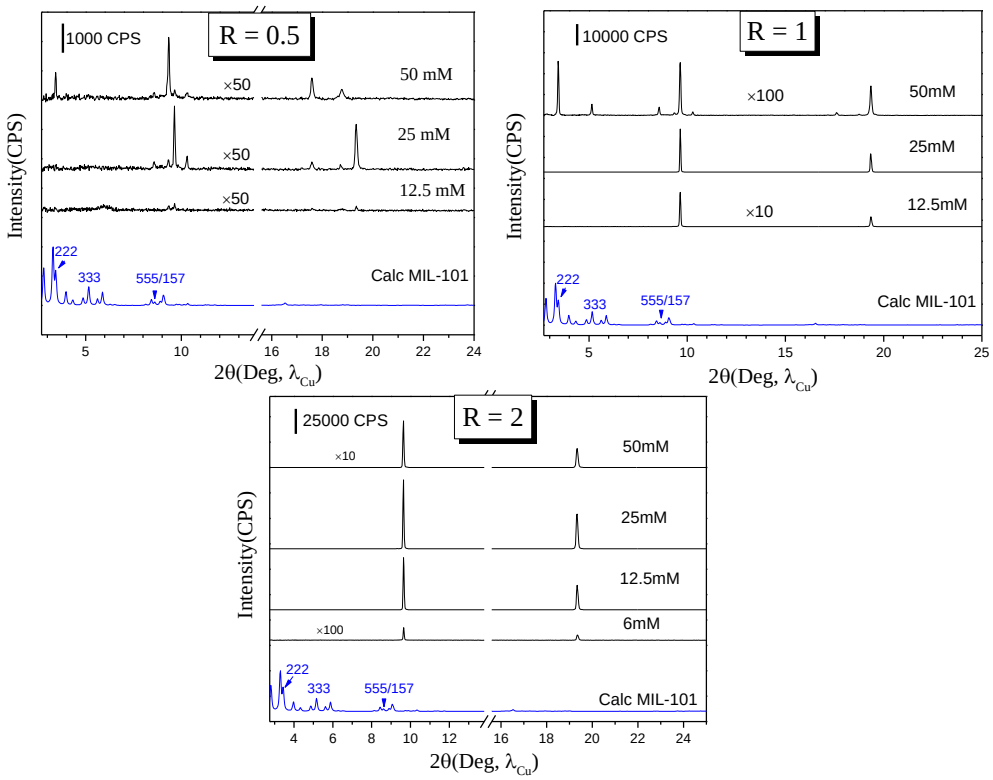

Figure 4.8 XRD patterns of MOF layers on surfaces prepared from solution with different composition (C_{Fe} and R). The Fe concentration C_{Fe} is indicated nearby each plot. The different sets of data correspond to different relative ratio of precursor in solution R. All samples were prepared at 90 °C for 24 h. The calculated PXRD pattern of MIL-101 phase is plotted in blue at bottom for comparison [10]. SEM images of sample prepared in conditions C_{Fe} = 6 mM and R = 2 are given in **Figure S4.2**. Details of XRD patterns for R = 1 and R = 2 are presented in **Figure S4.3.**

To summarize this section, depending on the ratio R = [L] / [Fe^{3+}], a transition from the formation of octahedral and/or flat hexagonal crystals to that of hexagonal pyramids is observed at R value close to 1: dominating formation of octahedral and/or flat hexagonal (or truncated octahedral) crystals is observed when R < 1 whereas formation of hexagonal crystals is greatly favored at R > 1. At equal amount of ligand and metal precursors, the starting precursor concentration appears critical as well to the formation of different types of crystals. A higher [Fe^{3+}] concentration sees the majority of octahedral and/or flat hexagonal crystallites, while, a progressive formation of hexagonal crystals is observed when C[Fe^{3+}] ≤ 25 mM.

4.2.2.2 Influence of additives

In order to further understand what happened during film preparation, we investigated the effect of adding acid or base in the solution. The idea was modifying the degree of ligand deprotonation, which is known to have strong influence on the homogeneous nucleation and growth of MOFs in solution [11,12]. For this purpose HCl or triethylamine (TEA) were added into the synthesis solution. Two different types of synthesis conditions were studied: the growth in presence of metal excess (R = 0.5) for which the main phase obtained is the MIL-101 phase and the growth in presence of ligand excess (R = 2) for which the major phase obtained is the MIL-88B phase. All samples were prepared for 24 h at T = 90 °C in solution with identical Fe^{3+} concentration C_{Fe} = 25 mM. **Table 4.2** summarizes the synthesis conditions of samples hereafter discussed.

Addition of HCl

Figure 4.9 compares the morphology of Fe/BDC films obtained without (a, b) and with (a1,a2,b1,b2) addition of 1 M HCl in solution with metal excess (a) or with ligand excess (b). For the two synthesis conditions (R = 0.5 and R = 2) very different morphologies are obtained in presence of HCl.

Table 4.2 Solution composition without and/or with additives for sample preparation

	Ratio	Concentration (mM)			
	R	C_{Fe}	C_{H2O}	C_{HCl}	C_{TEA}
1	0.5	25	0	0	0
2	0.5	25	555	10	0
3	2	25	0	0	0
4	2	25	555	10	0
5	0.5	25	0	0	10

When R = 0.5, where the formation of isolated octahedral MIL-101 crystallites (~ 750 nm thick) prevails in the neat precursor solution (**Figure 4.9(a)**), addition of HCl induces the formation a thick film (~ 2.3 μm thick) made of islands separated by cracks (**Figure 4.9(a1)**). Images at higher magnification show the formation of crystalline material exhibiting at majority octahedral structures, strongly suggesting the growth of MIL-101 phase (**Figure 4.9(a2)**). The formation of polycrystalline MIL-101 is confirmed because XRD patterns are matching well the calculated PXRD pattern of MIL-101 phase (**Figure 4.10(a)**). At R = 2, in presence of HCl, a dense film is also obtained while densely packed hexagonal MIL-88B crystallites were got without HCl. Only a few isolated oriented MIL-88B hexagonal pyramids (~ 3.1 μm high) are observed (**Figure 4.9(b1)**). They are embedded in a compact crystalline layer with a thickness of ~ 380 nm whose structure is difficult to identify, even though triangular and/or octahedral structure may be distinguished. In this case, XRD patterns (**Figure 4.10(b)**) show mainly two couples of peaks at 2θ = 9.17 °and 18.39 ° and 2θ ~ 9.53 °and 19.24 °whose position is different from the position usually find for MIL-88B oriented crystallites i.e. 2θ = 9.64 ° and 19.34 °. Again, as already outlined in **Section 4.2.1** (**Figure 4.3**), the observation of peaks slightly shifted to

lower angles with respect to the peaks assigned to 002 and 004 Bragg peaks of MIL-88B phase might be correlated to the observation of the thinner layer. Even if the SEM images show structural geometry atop of the layer that would sustain the growth of cubic MIL-101 phase, the formation of MIL-53 phase or MIL-88B phase with different texture cannot be totally discarded.

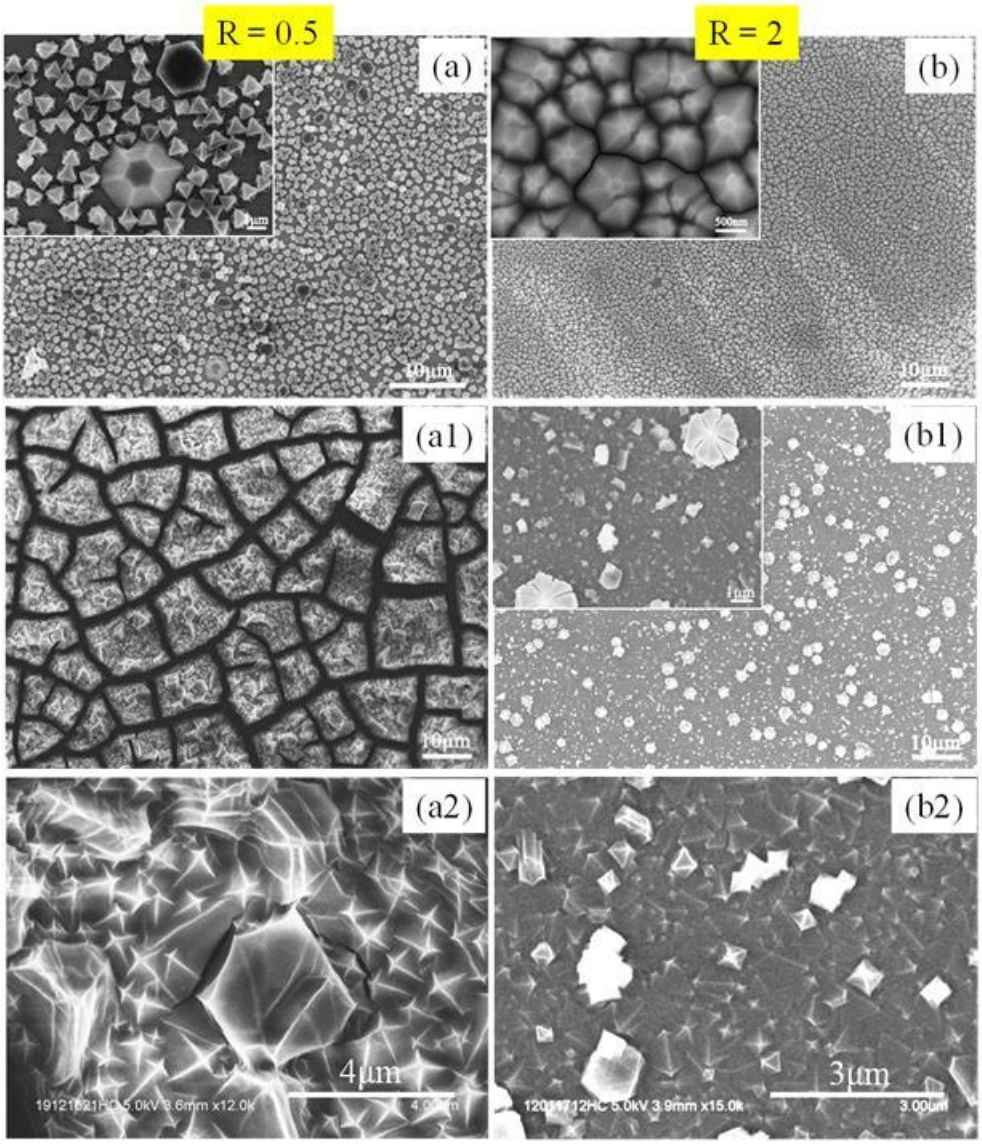

Figure 4.9 Comparison of film morphology obtained without (a,b) and with addition of 1M HCl (a1,a2,b1,b2) into the precursor solutions. The two column refers to samples prepared in solutions with metal excess R = 0.5 (left) or with ligand excess R = 2 (right) for which MIL-101 (a) or MIL-88B (b) phases are obtained at majority. The final HCl and H_2O concentrations in the solution were C_{HCl} = 10 mM and C_{H2O} = 555 mM. For all samples, C_{Fe} = 25 mM, T = 90 ^{o}C and the growth time is 24 h.

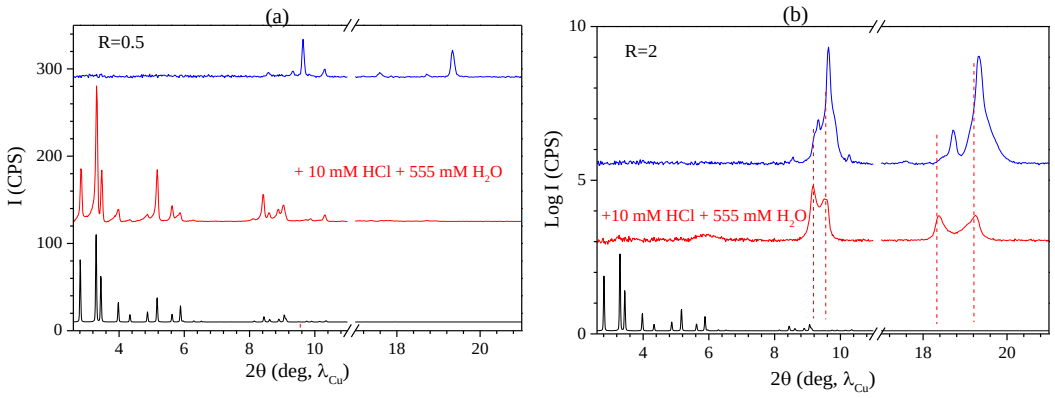

Figure 4.10 Comparison of XRD patterns of films on carboxylic terminated Si surfaces prepared in solutions without (blue plot) or with (red plot) addition of 1 M HCl solution. Samples were prepared either in solution with metal excess R = 0.5 (a) or with ligand excess R = 2 (b). For all the surfaces, C_{Fe} = 25 mM, T = 90 ^{o}C and the growth time is 24 h. SEM images of the films are shown in the **Figure 4.9**. Calculated XRD pattern of MIL-101 is plotted below for comparison (black plot).

Addition of triethylamine (TEA)

Figure 4.11 displays SEM images of Fe/BDC MOF prepared in solution with excess metal (R = 0.5) in which neat TEA was added. The morphology of sample prepared in solution without TEA addition is shown on **Figure 4.9(a)**.

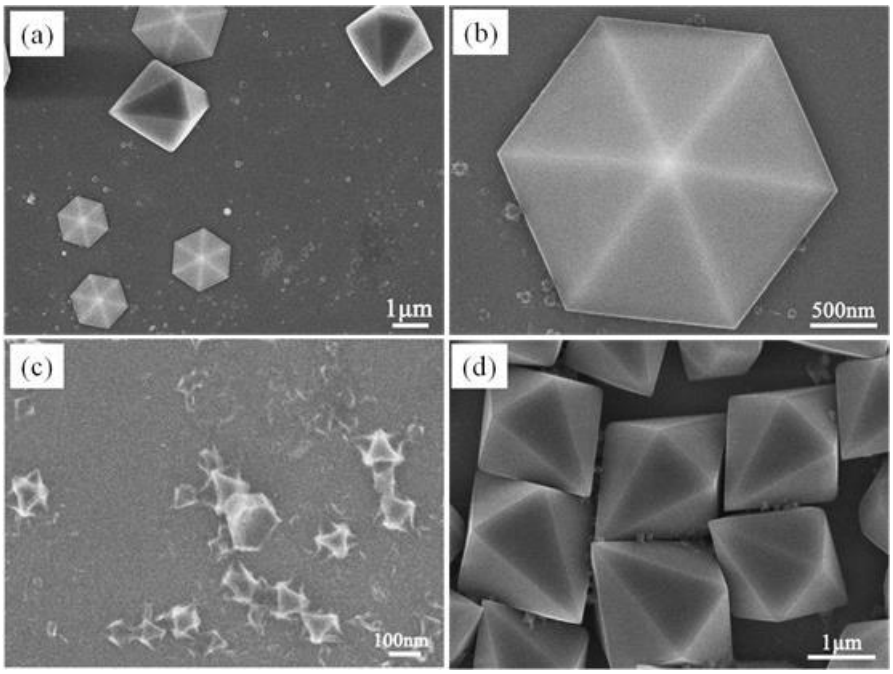

Figure 4.11: SEM images (a-d) of supported Fe/BDC MOF on surface prepared in solution with addition of 10 mM neat TEA in the precursor solution. Synthesis conditions: C_{Fe} = 25 mM, R = 0.5, T = 90 ^{o}C and the growth time is 24 h.

Addition of TEA was also found to tremendously modify the nucleation and growth but in a different way. Both on the surface and in solution the major phase obtained is the MIL-88B phase. We recall that in the standard conditions (without TEA) MIL-101 is the phase obtained at majority (**Figure. 4.4**) both on surface and in solution. On the surface the SEM images evidence the oriented growth of MIL-88B crystallites (**Figure 4.11(a,b)**) and the presence of randomly oriented MIL-88B crystallites (**Figure 4.11(a,d)**). Their bipyramidal shape suggests they were formed in homogeneous phase and deposited on the surface. Indeed, their size is comparable to that of crystallites collected in the solution. In addition, much smaller crystallites exhibiting octahedral or irregular hexagonal geometry are also observed that look like – on some area - in between the MIL-88B crystallites (**Figure 4.11(c)**). This issue is however difficult to clarify only on the basis of SEM images.

The XRD patterns show mainly the presence of the two sets of coupled peaks usually found in presence of MIL-88B crystallites. These peaks stand at $2\theta = 9.64\ ^\circ$ and $19.34\ ^\circ$ for the most intense and $2\theta = 9.33\ ^\circ$ and $18.72\ ^\circ$ for the less intense (**Figure 4.12**). Because only these peaks are observed we infer that there are the signatures of the *oriented* MIL-88B crystallites (002 and 004 Bragg reflections) as inferred previously. It is however surprising that no other peaks assigned to the randomly oriented bipyramids are observed. This might mean that no crystallographic planes would be in suited configuration (parallel to the surface) to get diffraction in the Bragg Brentano configuration used for the measurements. In addition to these intense peaks very tiny peaks are found at $2\theta \sim 16\ ^\circ$, $17\ ^\circ$ and $17.6\ ^\circ$ (insert of **Figure 4.12**).

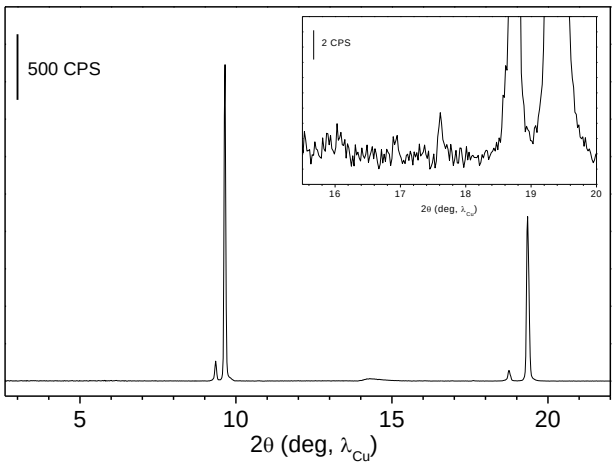

Figure 4.12 XRD patterns of Fe/BDC sample prepared in solutions with addition of 10 mM pure TEA. Synthesis conditions: C_{Fe} = 25 mM, T = 90 ^{o}C and the growth time is 24 h.

To sum up the effect of HCl or TEA addition:

- Addition of 1M HCl promotes/speeds up the nucleation and growth of MIL-101 phase and lead to the grow of a compact and thick polycrystalline MIL-101 layers in presence of metal excess in solution and also to a compact and continuous thinner layer but whose structural properties are not identified, in case of ligand excess in solution.
- Addition of neat TEA favors the nucleation and growth of MIL-88B phase.

4.2.3 Time evolution of the film morphology and structure

Within this section the time evolution of the morphology and/or structure of supported MOFs were investigated for three different synthesis conditions leading to the quasi selective growth of a dominant phase and/or morphology. The three synthesis conditions that will be presented are:

- Growth in solution with excess metal (R = 0.5) leading mainly to the formation of isolated MIL-101 crystallites with (111) texture
- Growth in solution with excess metal (R = 0.5) in presence of HCl leading to the growth of a compact and thick polycrystalline layer

- Growth in solution with ligand excess leading to the progressive growth of dense layer of closed-packed MIL-88B crystallites with (001) texture.

All samples were prepared at 90 ℃ and C_{Fe} = 25 mM for various exposure times from 2 h up to 24 h.

4.2.3.1 Growth in solution with metal excess (R = 0.5)

Figure 4.13 presents SEM images of surface-grown Fe/BDC MOFs after various exposure times in solution without (left) and with (right) 1 M HCl solution added in the precursor solutions. The images show an earlier nucleation onset in presence of HCl, after only 2 h growth the images show already high coverage of octahedral isolated crystallites or islands. The formation of a compact layer with cracks is observed since 4 h growth. By comparison 24 h growth is required to observed significant coverage (56 %) in case of no HCl addition. In conditions where low coverage is observed, characterizations at higher resolution by AFM show the staircase structure of the Si surface confirming the absence of an eventual continuous thin layer in between the isolated crystallites. Regarding the generation of cracks shown in **Figure 4.13(b3**,**b4)**, obvious cracks are already visible to optical light microscopy before exposure to vacuum of SEM characterizations, indicating that the formation of cracks can be attributed to synthesis process and/or the drying procedure after rinsing. While, during SEM characterizations, we do observe the apparent propagation of cracks due to the ultra high vacuum that induces the fast relaxation of molecules or solvents hosted in the pores of frameworks.

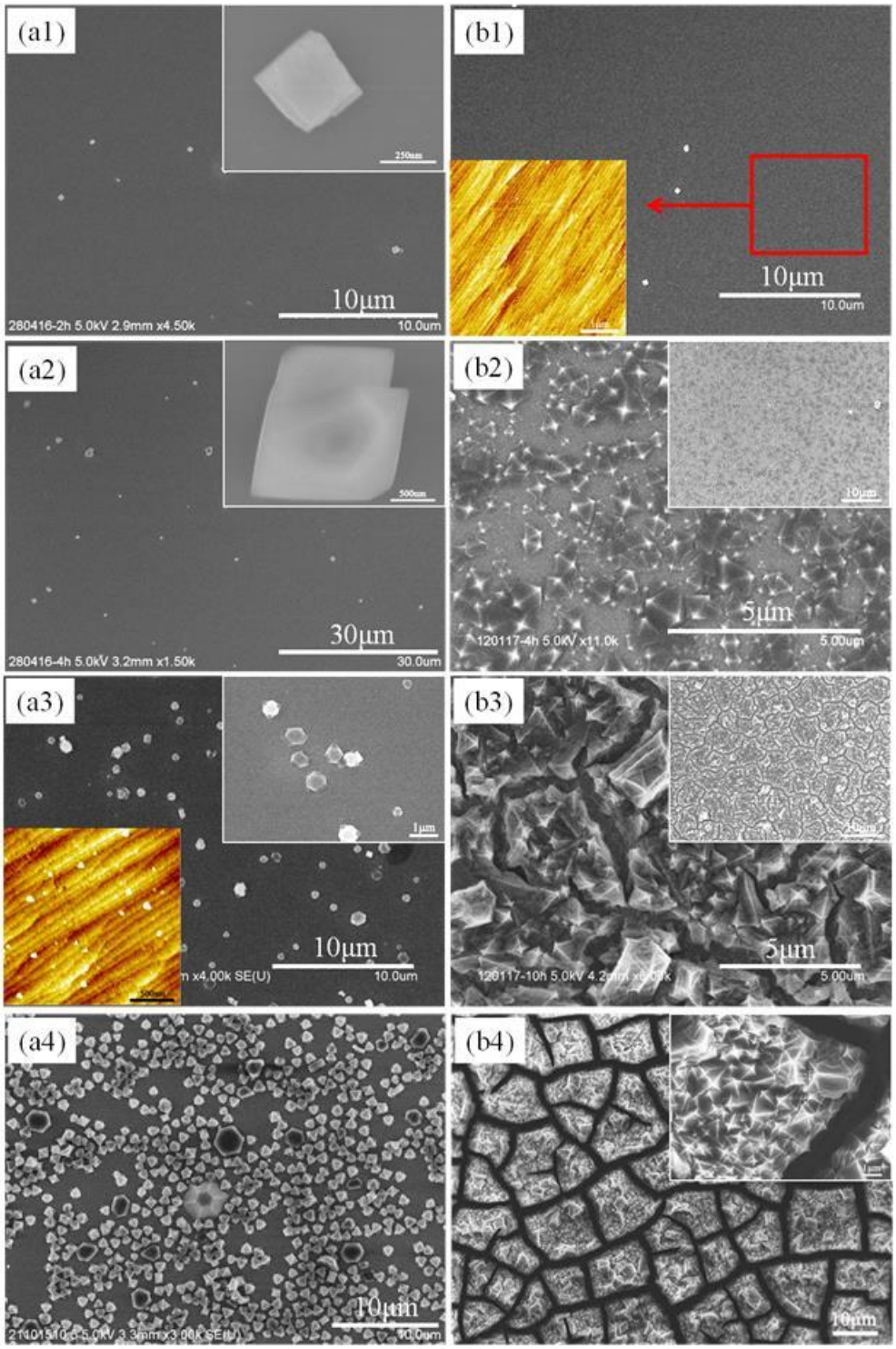

Figure 4.13 Time evolution of the morphology of films grown in solutions under R = 0.5 without (a) and with addition of 1M HCl solution (b). The synthesis conditions were: C_{Fe} = 25 mM, C_{BDC} = 12.5 mM, T= 90 ^{o}C, and the growth time is 2 h (1); 4 h (2); 10 h (3) and 24 h (4). The final HCl concentration is 10 mM.

XRD characterizations of the samples don't provide any structural signature for short time growths. XRD patterns in the two synthesis conditions after 24 h growth are shown in **Figure 4.10**.

Time evolution of the height and/or thickness of crystals and/or layers as inferred from cross-section SEM images are presented in **Figure 4.14**. In both cases the height/thickness more or less increases linearly with time indicating a constant growth rate which is ~ twice faster when HCl is added in solution.

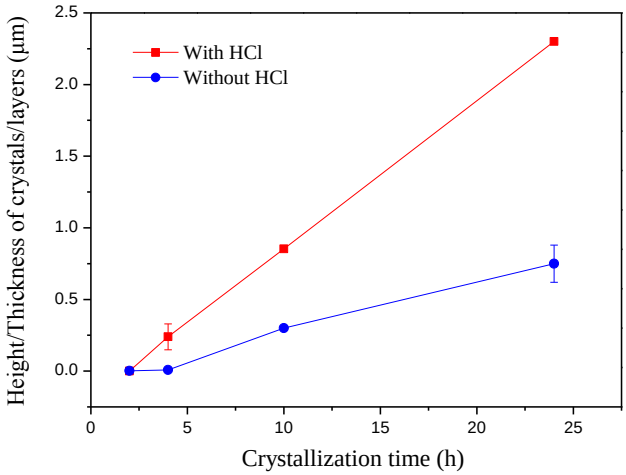

Figure 4.14 Time evolution of the height/thickness of isolated crystallites/layers grown in solutions without (blue plot) and with addition (red plot) of HCl solution.

4.2.3.2 Growth in solution with ligand excess (R = 2)

Figure 4.15 presents SEM images of Fe/BDC MOFs grown in solutions with ligand excess (R = 2) at 90 ℃ for various growth times (2 h, 4 h, 10 h and 24 h). Cross-section SEM images of samples prepared for shorter growth times are presented in Appendix 4 (**Figure S4.4)**.

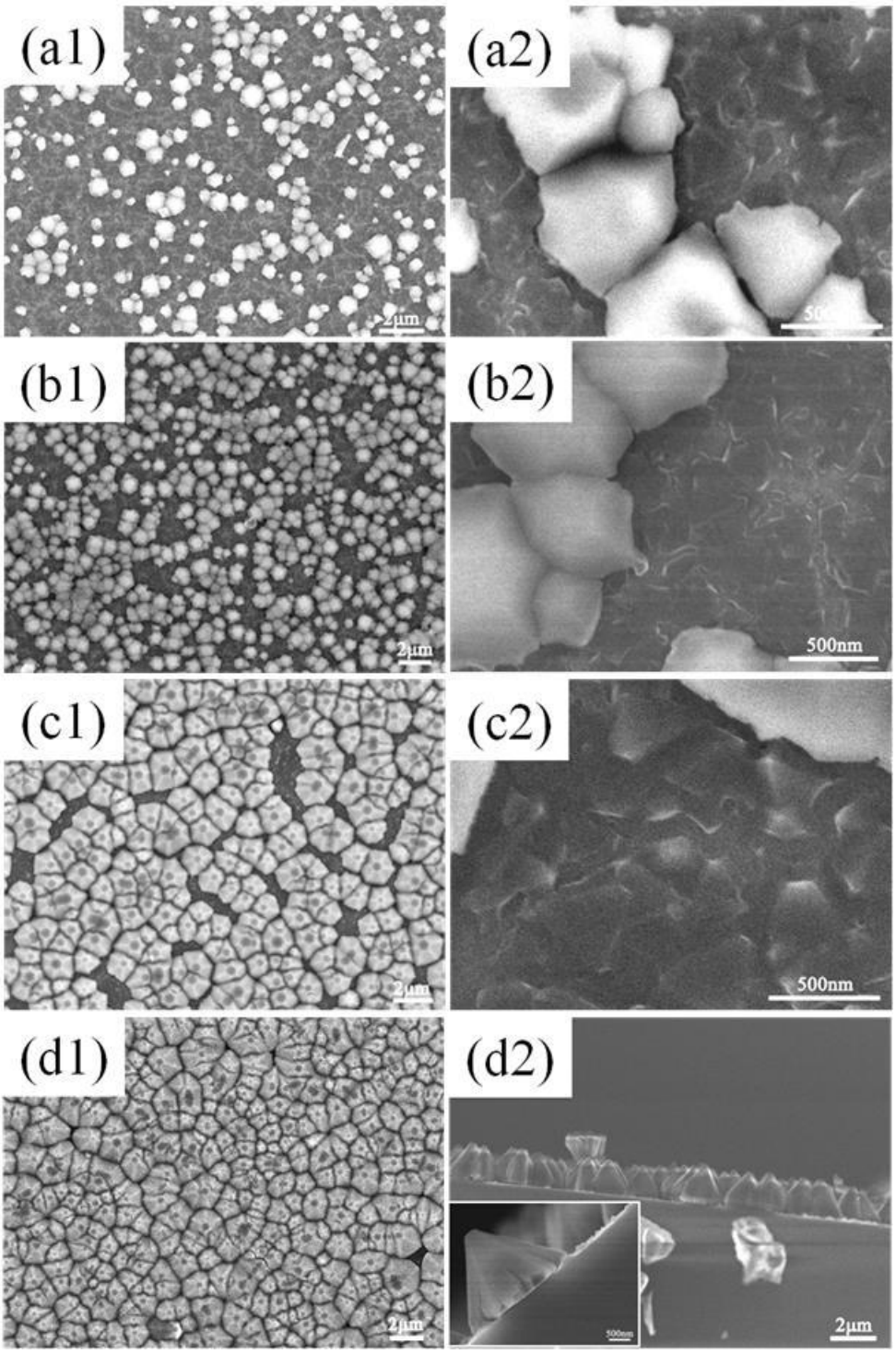

Figure 4.15 Large field (left column) and high magnification (right column) SEM images of MOFs grown in solution with ligand excess (R = 2). The synthesis conditions were: C_{Fe} = 25 mM, C_{BDC} = 50 mM, T= 90 ^{o}C, and the growth time was 2 h (a); 4 h (b); 10 h (c) and 24 h (d), respectively.

After 2 h crystallization the image shows a distribution of isolated crystallites with hexagonal symmetry. After longer exposures the coverage of hexagonal crystals

increases and the surface becomes more or less entirely covered after 10 h. Since the early stages, the images also show the existence of layers surrounding the already grown MIL-88B crystallites, indicating the co-nucleation and growth of different phases. The cross-section images shown in **Figure 4.15(d2)** indicate clearly that the pyramidal crystals are perpendicular to the Si substrate, implying they have preferential orientation. Evolution of the density of hexagonal pyramid crystallites, their height and the thickness of the layer between the hexagonal crystals as a function of exposure time are presented in **Figure 4.16**. Density of hexagonal crystallites slightly increases along with the crystallization time. The height of pyramids rises dramatically until the exposure time of 10 h, and then slowly increases with a longer exposure time in the solution. Contractively, the thickness of the layers between the hexagonal crystals more or less keeps a linear increase but at quite a slow growth rate (~ 2 nm/h).

The corresponding XRD patterns are depicted in **Figure 4.17**. The patterns for short growth times show the existence of two massif of three overlapping sharp peaks within the angular range 2θ = 9 - 10 °and 2θ = 18 - 20 °. The intensity of the couple of peak at 2θ = 9.64 ° and 19.34 ° increases of several order of magnitude with increasing time (notice that Y-axis is plotted in log scale to show more details of the peaks) whereas those of the 2 peaks at lower angles (2θ = 9.2 °and 18.46 °; 2θ = 9.33 ° and 18.72 °) increase slightly **(Figure 4.17 (A))**. The variations of the integrated intensity of the peak around 2θ = 9.64 °inferred from the XRD patterns and the normalized mass of MIL-88B crystallites are plotted as a function of crystallization time (**Figure 4.17(B)**). Mass of the hexagonal crystals was calculated through multiplying the volume density by the equivalent matter volume as-determined from the SEM images. The more or less similar tendency confirms the assignment of the couple of peaks at 2θ = 9.64 °and 19.34 °to the oriented MIL-88B crystallites. No XRD signature below 6 °where most of the intense peaks of cubic MIL-101 phase are expected is observed.

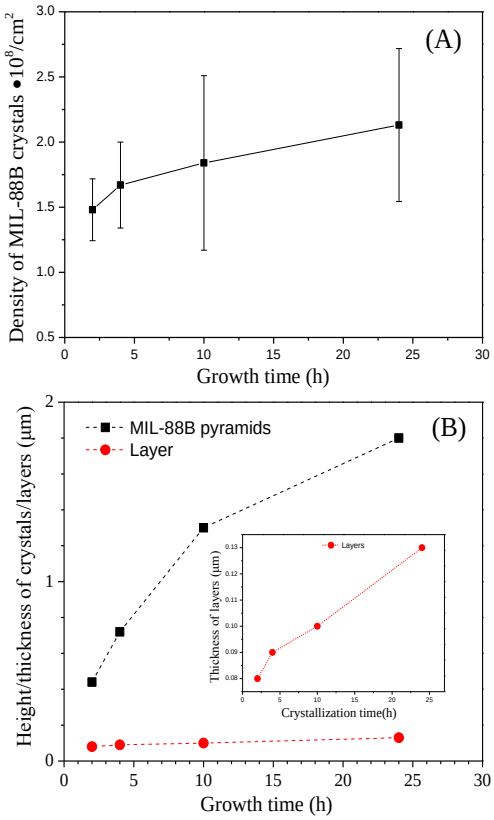

Figure 4.16 Time evolution of the density (A) and thicknesses (B) of the MIL-88B crystallites (black squares), and the layer in between the hexagonal MIL-88B crystallites (red dots).

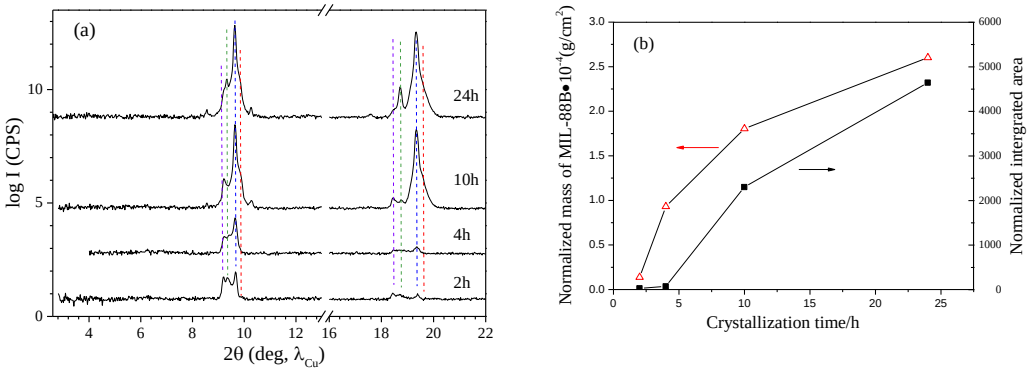

Figure 4.17: (a) Time evolution of XRD patterns of Fe/BDC MOFs grown in solution with ligand excess (R = 2). (b) Normalized mass of hexagonal crystals (red triangles) and normalized integrated intensity of Bragg peaks nearby the peak 2θ = 9.64 °from XRD patterns as a function of crystallization time. The calculated density of MIL-88B phase is 1.5 g/cm^3 [7]. The synthesis conditions were: C_{Fe} = 25 mM, C_{BDC} = 50 mM, T= 90 ^oC, and the growth time was indicated near to the plot in (a). The peak position is summarized in the **Table 4.3**.

Table 4.3 Experimental peak positions from XRD patterns in **Figure 4.17(a).**

Experimental peak position 2θ (deg, λ_{Cu})			
2h	4h	10h	24h
		8.55	8.55
9.2	9.2	9.2	9.2
9.33	9.33	9.33	9.33
9.45	9.42	9.45	
9.64	9.64	9.64	9.64
		10.29	10.29
			17.6
18.45	18.47	18.45	18.46
18.70	18.78	18.75	18.72
		19.1	19.1
19.34	19.34	19.34	19.34

4.3 Discussion

4.3.1 Structural identification

Regarding the hexagonally pyramidal crystals, XRD patterns always show two coupled peaks nearby 2θ = 9.64 ^{o} and 19.34 ^{o}. As we demonstrated in **Chapter 3** it can be assigned to MIL-88B phase with preferential orientation along [001] direction ,

but in a solvated form, in which solvents/molecules are captured in the pores of MIL-88B framework that induced the structural expansion and thus the shifting of XRD peaks. Shoulder or overlapped peaks close to these two coupled peaks are often observed as well, usually accompanied by the formation of compact and/or isolated layers composed of quasi-octahedral and/or unidentified crystals. The intensity of those shoulder peaks increases along with synthesis temperature, precursor concentration and crystallization time as we depicted in **Figure 4.3**, **Figure S4.3** and **Figure 4.17**. Three different hypotheses could be made addressing this issue. At first glance, this could be attributed to the appearance of the layers. The other explanation might be due to the uneven release of solvents/molecules trapped inside the framework of some MIL-88B crystals that drives the peak back to the "empty" position (near 9.24 ^{o}). But some crystals remain in the solvated form so that broad or shoulder peaks are found. Another possibility might be because of the deposition of powder (probably MIL-88B even though in low quantity) that formed in solution and precipitated onto the surface giving the XRD signature of solvated forms (with (100) or (101) planes detected) or dry form (with 001 plane detected). Actually, we do find some cases that the XRD patterns provides some additional peaks close to the two characteristic ranges once the deposited MIL-88B crystals occurred on the surface. But in most cases especially for samples prepared at 90 ^{o}C the SEM results see the absence of deposited huge MIL-88B crystals, but still the shoulder or broad peaks are observed. For the first hypothesis that it might be assigned to the layer, results after post-synthesis treatment as shown in **Chapter 3** (**Figure 3.17**) clearly manifest that the peaks shifted to a lower angle and experienced a huge decrease of peak intensity with the removal of pillared hexagonal crystals, suggesting that there is a strong correlation between them. In addition, the time evolution of film growth depicted in **Figure 4.16(B)** and **4.17(a)** apparently see an increase of peak intensity along with growth time whereas the thicknesses of the underneath layers increases at a extremely slow rate (~ 2 nm/h), ruling out the first hypothesis as well. So here we conclude the appearance of shoulder or overlapped peaks is due to the uneven release of solvents trapped inside the pores of MIL-88B framework. As with to the fragmented layers,

composed of octahedral and/or quasi-octahedral crystals between the large hexagonally pyramidal crystals that we usually observed when R ≥ 1, they can probably be assigned to MIL-101 with random orientation in spite of the absence of clear-cut signature.

For the isolated octahedral or truncated octahedral crystallites with clear flat-top facets, additional results (**Figure 4.8**) strongly suggest that both of them are mostly likely MIL-101 phase exhibiting preferred orientation along [111] plane, even though for the truncated octahedral crystals with non well-defined octahedral shape.

For the thick films prepared with addition of 10 mM HCl, it is apparent that they are MIL-101 films without any preferential orientation.

Once the phase identification is resolved, another point needs to be discussed here is what state of MIL-88B and MIL-101 crystals exists once two phases are observed at the same time. There are 6 ideal possibilities considering if an ultrathin layer that might be MIL-88B or MIL-101 exists. Schematic representation of these six possible combinations is given in **Figure 4.18**.

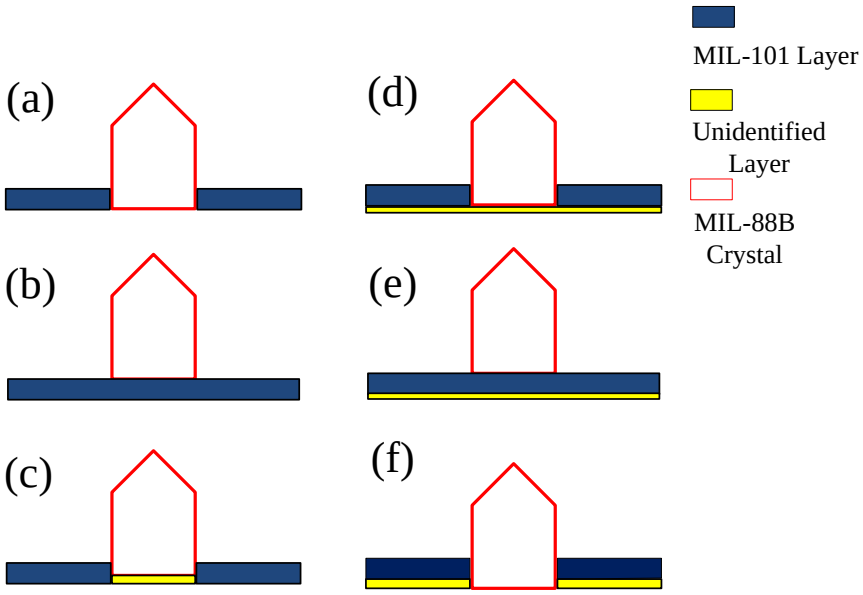

Figure 4.18 Schematic view of 6 potential combinations when two phases are observed grown on carboxylic terminated Si surfaces. Note that the unidentified layer if any might be MIL-101 or MIL-88B.

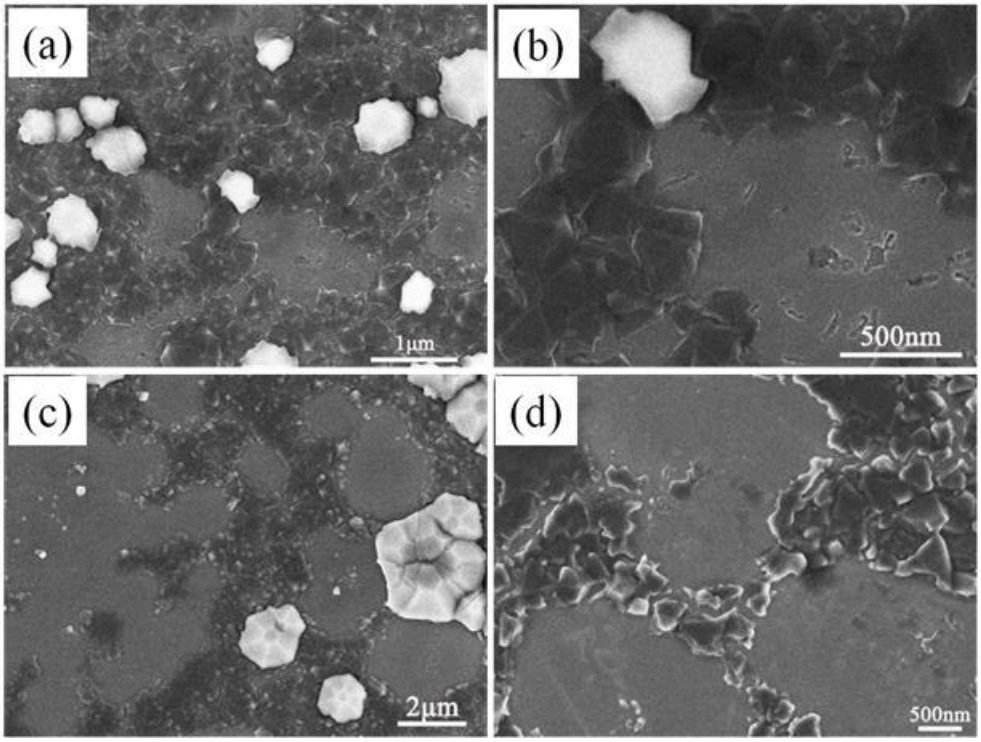

Figure 4.19 SEM images of films after scotching tests. The synthesis conditions were: C_{Fe} = 25 mM, C_{BDC} = 50 mM, T= 90 ^{o}C, and the growth time was 2 h (**a**,**b**) and 10 h (**c**,**d**).

Morphology of the films after peeling test as depicted in **Figure 4.19** indicates clearly that hexagonally-shaped pyramids are removed by adhesive tape, left with footprints surrounded by isolated islands composed of quasi-octahedral crystallites. No trace of octahedral MIL-101 crystals is found on top of the footprint. Combing with results of rinsing in soxhlet as shown in **Figure 3.17** (**Chapter 3**) done to the film that is comprised of two phases demonstrate clearly as well the footprint of hexagonal MIL-88B crystallites, we can exclude (**b**) and (**e**) in **Figure 4.18**. The observation of cross-section SEM images as displayed in **Figure 4.15(d2) and Figure S4.4** that MIL-101 layer or islands is directly connected to the substrate rules out the cases of (**d-f**). Indeed, at first glance, appearance of some holes on the track of MIL-88B crystals shown in **Figure 4.19(b)** makes us think that there might be a layer below the hexagonal crystals. Nevertheless, the interface between the MIL-88B crystal and Si substrate as given in **Figure 4.15(d2)** strongly suggests that there is nothing in

between. Therefore, the case of (**a**) is only considered in the film growth process when two phases are found ($R \geqq 1$). This probably explains why MIL-88B crystals are grown on carboxylic terminated Si surfaces along [001] direction. Since terephthalic acid molecules are configurated along [001] in the framework of MIL-88B, substitution of carboxylates of terephthalic acid through carboxylates of the monolayer grafted on Si substrate renders the growth of hexagonal crystal merely in [001] direction as schematically depicted in **Figure 3.24** (**Chapter 3**).

4.3.2 Effect of solution composition

Results shown in **Section 4.2.2** suggest clearly that excess of metal precursor and/or the addition of aqueous HCl solution substantially favor the formation of oriented and/or polycrystalline MIL-101 films, whereas excess of ligand and/or the introduction of weak base-TEA in a way facilitates the nucleation and growth of oriented hexagonal MIL-88B crystallites on functionalized Si surfaces bearing carboxylic ended groups. It has been known that deprotonation of neutral ligands is a prerequisite for crystallization to construct MOF frameworks. To realize that, as discussed by M. Li [11], base equivalents are usually needed to be introduced quite slowly either by vapor diffusion, as shown in the original synthesis of MOF-5 [12], or by in situ formation of dialkylamines from the decomposition of dialkylformamides with and even without heating [13,14]. Actually, the hydrolysis of DMF is a well established reaction in organic chemistry, which can happen both in acidic and basic environments [15-18]. For example, in the presence of hydroxide ions, decomposition of DMF can be accelerated even at room temperature with the liberation of dimethylamine and formate ions. The generation of dialkylamines will in return accelerate not only the deprotonation of linkers (BDC in our case) in solution but also the deprotonation of carboxylic terminated groups of the monolayer due to the lone pare electrons of N atom. Thereby, this makes the crystallization happen both in solution and at the interface between the substrate and solution. The possible reactions concerned above are summarized as follows:[11,16]

$$(CH_3)_2N\text{-}CHO + H_2O \longrightarrow HCOOH + (CH_3)_2NH \quad (4\text{-}1)$$

$$HOOC\text{-}Ar\text{-}COOH + 2(CH_3)_2NH \rightleftharpoons {}^{-}OOC\text{-}Ar\text{-}COO^{-} + 2[(CH_3)_2NH_2]^{+} \quad (4\text{-}2)$$

$${}^{-}OOC\text{-}Ar\text{-}COO^{-} + M^{3+} \rightleftharpoons MOF \quad (4\text{-}3)$$

In reactions, Ar stands for benzene ring. Meanwhile, the formic acid formed might further decompose into carbon monoxide and H_2O [19].

In the solutions containing only $FeCl_3$ $6H_2O$ and H_2BDC, the present of water makes the reaction of **Eq.4.1** realistic and explains that MOF may be synthesized. Increasing the amount of ligand while keeping other variables constant, will probably drive the reversible reaction of **Eq.4.2** to the right, inducing the formation of more MOF nuclei (both MIL-101 and MIL-88B) and then growth of MOF crystals but a dominating growth of MIL-88B was found. Low concentration of ligand likely limits this reaction, contributing to a low density of crystals as we observed in the case of excess of metal precursor. Additionally, with regard to temperature, a higher temperature will undoubtedly quicken the above reactions and thus promotes the nucleation and growth of crystals not only onto substrate but also in solution. This is consistent to the fact that we found much more matters on surfaces as well as in solution at higher temperature comparing with that at low temperature (70 ^{o}C).

When additive like aqueous HCl is introduced in, it is believed to catalyze the reaction **Eq.4.1** to the right, increasing the degree of deprotonation of –COOH. Favorable accessibility of deprotonated linkers gives rise to fast nucleation and growth of MOF. Reported as the kinetic phase [20,21], MIL-101 is most likely to emerge and expand on the surface, which will surely prevent the further formation of MIL-88B. Thick (2.3 μm) and polycrystalline film was obtained at last as displayed in **Figure 4.9(a1,a2)**. A thinner polycrystalline film (900 nm) prepared with addition of same amount of HCl (10 mM) but with less H_2O (35 mM H_2O) might be interpreted by **Eq.4.1** during which H_2O will be consumed (See supplementary information

Figure S4.5). Reducing of H_2O will in a sense slow down the reaction rate of **Eq.4.1** and hence make the construction of MOF slower. Nuclear Magnetic Resonance (NMR) measurements toward ^1H spectrum of DMF with addition HCl solution after 24 h treatment at 90 ^oC confirm the existence of DMF and H_2O, but the absence of chemical shift of DMA or DMACl (See **Figure S4.6**) [16,22]. No detectable signal indicates a pretty slow hydrolysis rate of **Eq.4.1** under the absence of H_2BDC. Introduction of organic alkali-triethylamine (10 mM) is primitively expected to promote the deprotonation of linkers. While, triethylamine first coordinates with Fe^{3+} to form reddish-brown colloidal clathrate or complexes ($Fe(TEA)^{3+}$) [23]. The complexation between Fe^{3+} and triethylamine inevitably decreases the available amount of trimers of FeO_6 octahedra and thereafter restricts the construction of MOF frameworks. On the other hand, the redundant may catalyze the reaction of **Eq.4.1** and/or directly react with H_2BDC to achieve the effective deprotonation of H_2BDC. Once the free triethylamine is all reacted, the complexes ($Fe(TEA)^{3+}$) is likely to decompose to supply the nutrition that reaction needs. The above two aspects comprehensively determine the nucleation and growth of MOF, exhibiting isolated oriented MIL-88B crystallites and tiny octahedral MIL-101 crystals in between. Introduction of equivalent amount of TEA to Fe^{3+} concentration into the original solution presents only the growth of low density of nanometer MIL-101 crystallites (See **Figure S4.7**), supporting the above inference. Nevertheless, a thorough and precise knowledge of synthesis pathways for different phases regarding the Fe^{3+}/H_2BDC system is still inaccessible because of the complexity of metal-anion-solvent interactions and high number of competing simultaneous events that occur during MOF formation.

4.3.3 Nucleation and growth

When R = 0.5 without any additive, MIL-101 formation remains very limited below 10 h. After 10 h, increase of coverage and density of μm-size octahedral crystals of the film show 3-dimentional expansion of particles, both in plane and out-of plane.

The vertical crystalline size of MIL-101 crystals from solutions without HCl solution after 4 h nearly maintains a linear increase, but showing a slow increase rate (~ 40 nm/h). Further, one may notice that even after 10 h crystallization tiny particulates (dozen nanometers) as shown in **Figure 4.13(a3)** can still be observed. This implies that either formation of particles is still going on or the growth of 'nuclei' is non-homogenous through the surface. Nevertheless, similar crystalline size is observed for the crystals on surface and the crystallites formed in solution. As we already discussed in the last chapter, the crystals on surface seems formed in solution at the initial stage, deposited onto the surface and grow subsequently.

Time dependence of film growth from solution containing HCl solution under the same ratio R = 0.5 (See **Figure 4.13(b1-b4)**) follows a Volmer-Weber growth mode [24], during which, a much larger density of isolated three-dimensional MIL-101 islands or clusters formed after 2 h crystallization and grew laterally and vertically until coalescence, resulting in rough and polycrystalline layer on the surface. More interesting, the thickness of polycrystalline films shows a linear increase along with time, suggesting a constant growth rate in this direction (~ 100 nm/h), which is much faster than the case without addition of HCl. Further expansion along the horizontal plane will greatly be restrained after crystal coalescence. This will surely introduce additional stress inside the layer, which might explain why we observed huge cracks at 24 h growth.

For the case of R = 2, the substrate experienced a co-nucleation of MIL-88B and MIL-101. Even at 2 h exposure in solution, 26 % of the surface was covered by MIL-88B crystals, while, most of the rest area was occupied by MIL-101 crystallites with a huge density. This will undoubtedly make the further nucleation pretty difficult. A slight variation of MIL-88B density might better illustrate this point. **Figure 4.20** presents the time dependence of crystal dimensions of hexagonal MIL-88B crystallites (a) and corresponding average growth rate (b) of in plane and out-of plane in varied growth periods. Once formed, hexagonal MIL-88B crystals proceed to expand quickly both laterally and vertically, inducing a rapid increase of surface

coverage and crystal dimension. Crystal coalescence is likely reached above 10 h crystallization when lateral growth rate is greatly slowed down, less than the vertical growth speed as depicted in **Figure 4.20(b)**. Crystal growth out-of plane is however continuing, but with a slow rate as confirmed by the slow increase of integrated area of (002) plane shown in **Figure 4.17(b)**. Meanwhile, one unnegligible factor is the existence of MIL-101 assemblies around hexagonal crystals, which will obviously obstruct the lateral expansion of hexagonal crystals. Cross-section SEM images displayed in **Figure 4.15(d2)** and **Figure S4.4(c)** show apparently that partial of some hexagonal crystals is above the underneath MIL-101 islands, providing evidences that MIL-88B crystals could overcome the barrier that MIL-101 assemblies exposed to proceed. With regard to the growth of MIL-101, it suggests a extreme slow growth rate (~ 2 nm/h) not only due to the spacial compression from MIL-88B crystals but also because of the deficient supply of precursors that are largely consumed by surface-mounted MIL-88B as well as bulk materials generated in solution.

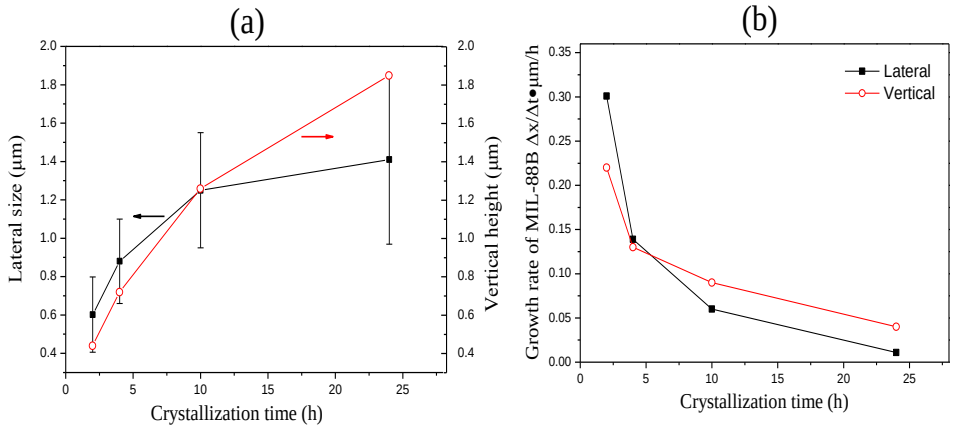

Figure 4.20 Time dependence of crystal dimensions of hexagonal MIL-88B crystallites (a) and corresponding average growth rate (b) in different growth period. Note that the diagonal of hexagon of MIL-88B crystals represents the lateral size. It might have errors depending on the compactness of the film. Growth condition: R = 2, [Fe^{3+}] = 25 mM and at 90 ^{o}C.

4.4 Conclusion

Depending on the synthesis conditions, including temperature, precursor concentration, ratio R of [L] to [Fe^{3+}], additives and reaction time, formation of two crystalline phases with variable symmetries and crystal density were observed. Temperature plays a key role in the onset formation of two different phases- MIL-101 and MIL-88B and their relative ratio through the existence of a temperature threshold T*. The results show different film morphologies going from isolated crystallites near the T* (~ 90 ℃ for R < 1 and 70 ^{o}C for R ≥ 1) to dense and more or less continuous films made of close-packed or interconnected crystallites above. T* depends not only on the ratio R but also the starting precursor concentration. Variation of ratio R makes Si surfaces experience a transition from the formation of mainly octahedral MIL-101 to that of hexagonal MIL-88B at R value close to 1: dominating formation of MIL-101 in [111] direction is found when R < 1 whereas growth of MIL-88B in [001] direction is greatly favored at R > 1. At R = 1, the starting precursor concentration is also critical to the formation of MIL-88B hexagonal crystallites. Addition of HCl (10 mM) plays an important role in the formation of compact and polycrystalline MIL-101 films. The above results might be understood in terms of the extent of DMF decomposition (or hydrolysis) that leads to the in-situ formation of dimethylamine, which determines the deprotonation of carboxylic groups and therefore affect the further coordination with the trimeric Fe^{3+}-oxygen octahedral clusters. Addition of TEA probably involves both the complexation of Fe^{3+} by TEA and also the effective boosting of ligand deprotonation, which interplay determining the final morphologies and structures of film.

Time dependence of film growth at excess of metal (R = 0.5) without additive demonstrate that oriented and isolated MIL-101 crystals are firstly nucleated in solution, deposited on surface and expanded vertically and laterally until 56 % of the surface was covered. Film growth under the same R value (R = 0.5) but with addition of HCl solution follows a Volmer-Weber growth mode, during which, large density of

isolated three-dimensional MIL-101 islands or clusters with random orientation formed after 2 h crystallization and grew much more fast both in-plane and out-of plane, resulting in dense and thick polycrystalline layers.

Whereas, at excess of ligand (R = 2), the surface sees a co-nucleation of MIL-88B and MIL-101, and then MIL-88B nuclei grow rapidly both laterally and vertically over time until coalescence (around 10 h). Crystal growth out-of plane is however continuing, but with a slow rate. In the meantime, the growth of MIL-101 is greatly restricted.

4.5 References

[1] N. Stock, S. Biswas, Synthesis of Metal-Organic Frameworks (MOFs): Routes to Various MOF Topologies, Morphologies, and Composites, Chem. Rev., 112 (2012) 933-969.

[2] G. Férey, Hybrid porous solids: past, present, future, Chem. Soc. Rev., 37 (2008) 191-214.

[3] C. Gerardin, M. In, L. Allouche, M. Haouas, F. Taulelle, In Situ pH Probing of Hydrothermal Solutions by NMR, Chem. Mater., 11 (1999) 1285-1292.

[4] D. Riou, G. Férey, Hybrid open frameworks (MIL-n). Part 3 Crystal structures of the HT and LT forms of MIL-7: a new vanadium propylenediphosphonate with an open-framework. Influence of the synthesis temperature on the oxidation state of vanadium within the same structural type, J. Mater. Chem., 8 (1998) 2733-2735.

[5] C. Livage, C. Egger, M. Nogues, G. Férey, Hybrid open frameworks (MIL-n). Part 5 Synthesis and crystal structure of MIL-9: a new three-dimensional ferrimagnetic cobalt(II) carboxylate with a two-dimensional array of edge-sharing Co octahedra with 12-membered rings, J. Mater. Chem., 8 (1998) 2743-2747.

[6] S. Bauer, C. Serre, T. Devic, P. Horcajada, J. Marrot, G. Férey, N. Stock, High-Throughput Assisted Rationalization of the Formation of Metal Organic Frameworks in the Iron(III) Aminoterephthalate Solvothermal System, Inorg. Chem., 47 (2008) 7568-7576.

[7] S. Surblé, C. Serre, C. Mellot-Draznieks, F. Millange, G. Férey, A new isoreticular class of metal-organic-frameworks with the MIL-88 topology, Chem. Commun., (2006) 284-286.

[8] E. Biemmi, T. Bein, N. Stock, Synthesis and characterization of a new metal organic framework structure with a 2D porous system: $(H_2NEt_2)_2[Zn_3(BDC)_4]\cdot 3DEF$, Solid. State. Sci., 8 (2006) 363-370.

[9] U. Mueller, M. Schubert, F. Teich, H. Puetter, K. Schierle-Arndt, J. Pastre, Metal-organic frameworks-prospective industrial applications, J. Mater. Chem., 16 (2006) 626-636.

[10] O. I. Lebedev, F. Millange, C. Serre, G. Van Tendeloo, G. Férey, First Direct Imaging of Giant Pores of the Metal−Organic Framework MIL-101, Chem. Mater., 17 (2005) 6525-6527.

[11] M. Li, M. Dincă, Reductive Electrosynthesis of Crystalline Metal–Organic Frameworks, J. Am. Chem. Soc., 133 (2011) 12926-12929.

[12] H. Li, M. Eddaoudi, M. O'Keeffe, O. M. Yaghi, Design and synthesis of an exceptionally stable and highly porous metal-organic framework, Nature, 402 (1999) 276-279.

[13] J. R. Long, O. M. Yaghi, The pervasive chemistry of metal-organic frameworks, Chem. Soc. Rev., 38 (2009) 1213-1214.

[14] D. J. Tranchemontagne, J. L. Mendoza-Cortes, M. O'Keeffe, O. M. Yaghi, Secondary

building units, nets and bonding in the chemistry of metal-organic frameworks, Chem. Soc. Rev., 38 (2009) 1257-1283.

[15] S. Liu, C. Wang, H. Zhai, D. Li, Hydrolysis of N,N-dimethylformamide catalyzed by the Keggin $H_3[PMo_{12}O_{40}]$: isolation and crystal structure analysis of $[(CH_3)_2NH_2]_3[PMo_{12}O_{40}]$, J. Mol. Struct., 654 (2003) 215-221.

[16] T. Cottineau, M. Richard-Plouet, J. -Y. Mevellec, L. Brohan, Hydrolysis and Complexation of N,N-Dimethylformamide in New Nanostructurated Titanium Oxide Hybrid Organic–Inorganic Sols and Gel, J. Phys. Chem. C., 115 (2011) 12269-12274.

[17] V. G. Golubev, T. P. Ryumina, Z. K. Vasil'eva, Corrosion of stainless steels in the dimethylformamide media of polyvinyl chloride fibre manufacturing, Fibre. Chem+., 18 (1987) 317-321.

[18] E. Buncel, E. A. Symons, The Inherent Instability of Dimethylformamide-Water Systems Containing Hydroxide Ion, Chem. Commun., 3 (1970) 164-165.

[19] Y. Wan, M. Alterman, M. Larhed, A. Hallberg, Dimethylformamide as a Carbon Monoxide Source in Fast Palladium-Catalyzed Aminocarbonylations of Aryl Bromides, J. Org. Chem., 67 (2002) 6232-6235.

[20] E. Stavitski, M. Goesten, J. Juan-Alcañiz, A. Martinez-Joaristi, P. Serra-Crespo, A. V. Petukhov, J. Gascon, F. Kapteijn, Kinetic Control of Metal–Organic Framework Crystallization Investigated by Time-Resolved In Situ X-Ray Scattering, Angew. Chem. Int. Ed., 50 (2011) 9624-9628.

[21] M. G. Goesten, P. C. M. M. Magusin, E. A. Pidko, B. Mezari, E. J. M. Hensen, F. Kapteijn, J. Gascon, Molecular Promoting of Aluminum Metal–Organic Framework Topology MIL-101 by N,N-Dimethylformamide, Inorg. Chem., 53 (2014) 882-887.

[22] G. R. Fulmer, A. J. M. Miller, N. H. Sherden, H. E. Gottlieb, A. Nudelman, B. M. Stoltz, J. E. Bercaw, K. I. Goldberg, NMR Chemical Shifts of Trace Impurities: Common Laboratory Solvents, Organics, and Gases in Deuterated Solvents Relevant to the Organometallic Chemist, Organometallics, 29 (2010) 2176-2179.

[23] H. M. Kothari, E. A. Kulp, S. J. Limmer, P. Poizot, E. W. Bohannan, J. A. Switzer, Electrochemical deposition and characterization of Fe_3O_4 films produced by the reduction of Fe(III)-triethanolamine, J. Mater. Res., 21 (2006) 293-301.

[24] M. L. Ohnsorg, C. K. Beaudoin, M. E. Anderson, Fundamentals of MOF Thin Film Growth via Liquid-Phase Epitaxy: Investigating the Initiation of Deposition and the Influence of Temperature, Langmuir, 31 (2015) 6114-6121.

Supplementary information of Chapter 4

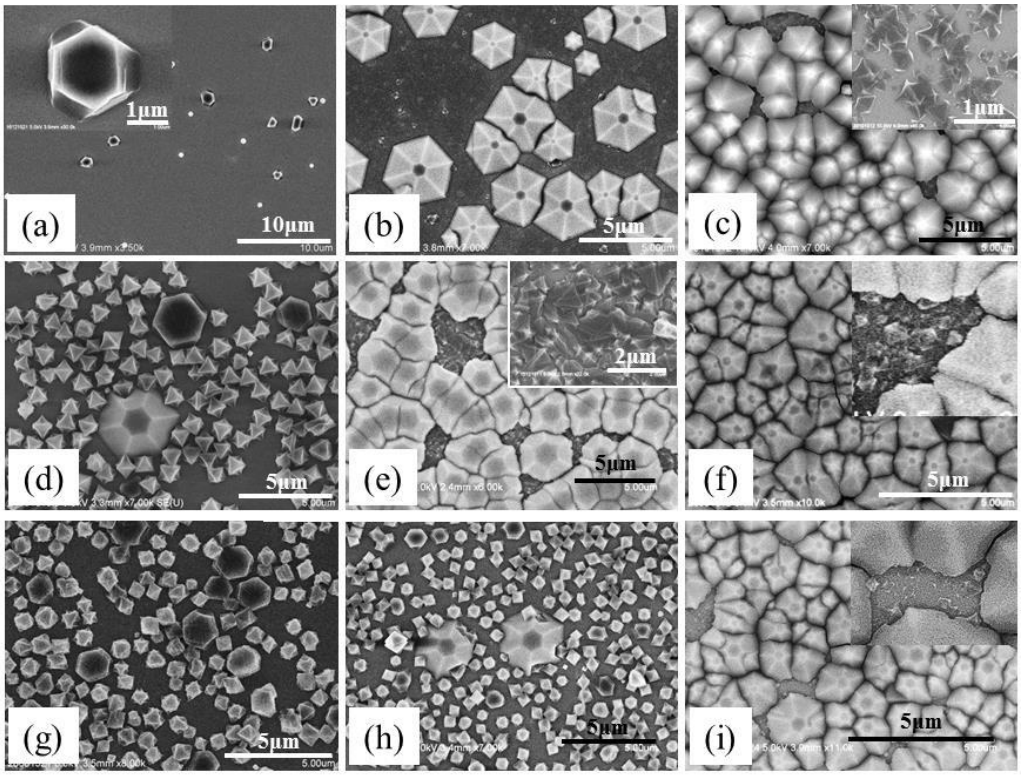

Figure S4.1 Film morphology as a function of the precursor concentration and ratio in solution. The rows correspond to different Fe^{3+} concentration: C_{Fe} = 12.5 mM (a,b,c); C_{Fe} = 25 mM (d,e,f) and C_{Fe} = 50 mM (g,h,i). The columns correspond to three different Ligand to Metal ratios R: R = 0.5 (a,d,g); R = 1 (b,e,h) and R = 2 (c,f,i). The synthesis temperature is 90 ^{o}C and the growth time is 24 h.

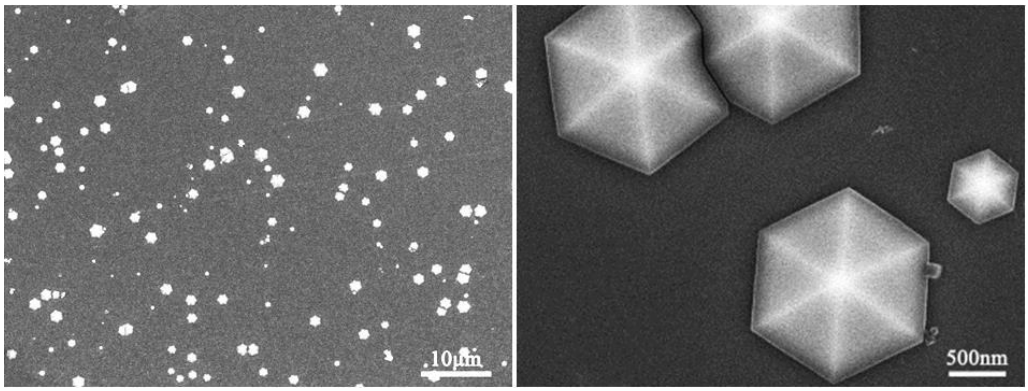

Figure S4.2 SEM images of film grown on Si-COOH surface at 90 ^{o}C in solution containing 6 mM [Fe^{3+}]. The growth time is 24 h and the R value is 2.

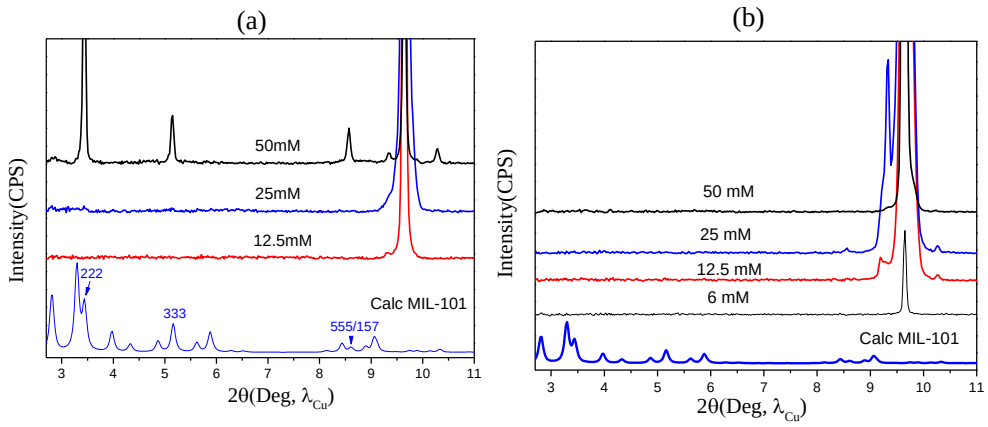

Figure S4.3 Short range XRD patterns of MOF films grown on carboxylic acid terminated surfaces at R = 1 (a) and R = 2 (b) as a function of [Fe^{3+}] concentration. [Fe^{3+}] concentration is given near to each plot. Growth time is 24 hours and the synthesis temperature is 90 ^{o}C for all samples. Calculated XRD pattern of MIL-101 is plotted underneath (blue) for comparison.

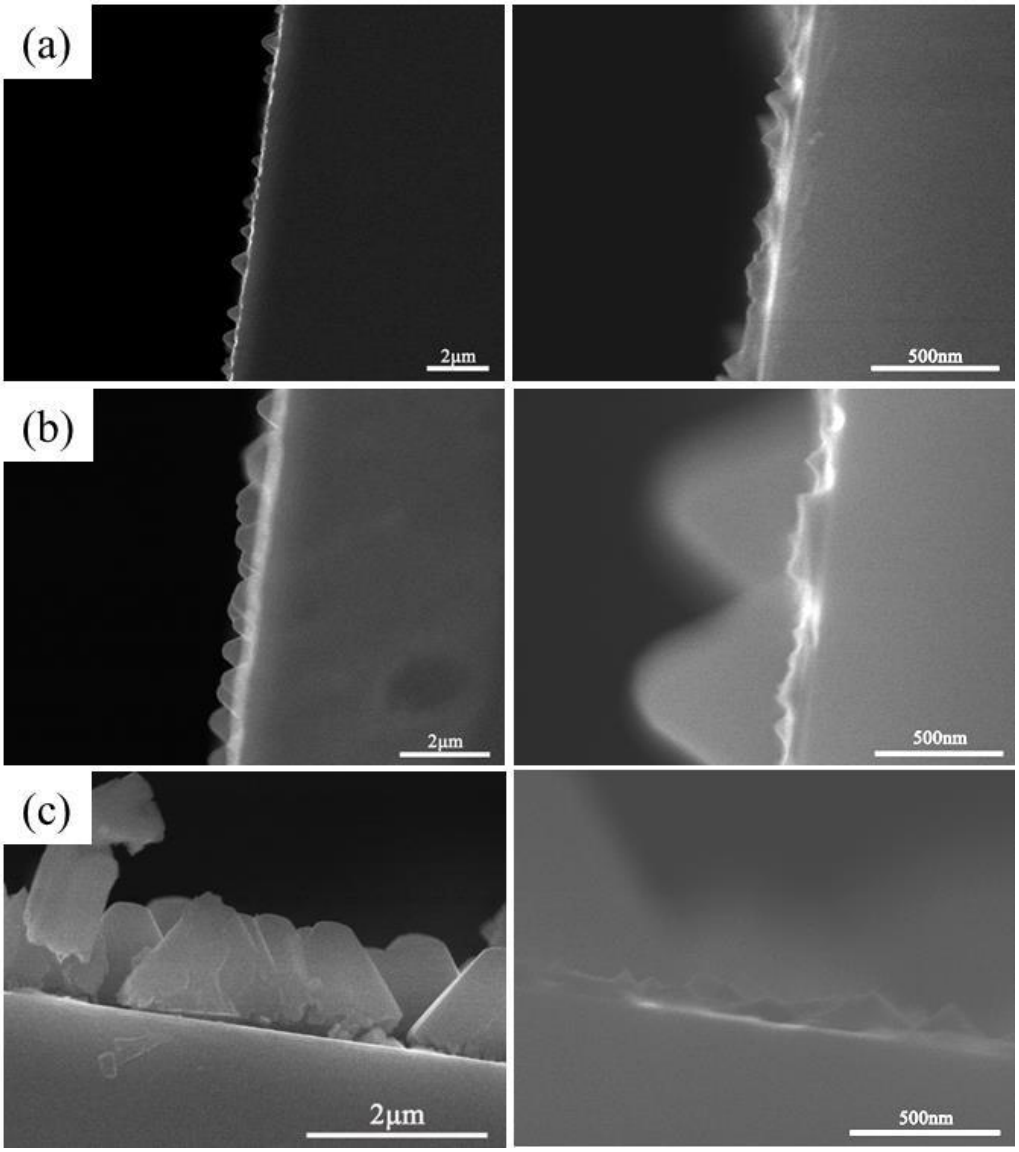

Figure S4.4 SEM images of cross-sections of films got on acid surfaces at 90 ^{o}C as a function of growth time: (a) 2 h; (b) 4 h; (c) 10 h. The ratio R equals to 2, C[Fe^{3+}] = 25 mM. Note that the thinner layers in right column are just between the big hexagonal crystals.

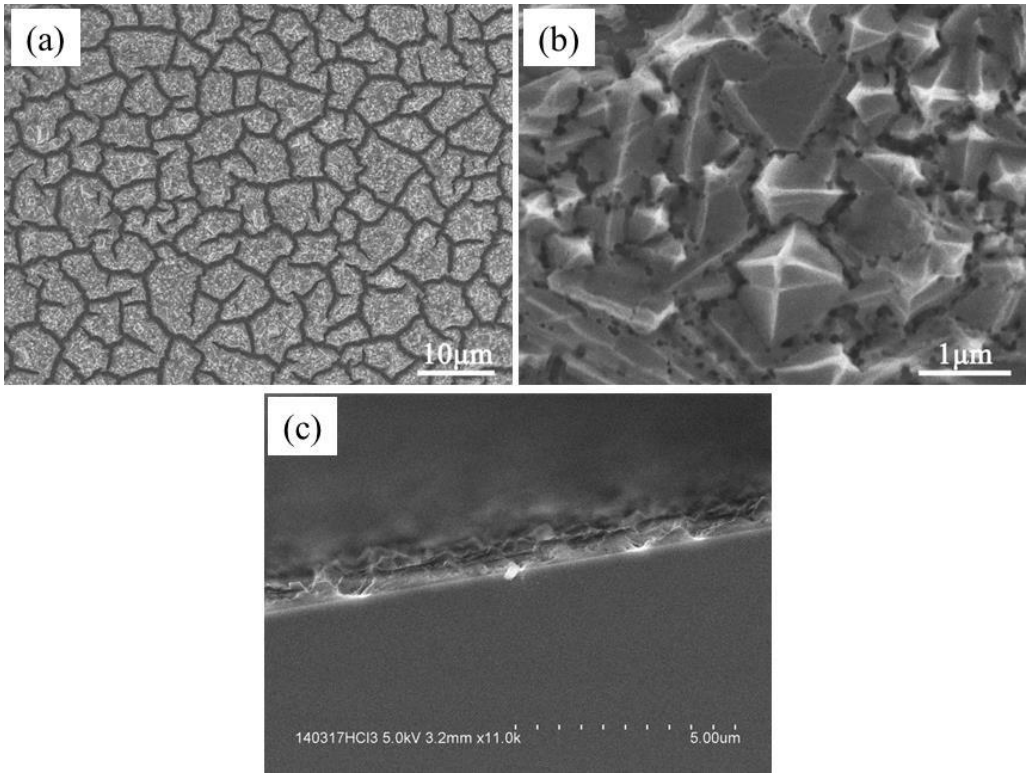

Figure S4.5 SEM images of sample obtained under R = 0.5 at 90 ^{o}C with addition of 12 M HCl solution. The final HCl and H_2O concentrations (of additive) in the synthesis solution are 10 mM and 35 mM, respectively. C_{Fe} = 25 mM and the growth time is 24 h.

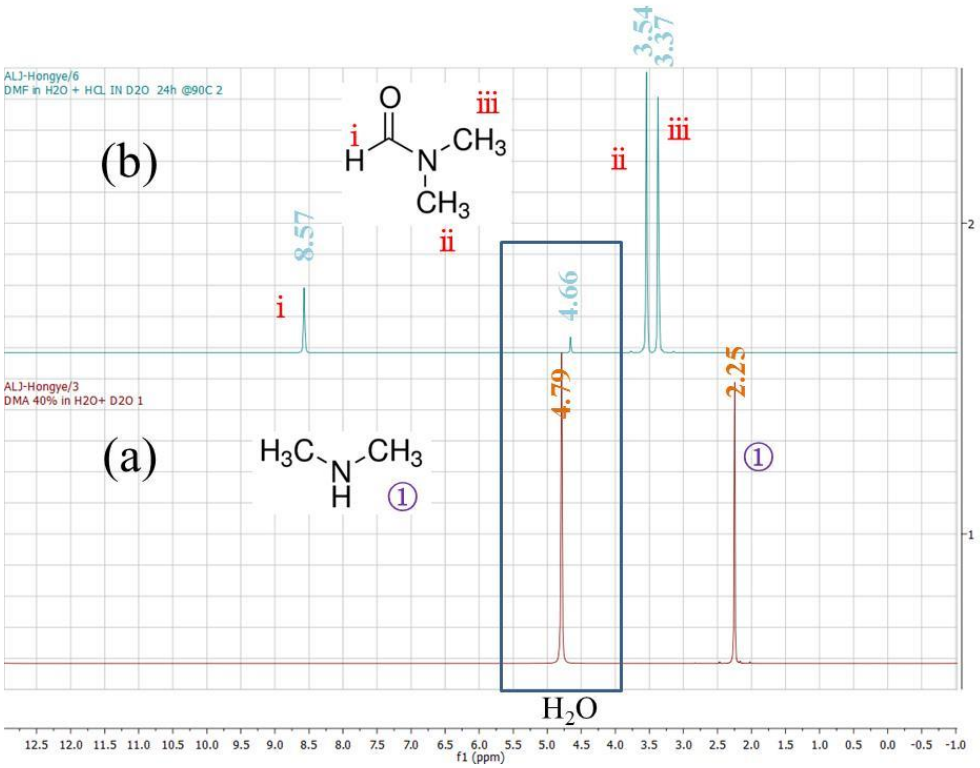

Figure S4.6: ^{1}H NMR spectra of 40 % DMA aqueous solution (a) and of DMF with addition of HCl solution after 24 h treatment at 90 ^{o}C (b).

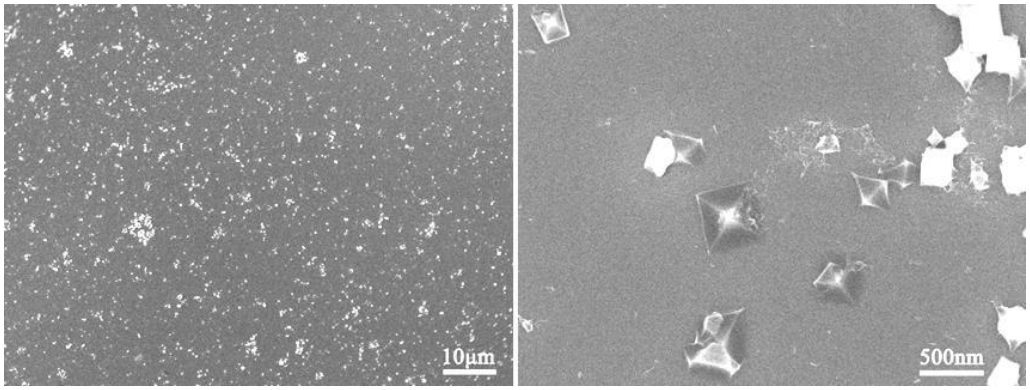

Figure S4.7 SEM images of film prepared with addition of 25 mM TEA on acid surfaces at 90 ^{o}C for 24 h growth. [Fe^{3+}] = 25 mM and R = 0.5.

Chapter 5: Nucleation and growth of Fe^{3+}/NDC MOF films on carboxylic functionalized Si surfaces

5.1 Introduction

As an analogue of MIL-88B(Fe), MIL-88C(Fe) is constructed from the connection of trimers of Fe(III)-oxygen octahedra that share a μ_3-O oxygen with dicarboxylates of 2,6-naphthalenedicarboxylic acid (H_2NDC). Owing to the rotation of trimeric Fe(III)-oxygen octahedra and aromatic rings around the O-O axis of the carboxylates, MIL-88C framework also exhibits reversible swelling and contraction phenomenon induced by associated host-guest interactions, without any apparent loss of crystallinity. While, unlike MIL-88B in which the plane of aromatic rings within the framework points to the interior of the tunnel (along [001] direction), those of MIL-88C are tangent to the tunnels. Combing with the slightly longer linkers, MIL-88C is prone to provide facile accessibility for molecule uptake and/or release comparing with MIL-88B [1,2]. To the best of our knowledge, there is still no report regarding the growth of MIL-88C on solid supports. Herein, the fabrication of Fe^{3+}/NDC MOF layers has been investigated on Si surfaces functionalized with carboxylic acid monolayer, onto which successful growth of Fe/H_2BDC MOFs have been observed in certain synthesis conditions. In the first part of this chapter the nucleation and growth of layers are investigated as a function of temperature, solution composition and crystallization time. The second part focuses on the properties of Fe^{3+}/NDC MOF layers regarding the adsorption and desorption of molecules. The nucleation and growth of MIL-88C are discussed at last by comparison with the system of Fe^{3+}/BDC.

5.2 Results

5.2.1 Influence of temperature

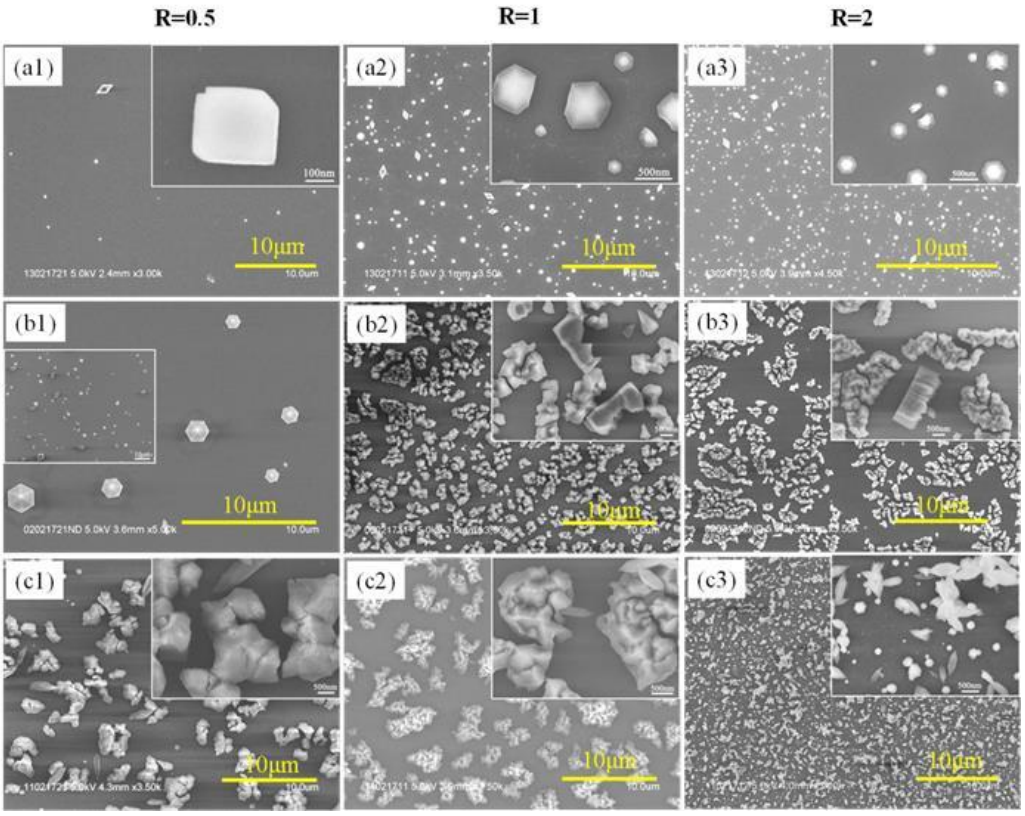

Figure 5.1 SEM images of films grown onto Si-COOH surfaces at different temperatures in Fe^{3+}/H_2NDC DMF solutions with variable R = ligand/metal ratios. From left to right the three columns show images of films grown in solution with R = 0.5, R = 1 and R = 2. The different rows correspond to three different temperatures: T = 70 ℃ (a), T= 90 ℃ (b) and T = 110 ℃ (c), respectively from top to bottom. For all samples C_{Fe} = 25 mM and the growth time is 24 h.

Figure 5.1 presents top view SEM images of layers grown on carboxylic terminated Si surfaces immersed in solution containing 25 mM [Fe^{3+}] and variable amount of H_2NDC for 24 h crystallization. When R kept at 0.5, the surface appears pretty empty except very few cubic crystals at 70 ^oC. Higher temperature evidences the increase of crystal density and also the intergrowth of hexagonal crystallites. At R = 2 and 1, the samples prepared at 70 ^oC both exhibit isolated nanometer crystals with well-defined hexagonal symmetry. Increasing the temperature to 90 ^oC, isolated assemblies of crystals are observed for both cases. An even higher temperature (110 ^oC) does not

improve the coverage of the film, but presents more randomly oriented dipyramidal prism crystals especially at the case of R = 2, which are considered as deposited powder from the solution because of the identical crystal dimension they have to the powder (See **Figure S5.1**). It is worth to note that only one phase with the same crystallographic shape was found in the powder due to the homogenous nucleation and growth at a given condition. Morphology of crystals evolves from hexagonal bipyramids to bipyramidal hexagonal prism as temperature increases, whereas the overall dimension becomes coarsened first and then thinner as depicted in **Figure S5.1**, while, crystals grown on the surface always possess mono-pyramidal shape. XRD patterns of the samples prepared at R = 2 as a function of temperature as well as the powder are presented in **Figure 5.2**. Their peak positions and possible assignments are listed in **Table 5.1**. Three main coupled peaks sometimes with shoulder peaks are observed for samples prepared at 90 ^{o}C and 110 ^{o}C, whereas two main coupled ones are found for the sample fabricated at 70 ^{o}C (see **Table 5.1**). Considering the crystal shape and the XRD pattern of the powder, we infer that the homogenous product is MIL-88C phase [1,2]. Regarding the structural identification of the layers grown on Si surfaces, none of them matches the pattern of the powder but near to 7.42 ^{o}, 14.87 ^{o} and 22.39 ^{o}, which are corresponding to the three reflections (002), (004) and (006) of MIL-88C, respectively. Taking the flexibility of MIL-88C frameworks and the crystalline shape into consideration, we think that the layers formed on functionalized Si surfaces with carboxylic terminated groups can be attributed to MIL-88C, but in a solvated form. The flexibility induced by interactions between the framework and trapped molecules will be thoroughly discussed later. The two little peaks found close to 10.67 ^{o} (2θ) of samples prepared at 70 and 110 ^{o}C can be assigned to the precipitated crystals from the solution as depicted in the inset images of **Figure 5.1(a3,c3)**. Note that XRD patterns of samples obtained in ratio R = 1 and 0.5 as a function of temperature indicate similar trend that three coupled intense peaks are always observed, but with a discrepancy of peak positions compared to the powder pattern (See **Figure S5.2**). To shortly summarize, as we showed for the system of Fe^{3+}/BDC the synthesis temperature also determinates the morphologies of

Fe^{3+}/NDC MOF films formed onto carboxylic acid terminated Si surfaces. At low temperature, isolated hexagonal pyramids occurred on the surface, whereas samples prepared at a higher temperature exhibit the appearance of separated assemblies of hexagonal crystallites and deposited powder on the surface is often observed. So in the coming sections, we will focus on the film preparation at 90 ^{o}C.

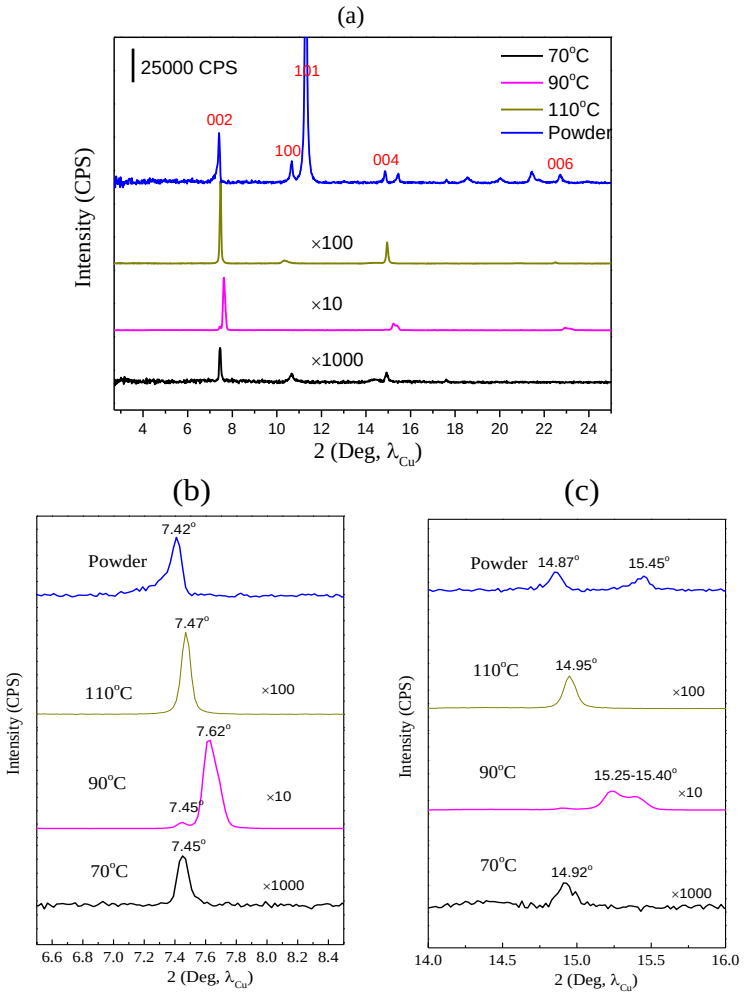

Figure 5.2: (a) XRD patterns of samples as shown in **Figure 5.1(a3,b3,c3)** after background correction. Powder obtained from the solution is plotted on top for comparison. Details in enlarged scale between 6.5-8.5 (b) and 14-16 (c) (2theta), respectively. Note that the pattern of powder is in dry form and different conditions give pretty similar PXRD patterns.

Table 5.1 Experimental peak positions extracted from **Figure 5.2** and their most potential assignments

Experimental peak position 2θ (deg, λ_{Cu})				Possible phase	Expected peak position	h k l scattering plane
T=70°C	T=90°C	T=110°C	Powder			
7.45	7.45 7.62	7.47	7.42	MIL-88C^{sol}	>7.42^{dry}	002
10.67	10.67	10.33	10.67	MIL-88C^{sol} MIL-88C	<10.67 10.67	100 100
			11.31	MIL-88C	11.31	101
14.92	14.92 15.25-15.4	14.95	14.87	MIL-88C^{sol}	>14.87^{dry}	004
17.6		17.6		Goethite FeO(OH)		
	22.94-23.17	22.5	22.39	MIL-88C^{sol}	>22.39^{dry}	006

5.2.2 Influence of solution composition

5.2.2.1 Influence of ratio of ligand to metal

As already presented in **Figure 5.1(b1,b2,b3)**, it compares the morphologies of films as a function of R. The layers grown with R ≥ 1 (excess of ligand and equal amount of ligand to metal) are composed of isolated bunch of pyramidal hexagonal prism crystals. The thicknesses for the bundle of crystals of R at 2 and 1 are 850 and 1050 nm, respectively. While at R = 0.5, apart from the appearance of hexagonally dipyramial crystallites, isolated crystals with well-defined hexagonal symmetry are also observed. XRD patterns of the above mentioned films as well as the powder

corresponding are plotted in **Figure 5.3**. The peak positions and most likely assignments are listed in **Table 5.2**.

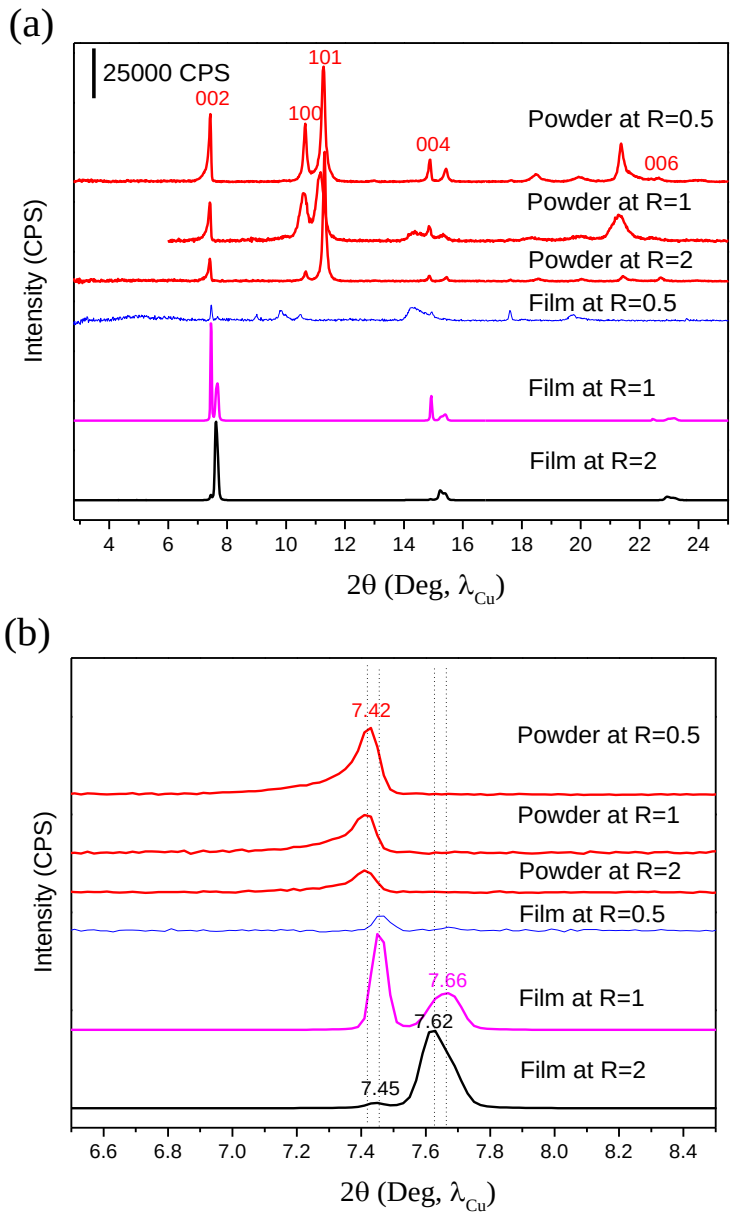

Figure 5.3: (a) XRD patterns of samples prepared in DMF solutions containing variable R ratios at 90 ^{o}C as shown in **Figure 5.1(b1,b2,b3)** after background correction. Patterns of powder obtained from various solutions are plotted on top for comparison. Details in enlarged scale between 6.5-8.5 ^{o} is presented in (b). The ratio R value is indicated next to each plot.

Table 5.2 Experimental peak positions extracted from **Figure 5.3** and their most potential assignments

Experimental peak position 2θ (deg, λ_{Cu})				Possible phase	Expected peak position	h k l scattering plane
R=2	R=1	R=0.5	Powder			
7.45 7.62	7.45 7.66	7.45	7.42	MIL-88C^{sol}	>7.42^{dry}	002
		9.0 9.82		MIL-88C^{sol}	<10.67	100
10.67		10.49	10.67	MIL-88C^{sol} MIL-88C	<10.67 10.67	100 100
	11.21		11.31	MIL-88C^{sol}	<11.31^{dry}	101
14.92 15.25-15.4	14.92 15.26-15.41	14.98	14.87	MIL-88C^{sol}	>14.87^{dry}	004
		17.6		Goethite FeO(OH)		
22.94-23.17	22.45 23-23.17		22.39	MIL-88C^{sol}	>22.39^{dry}	006

Powder XRD spectra suggest that an identical phase was formed independent of ratio of ligand to metal, which is consistent with the SEM images displayed in **Figure S5.1(b1,b2,b3)**. Films prepared at R = 2 and 1 provide several peaks mainly localized in three ranges that are close to the three reflections of (002), (004) and (006) of the powder. For the layer fabricated at R = 0.5, besides those peaks nearby the two main characteristic positions (7.42 ^{o} and 14.87 ^{o}), three additional peaks are also observed, which could be explained by the appearance of randomly oriented crystals shown in

Figure 5.1(b1). At last, one interesting point needs to be noted is that as ligand content increases, the size of resulted powder become smaller as clearly shown in **Figure S5.1(b1,b2,b3)**.

5.2.2.2 Influence of [Fe^{3+}] concentration

Based on the fact that only one phase was found referring to this system in spite of the ratio R. Morphologies of surfaces prepared at the ratio R = 2 and 1 appear pretty similar and there is little matter on the surfaces obtained at R = 0.5. Therefore, in all coming sections we only focus on the ratio R = 2, all films were prepared at 90 ^{o}C. **Figure 5.4** presents the morphologies of films grown onto Si-COOH surfaces as a function of [Fe^{3+}] concentration. As demonstrated in the figure, a main observation is that the layers grown on Si-COOH surfaces at R = 2 are composed of isolated assemblies of pyramidal crystals. A low concentration (3 mM) also evidences the existence of separated hexagonal crystallites. An even lower [Fe^{3+}] concentration at 1.5 mM only gives a low density of tilted and elongated hexagonal crystals as well as few hexagonal crystals that are perpendicular to the surface (See **Figure S5.3**). The distribution and evolution of the island area as a function of the Fe^{3+} concentration after processing the SEM images by the software SPIP is presented in **Figure 5.5**. In parallel, the evolution of surface coverage, density of isolated islands and thickness of the bundles of crystals are depicted in **Figure 5.6**. The surface coverage almost keeps constant around 30 %, whereas the mean island area increases with the increasing of [Fe^{3+}] concentration. With the increasing of [Fe^{3+}] concentration from 3 mM to 12.5 mM, the height of crystals increases from 400 nm up to around 1 μm. Keeping increasing the concentration, the sample sees a slight decrease of the height of assemblies of hexagonal crystals.

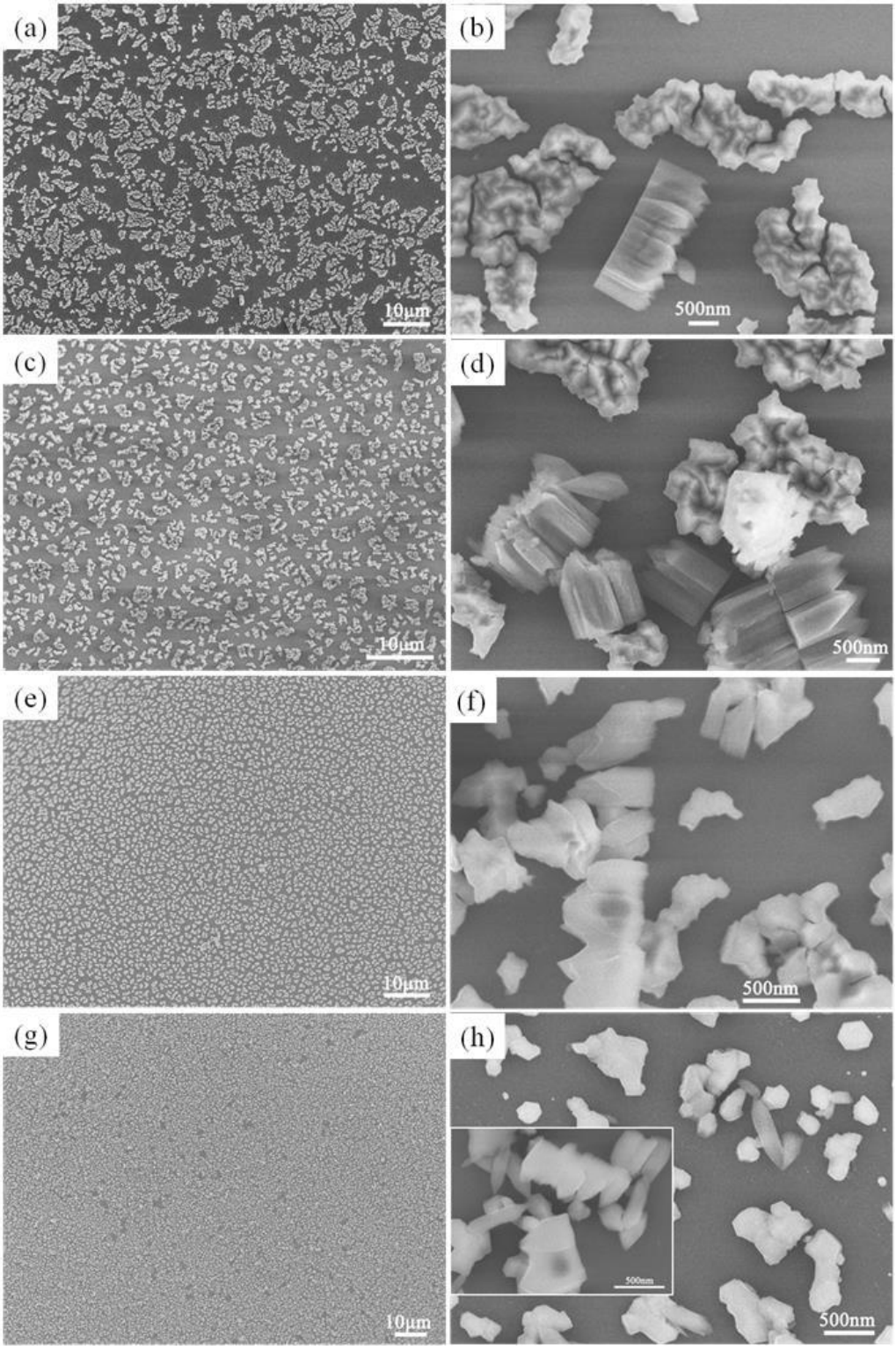

Figure 5.4 SEM images of films grown onto Si-COOH surfaces at 90 ^{o}C as a function of [Fe^{3+}] concentration. (a,b) 25 mM; (c,d) 12.5 mM; (e,f) 6 mM and (g,h) 3 mM. For all samples the ratio R equals 2, and the growth time is 24 h.

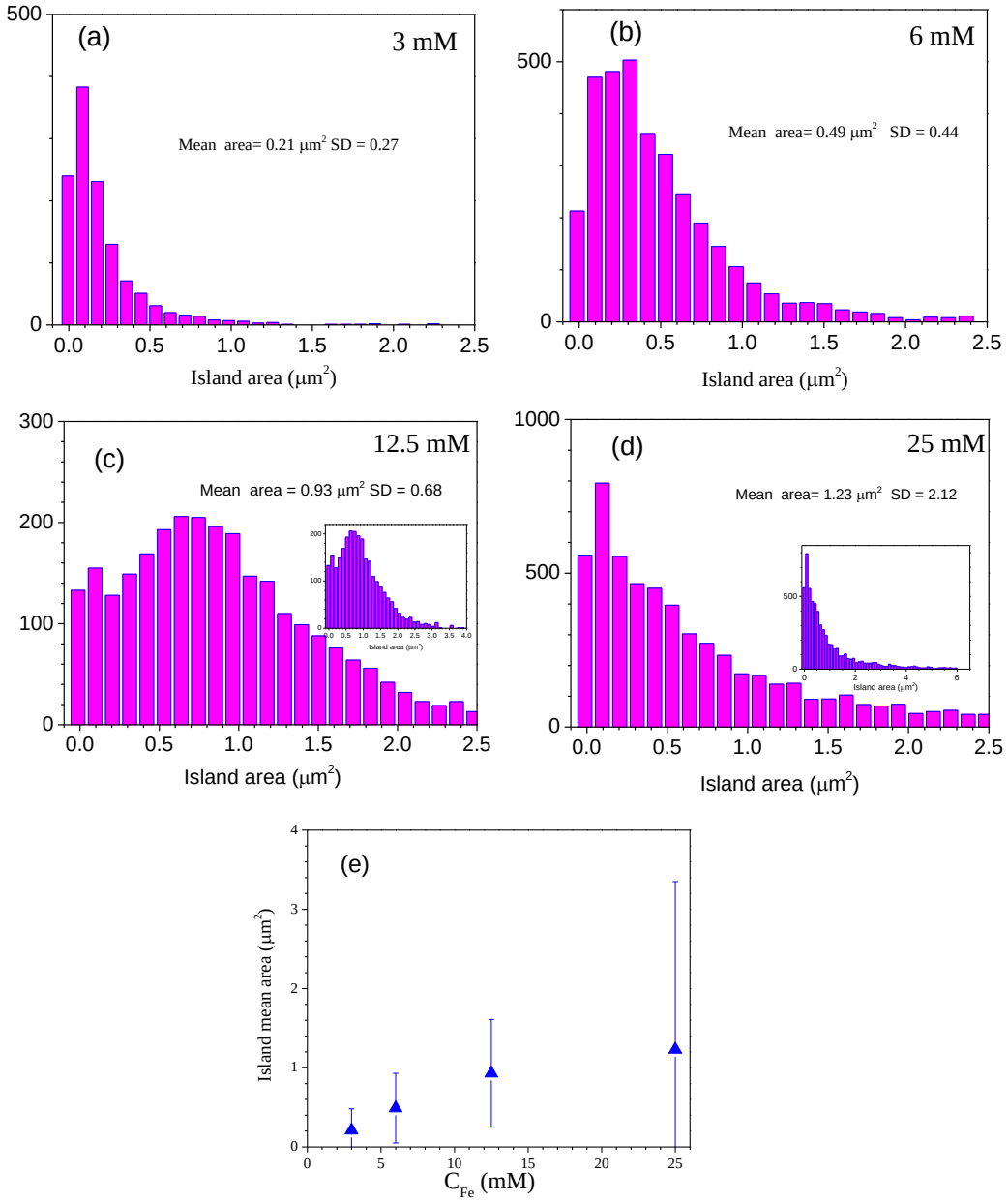

Figure 5.5 Distribution (a-d) and evolution (e) of the island area as a function of the [Fe^{3+}] concentration.

Interestingly, the density of isolated islands composed of hexagonal crystallites undergoes a substantial decrease after 3 mM and remains unchanged afterwards along with the increase of concentration. SEM images of the powder obtained from solution at each concentration are displayed in **Figure S5.4**. Similar phenomenon as with to the variation of crystal size is observed for the powder. At the [Fe^{3+}] concentration of 1.5 mM, the hexagonal and elongated crystals possess a mean aspect ratio around 5.7.

Increasing the concentration from 3 mM until to 12.5 mM, dipyramidal crystallites with increased size (both in a and c direction) are found, whereas a nearly constant aspect ratio (around 3.6) is kept. An even higher [Fe^{3+}] concentration (25 mM) contributes to the formation of massive crystals with an aspect ratio of appro. 2.8, but with small size, comparing with the ones generated at 12.5 mM.

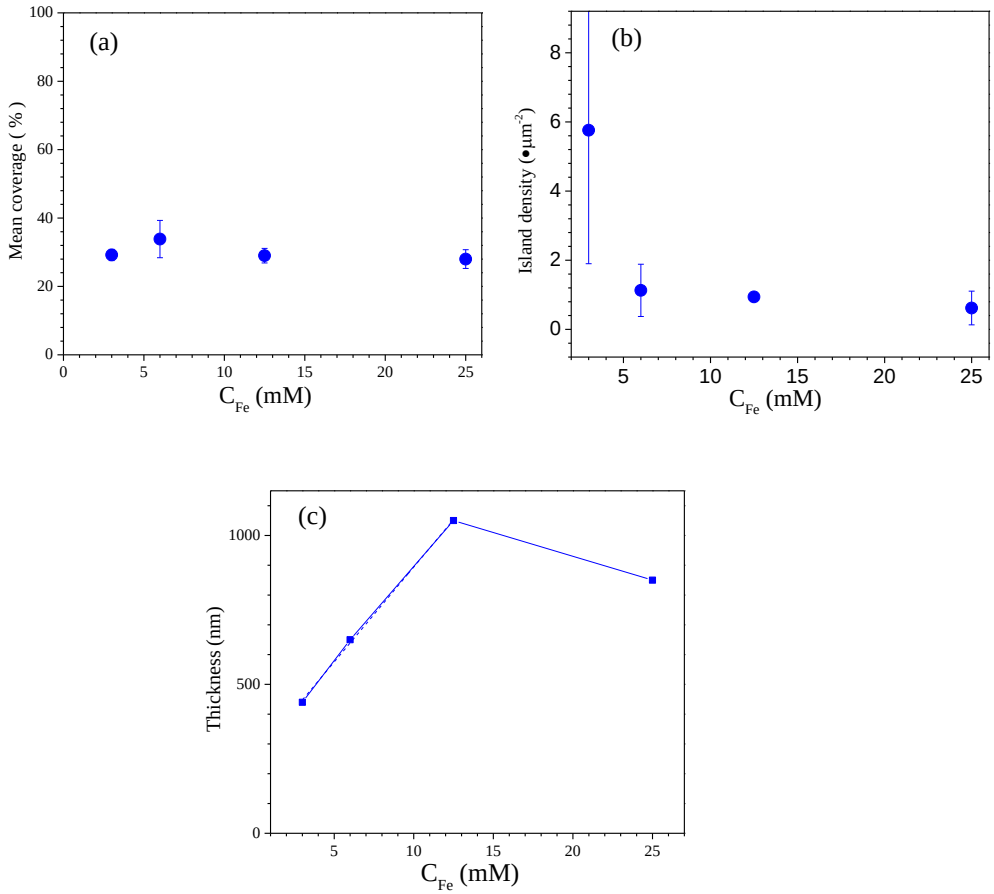

Figure 5.6 Island coverage (a), density (b) and thickness (c) as a function of Fe^{3+} concentration, deducted from SEM images processing (SPIP software).

Narrow range XRD patterns of films prepared in Fe^{3+}/H_2NDC solution with various [Fe^{3+}] concentrations ranging from 3 mM to 25 mM for 24 h growth are presented in **Figure 5.7**. The full range experimental XRD patterns are given in **Figure S5.5**.

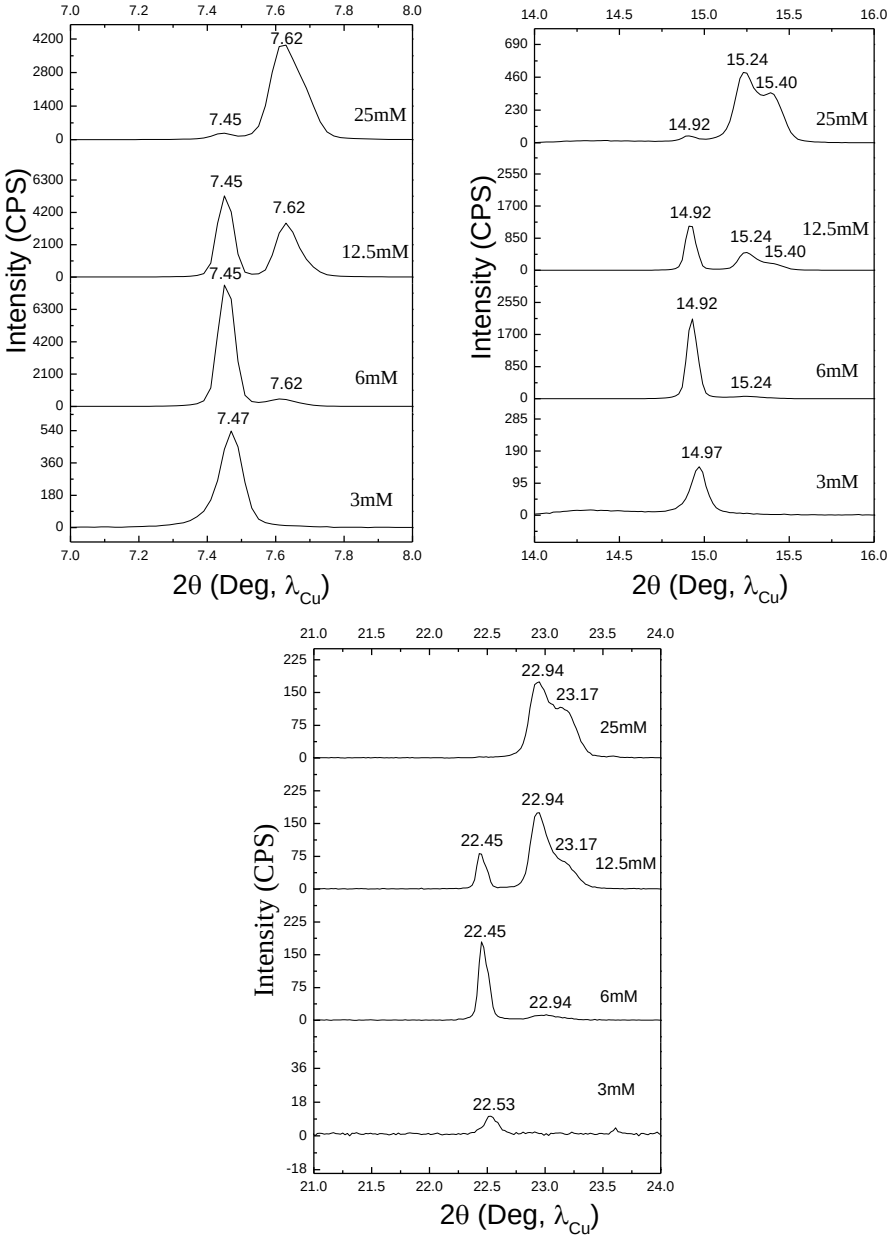

Figure 5.7 Narrow range XRD patterns of films prepared in Fe^{3+}/H_2NDC solution with various [Fe^{3+}] concentrations ranging from 3 mM to 25 mM for 24 h growth. The concentration is indicated next to each pattern.

Experimental peak positions extracted from **Figure 5.7** and their most potential assignments are presented in **Table 5.3**.

Table 5.3 Experimental peak positions extracted from **Figure 5.7** and their most potential assignments.

Experimental peak position 2θ (deg, λ_{Cu})					Possible phase	Expected peak position	h k l scattering plane
25mM	12.5mM	6mM	3mM	Powder			
7.45 7.62	7.45 7.62	7.45 7.62	7.47	7.42	MIL-88C^{sol}	>7.42^{dry}	002
			9.67		MIL-88C^{sol}	<10.67	100
10.67			10.56	10.67	MIL-88C^{sol} MIL-88C	<10.67 10.67	100 100
	11.16	11.15		11.31	MIL-88C^{sol}	<11.31^{dry}	101
14.92 15.25-15.4	14.92 15.25-15.4	14.92 15.24	14.97	14.87	MIL-88C^{sol}	>14.87^{dry}	004
			17.6		Goethite FeO(OH)		
22.94-23.17	22.45 22.94-23.17	22.45 22.94	22.53	22.39	MIL-88C^{sol}	>22.39^{dry}	006

XRD patterns of the as-prepared samples at 90 ^{o}C from solutions containing variable [Fe^{3+}] concentration clearly show the peaks are present in three characteristic ranges nearby the three reflections (002), (004) and (006) of MIL-88C which localizes at 2θ = 7.42 ^{o}, 14.87 ^{o} and 22.39 ^{o}, respectively, but always with a discrepancy. Shoulder and/or broad peaks are usually observed close to the three main peaks probably due to the uneven release of solvent that encapsulated inside the frameworks. Mass of the isolated bundles of hexagonal crystals was estimated from the crystalline

dimension and coverage as-determined from the SEM images as shown in **Figure 5.4**. In comparison with the integrated area of XRD peaks nearby the two (002) and (004) reflections of MIL-88C, the calculated mass of the layers grown onto carboxylic terminated Si surfaces as a function of [Fe^{3+}] concentration is plotted in **Figure 5.8**.

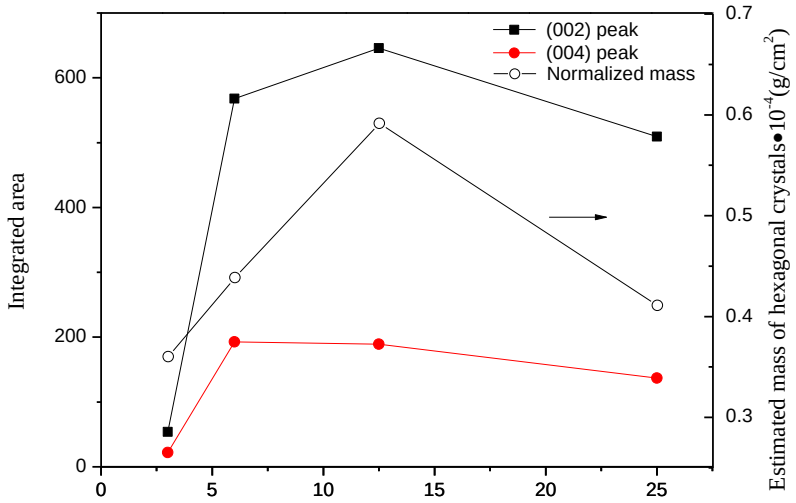

Figure 5.8 Normalized estimated mass of layers grown onto carboxylic ended Si surfaces as a function of [Fe^{3+}] concentration and normalized integrated intensity of the peaks nearby the two (002) and (004) reflections of MIL-88C phase. The calculated density of MIL-88C is 1.74 g/cm^3 [2].

The estimated mass of layers obtained on carboxylic terminated Si surfaces evidences an increase along with the increasing of the [Fe^{3+}] concentration up to 12.5 mM. Continuing increasing the concentration to 25 mM sees a decrease of the quantity of matter grown on the surface. The integrated area of XRD peaks close to the two main reflections (002) and (004) more or less follows the same trend, even if the increasing rate at beginning varies. Homogenous nucleation and growth in solution are in some sense promoted at higher concentration, which in turn will consume more precursors and hence influence the heterogeneous nucleation and growth on surface. This might explain why the decrease of matter at higher concentration is found at higher C[Fe^{3+}].

5.2.3 Influence of immersion time

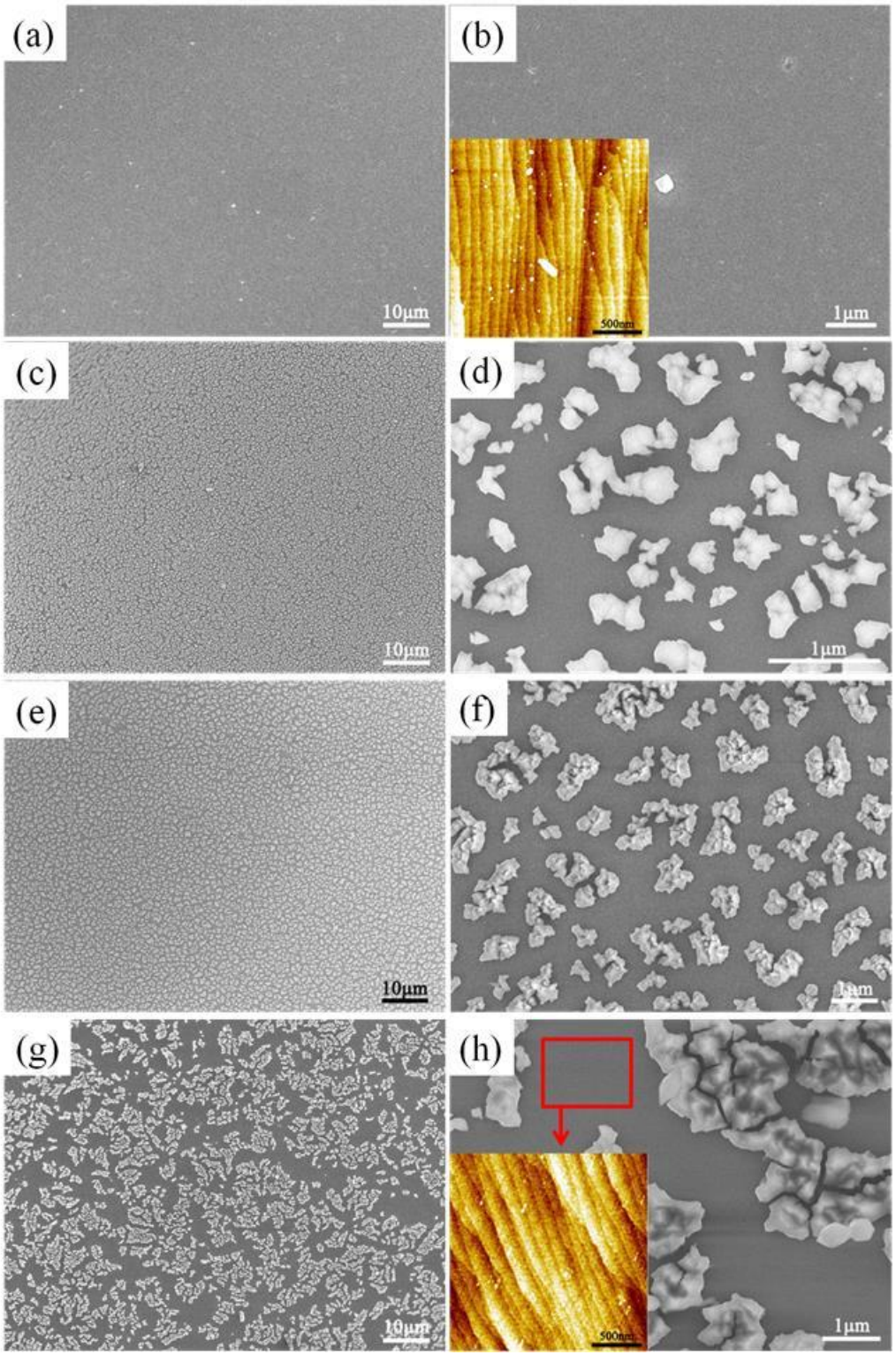

Figure 5.9 Morphologies of films grown onto Si-COOH surfaces at 90 °C as a function of immersion time: (a,b) 2 h; (c,d) 4 h; (e,f) 10 h and (g,h) 24 h. The inserted images in (b,h) are the representative AFM images showing the empty areas between the crystals. For all samples R equals 2 and [Fe^{3+}] is

fixed at 25 mM.

Morphologies of films grown onto Si-COOH surfaces at 90 ^{o}C as a function of immersion time are depicted in **Figure 5.9**. As we see clearly from **Figure 5.9(a,b)**, SEM images of sample after 2 h immersion in the crystallization solution is pretty empty except some cubic-like crystals. At longer immersion times (4 h, 10 h and 24 h), layers obtained on functionalized Si surfaces with carboxylic functional groups exhibit isolated assemblies of inter-grown and pyramidal crystals (see **Figure S5.6**). Representative AFM images as displayed in the inset images show the characteristic atomically-flat Si structure with terraces, ruling out the existence of thin layer through the surface. **Figure 5.10** depicts the distribution and evolution of crystal island area as a function of crystallization time and **Figure 5.11** presents the island coverage, density and thickness as a function of growth time, deducted from SEM images processing.

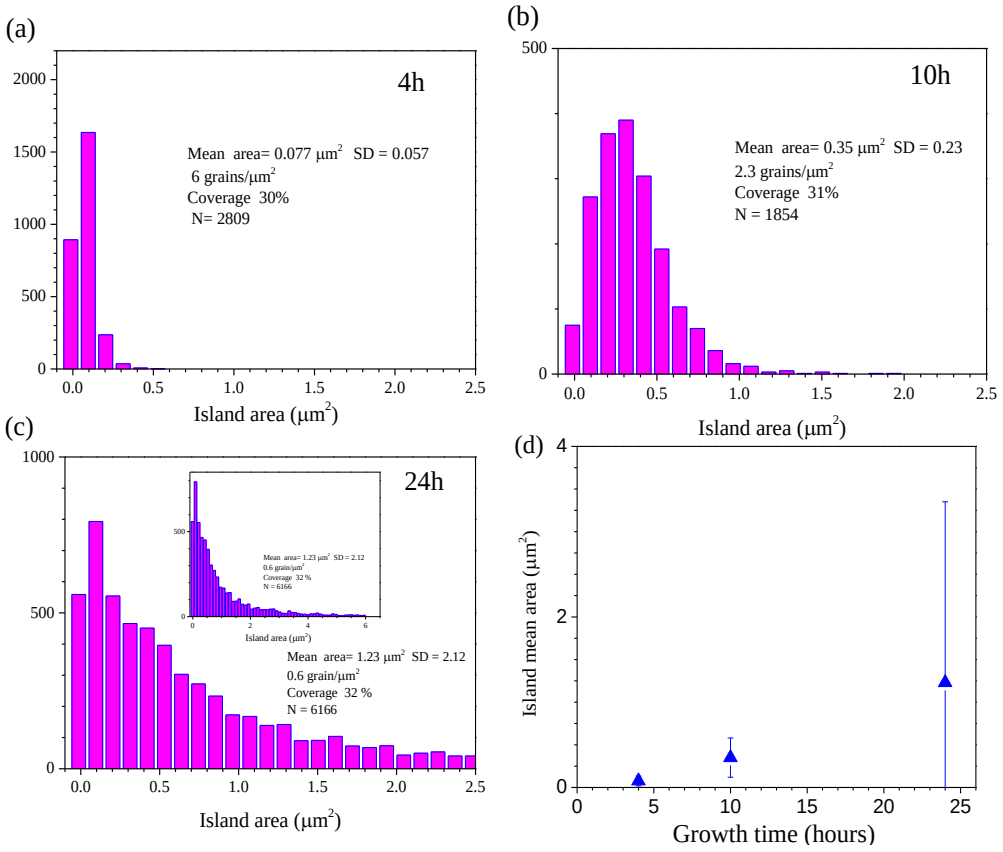

Figure 5.10 Distribution (a-c) and evolution (d) of the island area as a function of growth time.

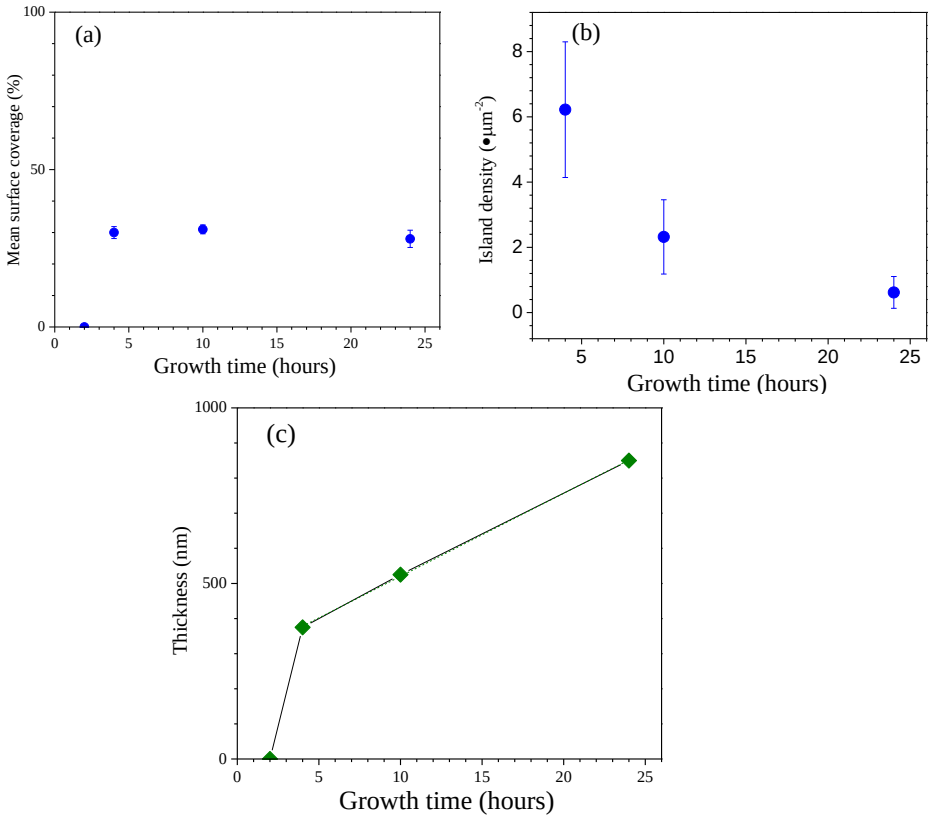

Figure 5.11 Island coverage (a), density (b) and thickness (c) as a function of growth time, deducted from SEM images processing (SPIP software).

The mean area of isolated assemblies of crystals increases over time, in contrary, the density of those islands declines after 4 h crystallization. Concurrently, the film coverage keeps almost unchanged. The height of bunches of hexagonal crystals increases dramatically after 2 h immersion and then grows linearly with a slower rate. Normalized mass of layers formed at various immersion times was also calculated by considering their vertical height and surface coverage obtained from the SEM images. The calculated values as well as the integrated area of peaks close to the two reflections (002) and (004) of MIL-88C phase is plotted in **Figure 5.12**. Amount of matters grown on surfaces increase dramatically along with immersion time at beginning. Apparent slower rate is observed above 10 h crystallization.

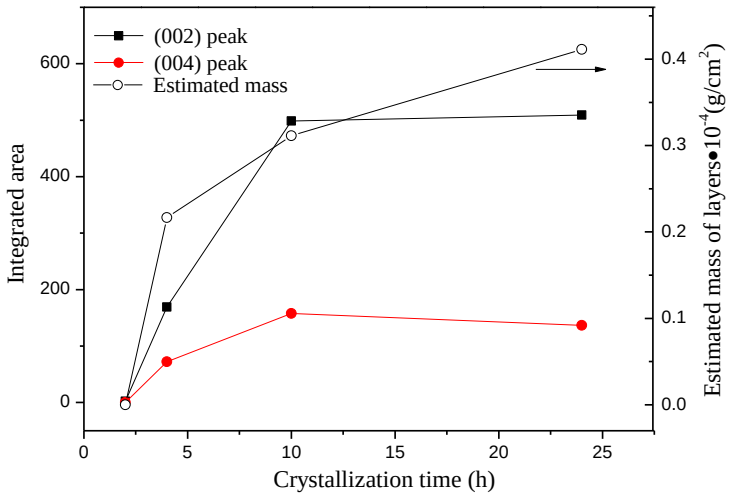

Figure 5.12 Normalized estimated mass of layers grown onto carboxylic ended Si surfaces as a function of immersion time and integrated intensity of the peaks nearby the two (002) and (004) reflections of MIL-88C phase. The calculated density of MIL-88C is 1.74 g/cm^3.

5.2.4 Effect of post-treatments

XRD spectra of the as-prepared films on carboxylic terminated Si surfaces always show a deviation from that of the powder (in dry form) and the simulated XRD pattern of MIL-88C. The discrepancy can be attributed to the existence of captured molecules/solvents inside the framework that evokes the structural change. Obvious shifting undergoes from low angle value to higher one with a long immersion time and a high precursor concentration as demonstrated in **Figure 5.13**. Post-treatment such as annealing and/or rinsing that makes the molecules release from the channels and/or cages of MIL-88C will probably see a shifting of relevant XRD peaks. Adsorption of molecules will undoubtedly make it shifted to a higher value.

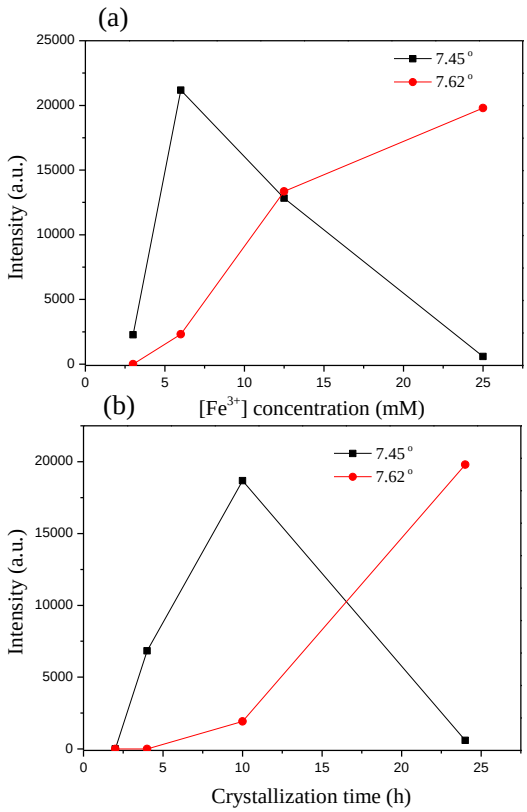

Figure 5.13 Evolution of the two main peak positions (at or nearby 7.45 ^{o} and 7.62 ^{o}) as function of [Fe^{3+}] concentration (a) and immersion time (b). All the samples were prepared at 90 ^{o}C and the ratio R was fixed at 2. For (b) the [Fe^{3+}] is 25 mM.

5.2.4.1 Thermal annealing

Figure 5.14(a) presents the peak evolution (the peak nearby 7.42 ^{o}) of the film along with annealing time in an oven at 150 ^{o}C. Apparently, the peak sees a left-shifting by 0.15 ^{o} upon heating, indicating clearly the structure of this layer is flexible. Time dependence of peak position and integrated area after various annealing time are also plotted in **Figure 5.14(b)**.

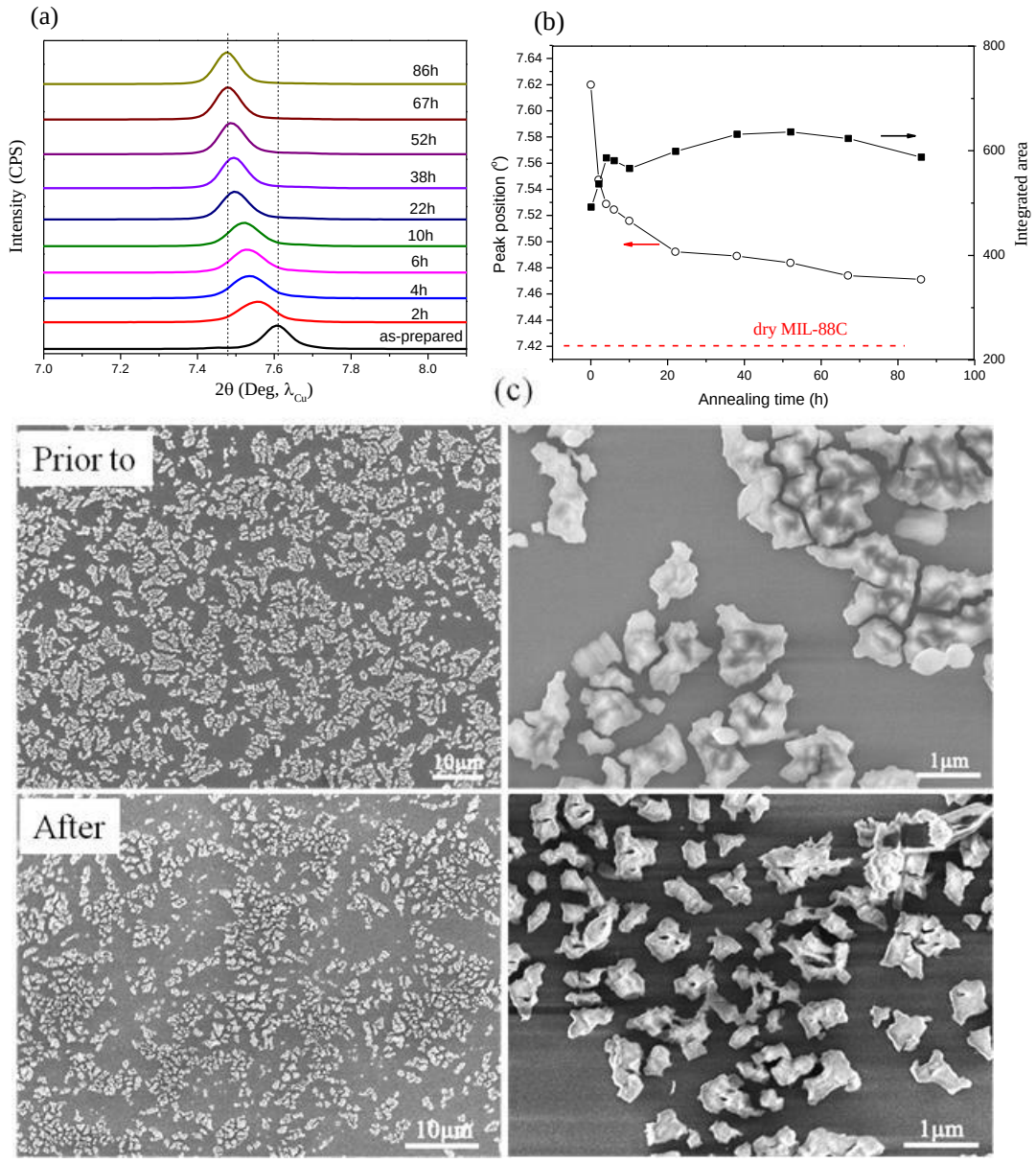

Figure 5.14 (a) Evolution of the XRD patterns after sequences of thermal annealing in an oven at 150 ^{o}C (narrow angular range). The annealing time is indicated for each sequence. (b) Variation of the peak position and its integrated area as a function of cumulated annealing time. (c) SEM images prior to (top) and after (below) annealing. Note that the sample was measured immediately after heating; the scanning for each spectrum needs 50 min. The synthesis conditions for this sample: [Fe^{3+}] = 25 mM, R = 2 and at 90 ^{o}C for one day growth.

Unlike the MIL-88B framework as we show in **Chapter 4**, peak intensity of this layer does not evidence a decrease, suggesting good thermal stability towards cyclic heating. In fact, SEM characterizations after annealing (**Figure 5.14(c)**) indicates that a large number of small pieces or islands are observed, probably originating from the

breakdown of the isolated large assemblies of hexagonal crystallites due to the thermal stress.

Due to the absence of most peaks of the surface-bound crystals, information about the lattice parameter reflecting the planes which are parallel to the surface is only available. A slight value increase of lattice parameter c ($c = 2d_{spacing}$) corresponds to the shifting of the peak to a lower angle. As elaborated by C. Serre and his co-workers [1,2], MIL-88C framework shrinks/swells ("breathing phenomenon") in large magnitude under external stimulus (temperature, pressure, molecule encapsulation...) with no apparent loss of crystallinity. Upon desorption of molecules/solvents by heating, MIL-88C framework tends to approach the so-called 'dry form' in which it possesses a smaller latter parameter in (a, b) plane whereas a larger parameter value in c direction, synergistically resulting in a small cell volume.

5.2.4.2 Soxhlet rinsing

In fact, rinsing the sample as shown in **Figure 5.4(c,d)** composed of isolated assemblies of pyramids in soxhlet with ethanol as the solvent gives similar result. **Figure 5.15** depicts the XRD patterns of sample before and after the rinsing procedure. The plot prior to rinsing shows three main peaks with shoulder peaks localized in three characteristic ranges that are near to the (002), (004) and (006) reflections of MIL-88C phase, respectively. After rinsing in soxhlet for 16 h, only three peaks at $2\theta = 7.43$, 14.89 and 22.41 ^{o} are observed, which nearly matching the (002), (004) and (006) reflections of PXRD of "empty" MIL-88C, strongly demonstrating the flexibility of MIL-88C framework and they are much more resistant to soxhlet rinsing comparing with the MIL-88B framework. Furthermore, this rinsing method is in short length and can be an alternative way for activating the MOFs in comparison with the previous one.

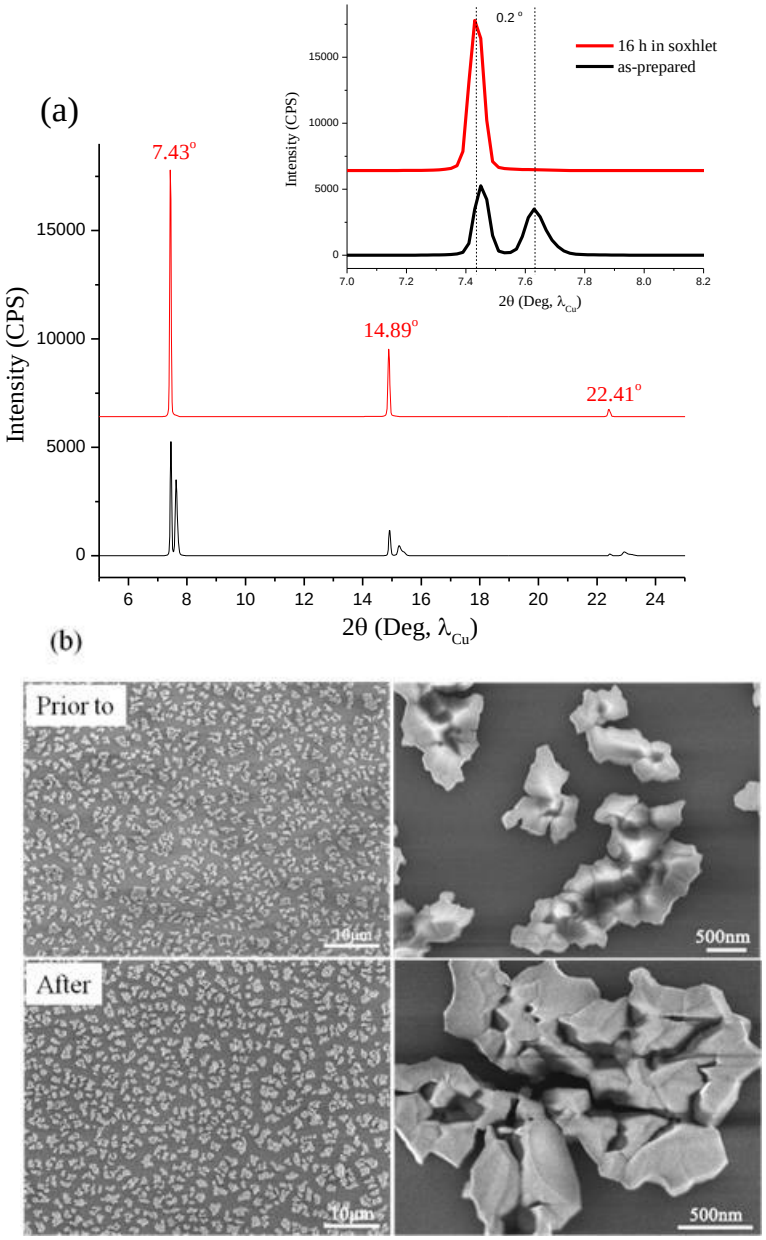

Figure 5.15 (a) XRD patterns before (black) and after (red) the rinsing in soxhlet with ethanol for 16 h. The inset plot is the zoomed range between 7 and 8.2 °. (b) SEM images showing the film morphology prior to (top) and after (below) rinsing. Synthesis condition for this sample: [Fe^{3+}] = 12.5 mM, R = 2, T = 90 °C, 24 h growth.

SEM images shown in **Figure 5.15(b)** confirms the still existence of layer after rinsing in soxhlet while zoomed image shows the isolated islands after rinsing for 16 h tend to split into small pieces/islands, which is consistent with the results shown in the previous section. Furthermore, the peak position remains unchanged with the further storage at ambient environment for 4 days (see supplementary information in

Figure S5.7), suggesting a good stability at ambient environment which is perspective for potential applications.

5.2.4.3 Solvent capture and release

To verify the accessibility of the porosity of those layers grown on carboxylic terminated Si surfaces, which is a prerequisite for many intriguing applications, tentative experiments involving the adsorption as well as desorption of small polar molecule (ethanol) was implemented by a Bruker machine equipped with a parallel beam. Evolution of the (002) reflection of the film as shown in **Figure 5.4(g,h)** upon ethanol adsorption and desorption with and without a poly(methyl methacrylate) (PMMA) dome is presented in **Figure 5.16**.

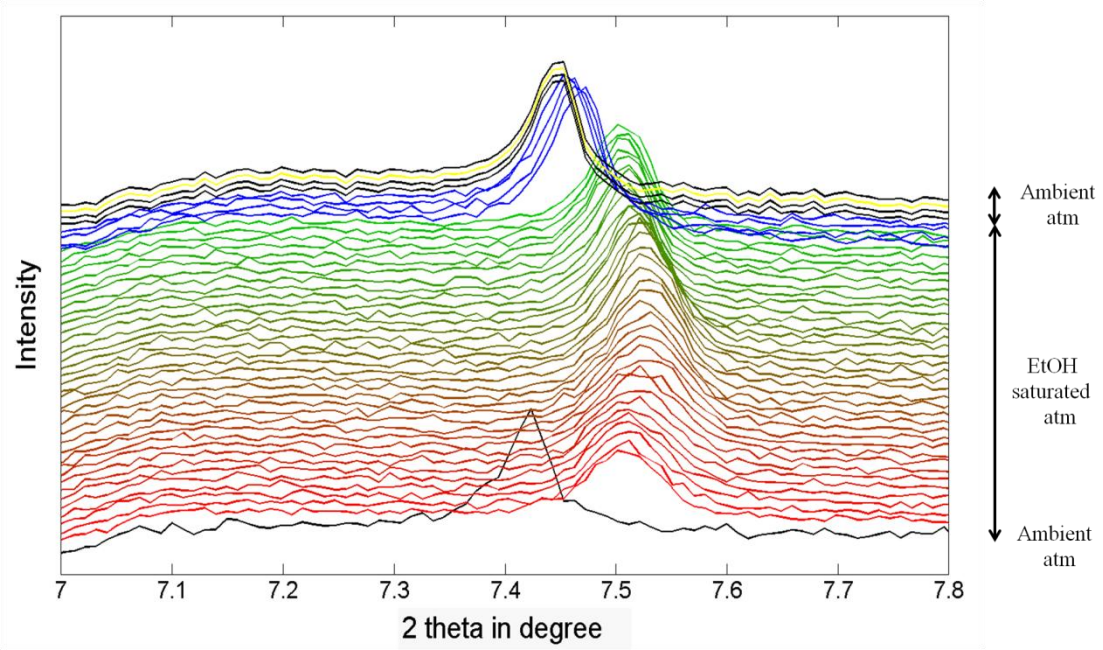

Figure 5.16 Evolution of XRD pattern of Fe^{3+}/NDC film as shown in **Figure 5.4(g,h)** exposed in saturated EtOH atmosphere. The sample was placed in a closed poly(methyl methacrylate) (PMMA) cell. XRD pattern was collected in air (black plot at bottom) prior to the insertion of EtOH inside the cell. Red to green plots was recorded under saturated EtOH atmosphere (cell closed). Blue to black plots (top) were recorded again in air after EtOH evaporation (without dome). Note that the spectra obtained within the dome, the interval between two adjacent spectra shown here is 20 min, whereas, after removing the dome, the interval is 2 min. For each spectrum, the scanning itself takes 20 s. All the measurements were done by a Bruker machine equipped with a parallel incidence beam and a position sensitive detector (PSD).

The (002) reflection of the surface-bound layer undergoes a rapid shifting (appro. 15 seconds) to a higher 2θ value once a droplet of ethanol is dropped on the surface. Afterwards, the surface was sealed by a PMMA dome, with another several drops of ethanol in the groove that surrounds the sample. Additional pressure will be induced thanks to the evaporation of ethanol inside the dome, which of course impels more ethanol molecules filling the pore channels and cages of MIL-88C framework. As the XRD spectra in early stage display that the peak continues shifting to higher angle in an extreme slow rate, corresponding to a structural expansion upon adsorption of ethanol molecules. Maximum intake amount is reached after around 7 h when the internal pressure increases, making the further capture of molecules difficult. Along with time, the framework goes through a release of ethanol molecules, showing a minor shifting back. After removing the top dome, we observed an instantaneous transferring to the lower 2θ value from XRD pattern, meaning structural contraction happened. The obvious hysteresis of molecule release is likely to be related to the associated interaction in terms of hydrogen bonds built between the trapped polar molecules and inorganic parts of the framework [1]. The schematic representation of changes in MIL-88C framework during molecule adsorption and desorption is depicted in **Figure 5.17**.

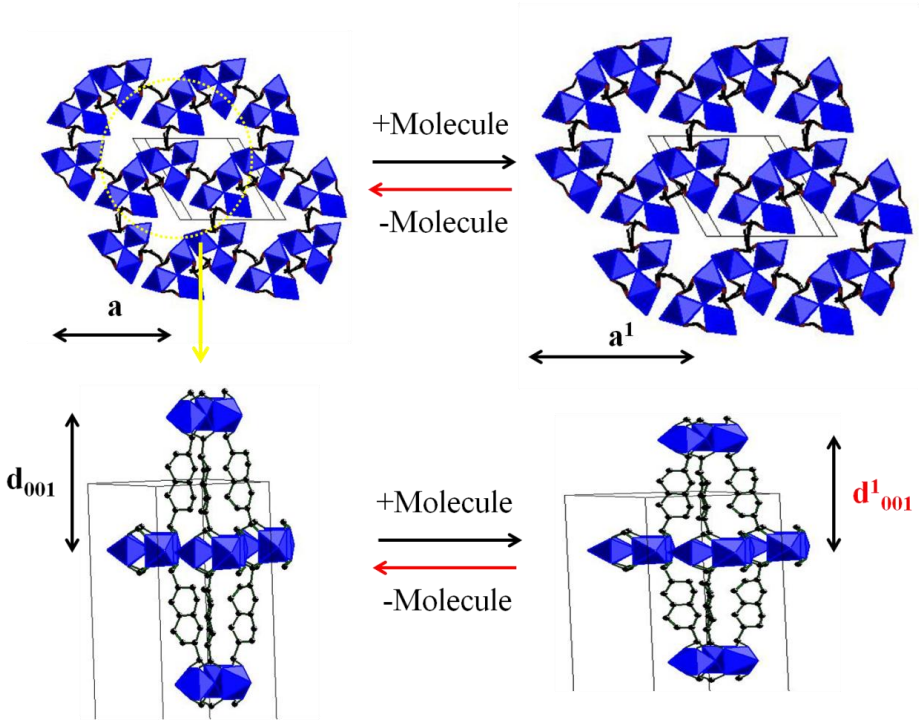

Figure 5.17 Schematic representations of changes in MIL-88C framework during molecule uptake and release. Notice that the lattice parameter c equals $2d_{spacing}$.

During uptake of molecules, the interplanar distance in c direction (d_{001}) of MIL-88C framework contracts, confirmed by an increase of two theta value of (001) reflection position. To maintain the integrity of framework, a swelling happens to that of (100) and (101) reflections, corresponding an overall expansion of MIL-88C framework as elucidated by C. Serre and his co-workers [1]. While, upon desorpion, the framework shows a reverse evolution.

5.3 Discussion

Different from the results as shown in **Chapter 4** (**Figure 4.15**) in which certain amount of isolated hexagonal MIL-88B crystals are already observed after 2 h immersion in solution, few nuclei are formed after 2 h crystallization for MIL-88C phase as depicted in **Figure 5.9(a,b)**. For a longer immersion time (4 h), the carboxylic terminated Si surface evidences the formation of large density of isolated assemblies of hexagonal MIL-88C crystallites instead of separated hexagonal crystals

that we found regarding the Fe^{3+}/BDC system, suggesting that an intergrowth took place between those MIL-88C crystals even at the initial stage. As shown in **Figure 5.11(c)**, film thickness increases drastically after 2 h incubation, suggesting a fast growth rate in vertical direction. After 4 h crystallization, the growth rate is more or less constant, but keeps at a low level (25 nm/h). Actually, lateral growth of the assembled MIL-88C crystals is also observed, as demonstrated by the increase of overall area of the separated hexagonal crystal islands. Nevertheless, given the similar film coverage, a somehow removal (dissolution and/or detachment) of assemblies of MIL-88C crystals from the substrate is anticipated for longer immersion in the heated precursors. Whereas, the MIL-88B crystals undergo an obvious growth both laterally and vertically over time until most of the surface is covered. A slow growth rate in normal direction was kept even after the coalescence of hexagonal MIL-88B crystallites.

Furthermore, since the preferential orientation along [001] direction is observed for the MIL-88C layers grown on functionalized Si surfaces with carboxylic acid termination, the carboxylates of the monolayer are considered to link with the trimers of metal-oxygen octahedra to initiate the nucleation and hence the further growth of MIL-88C crystallites along the direction normal to the substrate. The scheme of direct growth of MIL-88C crystals on carboxylic acid terminated Si surfaces is shown in **Figure 5.18**, similar to that of MIL-88B.

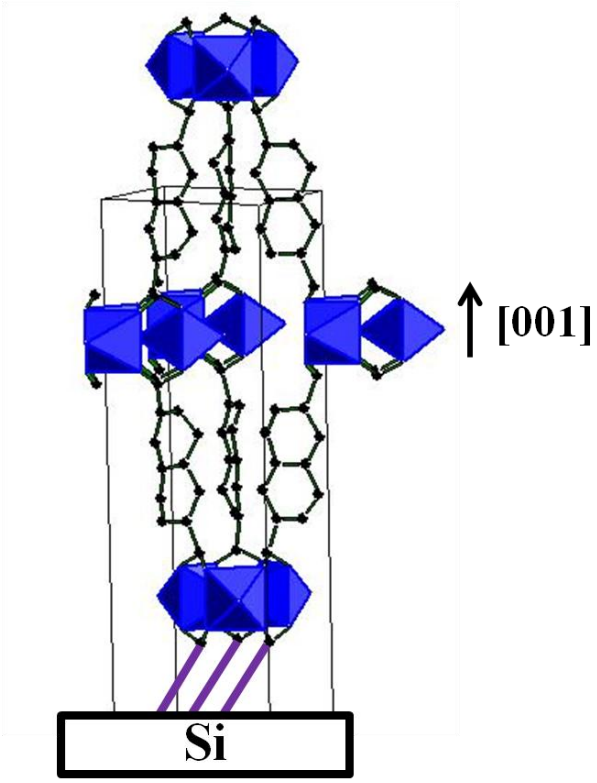

Figure 5.18 Scheme of direct growth of MIL-88C crystals onto carboxylic acid terminated Si surfaces. The monolayer grafted on Si is simplified as purple stick. The blue octahedron stands for the FeO_6 cluster and the black ball represents the carbon atom. Hydrogen atoms have been omitted for clarification.

5.4 Conclusion

Crystalline MIL-88C films were obtained on carboxylic acid terminated Si surfaces through a direct growth from DMF solutions only containing $FeCl_3 \cdot 6H_2O$ and H_2NDC. Depending on the synthesis conditions including temperature, ratio of ligand to $[Fe^{3+}]$ and $[Fe^{3+}]$ concentration, SEM results show morphologies with various surface coverage ranging from separated hexagonal crystals to layers composed of bundles of hexagonal crystallites. XRD results demonstrate that surface-bound MIL-88C crystals are preferably oriented in [001] direction and are in their solvated and swelled form. Tentative ex-situ and in-situ XRD measurements demonstrate clearly the flexibility and reversibility of MIL-88C framework during molecule adsorption and desorption. Time dependence of film growth indicates that MIL-88C crystallites nucleate after 2 h crystallization and grow vertically and laterally. Dissolution and/or detachment of crystals might happen considering the nearly unchanged film coverage over immersion time.

5.5 References

[1] C. Serre, C. Mellot-Draznieks, S. Surblé, N. Audebrand, Y. Filinchuk, G. Férey, Role of Solvent-Host Interactions That Lead to Very Large Swelling of Hybrid Frameworks, Science, 315 (2007) 1828-1831.

[2] S. Surblé, C. Serre, C. Mellot-Draznieks, F. Millange, G. Férey, A new isoreticular class of metal-organic-frameworks with the MIL-88 topology, Chem. Commun., (2006) 284-286.

Supplementary information of Chapter 5

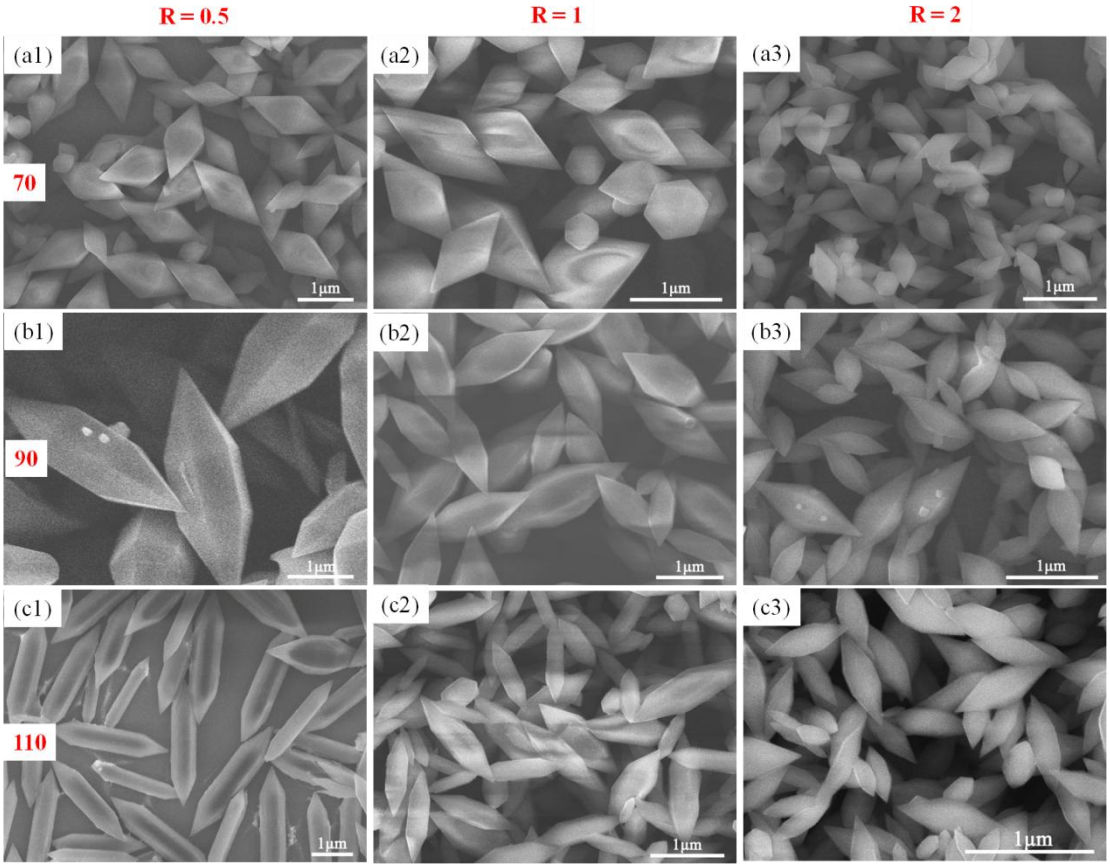

Figure S5.1 SEM images of powder formed at various conditions that were used for the film fabrication shown in **Figure 5.1**. From left to right the three columns show images of powder generated in solution with R = 0.5, R = 1 and R = 2. The different rows correspond to three different temperatures: T = 70 ℃ (a), T= 90 ℃ (b) and T = 110 ℃ (c), respectively from top to bottom. For all samples [Fe^{3+}] = 25 mM and the growth time is 24 h.

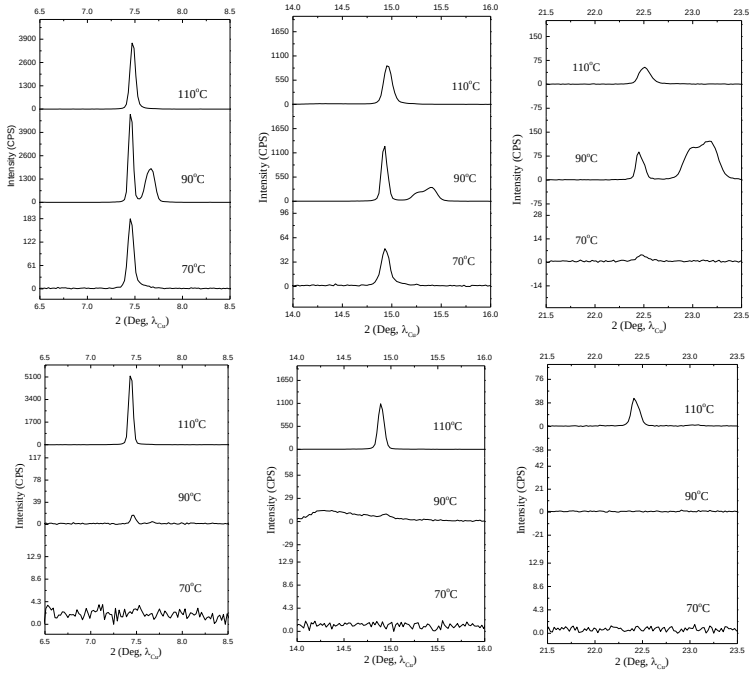

Figure S5.2 Narrow range XRD patterns of films prepared at different temperatures in Fe^{3+}/H_2NDC solutions with various R ratios. The top arrow corresponds to samples prepared at R = 1 whereas the below arrow shows the samples fabricated at R = 0.5. For all samples C[Fe^{3+}] is 25 mM and the growth time is 24 h.

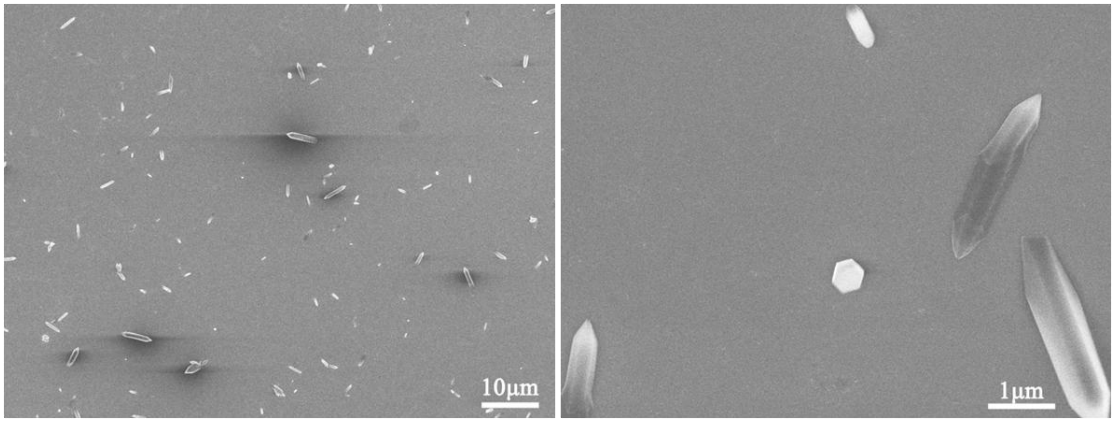

Figure S5.3 SEM images of film grown onto Si-COOH surface at 90 ^{o}C for 24 h growth with [Fe^{3+}] concentration of 1.5 mM. The ratio R is fixed at 2.

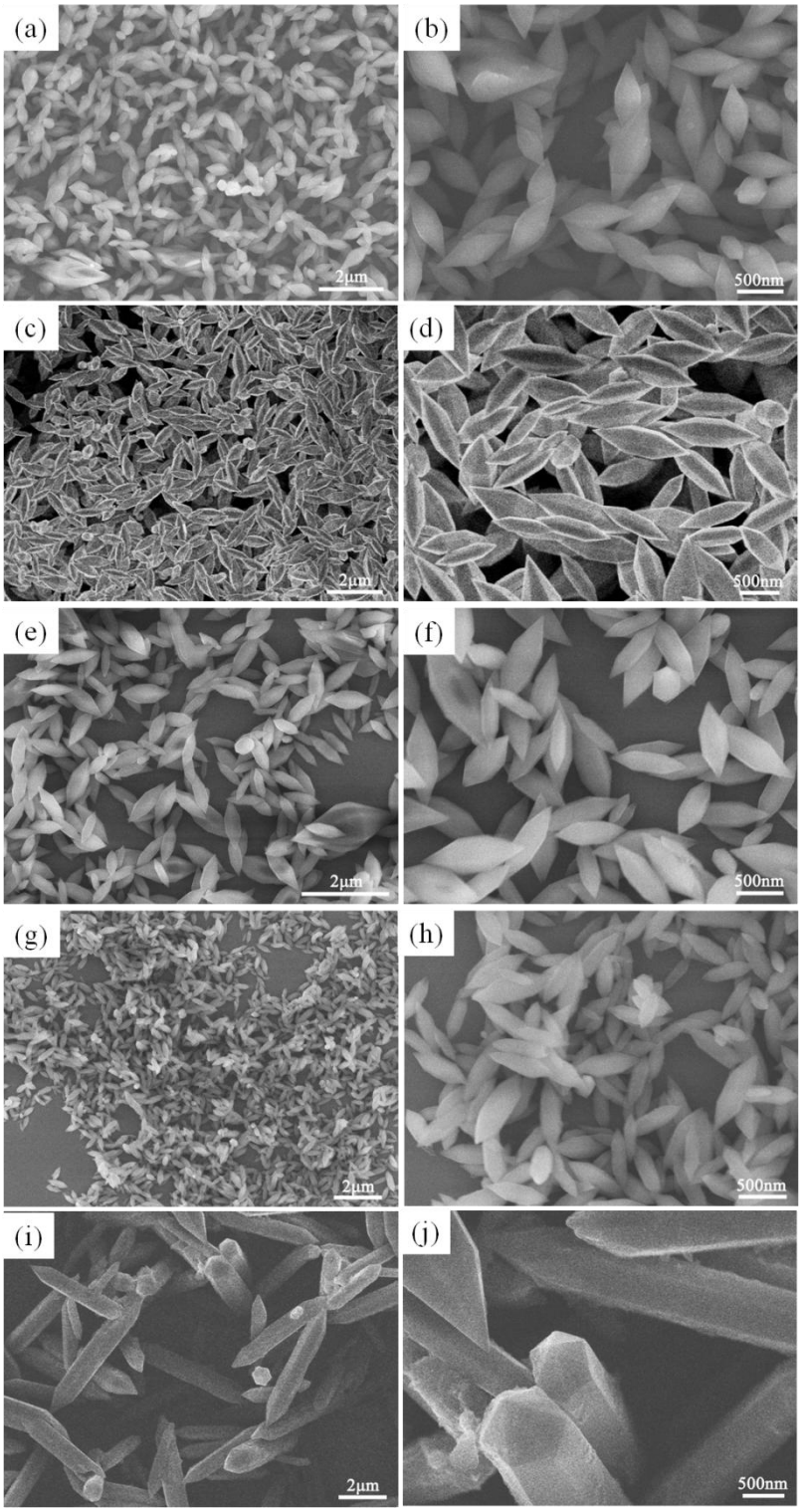

Figure S5.4 SEM images of powder formed at 90 ^{o}C with various [Fe^{3+}] concentrations that were used for the film fabrication. (a,b) 25 mM; (c,d) 12.5 mM; (e,f) 6 mM; (g,h) 3 mM and (i,j) 1.5 mM. The growth time is 24 h for all samples and R is fixed at 2.

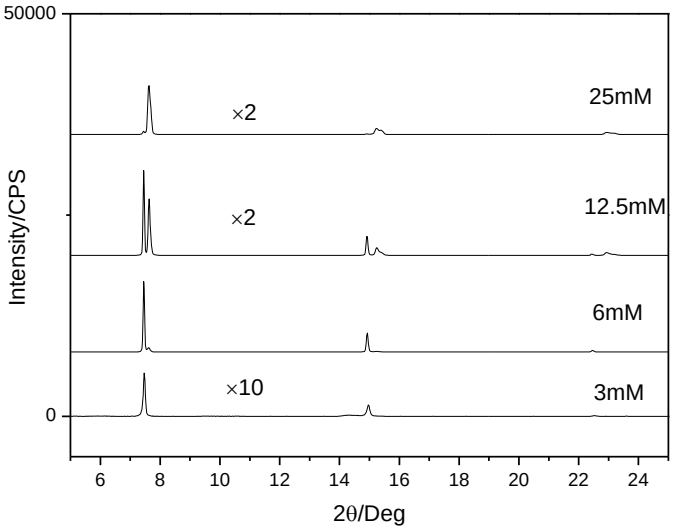

Figure S5.5 Full range XRD patterns of films prepared in Fe^{3+}/H_2NDC solution with various [Fe^{3+}] concentrations ranging from 3 mM to 25 mM for 24 h growth. The concentration is indicated next to each pattern. The ratio R is fixed at 2 and the temperature is 90 ^{o}C.

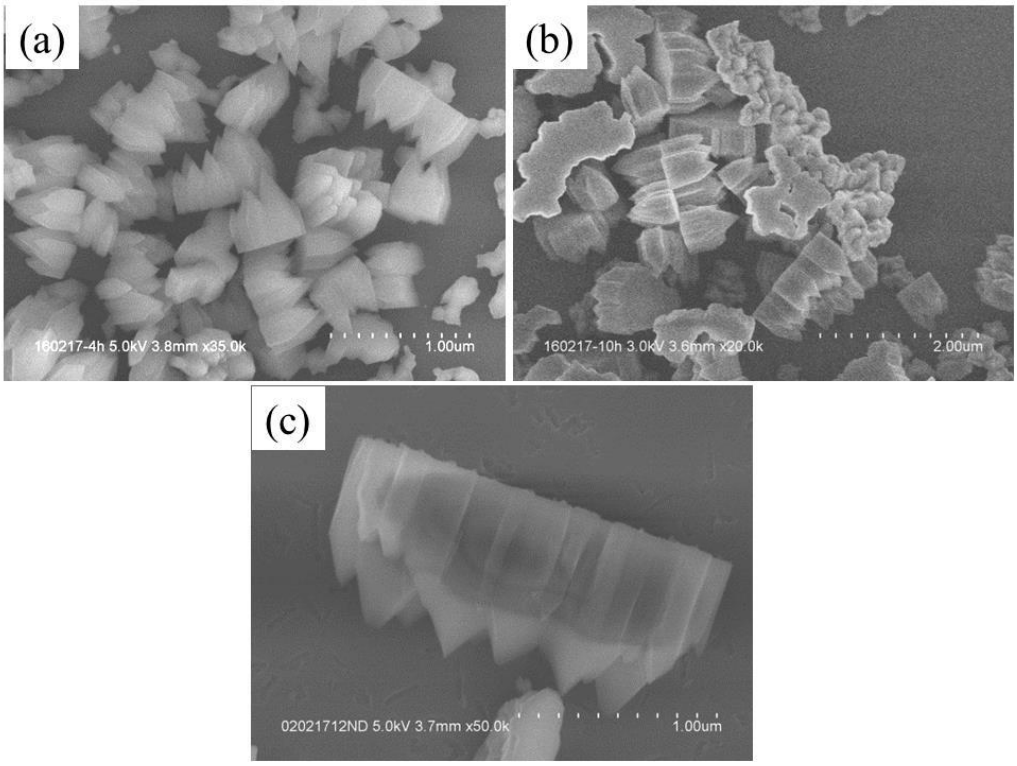

Figure S5.6 SEM images of assembled crystals formed at 90 ^{o}C at various immersion times: (a) 4 h; (b) 10 h and (c) 24 h. For all samples [Fe^{3+}] concentration is 25 mM and R is fixed at 2.

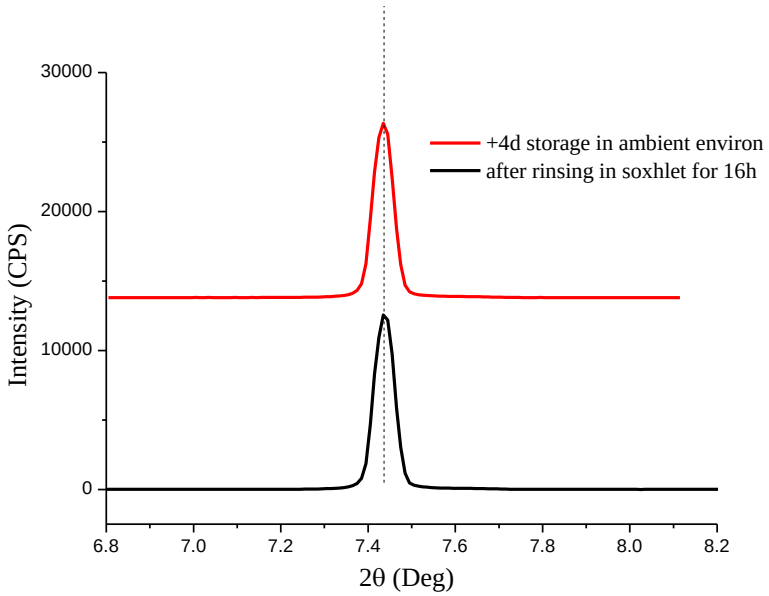

Figure S5.7 Short range XRD patterns of film after the rinsing in soxhlet with ethanol for 16 h (black) and the pattern after 4 more days storage at ambient environment (red).

General summary and conclusion

Within this thesis, two main aspects from the perspective of chemical terminations of functionalized Si surfaces and the synthesis conditions that both might affect the direct growth of Fe-based MOFs onto functionalized Si (111) surfaces from one solution containing the requisite precursors were considered.

For the Fe^{3+}/BDC system, a strong effect of surface chemistry on the formation of MOFs has been observed. Selective nucleation and controllable growth of MIL-88B (preferential orientation along [001] direction) were only found on carboxylic acid terminated surfaces whereas the formation of textured octahedral MIL-101 crystallites (111 direction) was observed irrespective of surface chemistry. The morphologies and relative amount of matters also depend on the synthesis conditions in terms of temperature, ligand to metal ratio, starting concentration and additives (proton and/or weak base).Various film morphologies from isolated crystallites to more or less continuous films made of close-packed or inter-grown crystallites for both MIL-101 and MIL-88B phases were obtained. The mechanism upon the distinct phase formation under various conditions might be discussed in the light of deprotonation of the organic linkers. Time dependence of film growth at ligand excess and at metal excess with addition of HCl demonstrates clearly that both of MIL-88B (oriented) and MIL-101 (non-oriented) crystallites follow a Volmer-Weber growth mode, whereas oriented MIL-101 crystals formed at excess of metal precursor deposited from solution and then grow up. Identification of the observed isolated layers between the hexagonal MIL-88B crystals found on acid terminated Si surfaces is difficult due to the absence of clear-cut XRD signature, possibility of the formation of different phases and the flexibility of MIL-88B and/or MIL-53 frameworks. Nevertheless, further study on the above issue and also selective growth of MIL-88B onto carboxylic acid surfaces from the dominantly homogeneous nucleation and growth of MIL-101 in solution still needs to be better understood.

For Fe^{3+}/NDC system, variable surface coverage ranging from separated hexagonal MIL-88C crystals to layers composed of isolated bundles of crystallites all with preferential (001) orientation were also observed using the same method as presented above. Evolution of MIL-88C crystallite size/shape along with crystallization time also suggests a Volmer-Weber growth mode plus Ostwald ripening. Tentative ex-situ and in-situ XRD measurements demonstrate clearly the flexibility and reversibility of MIL-88C framework during molecule adsorption and desorption.

To sum up, this dissertation enriches the concept of using SAMs with functional groups to control the orientation and/or growth of MOF films grown onto substrates. Interestingly, other aspect like solution composition which might affect the orientation and/or phase formation also needs to be considered, especially for systems in which multi-phases can be formed. In addition, the surface-attached MOFs with preferential orientation enabling the controlling of the pores/channels (in the cases of MIL-88B and MIL-88C perpendicular to the substrate) might open perspectives for the promising applications like adsorption of targeted molecules and/or chemical sensors.

université PARIS-SACLAY
ÉCOLE DOCTORALE
INTERFACES
Approches Interdisciplinaires : Fondements, Applications et Innovation

Titre : Etude de la croissance de films MOF sur des surfaces fonctionnalisées de silicium

Mots clés : Metal Organic Framework, surface fonctionnalisées, croissance, films minces

Résumé :
Ce travail porte sur l'étude de la croissance directe de couches de matériaux - métal-organiques frameworks (MOFs) - sur substrats de Si(111) fonctionnalisées avec différentes chimies de surface. Les couches de MOF à base de fer sont construites lors de la mise en contact du substrat de silicium avec une solution contenant des espèces Fe^{3+} et BDC ou NDC en proportions variables. La morphologie et la structure des couches sont étudiées par SEM, AFM et XRD.
Pour le système Fe/BDC, qui existe sous la forme MIL-101 ou MIL-88B en solution, les films sont systématiquement composés de cristallites MIL-101 isolés de forme octaédrique avec leur direction [111] perpendiculaire au plan de la surface si celle-ci est terminée par des groupements pyridyles ou hydroxyles. Sur les surfaces avec une terminaison acide (COOH), l'excès de cations métalliques favorise la formation de couches similaires (cristallites MIL-101). L'analyse des données suggère que les cristallites sont d'abord formés en solution et qu'ils s'adsorbent progressivement en formant néanmoins une liaison forte avec le substrat.
La croissance de cristaux MIL-88B avec une texture (001) est uniquement observée sur des surfaces fonctionnalisées COOH et en présence d'un excès de ligands. L'introduction d'une faible quantité de HCl favorise cependant la formation de couches polycristallines et continues de MIL-101. L'addition de triéthylamine favorise la formation de MIL-88B. L'analyse des données indique que la formation des couches MIL-88B et MIL-101 (en présence de HCl) suit une loi de croissance de Volmer-Weber sur les surfaces COOH, au cours duquel les cristaux isolés nuclèent et se développent latéralement et verticalement sur la surface. L'ancrage des cristallites (MIL-88B) sur la surface est cependant faible.
Des films texturés MIL-88C ont également été obtenus sur des surfaces COOH. Les mesures expérimentales ex situ et in situ de XRD démontrent clairement la flexibilité et la réversibilité du cadre MIL-88C pendant l'adsorption et la désorption des molécules.

Title : Study of the growth of MOF films on functionalized Si surfaces

Keywords : Metal Organic Framework, Surface functionalization, Growth, Thin films

Abstract :

This work investigates the direct growth of materials - metal-organic frameworks (MOFs)-onto functionalized Si(111) substrates with different surface chemistries. Fe-based MOFs layers are obtained by exposing the silicon substrate to a solution containing Fe^{3+} and BDC or NDC in variable amounts. The morphology and structure of MOFs films are investigated by SEM, AFM and XRD.
For Fe^{3+}/BDC system, which may exist as MIL-101 and MIL-88B phases in solution, films always consist of isolated octahedral MIL-101 crystallites with the [111] direction perpendicular to the plane of pyridyl and hydroxyl terminated surfaces. On acid terminated surfaces (COOH), similar layers are obtained (isolated MIL-101 crystallites) when metal cations are in excess in solution. Data analysis suggests that crystallites are first formed in solution and then adsorbed on the surface with further growth. A strong linkage with the substrate is however observed.
The growth of MIL-88B crystals with (001) texture is only observed onto COOH-functionalized surfaces and greatly favored by an excess of ligand in solution. In such conditions, addition of small amount of HCl promotes the formation of polycrystalline and continuous MIL-101 layers. Addition of triethylamine favors formation of MIL-88B crystals. Data analysis suggests that both the MIL-88B and MIL-101 (in the presence of HCl) crystallites follow a Volmer-Weber growth mode, during which isolated crystals formed and grow laterally and vertically on the surface. A weak adhesion of MIL-88B crystals with the substrate is nevertheless found.
Textured MIL-88C films are obtained on COOH-terminated surface in all conditions. Ex-situ and in-situ XRD measurements demonstrate clearly the flexibility and reversibility of MIL-88C framework during molecule adsorption and desorption.

Université Paris-Saclay
Espace Technologique / Immeuble Discovery
Route de l'Orme aux Merisiers RD 128 / 91190 Saint-Aubin, France